

Investigating Fracture Network Creation during Hydraulic
Stimulation in Enhanced Geothermal Reservoirs

A DISSERTATION
SUBMITTED TO THE DEPARTMENT OF
ENERGY RESOURCES ENGINEERING
AND THE COMMITTEE ON GRADUATE STUDIES
OF STANFORD UNIVERSITY
IN PARTIAL FULFILLMENT OF THE REQUIREMENTS
FOR THE DEGREE OF
DOCTOR OF PHILOSOPHY

Ayaka Abe

August 2021

© 2021 by Ayaka Abe. All Rights Reserved.

Re-distributed by Stanford University under license with the author.



This work is licensed under a Creative Commons Attribution-Noncommercial 3.0 United States License.

<http://creativecommons.org/licenses/by-nc/3.0/us/>

This dissertation is online at: <https://purl.stanford.edu/bg829nj2270>

I certify that I have read this dissertation and that, in my opinion, it is fully adequate in scope and quality as a dissertation for the degree of Doctor of Philosophy.

Roland Horne, Primary Adviser

I certify that I have read this dissertation and that, in my opinion, it is fully adequate in scope and quality as a dissertation for the degree of Doctor of Philosophy.

Anthony Kovsky

I certify that I have read this dissertation and that, in my opinion, it is fully adequate in scope and quality as a dissertation for the degree of Doctor of Philosophy.

Hamdi Tchelepi

Approved for the Stanford University Committee on Graduate Studies.

Stacey F. Bent, Vice Provost for Graduate Education

This signature page was generated electronically upon submission of this dissertation in electronic format. An original signed hard copy of the signature page is on file in University Archives.

Abstract

During hydraulic stimulation treatment in an enhanced geothermal (EGS) reservoir, it has been suggested that a complex fracture network including both preexisting natural fractures and newly formed fractures is created. In this stimulation mechanism, a fracture propagating from a preexisting natural fracture and the interaction of newly formed fractures and preexisting natural fractures play an important role in the creation of a fracture network. Analyzing the interaction between preexisting fractures and newly formed fractures during hydraulic stimulation is thus necessary to understand the creation of a fracture network. We approached to this research question with laboratory and numerical experiments for an EGS reservoir where large preexisting fractures dominate. Laboratory scale hydraulic fracturing experiments were conducted to investigate how a fracture network is created when a propagating hydraulic fracture and a preexisting fracture interact. The physics-based numerical model developed in this work was used to investigate fracture network creation from a small scale area including a small number of fractures to a reservoir scale with tens of fractures. We analyzed the geological factors that affect the fracture network patterns through the laboratory and numerical experiments. We observed that the stress state and preexisting fracture orientation affect the fracture propagation pattern in the laboratory experiments. The numerical analysis shows that the stress field induced by an upstream hydraulic fracture causes asymmetric distributions of normal and shear stresses along the preexisting fracture when they intersect, which resulted in initiation of a wing crack from the fracture tip on the side with larger angles. The numerical results also showed that the complexity of the created fracture network is affected by the fracture intersection angle, stress state, and injection rates. We reviewed past EGS projects and analyzed the stimulation mechanism during their hydraulic stimulation treatment. This study implies that stimulating a reservoir with poorly oriented preexisting fractures may result a

complex and broad shaped fracture network, which would be beneficial for energy recovery.

Acknowledgements

This dissertation would not have been possible without the contribution of many people who supported me academically and mentally. Most importantly, I would like to thank my advisor Dr. Roland Horne for his tireless support and thoughtful guidance. Roland always gave me any support and encouragement, and provided me the independence to proceed my research. I was able to try challenging things that extended my research thanks to his patience and support.

I am thankful to my committee, Dr. David Pollard, Dr. Hamdi Tchelepi, Dr. Tony Kavscek, and Dr. Lou Durlofsky for their insights and suggestions on my dissertation. Their feedback have undoubtedly strengthened my understanding and the quality of the work. Thank you Dr. Pollard for always listened to me carefully and directed me to the right direction. I was inspired by many of his papers and how he approaches research questions.

I was fortunate to have opportunities to discuss and receive invaluable feedback from Dr. Wei Cai, Dr. Paul Segall, Dr. Mark Zoback, Dr. Mohammad Karimi-Fard, Dr. Adrian Lew, and Dr. Mark McClure. I would like to thank Dr. Elliot Kim for his support and guidance on the laboratory hydraulic fracturing experiments. I would like to thank Dr. Elizabeth Ritz for providing her code for DDM with complementarity. This research code was used to compute the mechanical changes of fractures by being integrated to the numerical model used in this work.

Thank you my current and former colleagues in the Stanford Geothermal Program, Halldora Gudmundsdottir, Dr. Rita Okoroafor, Dr. Noe Pollack, Dr. Yuran Zhang, Jabs Aljubran, Dr. Carla Co, Dr. Xuhua Gao, Dr. Adam Hawkins, Dr. Renfeng Jiang, Dr. Kewen Li, Dr. Jack Norbeck, Dr. Anna Suzuki, and Dr. Yang Wong. I am grateful to share lots of fond memories with you all. I have had a wonderful time with my officemates, Farzaneh, Manju, Medalsa, Karine, and Menyao. I appreciate the fun, relaxing, and helpful conversation we had at office. I would also like to thank the staffs

from the ERE department, Joanna, LyriSSa, Arlene, Diane, Yolanda, and Eric for their continuous and invaluable support.

The experiences of internship at Ormat Technologies were great opportunities too. I would like to thank my mentor Mr. John Murphy for his support and guidance on my internship projects. I was able to learn how my research could contribute to the real-world problems and learned how to handle real dataset from commercial geothermal fields. The financial support of the Ito Foundation for International Education Exchange, by Ms. Margot Leidig through the grant of the Calvin Enderlin Earth Sciences Fellowship, the industrial affiliates of the Stanford Center for Induced and Triggered Seismicity are gratefully acknowledged.

Finally, I would like to express my deepest gratitude to each of my family for their encouragement and support. Especially I thank my husband Keigo and our son Kento for unqualified love, encouragement, and support.

Contents

Abstract.....	iv
Acknowledgements	vi
List of Tables	xii
List of Figures.....	xiv
1 Introduction.....	1
1.1 Background and Motivation	1
1.2 Scope of Work	4
2 Numerical Modeling Methodology.....	6
2.1 Introduction.....	6
2.2 Simulator Overview	7
2.3 Fracture Deformation.....	9
2.4 Fracture Propagation.....	11
2.5 Aperture Calculation.....	14
2.6 Fluid Flow between Fracture Surfaces	16
2.7 Propagating fracture cross/follow criteria.....	17
2.8 Sequential Method	20
2.9 Verification of the numerical model	22
2.9.1 Hydraulic fracture propagation.....	22
2.9.2 Wing crack propagation	29
2.9.3 Propagating fracture cross/follow criteria	35
2.9.4 Verification of Modified DDM	38
2.10 Summary	42
3 Investigating the Effect of Wing Cracks on EGS Reservoir Permeability Enhancement.....	44

3.1	Introduction.....	44
3.2	Wing crack propagation driven by fluid injection	46
3.2.1	Wing crack propagation from varied fracture angles	46
3.2.2	Wing crack propagation from varied injection pressure	51
3.3	Discussion and Conclusion	53
4	3D-Printed Core Hydraulic Stimulation Experiments	55
4.1	Introduction.....	55
4.2	Analytical model.....	56
4.3	Methodology	58
4.3.1	Methodology Comparison with Lab Experiment Data.....	61
4.3.2	The Offset of Discontinuous Crossing	62
4.3.3	Discussion	63
4.3.4	Laboratory Scale Experiments Using 3D Printed Core Samples	64
4.4	Sample Materials	64
4.5	Experiment Preparation	66
4.5.1	Determination of the Frictional Coefficient	66
4.5.2	Determination of the Stress Intensity Factor of the Initial Crack.....	66
4.6	Numerical Results.....	68
4.7	Experimental Results	70
4.7.1	Test Case 1	70
4.7.2	Test Case 2	73
4.7.3	Test Case 3	75
4.8	Discussion and Summary.....	76
5	Cement Core Hydraulic Stimulation Experiments.....	78
5.1	Introduction.....	78
5.2	Laboratory scale hydraulic fracturing experiment.....	81
5.2.1	Sample Preparation.....	81
5.2.2	Determination of Material Properties.....	82
5.2.3	Experiment Apparatus	84
5.2.4	Results	85
5.3	Numerical Analysis.....	88
5.3.1	Numerical Experiment Setup	89

5.3.2	Comparison between Laboratory and Numerical Experiments.....	91
5.3.3	Analysis of Deformation and Stress Concentrations.....	93
5.1	Analysis of Aperture along newly formed fractures.....	96
5.2	Discussion.....	98
5.3	Summary.....	102
6	Investigating Stress Shadowing Effects and Fracture Propagation Patterns.....	104
6.1	Introduction.....	104
6.2	Investigating the effect of fracture orientation and stress state	106
6.2.1	Parameters	107
6.2.2	Propagating fracture cross or follow decision	108
6.2.3	Results on varied orientations and stress states.....	108
6.2.4	Analysis of stresses along natural fracture	113
6.3	Investigating the effect of fracture size.....	117
6.3.1	Results	118
6.4	Comparison of Injection Rate	119
6.4.1	Results	120
6.5	Discussion and Summary.....	123
7	Fracture Network Creation and Stimulation Mechanism of Basel- 1 and Fenton Hill Phase-2 EGS Reservoirs.....	127
7.1	Introduction.....	127
7.1.1	Fenton Hill Phase-2 EGS Project	128
7.1.2	Basel EGS Project	130
7.2	Simulator Overview.....	134
7.3	Investigation on Fracture Network Creation and Stimulation Mechanism of Basel-1 and Fenton Hill Phase-2 EGS Reservoirs	137
7.3.1	Initial conditions, boundary conditions, and assumptions.....	138
7.3.2	Discrete Fracture Network (DFN) Stochastic Generation.....	138
7.3.3	Choosing an Aperture Model	141
7.3.4	Analysis of the Fracture Cross/Follow Criteria in Fenton Hill Phase-2 Reservoir	144
7.3.5	Analysis of the Fracture Cross/Follow Criteria in Basel EGS Reservoir.....	145

7.3.6	Model parameters	146
7.4	Results.....	149
7.4.1	Fenton Hill Phase-2 EGS reservoir	149
7.4.2	Basel EGS reservoir	153
7.4.3	Comparison between Fenton Hill and Basel cases.....	156
7.5	Discussion and Summary.....	157
8	Conclusion.....	160
8.1	Summary.....	160
8.2	Recommendations for Future Work	162
9	Bibliography.....	164

List of Tables

Table 2.1: Parameters used in the numerical simulation	25
Table 2.2: Summary of the comparison	26
Table 2.3: Parameters used in the numerical simulation	30
Table 3.1: Parameters used in the numerical simulation	47
Table 3.2: Wing crack length after injection. θ is the angle of the main preexisting fracture toward the least principal stress, w is wing crack length, f is the main preexisting fracture half length.....	48
Table 3.3. Wing crack length and its average angles for a preexisting fracture with $\theta = 75$ degrees.	52
Table 4.1: Comparison with Lab Experiment Results.....	61
Table 4.2: Sample material properties	65
Table 4.3: Stress property during the experiment	68
Table 4.4: Parameters used in the numerical experiment.....	69
Table 4.5: The summary of the experiment results	70
Table 4.6: Stress properties during the experiment	71
Table 4.7: Stress property during the experiment	74
Table 4.8: Stress property during the experiment	75
Table 5.1: Sample material properties	82
Table 5.2: Stress properties during the experiment to determine the critical stress intensity factor	84
Table 5.3: The results of the experiments	86

Table 5.4: Photos of the fracture pattern created during the experiment. HF shows a hydraulic fracture, NF shows a preexisting natural fracture, and WC shows a wing crack.	87
Table 5.5: Parameters used in the numerical simulation	90
Table 5.6: The results of the numerical experiments	91
Table 5.7: The average aperture and its standard deviations of six points from the hydraulic fracture and the wing crack in test case #3.....	98
Table 7.1: Parameters used for Fenton Hill setting	147
Table 7.2: Parameters used for Basel setting.....	147
Table 7.3: Parameters used in the numerical simulation for both Fenton Hill and Basel settings	148

List of Figures

Figure 2.1: The magnitude of the largest principal stress. The orange triangle represents a propagating fracture, and the yellow line represents an intersecting preexisting fracture with 90 degrees. Left: $K_I = 1.0$, $K_{II} = 0.0$, Center: $K_I = 0.6$, $K_{II} = 0.53$, Right: $K_I = 0.3$, $K_{II} = 0.71$ 19

Figure 2.2: Flow chart for this numerical simulation. Superscript v is the number of iterations in the current time step. The variable with superscript v means the value is the one calculated from the current iteration. The variable with superscript $v-1$ means the value is the one calculated from the previous iteration. 21

Figure 2.3: Left: The schematic of a fracture with the PKN model (Gidley et al., 1989), Right: The schematic of a fracture with the GdK model (Geertsma & de Klerk, 1969)..... 24

Figure 2.4: Schematic of the geometry of the injection well 26

Figure 2.5: Fracture half-length comparison among numerical, KGD and PKN models with the injection rate $1.0e-3$ [m³/s] 27

Figure 2.6: Fracture half-length comparison among numerical, KGD and PKN models with the injection rate $1.0e-2$ [m³/s] 27

Figure 2.7: Fracture half-length comparison among numerical, KGD and PKN models with the injection rate $1.0e-1$ [m³/s] 28

Figure.2.8 Fracture half-length comparison between different grid sizes..... 28

Figure 2.9: Left: normalized wing crack length with different stress ratio by analytical and numerical models, Right: normalized Mode I stress intensity factor and the normalized wing crack length. 32

Figure 2.10: The critical values K_I and K_{II} required for propagation under mixed Mode I and Mode II displacements from this model (right) and by Thomas and Pollard (1993). 33

Figure 2.11: (a) Fracture trajectory of a preexisting fracture orienting at 60 degrees and wing cracks, (b) Wing crack trajectory, (c) preexisting fracture and wing crack trajectory by Mutlu and Pollard (2008), (d) Observed wing crack in the field (Joussineau et al., 2007). 33

Figure 2.12: (a) The normal and shear displacements of a preexisting fracture orienting at 60 degrees and wing cracks, (b) Normal displacement of the main preexisting fracture, (c) Normal displacement of the main preexisting fracture by Mutlu and Pollard (2008), (d) Normal displacements of the wing crack , (e) Normal displacements of the wing crack by Mutlu and Pollard (2008) and the analytical solution by Lehner and Kachanov (1996). 34

Figure 2.13: Criterion if fracture crosses or not for orthogonal intersection angle. 36

Figure.2.14: An example of the propagating fracture cross/follow criteria by a fracture with $K_I = 0.6$ and $K_{II} = 0.53$. Left: the fracture cross/follow criteria applied to the side with weaker stress concentration, Right: the fracture cross/follow criteria applied to the side with stronger stress concentration. 37

Figure 2.15: Fracture half-length comparison among numerical, KGD and PKN models with the injection rate $1.0e-3 [m^3/s]$ 39

Figure.2.16: Fracture half-length comparison among numerical, KGD and PKN models with the injection rate $1.0e-2 [m^3/s]$ 39

Figure 2.17: Fracture half-length comparison among numerical, KGD and PKN models with the injection rate $1.0e-1 [m^3/s]$ 40

Figure 2.18: Left: normalized wing crack length with different stress ratio by analytical and numerical models, Right: normalized Mode I stress intensity factor and the normalized wing crack length..... 41

Figure 2.19: (a) Fracture trajectory of a preexisting fracture orienting at 60 degrees and wing cracks, (b) Wing crack trajectory,..... 41

Figure 2.20: (a) The normal and shear displacements of a preexisting fracture orienting at 60 degrees and wing cracks, (b) Normal displacement of the main preexisting

fracture by Mutlu and Pollard (2008), (c) Normal displacements of the wing crack by Mutlu and Pollard (2008) and the analytical solution by Lehner and Kachanov (1996).	42
Figure 3.1: The stimulation result for the wing crack for a fracture $\theta=45$. Top: Fracture trajectory, Left bottom: Normal and shear displacements at the end of stimulation when $P_f=23$ MPa and after the stimulation when $P_f=18$ MPa, Right bottom: Fracture transmissivity	49
Figure 3.2: The stimulation result for the wing crack for a fracture $\theta=60$. Top: Fracture trajectory, Left bottom: Normal and shear displacements at the end of stimulation when $P_f=23$ MPa and after the stimulation when $P_f=18$ MPa, Right bottom: Fracture transmissivity	50
Figure 3.3: The stimulation result for the wing crack for a fracture $\theta=60$. Top: Fracture trajectory, Left bottom: Normal and shear displacements at the end of stimulation when $P_f=23$ MPa and after the stimulation when $P_f=18$ MPa, Right bottom: Fracture transmissivity	51
Figure 3.4: Top: Wing crack trajectory, Bottom: Wing crack transmissivity, Left: The maximum BHP 23 MPa, Middle: The maximum BHP 24 MPa, Right: The maximum BHP 25 MPa.....	53
Figure 4.1: An example of a fracture process zone and fracture-chance segment ($\sigma_{xx}=70$ MPa, $\sigma_{yy}=35$ MPa, $\sigma_{xy}=0$ MPa, and $T_0=-10$ MPa). Fracture-chance segment is shown in green line, fracture process zone is the area surrounded by the blue line. A mode I fracture is located at $x < 0$ and $y = 0$	59
Figure 4.2: (Left) An example of discontinuous crossing observed in the field, (Right) A sketch of a sample showing both continuous and discontinuous crossing (Renshaw & Pollard ,1995)	62
Figure 4.3: (Left) Discontinuous offset length r , (Right) The relationship between discontinuous offset length and $T_0 - \sigma_{yy}^r$ ($K_{IC} = 1\text{MPa} \cdot \sqrt{m}$).....	63
Figure 4.4: Sketches of the sample.....	65

Figure 4.5: (Left) Ground surfaces of the cut, (Center and right) Initial crack	66
Figure 4.6: Samples used to measure the frictional coefficient.....	66
Figure 4.7: (Left) A sketch of the sample, (Right) The sample used in this experiment	67
Figure 4.8: The sample after hydraulic fracturing.....	68
Figure 4.9: (Left) Numerical results with parameters in Table 4.4 and the varied stress ratio and the fracture angle. A hydraulic fracture is expected to cross in the area with blue dots, it is expected to terminate in the area with black dots, and pink dots show the area categorized in pattern3, where a propagating fracture is expected to cross half of the cases. (Right) Analytical results of Renshaw and Pollard (1995) with parameters in Table 4.4. A propagating fracture is expected to cross in the area above the line...	69
Figure 4.10: Pressure profiles and water flow rate during the experiment	72
Figure 4.11: The sample after experiment.....	72
Figure 4.12: The sample after the experiment.....	74
Figure 4.13: Pressure profiles and water flow rate during the experiment	74
Figure 4.14: The sample after experiment.....	75
Figure 4.15: Pressure profiles and water flow rate during the experiment	75
Figure 5.1: Left: A photo of the sample before the experiment, Middle: Shape of the waxed paper embedded in the sample, Right: Sketches of the cross section of the sample, both are side views with 90 degrees difference.....	80
Figure 5.2: Experiment apparatus and sample assembly.....	85
Figure 5.3: Photo of a wing crack surface (Test case #6)	87
Figure 5.4: Injection pressure and flow rate profiles during the test case with preexisting fracture orienting at 45 degrees and uniaxial stress 5.25MPa (Test case #5).....	88

Figure 5.5: Numerical experiment setup. Left: The symmetry setting with image displacements across $y = 0$ to render the bottom boundary condition with the full-space solution, Right: the main simulation domain..... 89

Figure 5.6: Summary of the results: The red line shows the location of the injection well; the black lines are the preexisting fractures, while the blue lines show the newly formed fractures, including a hydraulic fracture initiated from the injection well and wing cracks. 92

Figure 5.7: The wellbore fluid pressure observed during numerical simulation. Left: The case with preexisting fracture orientation of 45 degrees and the uniaxial stress 5.25 MPa (Test case #5), Right: The case with preexisting fracture orientation of 60 degrees and the uniaxial stress 7.0 MPa (Test case #4). 92

Figure 5.8: The shear displacement and the normal and shear stresses along the preexisting fracture orienting at 45 degrees with uniaxial stress 5.25 MPa (Test case #5). HF indicates a hydraulic fracture, NF indicates a preexisting natural fracture, and WC indicates a wing crack. 95

Figure 5.9: The normal and shear displacements and the normal and shear stresses along the preexisting fracture orienting at 60 degrees with uniaxial stress 5.25 MPa (Test case #3). HF indicates a hydraulic fracture, NF indicates a preexisting natural fracture, and WC indicates a wing crack. 95

Figure 5.10: Left: The contour of the magnitude of σ_{xx} , Right: The displacement field. Both show the domain when the length of the wing crack is 5 cm with a preexisting fracture orienting at 45 degrees and uniaxial stress 5.25 MPa. 96

Figure 5.11: Left: The photo of the sample cut in half after experiment (Test case #3), Center: CT data 3D visualization. White area expresses low density region, Right: CT data two-dimensional visualization showing the wing crack (above) and the hydraulic fracture (below). White area expresses high density region. HF indicates a hydraulic fracture, NF indicates a preexisting natural fracture, and WC indicates a wing crack. 96

Figure 6.1: Model configuration: An injection well located at the center of the domain initiates a hydraulic fracture (HF). The propagating hydraulic fracture intersects a preexisting natural fracture (NF) at each side. 107

Figure 6.2: Summary of the results: Each plot shows the fracture pattern at the end of simulation of 100 sec. The red dot shows the location of the injection well; the blue lines are the preexisting fractures, while the black lines show the newly formed fractures, including a hydraulic fracture initiated from the injection well and wing cracks. 110

Figure 6.3: The fracture trajectories and fluid pressures when the preexisting fractures are oriented at 60 degrees to the maximum horizontal stress at the end of simulation. 110

Figure 6.4: The normal stress and shear stress distribution along a preexisting fracture with the stress ratio 1.1 when a propagating fracture hits the preexisting fracture. The dotted lines show the normal and shear stress by the remote stresses. The plot shows that the side that initiates a wing crack ($x = 0.5$ m to 1.0 m) is under larger shear stresses and smaller normal stresses compared to the other side ($x = 0.0$ m to 0.5 m). 111

Figure 6.5: The fluid pressure at the propagation front of a wing crack fracture vs wing crack length 111

Figure 6.6: The shear displacements of a preexisting fracture orienting at 60 degrees. Left: when the stress ratio is 1.1, Right: when the stress ratio is 3.0. The left plot shows that the side that initiates a wing crack ($x = 0.5$ m to 1.0 m) has larger shear displacement while the other side has no shear displacement ($x = 0.0$ m to 0.5 m). . 112

Figure 6.7: The shear displacements of a preexisting fracture orienting at 45 degrees. Left: when the stress ratio is 1.1, Right: when the stress ratio is 3.0. The left plot shows that the side that initiates a wing crack ($x = 0.5$ m to 1.0 m) has larger shear displacement compared to the other side ($x = 0.0$ m to 0.5 m). 114

Figure 6.8: The normal and shear stresses acting on a natural fracture orienting at 15, 30, 45, 60, and 75 degrees, respectively with net pressure of 1MPa, and fracture length of 6m..... 114

Figure 6.9: The fluid pressure needed to initiate a wing crack on each side of a natural fracture. The results of the experiments are shown in blue, yellow, and green boxes. 117

Figure 6.10: Summary of the results: Each plot shows the fracture pattern at the end of simulation of 100 sec. The red dot shows the location of the injection well; the blue lines are the preexisting fractures, while the black lines show the newly formed fractures, including a hydraulic fracture initiated from the injection well and wing cracks. The upper plots show the cases with a natural fracture with a length of 2 m, the lower plots show the cases with a natural fracture with a length of 5 m..... 118

Figure 6.11: Simulation setup. An injection well located at the center of the domain initiates a hydraulic fracture (red dot). Propagating hydraulic fracture and wing cracks intersect to preexisting natural fractures (blue lines). 120

Figure 6.12: Fracture trajectories and fluid pressures in each stress ratio and injection rate at the end of simulation time. 122

Figure 6.13: Transmissivity of fractures with the stress ratio 1.5 cases (low injection rate: above, high injection rate: below) 122

Figure 6.14: Left: The location of the natural fracture and x axis, Right: The Coulomb stress along the natural fracture with high injection and low injection rate cases. The fluid pressures inside intersecting fractures are assumed to be the same as the wellbore fluid pressure, which are 12.0 MPa with the high injection rate case and 10.5MPa with the low injection rate case. 123

Figure 7.1: Mohr diagram showing the the coefficient of friction 0.6. 1) hydrostatic condition, 2) 79.6MPa, maximum BHP during stimulation..... 134

Figure 7.2: Flow chart for this numerical simulation. Superscript v is the number of iterations in the current time step. The variable with superscript v means the value is

the one calculated from the current iteration. The variable with superscript v-1 means the value is the one calculated from the previous iteration.	137
Figure.7.3: Left: Fracture length distribution, Center: Fracture orientation distribution, Right: An illustration of a realization of initial natural fracture geometry used in the simulation.	140
Figure 7.4: Left: Fracture length distribution, Center: Fracture orientation distribution, Right: An illustration of a realization of initial natural fracture geometry used in the simulation.	141
Figure 7.5: Wellbore fluid pressure. Left: with shear dilation angle of 0 degree, Right: with shear dilation angle of 2 degrees.	142
Figure 7.6: Wellbore fluid pressure. Left: with shear dilation angle of 0 degree, Right: with shear dilation angle of 2 degrees.	143
Figure 7.7: The propagating fracture cross/follow criteria with left-lateral shear displacement ($K_{II} < 0$). The area above the blue line shows the condition where a propagating fracture crosses a preexisting natural fracture intersecting with 53 degrees.	144
Figure 7.8: The propagating fracture cross/follow criteria with right-lateral shear displacement ($K_{II} > 0$). The area above the blue line shows the condition where a propagating fracture crosses a preexisting natural fracture intersecting with 22°	146
Figure 7.9: Bottomhole pressure at 3.6km depth and injection rate during the Expt. 2018 at well EE-2 (extracted from Fig. 6-5 in Brown et al., 2012).....	150
Figure.7.10: Fracture network created during the numerical experiment. The black lines are preexisting fractures and the blue lines are newly formed wing cracks.	151
Figure 7.11: Fluid pressure distribution after injection.	151
Figure 7.12: Observed and simulated bottomhole pressures and observed and input injection rates.....	152
Figure 7.13: Distribution of the microseismicity.	152

Figure 7.14: Wellhead pressure and injection rate (Häring et al., 2008)..... 153

Figure 7.15: Fracture network created during the numerical experiment. The black lines are preexisting fractures and the blue lines are newly formed wing cracks. Red circle shows the injection well location..... 154

Figure 7.16: Fluid pressure distribution after injection. The red dot shows the injection well location. 154

Figure 7.17: The observed and simulated BHP and flow rate. The bottomhole pressure was calculated by adding the hydrostatic pressure at 5km depth and the effect of wellbore friction. The bottomhole pressure was calculated from the wellhead pressure profile including the effect of friction. The effect of pressure loss due to the friction was less than 0.3 MPa. 155

Figure 7.18: Distribution of the microseismicity on the top view..... 155

Figure 7.19: Plots showing the criteria of fracture cross/follow in Fenton Hill and Basel settings. The orange line shows the friction coefficient 0.6 used in this study. 156

Chapter 1

1 Introduction

1.1 Background and Motivation

Fractures are the main pathway for fluid in a reservoir such as enhanced geothermal systems (EGS) and unconventional oil and gas where the permeability is very low. Reservoir permeability is enhanced by performing hydraulic stimulation, which is a key technology that has been used widely both in unconventional oil and gas and geothermal applications. The reservoir is stimulated by shear stimulation of preexisting natural fractures and by propagation of newly created hydraulic fractures. Propagation of newly created hydraulic fractures improves fracture connectivity and increases the contact area for fluid that flows between wells and reservoir by creating a fracture network in the reservoir.

Observations of microseismicity show that a complex fracture network is often created during a hydraulic stimulation treatment in an EGS reservoir. The main mechanism of reservoir permeability enhancement was long believed to be shear dilation of preexisting natural fractures. However, the facts that: 1) bottomhole pressure exceeded the least principal stress, 2) pressure limiting was observed, and 3) fluid injection from a wellbore was through a preexisting fracture in most of the EGS projects, suggest that newly formed fractures propagated in the reservoir during stimulation (McClure & Horne, 2014). This stimulation mechanism including both creating new fractures and stimulating preexisting natural fractures has been called “Mixed-Mechanism Stimulation”, originally suggested in the unconventional oil and gas industry (Maxwell et al., 2013; Weng, 2015; Weng et al., 2011; Wu & Olson, 2014b) and later suggested to be the common stimulation mechanism

in enhanced geothermal reservoirs (Jung, 2013; Kamali & Ghassemi, 2016; McClure, 2014; McClure & Horne, 2014; Norbeck et al., 2018).

Since the mineback experiments by Warpinski and Teufel (1987), it has long been observed that a hydraulic fracture often follows a preexisting fracture and branches into multiple fractures, and makes a complex fracture network. Field observations in the Fenton Hill EGS project in the United States implied that a complex fracture network was created by the mixed-mechanism stimulation (Brown et al., 2012; Norbeck et al., 2018). A fracture network including both natural fractures and hydraulic fractures propagated from the injection well has been created in the EGS Collab project, United States (Fu et al., 2020; Kneafsey et al., 2019, 2020). A reoriented microseismic cloud was observed due to a strong stress heterogeneity and the intersection between the hydraulic fracture and natural fractures during the hydraulic fracturing experiment in the Grimsel Test Site, Switzerland (Amann et al., 2018; Dutler et al., 2020, 2019; Gischig et al., 2020). Also, several other intermediate scale hydraulic stimulation experiments have been conducted to better understand hydraulic stimulation mechanisms such as the projects at Bedretto Underground Laboratory for Geoenergies in Switzerland (Gischig et al., 2020; Shakas et al., 2020), Äspö Hard Rock Laboratory, Sweden (López-Comino et al., 2017; Niemz et al., 2020; Zang et al., 2017), Utah FORGE, United States (Moore et al., 2020), and the Reiche Zeche underground lab in Freiberg, Germany (Boese et al., 2020, 2021; Dresen et al., 2019).

The mixed-mechanism stimulation is now widely accepted to model a hydraulic stimulation in geothermal reservoirs (e.g. Kamali & Ghassemi, 2016, 2018; Maxwell, Weng, Kresse, & Rutledge, 2013; Norbeck et al., 2018; Norbeck & Shelly, 2018; Weng et al., 2011). In mixed-mechanism stimulation, it is suggested that new fractures are initiated from sheared preexisting natural fractures and propagate in the reservoir. In hydraulic stimulation in an EGS reservoir, the target formation is often granitoid which has high tensile strength. Because it is hard to initiate new fractures from a wellbore drilled into granitoid, injected fluid flows into preexisting natural fractures which then slide and dilate at a lower pressure than required for initiating a new fracture. Therefore it is likely that new fractures are created from the tips of stimulated preexisting natural fractures as stress concentrates at the crack tips (McClure & Horne, 2014). The resulting fracture

network complexity is strongly influenced by the distribution of the preexisting natural fractures and in-situ stress state (Weng, 2015).

How hydraulic fractures intersect with preexisting natural fractures has been extensively studied experimentally and numerically, especially in unconventional oil and gas settings. In an unconventional oil and gas reservoir, hydraulic fractures dominate the fracture network most of the cases, so a microseismic cloud expands along the direction perpendicular to the least principle stress. On the other hand, in an EGS reservoir, the microseismic cloud often migrates broadly, indicating that natural fracture orientations and distribution are also key factors that affect hydraulic fracture treatment. Indeed, unlike in unconventional oil and gas reservoirs, larger natural fractures dominate the fracture network in EGS reservoirs. This is because the matrix rock is stiffer in EGS reservoirs, and natural fractures are larger compared to those in unconventional reservoirs. However, how a preexisting natural fracture plays a role in creating a fracture network in combination with hydraulic fractures has not been fully investigated. It is observed that new fractures are initiated from sheared preexisting natural fractures from near their edges or at points of stress concentration where shearing is inhibited. This secondary fracture initiating from a sheared preexisting natural fracture is called a “wing crack” or a “splay fracture”, which has been observed in laboratory-scale experiments (e.g. Abe et al., 2021; Erdogan & Sih, 1963; Zoback, 2007) and field scale observations (e.g. Joussineau et al., 2007; Mutlu & Pollard, 2008; Thomas & Pollard, 1993). Also, how fluid flows in a fracture network created by hydraulic stimulation remains unclear.

Fracture propagation from a natural fracture and the interaction between newly formed fractures and preexisting fractures play an important role in creation of a complex fracture network. Especially in an EGS reservoir, preexisting fractures are expected to be large and dominant in a reservoir, while planar hydraulic fractures extending from an injection well dominate in an unconventional oil/gas reservoir. Hydraulic stimulation is performed in a less permeable geothermal reservoir, which may mean that the preexisting fractures are poorly connected. To better understand how fractures interact mechanically, how newly formed fractures propagate in a reservoir, and how fluid flows in a fracture network, it is essential to develop a model based on fracture mechanics and fluid mechanics. To better understand fracture network creation, we developed a physics-based

numerical model that combines fluid flow between fracture surfaces, fracture deformation, and fracture propagation driven by fluid injection. We investigated the stimulation mechanism in an EGS reservoir with numerical and laboratory experimental approaches and applied them to analyze field scale experiments which are explained in the following chapters.

1.2 Scope of Work

The main focus of this research was to investigate the mechanism of fracture network creation including both preexisting fractures and newly formed fractures in a tight reservoir by hydraulic stimulation. The key unanswered questions are related to modeling mechanical interaction between fractures and local stress change caused by fluid injection and fracture opening/shearing, and applications of those models to investigate practical problems in the industry.

The physics controlling each phenomenon of the reservoir stimulation and the fracture network creation affect one another in complex ways. Developing a physics-based numerical model that combines each mechanism will enable us to interpret the stimulation from observable data such as well logs, microseismicity migration, and wellbore pressure response. We describe the framework and each component of the model in Chapter 2 and verify its accuracy and applicability for the problems of interest. In Chapter 3, we describe the use of the developed model to simulate a wing crack propagation from a sliding preexisting fracture driven by fluid injection. How a wing crack contributes to reservoir permeability and storativity was investigated. Chapter 4 and 5 describe the use of cement and 3D-printed core samples to investigate the interaction between newly formed fractures and a preexisting fracture. The samples include embedded preexisting fracture inside the core. The results were then analyzed by the numerical model. These chapters also serve as the verification of the numerical model because the laboratory experiments are considered as true results that can verify the numerical results. Chapter 6 details the use of the numerical model to investigate the relationship between state of stress, orientation of preexisting fractures, injection rate, and fracture network patterns. The stress acting on a fracture and fracture displacements were analyzed to better understand what factors make

pattern differences. The topic of Chapter 7 is reservoir scale hydraulic stimulation modeling by using the observed data from two past EGS projects. The wellbore pressure and microseismicity migration were analyzed and compared between the numerical results and actual data. In this work, we started from development and verification of the model, conducted small scale numerical simulation and core scale laboratory experiments, then finally performed reservoir scale investigation.

Chapter 2

2 Numerical Modeling Methodology

2.1 Introduction

Numerical modeling of hydraulic stimulation for EGS and unconventional oil and gas reservoirs is used for deciding stimulation design, optimizing production, and assessing the risk of injection-induced seismicity. During a hydraulic stimulation treatment, injected fluid flows mainly between preexisting and newly created fracture surfaces because of the low permeability of the matrix rock in the reservoir where hydraulic stimulation is performed. Given that the fluid pressure between fractures drives fracture deformation and propagation, the stimulation process largely depends on the interaction between fluid flow and geomechanical changes in the reservoir. Traditional hydraulic fracturing semianalytical models such as the PKN model (Nordgren, 1972; Perkins & Kern, 1961) and the GdK model (Geertsma & de Klerk, 1969) assume one biwing tensile crack propagating perpendicular to the least principal stress in the reservoir. However, it is known that the preexisting natural fractures exist in the reservoir and they play an important role on the reservoir stimulation. Especially in EGS reservoirs, large preexisting natural fractures dominate in the reservoir and affect the overall stimulation results. Therefore the interaction between fluid and fracture, and also between fracture and another fracture need to be better understood.

The physical processes controlling each phenomenon of the fracture network creation complexly interact one another. Injected fluid changes the traction acting on the fracture surfaces, the fractures then deform and propagate, which changes fluid flow by creating volume to store fluid in the reservoir. Physics-based numerical modeling that combines each mechanism will enable us to interpret the observable data such as

well logs, microseismicity migration, and wellbore pressure response. To better understand the mechanics of hydraulic stimulation and the reservoir during and after the simulation, we developed a physics-based numerical models and described in this chapter.

2.2 Simulator Overview

The simulator explained in this chapter was used to model fracture network creation during hydraulic stimulation in low permeable reservoirs such as EGS and unconventional oil and gas reservoirs. The reservoir we modeled is a full-space, horizontal, isotropic, and homogeneous two-dimensional domain with vertical fractures assuming the plane-strain condition. Linear elastic fracture mechanics (LEFM) is assumed. Heat transfer and thermoelasticity are not considered. Matrix rock permeability is negligible and no leak-off is considered. The preexisting natural fractures initially have no deformations. The orientation of remote stresses is uniform. Fluid flow is single-phase. The boundary condition of the injection well is specified as a constant-rate mass flow rate.

With the boundary element method, only the fractures are discretized and the surrounding rock in the reservoir is not. Also, the boundary element method is not capable of including heterogeneity in the surrounding domain. Therefore, the model assumes temperature is constant and surrounding rock is not permeable. There has been a study that combined FEM and BEM to incorporate the heat transfer, leak-off, and corresponding thermoporoelasticity changes (Norbeck et al., 2016). However, in this study, we focused on the behavior of fractures and their propagation and interactions, therefore, we used BEM for effective computation. Heat transfer may be important to model reservoir permeability enhancement because thermal contraction may be one of the mechanisms of shear stimulation, however is a separate issue. With regard to leak-off, granitic basements usually have permeability as low as 1 microdarcy ($1.0 \times 10^{-18} \text{ m}^2$) so the leak-off to the pores is negligible, although there may be cross-cutting natural fractures that do not contribute to flow but contribute to fluid storage. These should be considered by extending this research in future study. EGS reservoirs are located deep

underground in respect to fracture sizes, so the effect of the ground surface is negligible. The assumption of vertical fractures was made because the dominant fracture orientations have been almost vertical (Deichmann et al. 2014; Brown, 1989), in most of the EGS sites. Fractures are discretized into grids. Deformation, stresses, and fluid flow are calculated at the center of each grid and they are assumed to be uniform in the grid.

Fracture deformation is computed by the two-dimensional displacement discontinuity boundary element method (DDM). The flow equations and DDM are solved by fully implicit sequential strategy following (Kim et al. 2011; McClure 2012; Norbeck 2016). DDM is solved in two different methods: the first method is to employ the complementarity formulation and solved with PATH solver (Ritz et al., 2015), and the second method is to modify the coefficient matrix of the original DDM to overcome the known problem that fracture surfaces can overlap with compressive normal stress and to include the friction problem (McClure, 2012). Fracture deformation and fluid flow are coupled by sequential method.

To make this model computationally efficient and to focus on the main research questions, there are some limitations. This model does not consider fluid leak-off to the matrix rock and heat transfer. The fluid density and viscosity are constant. Although there are some limitations by not considering the matrix fracture mass and heat transfer, the model is computationally effective and appropriate for modeling fluid flow during hydraulic stimulation, fracture propagations, and mechanical interactions between fracture which occur over a short time period. To model fracture network with a small number of fractures, in Chapter 3, 5, and 6, we used DDM with PATH solver described in this chapter. To model a reservoir scale in Chapter 7, we used the DDM modified by McClure (2012) and generated preexisting fractures stochastically. The way the DDM and flow equation are coupled is also different for the reservoir scale model. The details of this method are described in Chapter 7.

The following sections describe the theories and implementation of each element of this model. The model is finally verified by comparing to analytical models, semianalytical models, and other numerical results.

2.3 Fracture Deformation

In this model, fracture deformation including shear displacements, apertures, and propagation are calculated numerically. To model fracture deformation, which is the main component of this model, we used two-dimensional displacement discontinuity boundary element method (DDM) from Ritz et al., (2015), with integrated complementarity. The DDM handles problems including domains that have slit-like fractures. The DDM is a powerful method that is useful to compute the stress shadowing effect, which is the stress field induced by the deformation of other nearby fractures in a computationally effective way because only the fractures are discretized. The original implementation of the DDM needed to be updated to model wing crack propagation because it does not support the frictional contact problems. The DDM also allows two fracture surfaces overlapping each other with compressive normal stress, which is not physically appropriate (Crouch & Starfield, 1983). To overcome these limitations, the DDM solutions with a complementarity algorithm were evaluated by Mutlu and Pollard (2008). The authors concluded that the complementarity algorithm increases accuracy in the boundary value problems involving frictional interfaces in contact. They also showed that curved wing crack propagation was modeled reasonably with the DDM with complementarity. Ritz et al. (2012) later presented a two-dimensional DDM in combination with a mixed complementarity problem solver (Dirkse & Ferris, 1993; Ferris & Munson, 1999, 2000). The authors validated the model with intersecting, branching, splayed, curved, and other types of nonplanar fractures. The complementarity algorithm keeps contact boundary conditions along the cracks that are physically appropriate so that variable friction and frictional strength can be included in the DDM model.

In the DDM, a fracture is treated as one-dimensional line discretized into elements with each element having its normal and shear stresses and normal and shear displacements. Normal stress σ_{nn}^i and shear stress σ_{ns}^i acting on the i -th element ($i = 1$ to N) of a fracture, are related to normal displacement D_n^j and shear displacement D_s^j for all other elements including itself by $j = 1$ to N .

$$\begin{cases} \sigma_{nn}^i = A_{nn}^{ij} D_n^j + A_{ns}^{ij} D_s^j \\ \sigma_{ns}^i = A_{sn}^{ij} D_n^j + A_{ss}^{ij} D_s^j \end{cases} \quad \text{for } i, j = 1 \text{ to } N, \quad (2.1)$$

where A_{nn}^{ij} , A_{ns}^{ij} , A_{sn}^{ij} , and A_{ss}^{ij} are the coefficient of influence from the DDM formulation by Crouch and Starfield (1983). By using the DDM formulation, the mechanical equilibrium is expressed as:

$$\text{Normal stress: } \sigma_n^f = \sigma_n^r + P_f + A_{nn} D_n + A_{ns} D_s, \quad (2.2)$$

and:

$$\text{Shear stress: } \sigma_s^f = \sigma_s^r + A_{sn} D_n + A_{ss} D_s, \quad (2.3)$$

where σ_n^r and σ_s^r are the remote stresses, and σ_n^f and σ_s^f are the traction acting at the center of each boundary element. σ_n takes tension as positive, σ_s takes right lateral as positive, D_n is negative when it is open, and D_s is positive in left lateral by following (Crouch & Starfield, 1983).

The complementarity formulation is modified from the original formulation by Ritz et al. (2015) to include the mechanically induced stresses induced by previous slip on the fracture. The shear displacement at the current time step is expressed by adding the relative change occurring at the current time step to the shear displacement at the previous time step as:

$$\Delta D_s^t = D_s^t - D_s^{t-1}, \quad (2.4)$$

where ΔD_s^t is the change of the shear displacement induced due to the current shear slip. ΔD_s^t is decomposed into the slip into the right lateral slip ΔD_s^R and the left lateral slip ΔD_s^L following Ritz et al. (2015) as:

$$\Delta D_s^t = (\Delta D_s^L)^t - (\Delta D_s^R)^t. \quad (2.5)$$

As described by the Coulomb criterion, the fracture sticks when the shear stress is smaller than the frictional strength and it slides when the shear stress is equal to the frictional strength (Jaeger et al., 2007). This statement is expressed in the complementarity formulation as:

$$|\sigma_s^f| \leq -f\sigma'_n + S_f \perp 0 \leq \Delta D_s^t. \quad (2.6)$$

The symbol \perp means either the left hand side or the right hand side is an equality and the product of the two components is zero. When the shear stress and the shear displacement are decomposed into the right lateral component and the left-lateral component,

$$0 \leq -\sigma_s^f - f\sigma'_n + S_f \perp 0 \leq (\Delta D_s^R)^t, \quad (2.7)$$

$$0 \leq \sigma_s^f - f\sigma'_n + S_f \perp 0 \leq (\Delta D_s^L)^t, \quad (2.8)$$

where $\sigma'_n = \sigma_n^r + P_f$ is the effective normal stress. The effective normal stress and the normal displacement are also in the complementarity relationship because the fracture is open when the normal component of traction equilibrates with the fluid pressure, and the fracture is closed when the effective normal stress is compressive:

$$D_n \leq 0 \perp \sigma_n^f \leq 0. \quad (2.9)$$

The equations 2.7, 2.8, and 2.9 are the modified complementarity equations used in this study.

2.4 Fracture Propagation

Fractures propagate when the stress intensity factor at the fracture tip reaches the critical stress intensity factor, which is a material-constant value. The stress intensity factor was introduced by Irwin (1957) based on the stress analysis around a fracture tip assuming linear elastic fracture mechanics (LEFM). LEFM is known to be accurate to compute the stress field induced by a fracture tip in a brittle material. The stress intensity factors define the state of stress around a fracture tip in an elastically loaded material. Irwin (1957) wrote the stress field near a fracture tip in a closed form solution by using the stress intensity factor. The expression of the stress intensity factor depends on the shape of the fracture. For example, the stress intensity factor for a Mode I opening mode slit-like crack tip is $K_I = \sqrt{\pi a}$, where a is the fracture half length. Because the stress intensity factor depends on the shape of the fracture, this expression is not suitable for a numerical modeling which include curved fractures. Olson (1991) suggested the

expressions to calculate the stress intensity factors from the displacements at the elements of a fracture tip computed numerically by the DDM. The stress intensity factors for Mode I, K_I and a sliding mode Mode II, K_{II} are given as:

$$K_I = 0.798 \frac{D_n E \sqrt{\pi}}{4(1-\nu^2)\sqrt{P}}, \quad (2.10)$$

and:

$$K_{II} = 0.798 \frac{D_s E \sqrt{\pi}}{4(1-\nu^2)\sqrt{P}}, \quad (2.11)$$

where D_n and D_s are the normal and shear displacements for a fracture tip element respectively, E is the Young's modulus, ν is Poisson's ratio, and P is the length of the fracture tip element (Mériaux & Lister, 2002; Olson, 1991). The author verified the equations with the analytical solutions for straight cracks. Thomas and Pollard (1993) also verified that these stress intensity factors match with the analytical solution that describes the stress intensity factors of a circular arc crack. Mériaux and Lister (2002) updated the correction factor to have better accuracy from 0.806 to 0.798. Ritz et al. (2012) then confirmed that these stress intensity factors by DDM with complementarity showed a good match with analytical stress intensity factors. The fracture propagation trajectory can be calculated by the maximum circumferential stress theory (Erdogan & Sih, 1963). Erdogan and Sih (1963) stated the theory for a crack extension in a brittle material under plane strain condition that:

- (a) The crack extension starts at its tip in radial direction,
- (b) The crack extension starts in the plane perpendicular to the direction of greatest tension.

Erdogan and Sih (1963) discussed that this maximum stress theory should be regarded as a practical design, because the assumption that the crack extension starts at its tip is based on the stress singularity at the fracture tip, which is a nonphysical assumption (Mutlu & Pollard, 2008). Barenblatt's theory of so-called equilibrium cracks suggested the finite normal stress applied ahead of the fracture tip and the surfaces of the fracture close smoothly (Barenblatt, 1962). With this assumption, the stress intensity

factor needs to be zero for a fracture criterion, and the cohesive forces act near the fracture tip to reduce the stress concentration along the near-tip region. Mutlu and Pollard (2008) applied this theory to model the propagation of multiple wing cracks behind the fracture tip numerically. Their numerical results with the linear cohesive end zone showed that the maximum tangential tension appeared just behind the fracture tip. This theory is more realistic based on the field observation that wing cracks initiate behind the fracture tip and multiple wing cracks propagate from near the fracture tip. Multiple wing cracks can propagate from a single natural fracture because there are notches or key stones that make stress concentrations. Although Barenblatt's equilibrium crack concept is more realistic to model fracture propagation from a fracture with Mode II deformation, we assumed uniform cohesion and the coefficient of friction, and assumed a single fracture propagation from the fracture tip to simplify the problem. This assumption may underestimate the effect of wing cracks on the reservoir permeability enhancement because it is more likely that multiple wing cracks propagate from one preexisting natural fracture.

Fracture propagation starts in a plane normal to the direction of least principal stress such that $\tau_{r\theta} = 0$. The angle of maximum tangential tension θ_0 derived from the state of stresses near a fracture tip is given in polar coordinates as:

$$\sigma_{\theta}\sqrt{2\pi r} = \text{constant} = \cos\frac{\theta_0}{2} \left[K_I \cos^2\frac{\theta_0}{2} - \frac{3}{2}K_{II} \sin\theta_0 \right] = K_{Ic}, \quad (2.12)$$

$$\tau_{r\theta} = \frac{1}{\sqrt{2\pi r}} \cos\frac{\theta_0}{2} [K_I \sin\theta_0 + K_{II}(3\cos\theta_0 - 1)] = 0, \quad (2.13)$$

give:

$$\theta_0 = \pm\pi, \quad (2.14)$$

$$K_I \sin\theta_0 + K_{II}(3\cos\theta_0 - 1) = 0. \quad (2.15)$$

These equations give the propagation angle for pure Mode I $\theta_0 = 0^\circ$ and for pure Mode II $\theta_0 = -70.5^\circ$ (Ingraffea, 1987). Thomas and Pollard (1993) rewrote the original equations and solved directly for θ_0 as:

$$\theta_0 = \sin^{-1}\left(\frac{K_{II}}{K_I} \cos\phi\right) - \tan^{-1}\left(3\frac{K_{II}}{K_I}\right). \quad (2.16)$$

Crack extension begins when the maximum circumferential stress reaches a critical stress intensity factor,

$$\cos \frac{\theta_0}{2} \left[K_I \cos^2 \frac{\theta_0}{2} + \frac{3}{2} K_{II} \sin \theta_0 \right] \geq K_{IC}, \quad (2.17)$$

where θ_0 is the fracture propagating direction, K_{IC} is the critical stress intensity factor (Ingraffea, 1987). Thomas and Pollard (1993) showed through laboratory experiments that this method reproduced a smoothly curved crack path.

In the present work, a propagating wing crack is divided into small boundary elements. New elements are added when the propagation criterion is satisfied at the crack tip. We assumed that fracture propagation occurs with pure Mode I propagation and did not consider Mode II and Mode III propagation. The Mode I critical stress intensity factor of rocks is typically $\sim 1/10$ smaller than the Mode II and the Mode III critical stress intensity factors so that the propagated fracture segment has only Mode I opening displacement (Mutlu & Pollard, 2008). Also, pure Mode II and Mode III propagations are rarely observed in the field or in experiments with brittle materials (Petit & Barquins, 1988).

2.5 Aperture Calculation

Fractures in a reservoir have rough surfaces and varied apertures. Also, flow in a fracture under a compressive stress occurs as fracture surfaces are not parallel smooth plates (Neuzil & Tracy, 1981). The relationship between the fracture surface roughness and fracture deformation has been studied experimentally and numerically. The works done by Bandis et al. (1981, 1983) investigated the joint deformation in relation to varied roughness. The authors performed the experiments to measure the fracture deformation by applying normal and shear loads. Based on the measured data, 2 mm of shear displacement caused the aperture of 0.03 to 0.25 mm (Bandis et al., 1983) and also applying 30 MPa of normal stress reduced 0.25 mm to 0.04 mm of aperture depending on the roughness of the interface (Barton et al., 1985).

Empirical models are defined to describe the apertures as a function of effective normal stress and shear displacements (Barton et al., 1985; Willis-Richards et al., 1996). Co et al. (2017) investigated the effects of fracture roughness on the aperture by varying the normal and shear stresses applied to the two parallel rough surfaces with DDM. The authors demonstrated the flow channeling effect due to the fracture roughness. They also showed that the permeability of a closed fracture increases as the shear stress applied increases and compressive stress applied decreases.

In this work, we employed the equation derived by Willis-Richards et al. (1996) to compute the aperture of a closed fracture. In this study, “closed” fracture is a fracture with the compressive normal stress acting along the fracture surfaces. The fracture surfaces are in contact but fluid still flow between the surfaces because of the roughness of the surfaces. There are two types of aperture, void aperture and hydraulic aperture. Void aperture is the pore volume per unit area of a fracture, and hydraulic aperture is the effective aperture for flow in a fracture. In this research, void aperture and hydraulic aperture are assumed to be the same as we assume that the fracture surfaces are relatively smooth. The aperture of a closed fracture is given by:

$$e = \frac{e_0}{1+9\sigma'_n/\sigma_{nref}} + D_s \tan \frac{\varphi}{1+9\sigma'_n/\sigma_{nref}}, \quad (2.18)$$

where e_0 is the aperture at zero effective stress, φ is the dilation angle, σ_{nref} is the effective normal stress applied to cause a 90% reduction of aperture (Willis-Richards et al., 1996).

When the element opens, we assume that the total aperture is the sum of the normal displacement computed by DDM and the hydraulic aperture as:

$$E = D_n + e_0. \quad (2.19)$$

The transmissibility is calculated with the cubic law (Zimmerman & Bodvarsson, 1996) as:

$$T_{i,j} = k_i A_i = \frac{w_i E_i^3}{12}, \quad (2.20)$$

where A_i is the area of the interface between two fracture elements, k_i is the permeability of the fracture element, w_i is the width of the element, and E_i is the total aperture. Karimi-Fard et al., (2004) introduced equations to show the geometric part of the transmissibility of single fracture elements and fracture intersection. The geometric transmissibility with two elements is:

$$T_{i,j} = \frac{\alpha_i \alpha_j}{\alpha_i + \alpha_j} \text{ with } \alpha_i = \frac{k_i A_i}{D_i}, \quad (2.21)$$

where D_i is the distance between the center of the two elements. Transmissibility of an intersection with multiple fractures is:

$$T_{i,j} = \frac{\alpha_i \alpha_j}{\sum_{k=1}^n \alpha_k}, \quad (2.22)$$

where n is the number of connections at an intersection.

2.6 Fluid Flow between Fracture Surfaces

Hydraulic stimulation treatments are performed in low permeability rock. In this study, the permeability of matrix rock was considered to be negligible. Although there are some limitations by not considering the matrix fracture mass and heat transfer, the model is computationally effective and appropriate for modeling fracture propagations which occur over a short time period.

Fluid flow in a fracture can be assumed to be a single-phase flow. The unsteady-state fluid mass conservation equation in a fracture is written as:

$$\frac{\partial(\rho E)}{\partial t} = \nabla \cdot (q_{flux}) + s_a, \quad (2.23)$$

where ρ is the fluid density, t is time, q_{flux} is mass flow rate per cross sectional area of flow, E is the aperture, and s_a is a source term (mass per time) such as well injection or production (Aziz & Settari, 1979). Fluid is assumed to flow in a fracture with smooth parallel walls. By using the cubic law, the same equation is derived by assuming Darcy's flow for the flow in porous media (Zimmerman & Bodvarsson, 1996). Assuming Darcy's flow in one dimension and applying the cubic law, q_{flux} is:

$$q_{flux} = -\frac{e^3 w \rho}{12\mu} \Delta P, \quad (2.24)$$

where μ is the fluid viscosity, and P is the fluid pressure. This expression is also known as the Plane Poiseuille flow which is the solution to the Navier-Stokes equation for the flow between those parallel plates. The Plane Poiseuille flow describes laminar flow between two parallel plates (Zimmerman & Bodvarsson, 1996). Here we assumed the fluid density and viscosity are constants and do not depend on the temperature and pressure.

The flow equations and fracture deformation are solved by a fully implicit sequential strategy (Kim et al., 2011; McClure, 2012; Norbeck, 2016). In the sequential scheme, the fracture deformation is solved first with fixed fluid pressures, then the flow equation is solved with determined fracture displacements in each iteration until the convergence criteria are satisfied, The Newton-Raphson method is used to solve the system of nonlinear equations as the transmissivity matrix and the accumulation term are nonlinear.

2.7 Propagating fracture cross/follow criteria

The analytical model for the propagation criterion was developed by Renshaw and Pollard (1995) for an orthogonal intersection and later extended for a nonorthogonal intersection (Gu & Weng, 2010; Gu et al., 2011). Renshaw and Pollard (1995) conducted theoretical and experimental work to analyze the mechanism of younger fractures propagating across older fractures oriented perpendicular to the approaching fracture. They stated the criterion as “compressional crossing will occur if the magnitude of the compression acting perpendicular to the frictional interface is sufficient to prevent slip along the interface at the moment when the stress ahead of the fracture tip is sufficient to initiate a fracture on the opposite side of the interface”. The stress field induced by the fracture tip was calculated and the condition where the slip along the frictional interface would not occur was derived based on the Mohr–Coulomb failure criterion. Their model is based on the linear elastic fracture mechanics solution for the stresses near a fracture tip and calculates the stresses needed to cause slip on the

preexisting interface. Gu and Weng (2010) applied the criterion for a fracture approaching a frictional interface at a nonorthogonal angle. The authors later verified their model with laboratory experiments (Gu et al., 2011).

This propagating fracture crossing or following a preexisting natural fracture has been discussed in a context of hydraulic fracturing in an unconventional oil and gas reservoir where a propagating hydraulic fracture mainly has Mode I displacements. However, when a fracture with Mode I and Mode II deformations such as a wing crack propagates in a reservoir, induced stress fields by both Mode I and II deformations need to be considered. Wu and Olson (2014) suggested the formulation that includes the stress field induced both by Mode I and Mode II deformations based on the principle of superposition as:

$$\sigma_{ij}^{(total)} = \sigma_{ij}^{(remote)} + \sigma_{ij}^{(I)} + \sigma_{ij}^{(II)}, \quad (2.25)$$

where $\sigma_{ij}^{(remote)}$ is the remote stresses, $\sigma_{ij}^{(I)}$ is the stresses induced by the mode I deformation, and $\sigma_{ij}^{(II)}$ is the stresses induced by the Mode II deformation. The singular stress field ahead of a crack tip under Mode I and Mode II loading in an isotropic linear elastic material under the plane-strain condition are expressed in closed form (Anderson, 2005):

$$\sigma_{xx}^{(I)} = \frac{K_I}{\sqrt{2\pi r}} \cos \frac{\theta}{2} \left(1 - \sin \frac{\theta}{2} \sin \frac{3\theta}{2}\right), \quad \sigma_{xx}^{(II)} = \frac{K_{II}}{\sqrt{2\pi r}} \left[-\sin \frac{\theta}{2} \left(2 + \cos \frac{\theta}{2} \cos \frac{3\theta}{2}\right)\right], \quad (2.26)$$

$$\sigma_{yy}^{(I)} = \frac{K_I}{\sqrt{2\pi r}} \cos \frac{\theta}{2} \left(1 + \sin \frac{\theta}{2} \sin \frac{3\theta}{2}\right), \quad \sigma_{yy}^{(II)} = \frac{K_{II}}{\sqrt{2\pi r}} \sin \frac{\theta}{2} \cos \frac{\theta}{2} \cos \frac{3\theta}{2}, \quad (2.27)$$

$$\sigma_{xy}^{(I)} = \frac{K_I}{\sqrt{2\pi r}} \cos \frac{\theta}{2} \sin \frac{\theta}{2} \cos \frac{3\theta}{2}, \quad \sigma_{xy}^{(II)} = \frac{K_{II}}{\sqrt{2\pi r}} \cos \frac{\theta}{2} \left(1 - \sin \frac{\theta}{2} \sin \frac{3\theta}{2}\right), \quad (2.28)$$

where K_I and K_{II} the Mode I and the Mode II stress intensity factors respectively, r and θ are the polar coordinate with the origin at the fracture tip, assuming tension is positive.

Maximum magnitude of the stress components is found at the critical radius $r = r_c$ where the least principal stress is the same as the tensile strength. The area within $r = r_c$ is referred to as the fracture process zone where the inelastic deformation exists. Then the normal stress and the shear stress along the frictional interface are calculated and plugged in to the Mohr–Coulomb failure criterion:

$$|\sigma_s(r = r_c, \theta =)| < \mu\sigma_n(r = r_c, \theta =) + S_0, \quad (2.29)$$

where $\sigma_s(r = r_c, \theta =)$ and $\sigma_n(r = r_c, \theta =)$ are the shear and the normal stresses acting along the preexisting fracture at the distance r_c , from the intersection, respectively, μ is the frictional coefficient, and S_0 is cohesion.

With Mode I fracture, the intersecting fractures cross/follow criteria depends on the stress state, the frictional coefficient, and the intersection angle. When the propagating fracture has both Mode I and Mode II deformations, the cross/follow criteria is also affected by the ratio of the Mode I and the Mode II stress intensity factors. Figure 2.1 shows the magnitude of the largest principal stress induced by a fracture with different ratio of Mode I and Mode II stress intensity factors. The critical Mode I stress intensity factor is assumed to be $1.0 \text{ MPa} \cdot \sqrt{m}$. The propagation of a fracture with Mode I and II occurs when the maximum circumferential stress reaches a critical, material-constant value as:

$$\cos \frac{\theta_0}{2} \left[K_I \cos^2 \frac{\theta_0}{2} + \frac{3}{2} K_{II} \sin \theta_0 \right] \geq K_{IC}, \quad (2.30)$$

where θ_0 is the fracture propagating direction, K_{IC} is the critical stress intensity factor (Ingraffea, 1987).

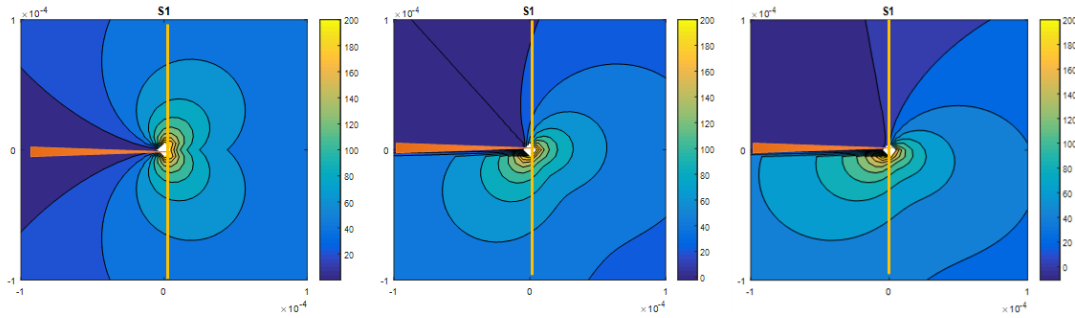


Figure 2.1: The magnitude of the largest principal stress. The orange triangle represents a propagating fracture, and the yellow line represents an intersecting preexisting fracture with 90 degrees. Left: $K_I = 1.0$, $K_{II} = 0.0$, Center: $K_I = 0.6$, $K_{II} = 0.53$, Right: $K_I = 0.3$, $K_{II} = 0.71$

As Figure 2.1 shows, the stress distributions acting along the preexisting fracture is not symmetric when Mode II deformation occurs. Therefore, the Mohr–Coulomb

failure criterion needs to be considered at both sides, and when both sides are in “stick” condition, a propagating fracture can cross the preexisting fracture.

2.8 Sequential Method

The DDM and flow equation are coupled by fully implicit sequential strategy (Kim et al. 2011; McClure 2012; Norbeck 2016). Inside one iteration in a time step, the DDM with complementarity formulation is solved by fixed fluid pressure from previous iteration, the flow equation then is solved with fixed normal and shear displacements. The flow equation for p_f is solved by the residual equations as:

$$R_{p_f} = \nabla \cdot (q_{flux}) + s_a - \frac{\partial(\rho E)}{\partial t}, \quad (2.31)$$

where R_{p_f} is the residual equation for fluid pressure, ρ is the fluid density, μ is fluid viscosity, t is time, q_{flux} is the mass flow rate per cross sectional area of flow, E is the aperture, and s_a is a source term (mass per time) such as well injection or production. This is written in the discretized form as:

$$R_{p_f} = \left(\frac{\rho}{\mu}\right) \sum_{q=1}^Q T_{qn}^{t+1} (P_q^{t+1} - P_n^{t+1}) + s_n^{t+1} - 2a_n h \rho \frac{E_n^{t+1} - E_n^t}{dt^{t+1}}, \quad (2.32)$$

where the superscript t is the value from the previous time step, the super script $t+1$ is the value in current time step, a_n is half length of the element, h is the fracture height, μ is fluid viscosity, dt is time step, t is the number of time step, P_n is the fluid pressure at n -th element, P_q is the fluid pressure at the elements that are connected to the n -th element, Q is the number of elements connected to the n -th element, and T_{qn} is the geometric transmissivity between element n and q . The fluid density and viscosity are assumed to be constants and do not depend on the temperature and pressure.

The fluid pressure is updated by the spacing vector $dP^{(k)}$ calculated by the Jacobian matrix $J_{ij} = \frac{\partial R_i}{\partial P_j}$ as:

$$dP_n^{(k)} = P_n^{(k+1)} - P_n^{(k)}, \quad (2.33)$$

where

$$J * dP = -R. \tag{2.34}$$

Finally, the computation proceeds to the next time step after the convergence of p_f .

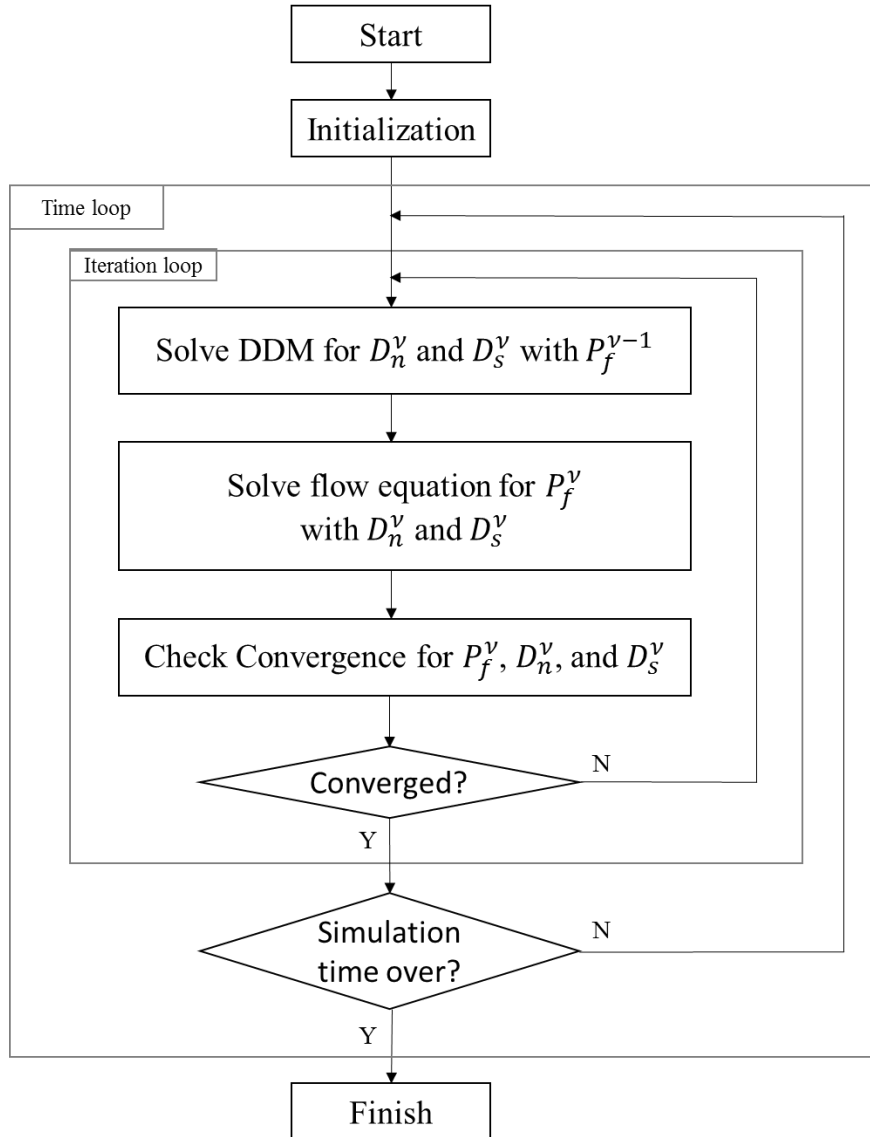


Figure 2.2: Flow chart for this numerical simulation. Superscript v is the number of iterations in the current time step. The variable with superscript v means the value is the one calculated from the current iteration. The variable with superscript $v-1$ means the value is the one calculated from the previous iteration.

2.9 Verification of the numerical model

To verify the accuracy of the numerical model in coupling fluid flow and fracture deformation/propagation, we modeled fracture deformation and propagation driven by fluid injection and compared to available analytical or numerical results. In these experiments, we modeled a hydraulic fracture propagating from an injection well, and a wing crack propagating from a tip of a sheared preexisting fracture. The numerical results were compared to other numerical results and analytical or semianalytical solutions. Fracture deformation by DDM with PATH solver were well verified for its accuracy especially for a natural fracture and faults deformations by Ritz et al. (2012, 2015) so we do not test the accuracy of the fracture deformation by DDM with complementarity in this section.

2.9.1 Hydraulic fracture propagation

To verify the accuracy of the numerical model in coupling fluid flow and fracture deformation/propagation, we modeled a single hydraulic fracture propagation extending from an injection well. The numerical results were compared to analytical and semianalytical solutions.

2.9.1.1 Hydraulic fracture analytical solution

Hydraulic fracture length was calculated by using analytical solutions assuming plane strain condition and the fluid pressure inside was uniform. The critical stress intensity factors for a straight crack are:

$$\begin{Bmatrix} \Delta u_I \\ \Delta u_{II} \\ \Delta u_{III} \end{Bmatrix} = \begin{Bmatrix} \Delta \sigma_I \\ \Delta \sigma_{II} \\ \frac{\Delta \sigma_{III}}{1-\nu} \end{Bmatrix} \frac{2(1-\nu)}{\mu} (a^2 - x^2)^{1/2}, \quad (2.35)$$

where $\Delta \sigma_m$ is the driving stress, ν is poisson's ration, μ is shear modulus, a is crack half length, and x is the distance from the center of a crack (Pollard & Segall, 1987). Injected volume is the same as the volume inside a fracture assuming no leak-off,

$$qt = \Delta \sigma_I \frac{2(1-\nu)}{\mu} h_f a^2, \quad (2.36)$$

where q is the volumetric flow rate, t is injection time, h_f is the fracture height in the direction perpendicular to the propagating direction. Also, the stress intensity factor at a propagating fracture tip is the same as the critical stress intensity factor of the matrix rock. The fluid pressure inside a fracture is expressed as:

$$\Delta\sigma_I = \frac{K_{IC}}{\sqrt{\pi a}}. \quad (2.37)$$

Combining Equations 2.36 and 2.37, the fracture half-length from the analytical solution is:

$$L(t) = \left(\frac{\mu q t}{K_{IC} 2\pi^{3/2} (1-\nu) h_f} \right)^{\frac{2}{3}}. \quad (2.38)$$

2.9.1.2 Hydraulic Fracture Semi-Analytical Solutions for 2D with no Leak-off

A hydraulic fracture is defined as a Mode I fracture extending perpendicular to the least principal stress created by a hydraulic fracturing operation that injects fluid in a higher pressure than the least principal stress. In most of the cases, a hydraulic fracture propagate vertically except the reverse faulting regime (Gidley et al., 1989). The most used semianalytical models without leak-off are the PKN model and the GdK model. Both models assume a vertical rectangular fracture with two-dimensional and linear fracture propagation in plane strain conditions.

The PKN model is an improved version of the PK model, which was suggested by Perkins and Kern (1961). The geometry of a two-dimensional fracture in the PK model is shown in Figure 2.3. In the PK model, the fracture has a fixed height which is independent of the fracture length, each vertical cross section is independent, a fluid pressure in a vertical section is constant, the vertical cross section is an elliptic shape, and fluid flows with the Newtonian flow (Perkins & Kern, 1961). One drawback of the PK model is if no leakoff is assumed, the model has significant numerical error as it ignores the influence of the fracture width growth rate on the flow rate. Nordgren (1972) corrected the effect of the growth rate and suggested the PKN model so that there is little numerical error in case of no leak-off.

Figure 2.3 shows the GdK model for a vertical rectangular fracture propagation. The assumptions in the GdK model are that the fracture height is fixed, the stiffness of the rock affects only in the horizontal cross section, the fracture width is constant in the vertical direction as the model is based on the plane strain condition, and fluid pressure gradient is calculated by the flow resistance in a narrow rectangular slit (Geertsma & de Klerk, 1969). Both models provide a closed-form solution for fracture half length, maximum fracture width, and injection pressure in respect to the constant injection rate and time. The equations for a fracture half-length for a constant injection rate are expressed as:

$$\text{GdK model: } L(t) = 0.48 \left[\frac{Gq_i^3}{(1-\nu)\mu h_f^3} \right]^{1/6} t^{2/3}, \quad (2.39)$$

$$\text{PKN model: } L(t) = 0.45 \left[\frac{Gq_i^3}{(1-\nu)\mu h_f^4} \right]^{1/5} t^{4/5}, \quad (2.40)$$

where G is the shear modulus, q_i is the injection rate, ν is the poisson's ratio, μ is the water viscosity, and h_f is the fracture vertical extent height.

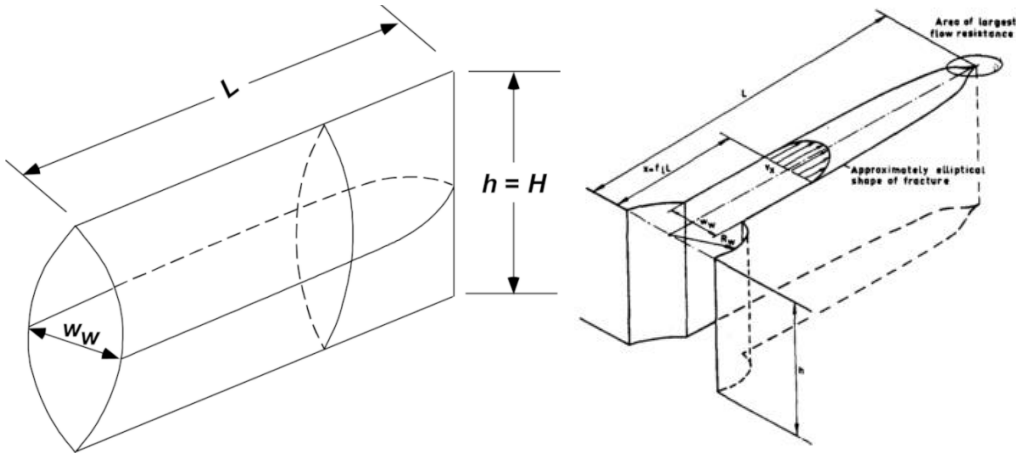


Figure 2.3: Left: The schematic of a fracture with the PKN model (Gidley et al., 1989), Right: The schematic of a fracture with the GdK model (Geertsma & de Klerk, 1969)

2.9.1.3 Numerical Model Setup

Water was injected to the injection well at a constant injection rate. A hydraulic fracture propagated from the injection well to the direction perpendicular to the minimum horizontal stress. A new element was added to the fracture tip when the stress intensity factor exceeded the critical stress intensity factor.

Table 2.1: Parameters used in the numerical simulation

Grid length	0.01	m
Time step	0.01	s
Injection Rate	0.01	m ³ /s
Total simulation time	30	min
Maximum horizontal stress	70	MPa
Minimum horizontal stress	40	MPa
Critical stress intensity factor	0.5	MPa
Shear modulus	15	GPa
Poisson's ratio	0.25	-
Fracture height	50	m
Water density	920	kg/m ³
Water viscosity	1.0e-9	MPa.s
Reference hydraulic aperture	1.0e-5	m
Reference effective normal stress	25	MPa

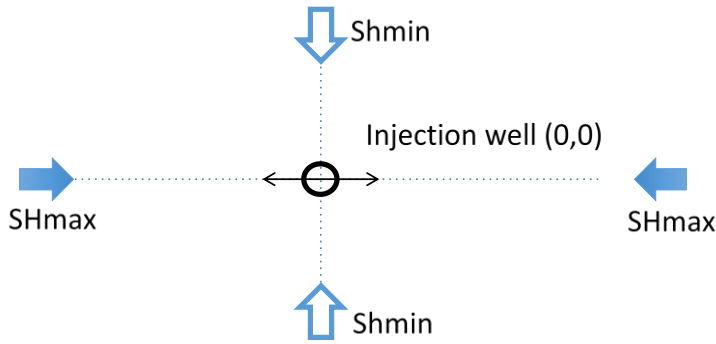


Figure 2.4: Schematic of the geometry of the injection well

2.9.1.4 Results

2.9.1.4.1 Comparison by Various Injection Rate

Fracture half-length after 30 minutes of injection were compared among numerical, KGD, and PKN models. Table 2.2 shows the difference between numerical results and KGD or PKN model results. The numerical model showed good agreement with the KGD model as shown in Figure 2.5, Figure 2.6, and Figure 2.7. This is because the cross-sections of a fracture in the direction perpendicular to the propagating direction are the same shape in both numerical and KGD models. The vertical cross section of the PKN model is an elliptic shape, therefore the volume that stores fluid is smaller in the vertical extent compared to the KGD and numerical models, which makes the length of the PKN model longer than the other two models.

Table 2.2: Summary of the comparison

Injection rate [m ³ /s]	KGD [m]	PKN [m]	Numerical [m]	Difference between KGD and Numerical	Difference between PKN and Numerical
1.0e-3	52.3	57.3	50.3	4.0%	14.0%
1.0e-2	165.5	228.3	158.2	4.6%	44.3%
1.0e-1	523.3	908.8	487.0	7.5%	86.6%

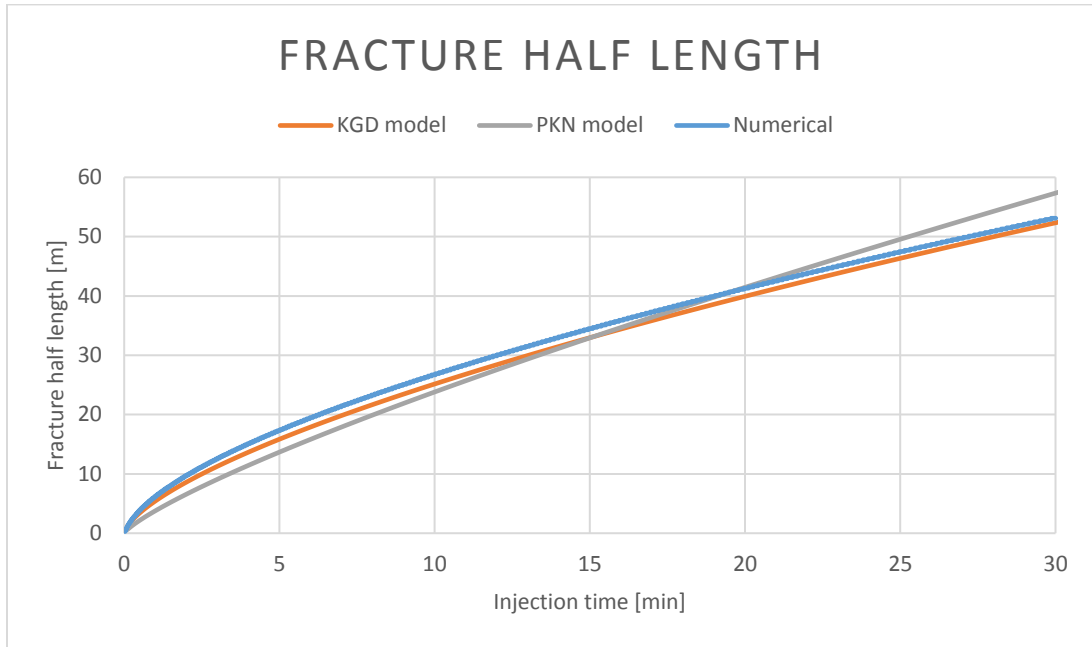


Figure 2.5: Fracture half-length comparison among numerical, KGD and PKN models with the injection rate $1.0e-3$ [m³/s]

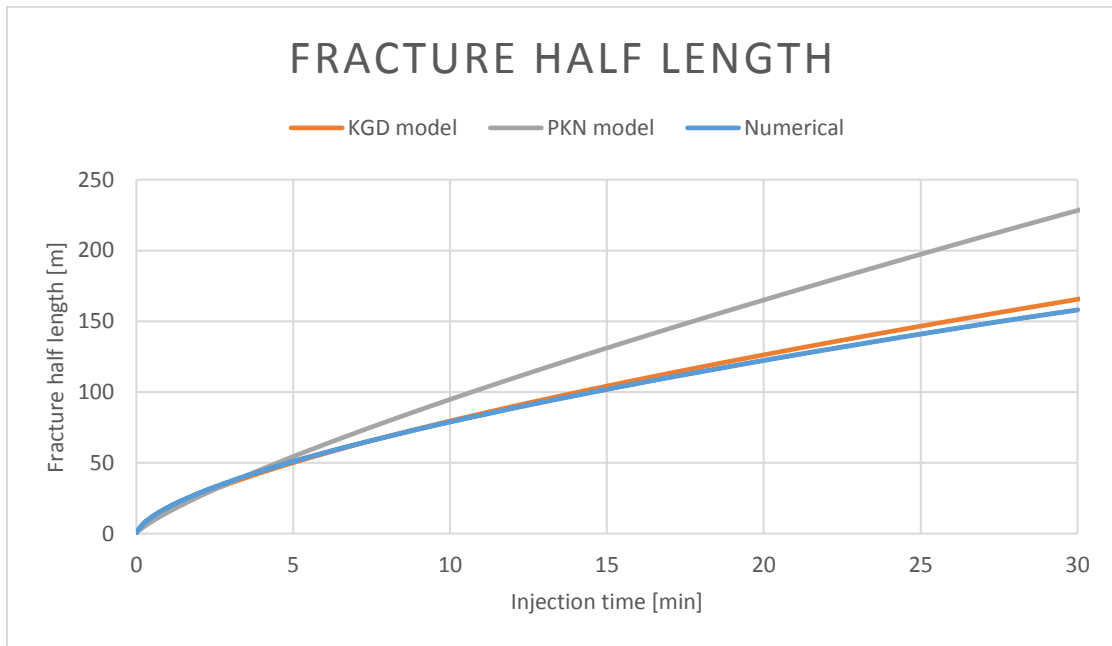


Figure 2.6: Fracture half-length comparison among numerical, KGD and PKN models with the injection rate $1.0e-2$ [m³/s]

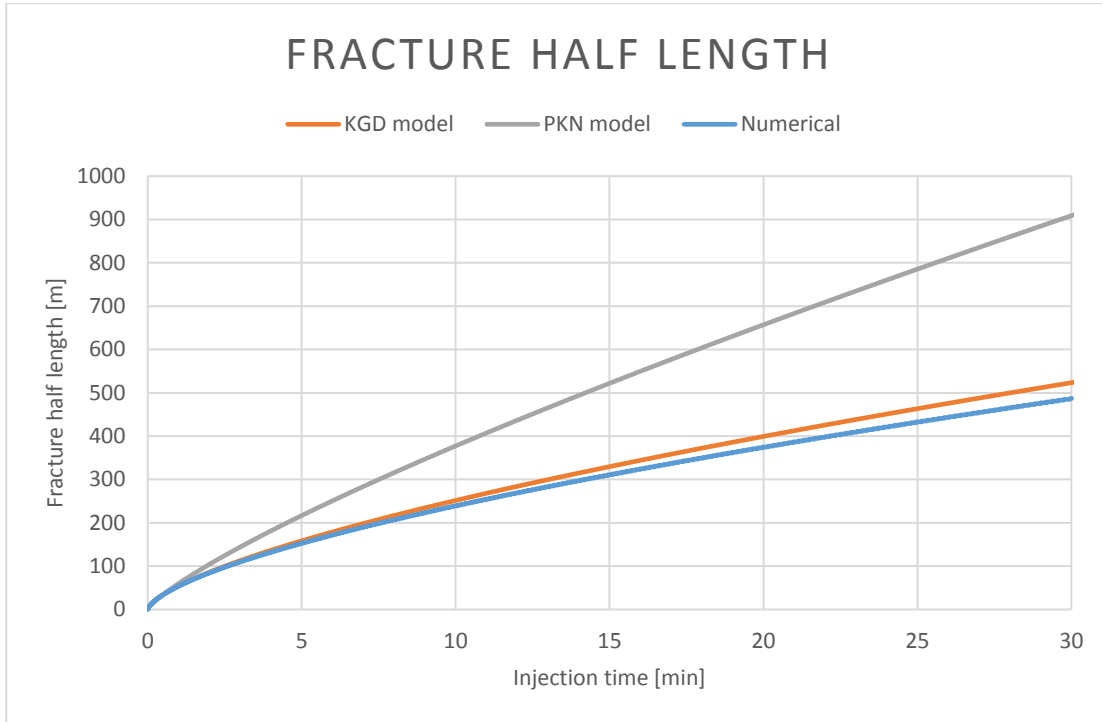


Figure 2.7: Fracture half-length comparison among numerical, KGD and PKN models with the injection rate $1.0e-1$ [m³/s]

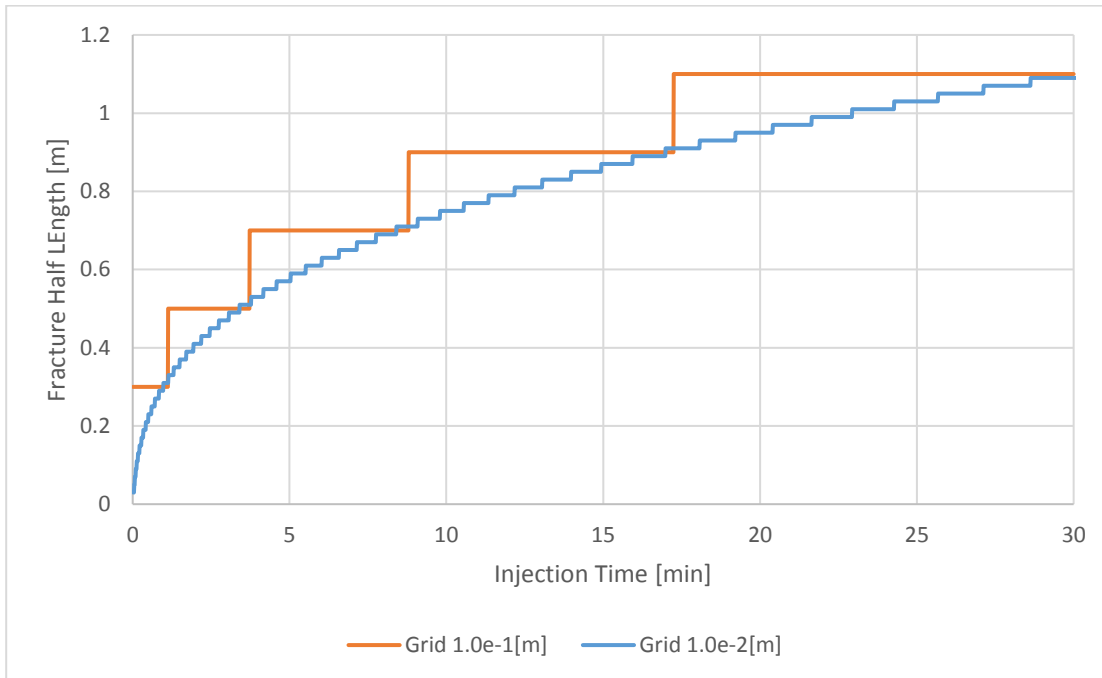


Figure.2.8 Fracture half-length comparison between different grid sizes

2.9.1.4.2 Comparison by Grid Size

To verify the numerical stability in grid size, we changed grid size and compared the fracture half-length in time. Grid sizes compared in this study were 0.1 m and 0.01 m. Parameters used are the same as listed in Table 2.1.

Figure.2.8 shows that the fracture propagation occurred almost the same timing regardless of the grid size. With a larger grid size, the fracture length was overestimated to one grid size at most. This verified that the fluid flow and fracture deformation were calculated reasonably regardless of the grid size.

2.9.2 Wing crack propagation

Outcrop observations show that a slipping fracture loaded in compression accumulates local tensile stress concentrations near the fracture tips, and then initiates secondary opening fractures which are called wing cracks or splay fractures (Cooke et al., 2000; Cruikshank & Aydin, 1994; Segall & Pollard, 1983). The mechanism of the creation of a newly formed fracture initiated from a sliding preexisting fracture has been studied based on field observation and analytical, numerical, and experimental works (Erdogan & Sih, 1963; Thomas & Pollard, 1993; Joussineau et al., 2007; Mutlu & Pollard, 2008). As reported by Mutlu and Pollard (2008), laboratory experiments on wing crack propagation from a single flaw under compression have been carried out in glass or plastic (Brace & Bombolakis, 1963; Hoek & Bieniawski, 1965; Horii & Nemat-Nasser, 1986) as well as in rocks (Bobet & Einstein, 1998; Li et al., 2005; Petit & Barquins, 1988; Sahouryeh et al., 2002). The observations of these laboratory experiments are similar to those observed in outcrops where wing cracks propagate from the tips of the slipping fracture toward the direction perpendicular to the least principal stress.

Analytical solutions that describe the relationship between the sliding preexisting fracture and the length and the kink angle of the initiating wing crack were developed in the literature (Horii & Nemat-Nasser, 1986; Lehner & Kachanov, 1996). To verify the model accuracy for wing crack propagating trajectory, length, and deformation, we modeled a preexisting fracture orienting at 60 degrees toward the direction of the least principal stress with the parameters listed in Table 2.3 and

compared the numerical results with the analytical solutions by Horii & Nemat-Nasser, (1986) and the numerical results by Mutlu and Pollard (2008).

Table 2.3: Parameters used in the numerical simulation

Preexisting fracture length	2.0	m
Preexisting fracture grid length	1.0e-2	m
Wing crack grid length	1.25e-3	m
Maximum horizontal stress	40	MPa
Minimum horizontal stress	5	MPa
Critical stress intensity factor	1.5	MPa
Young's modulus	20	GPa
Poisson's ratio	0.2	-
Friction coefficient	0.6	-
Cohesion	0.0	MPa

2.9.2.1 Verification of Wing Crack Length with Analytical Solution

We compared the wing crack length in respect to the stress ratio acting on the preexisting fracture between the analytical solution and the numerical result. S_{hmin} and fracture orientation were varied. Fluid pressure was set to be 0 MPa and no injection/production occurred. Fracture tips and the root of the wing crack are meshed finer so that the intersection with a kink angle can be modeled more stably.

Firstly we compared our model for the mixed Mode I and Mode II propagation with the analytical solution by Thomas and Pollard (1993) (Figure 2.10). Our model is correctly implemented to compute the propagation criteria for the mixed Mode I and Mode II propagation. Figure 2.9 shows the comparison between numerical and analytical results. The analytical estimate of wing crack lengths are larger than the numerical results especially when the stress ratio is below 0.15. The wing crack curves

with numerical result, but the analytical solution assumes straight wing crack, therefore, the analytical solution may deviate from the actual setting with small stress ratio.

2.9.2.2 Verification of Wing Crack Trajectory and Deformation

We compared the numerical results of wing crack trajectory and normal/shear displacements with Mutlu and Pollard (2008). The analytical solution that describes the normal displacement of a wing crack (such as Lehner & Kachanov, 1996) is not quite accurate because of its assumption of straight wing crack perpendicular to the least principal stress. Mutlu and Pollard (2008) setup the DDM code with complementarity formulation and verified their model with various analytical solutions and field observations. Our numerical code and Mutlu and Pollard (2008) are essentially the same except fluid flow and the complementarity formulation and its solver used.

Figure 2.11 and Figure 2.12 show the modeled fracture trajectory and the normal and shear displacements of a wing crack initiated from a preexisting fracture orienting at 60 degrees toward the direction of the maximum horizontal stress. The wing crack length was 0.225 m and the stress ratio S_2/S_1 was 0.125. The wing crack initiated with the kink angle of 70.5 degrees and turned to the direction perpendicular to the least principal stress. This type of trajectory is often observed in the field (Figure 2.11d) and reasonably matching to the result of Mutlu and Pollard (2008) (Figure 2.11c). The opening displacements of the wing crack showed convex feature and the tips of the main preexisting fracture have the opening displacements, which are modeled by Mutlu and Pollard (2008) as well (Figure 2.12).

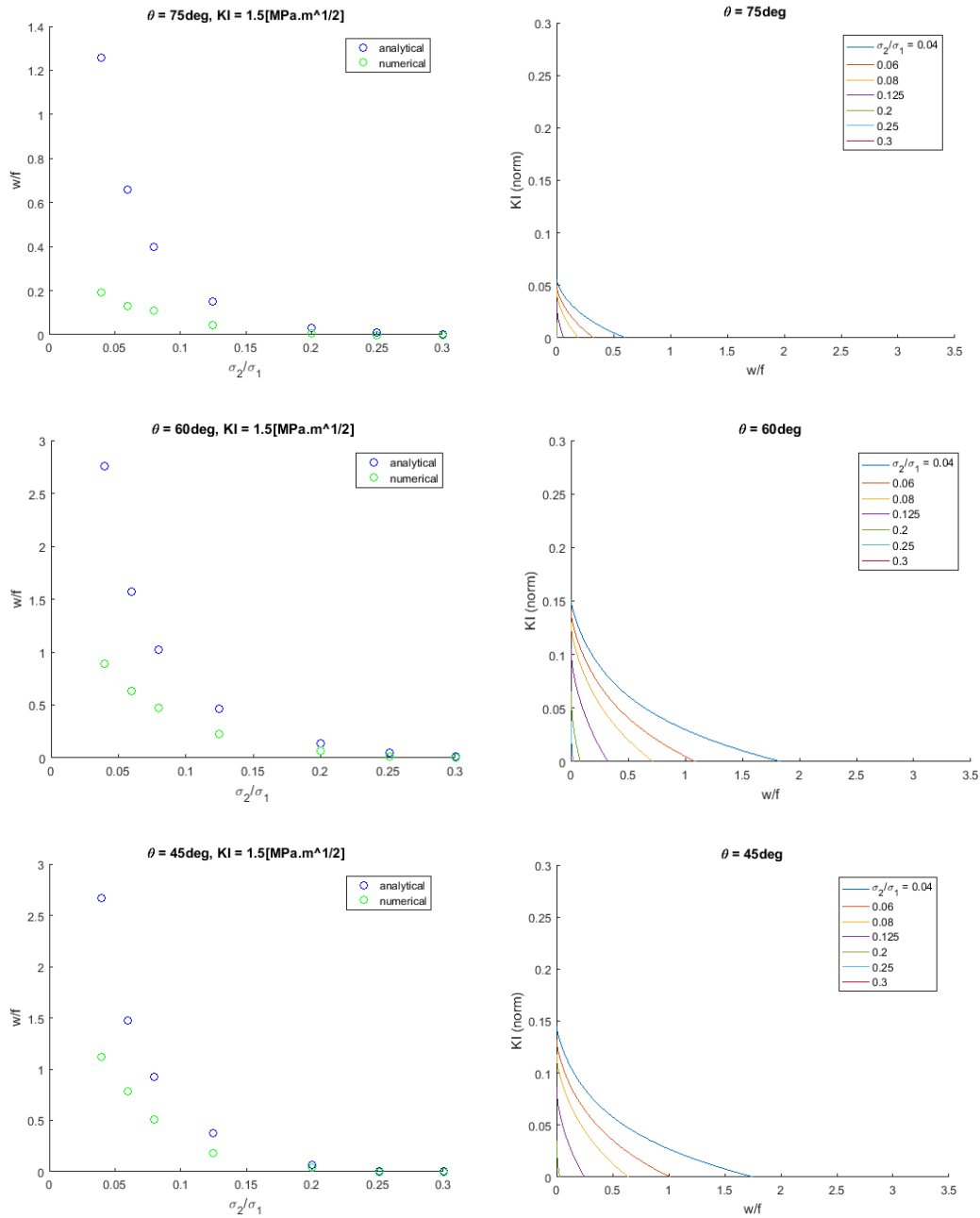


Figure 2.9: Left: normalized wing crack length with different stress ratio by analytical and numerical models, Right: normalized Mode I stress intensity factor and the normalized wing crack length.

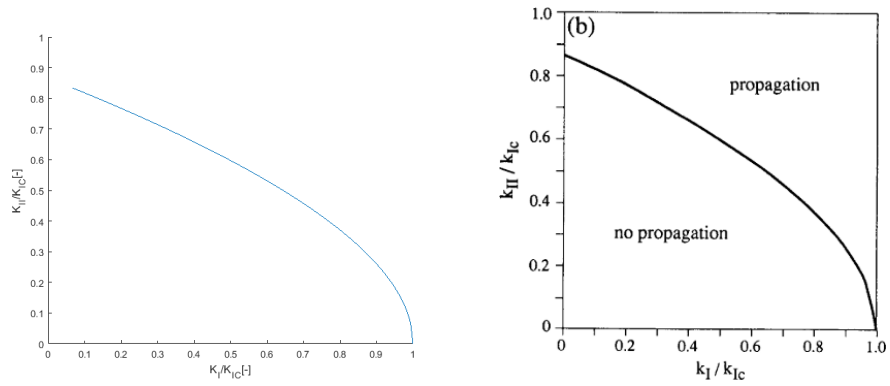


Figure 2.10: The critical values K_I and K_{II} required for propagation under mixed Mode I and Mode II displacements from this model (right) and by Thomas and Pollard (1993).

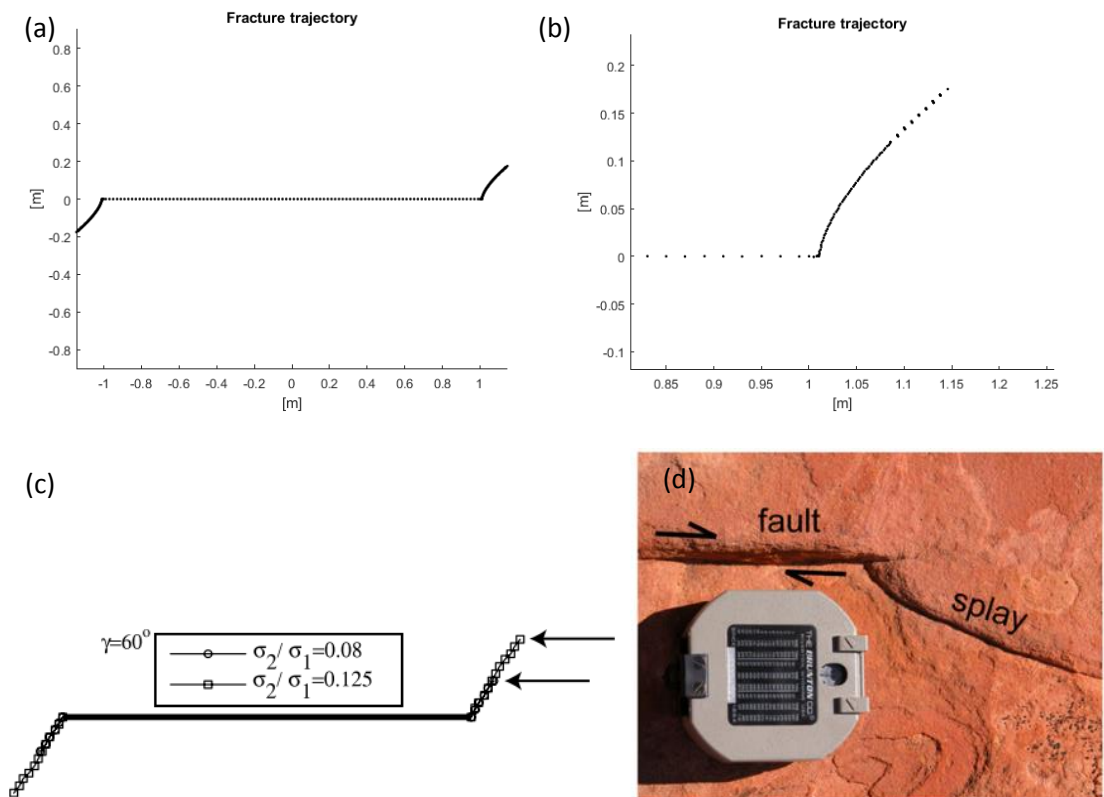


Figure 2.11: (a) Fracture trajectory of a preexisting fracture orienting at 60 degrees and wing cracks, (b) Wing crack trajectory, (c) preexisting fracture and wing crack trajectory by Mutlu and Pollard (2008), (d) Observed wing crack in the field (Joussineau et al., 2007).

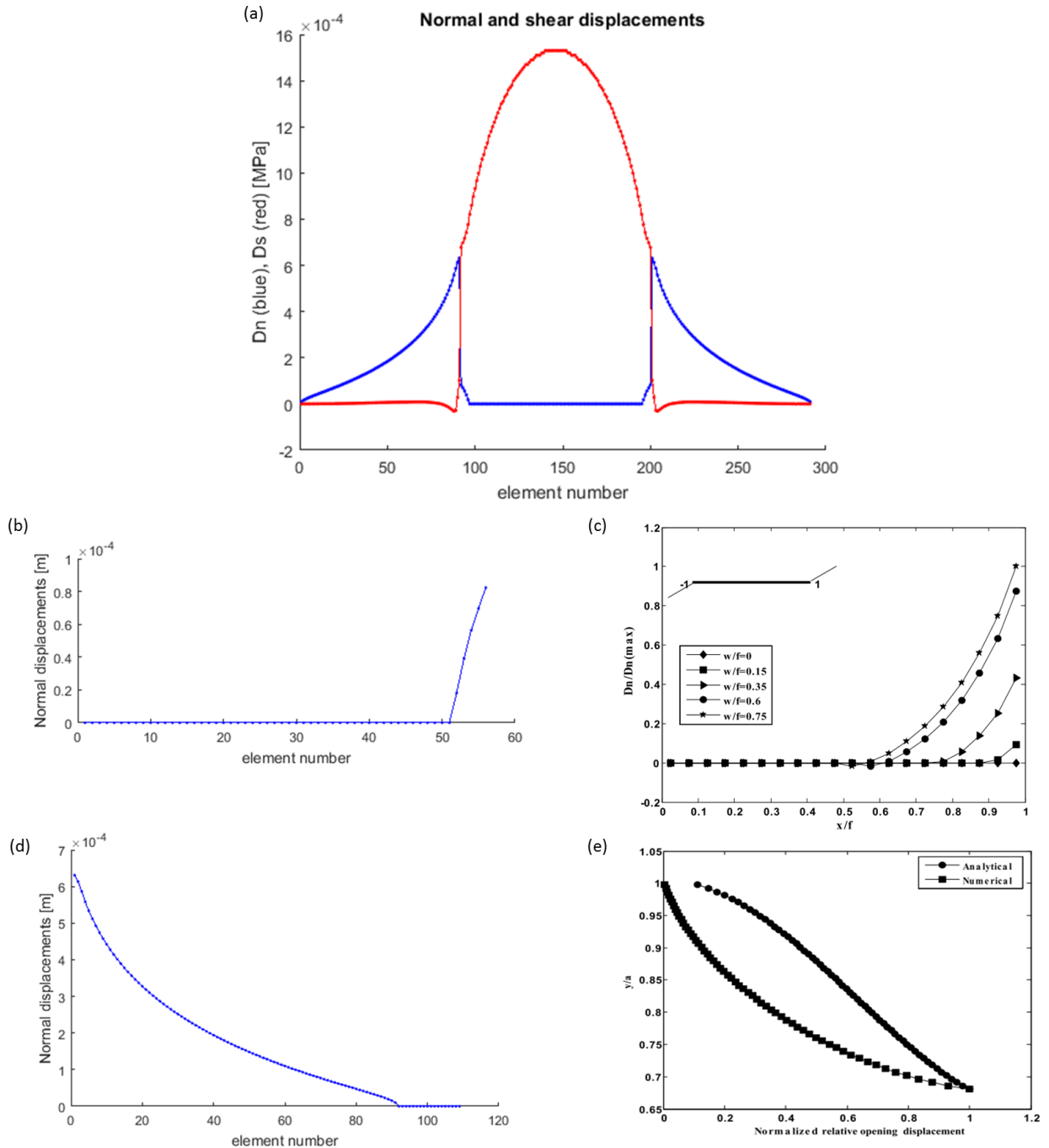


Figure 2.12: (a) The normal and shear displacements of a preexisting fracture orienting at 60 degrees and wing cracks, (b) Normal displacement of the main preexisting fracture, (c) Normal displacement of the main preexisting fracture by Mutlu and Pollard (2008), (d) Normal displacements of the wing crack, (e) Normal displacements of the wing crack by Mutlu and Pollard (2008) and the analytical solution by Lehner and Kachanov (1996).

2.9.3 Propagating fracture cross/follow criteria

To verify the implementation of the code and computation results by our simulator, the results for propagating fracture cross/follow criteria were compared with analytical models and the results were discussed.

2.9.3.1 Comparison with Analytical model

The analytical model developed by Renshaw and Pollard (1995) and later extended by Gu and Weng (2010) is based on the linear elastic fracture mechanics solution for the stresses near a fracture tip and calculate the stresses needed to cause slip on the pre-existing interface (Renshaw & Pollard, 1995). Following Irwin (1956), the stress field near the end of a brittle tensile fracture in plane strain situations is approximated as:

$$\sigma_{xx}^c = \frac{K_I}{\sqrt{r}} \left\{ \cos \frac{\theta}{2} \left[1 - \sin \frac{\theta}{2} \sin \frac{3\theta}{2} \right] \right\}, \quad (2.41)$$

$$\sigma_{yy}^c = \frac{K_I}{\sqrt{r}} \left\{ \cos \frac{\theta}{2} \left[1 + \sin \frac{\theta}{2} \sin \frac{3\theta}{2} \right] \right\}, \quad (2.42)$$

$$\tau_{xy}^c = \frac{K_I}{\sqrt{r}} \left\{ \sin \frac{\theta}{2} \cos \frac{\theta}{2} \cos \frac{3\theta}{2} \right\}, \quad (2.43)$$

where K_I is the mode I stress intensity factor, r and θ are the polar coordinate with the origin at the fracture tip. The maximum magnitude of the stress components is found at the critical radius $r = r_c$. The area within $r = r_c$ is referred to as the fracture process zone where the inelastic deformation exists. Renshaw and Pollard (1995) assumed that the tensile stress induced by the fracture tip must be equal to the tensile strength where $\sigma_{yy} = T_0$. Then they derived the crossing/terminating threshold for the fracture intersecting the fracture with $\theta = \frac{\pi}{2}$ as:

$$\frac{-\sigma_{xx}^r}{T_0 - \sigma_{yy}^r} > \frac{0.35 + \frac{0.35}{\mu}}{1.06}, \quad (2.44)$$

where σ_{xx}^r and σ_{yy}^r are remote stresses, and μ is the frictional coefficient of the fracture.

In extended fracture crossing criterion, Gu and Weng (2010) updated the normal and shear stresses used for the criterion by including nonorthogonal fractures as

$$\tau = K \sin \frac{\theta}{2} \sin \frac{3\theta}{2} \sin 2\theta + K \sin \frac{\theta}{2} \cos \frac{3\theta}{2} \cos 2\theta - \frac{S_{Hmax} - S_{hmin}}{2} \sin 2\theta, \quad (2.45)$$

$$\begin{aligned} \sigma_n = & K + K \sin \frac{\theta}{2} \sin \frac{3\theta}{2} \cos 2\theta - K \sin \frac{\theta}{2} \cos \frac{3\theta}{2} \sin 2\theta \\ & + \frac{S_{Hmax} + S_{hmin}}{2} - \frac{S_{Hmax} - S_{hmin}}{2} \cos 2\theta, \end{aligned} \quad (2.46)$$

where τ is shear stress acting on the preexisting fracture near the crack tip, μ is frictional coefficient, σ_n is normal stress acting on the preexisting fracture near the crack tip, S_0 is cohesion of the interface, K represents the stress level required to reinitiate a fracture on the other side of the interface, θ is the angle between the propagating fracture and preexisting fracture, S_{Hmax} is the maximum principal stress, and S_{hmin} is the minimum principal stress. When the interface slips, the propagating fracture cannot initiate fracturing on the other side of the interface surface, and the propagation stops.

Figure 2.13 shows the Renshaw and Pollard (1995), Gu and Weng (2010), and this model's cross/follow criterion for a orthogonal fracture. If the frictional coefficient and stress ratio locate right side of the line, the propagating fracture crosses the preexisting fracture. If they locate left side of the line, the propagating fracture stops at the preexisting fracture. The results of this model and Gu and Weng (2010) perfectly match because these models are essentially the same for a pure Mode I fracture.

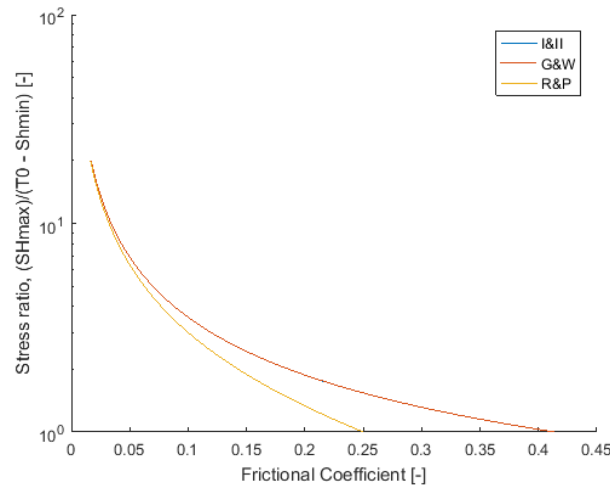


Figure 2.13: Criterion if fracture crosses or not for orthogonal intersection angle.

2.9.3.2 Comparison with varied deformations

The cross/follow criteria for mixed Mode I and Mode II propagation is discussed in this section. Both sides of the intersecting preexisting fracture needs to be considered for the cross/follow criteria because the induced stress field around the fracture tip is asymmetric with the mixed Mode I and Mode II propagation.

Figure.2.14 shows if each side of the preexisting fracture slips or not by the induced stress field. S_{hmin} was 10 MPa, T_0 was 0 MPa, and S_{Hmax} was varied. As Figure.2.14 shows, the fracture cross/follow criteria depend on the stress ratio and the coefficient of friction. One side is under weaker tension compared to the other side because shear displacements induce strong tension field around the fracture tip. The induced stress acting on the weaker side becomes smaller as the magnitude of the shear displacement increases, which makes the preexisting fracture in stick condition (Figure 2.1). On the other hand, the induced stress acting on the stronger side becomes larger as the magnitude of the shear displacement increases, which makes the preexisting fracture in slip condition (Figure 2.1). It has been known that to the propagating fracture cross/follow criteria depends on the stress ratio, the friction coefficient, and the intersection angle (Gu & Weng, 2010; Gu et al., 2011; Renshaw & Pollard, 1995), but also the magnitude of the shear displacement contributes to the propagating fracture cross/follow criteria.

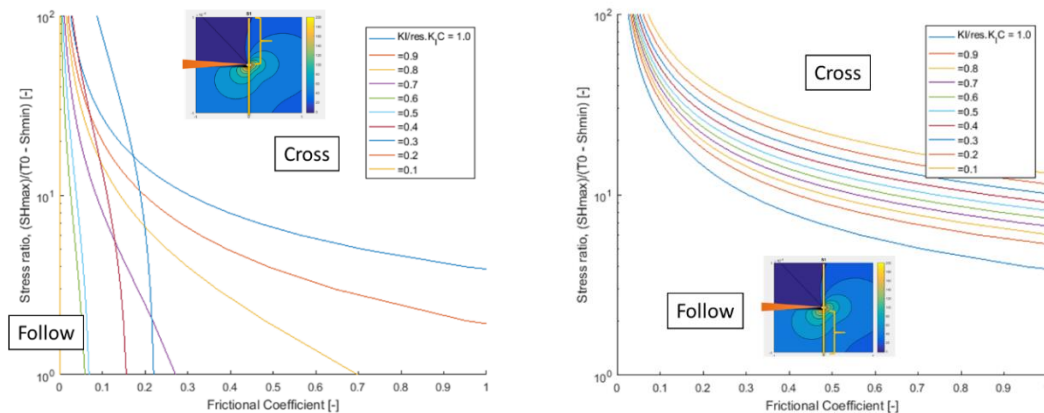


Figure.2.14: An example of the propagating fracture cross/follow criteria by a fracture with $K_I = 0.6$ and $K_{II} = 0.53$. Left: the fracture cross/follow criteria applied to the side with weaker stress

concentration, Right: the fracture cross/follow criteria applied to the side with stronger stress concentration.

2.9.4 Verification of Modified DDM

In Section 7.2, we described how we coupled fracture deformation and fluid flow without using complementarity formulation. The numerical method using complementarity formulation explained in this chapter is capable of computing fracture deformation of nonplanar fractures accurately, however, it is computationally expensive and not suitable for computing reservoir scale simulation. The methodology implemented by following McClure (2012) modifies DDM formulation so that shear sliding under compression and curved fracture propagation and deformation are calculated at reasonable accuracy. This numerical model can compute reservoir scale simulation computationally reasonably.

In this section, we modeled hydraulic fracture and wing crack propagation, and compared the results with analytical, semianalytical, and numerical results that were explained in Section 2.9.1 and 2.9.2 to verify the accuracy of the modified DDM. The parameters used for hydraulic fracture propagation is listed in Table 2.1 and the parameters used for wing crack propagation is listed in Table 2.3.

Figure 2.15, Figure.2.16, and Figure 2.17 show the fracture half-length after 30 minutes of injection. The numerical model showed reasonably good agreement with the semianalytical models. The model assumes plane strain condition, which is the same as KGD model, but the numerical model shows longer fracture length than KGD model and shows close trend with PKN model. The fracture length is also affected by the fracture transmissivity calculation. The transmissibility of the numerical model may be higher than the assumption of KGD model, which made the fracture length of the numerical model longer than the KGD model.

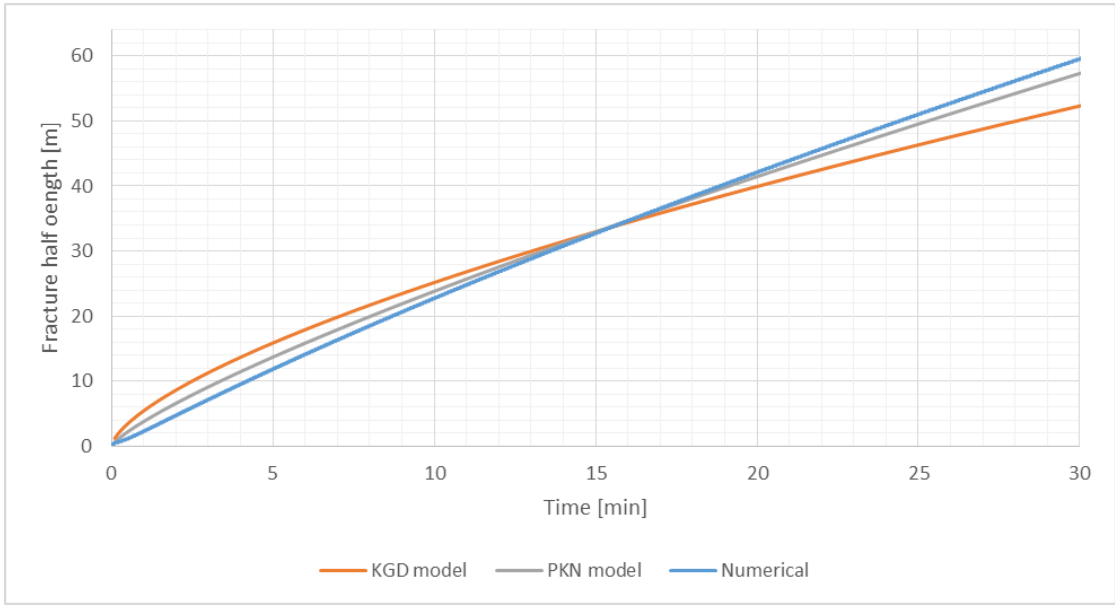


Figure 2.15: Fracture half-length comparison among numerical, KGD and PKN models with the injection rate $1.0e-3$ [m³/s]

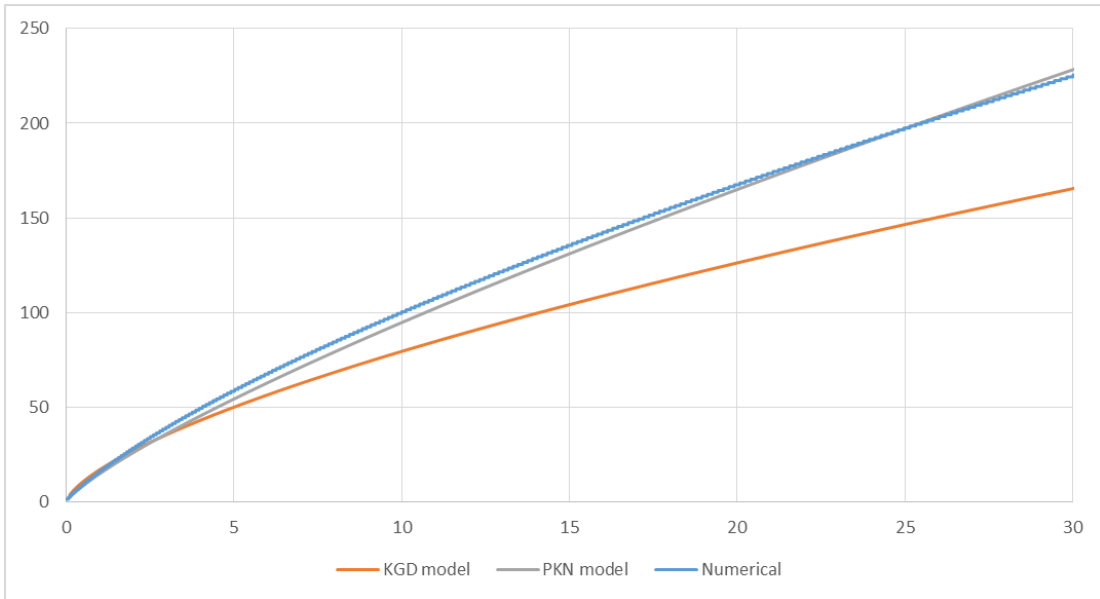


Figure.2.16: Fracture half-length comparison among numerical, KGD and PKN models with the injection rate $1.0e-2$ [m³/s]

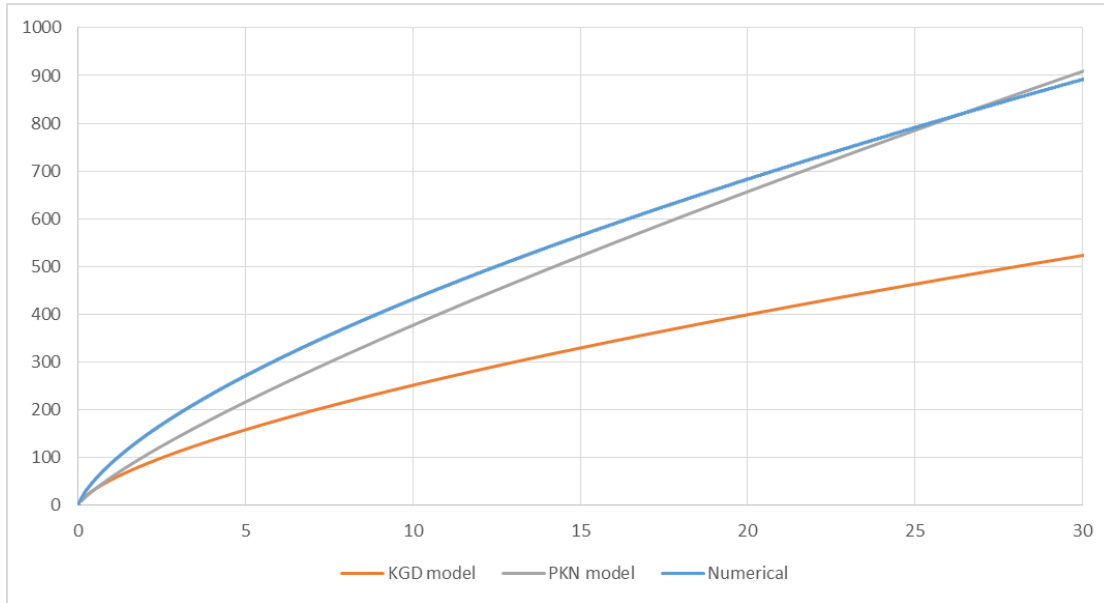


Figure 2.17: Fracture half-length comparison among numerical, KGD and PKN models with the injection rate $1.0e-1$ [m^3/s]

Figure 2.18, Figure 2.19, and Figure 2.20 show the modeled wing crack trajectory, deformation, and length. The preexisting fracture initiating wing cracks oriented at 60° toward the direction of the maximum horizontal stress. The wing crack length was 0.07 m and the stress ratio S_2/S_1 was 0.125. Overall, the modified DDM computes wing crack propagation reasonably accurately. However, the modified DDM model did not reproduce the opening displacement around the tips of the main preexisting fracture. Therefore, the wing crack did not have shear deformation and it propagated straight. The length of the wing crack shows shorter profile than the analytical and numerical result with complementarity solver (Figure 2.18).

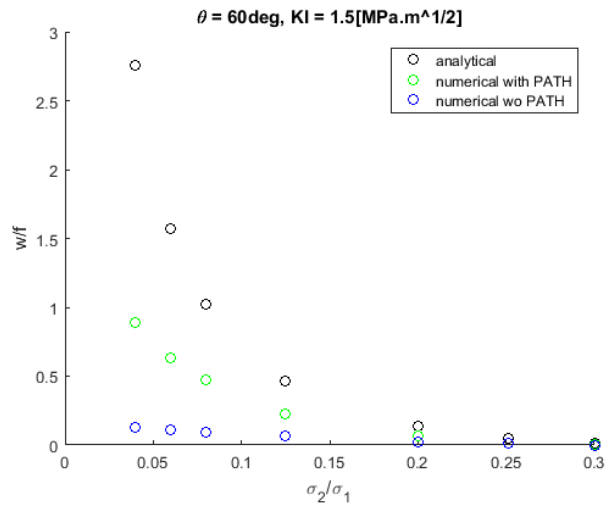


Figure 2.18: Left: normalized wing crack length with different stress ratio by analytical and numerical models, Right: normalized Mode I stress intensity factor and the normalized wing crack length.

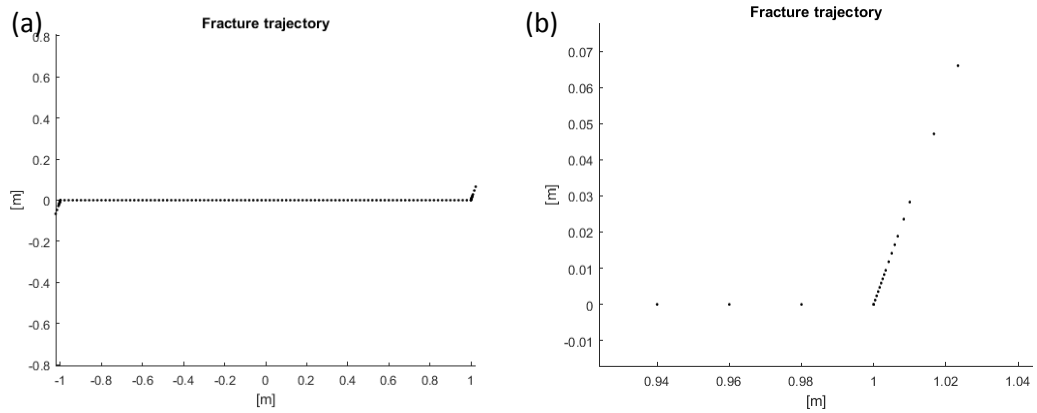
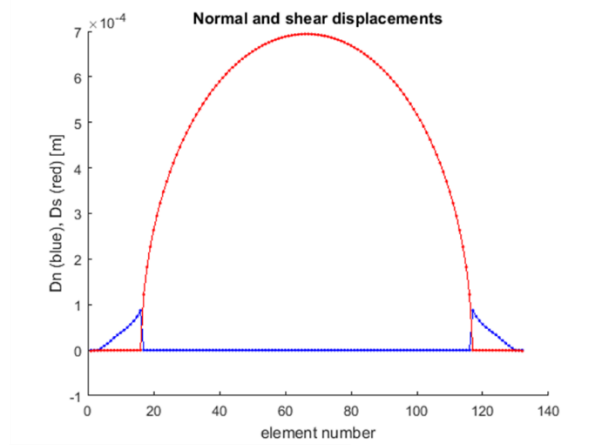
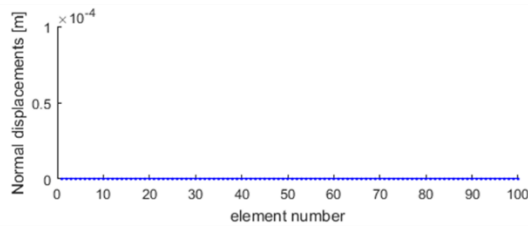


Figure 2.19: (a) Fracture trajectory of a preexisting fracture orienting at 60 degrees and wing cracks, (b) Wing crack trajectory,

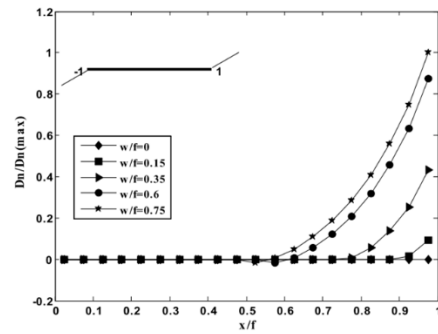
(a)



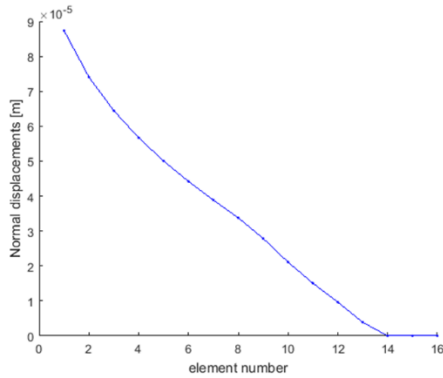
(b)



(c)



(d)



(e)

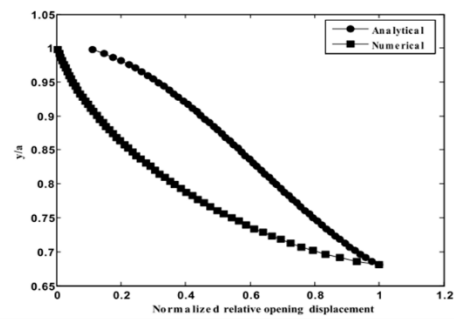


Figure 2.20: (a) The normal and shear displacements of a preexisting fracture orienting at 60 degrees and wing cracks, (b) Normal displacement of the main preexisting fracture by Mutlu and Pollard (2008), (c) Normal displacements of the wing crack by Mutlu and Pollard (2008) and the analytical solution by Lehner and Kachanov (1996).

2.10 Summary

In this chapter, we described the physics-based numerical modeling that combines fracture deformation, propagation, and fluid flow, and verified its accuracy by

comparing to analytical, semianalytical, and another numerical results. The model is able to simulate fracture deformation and propagation driven by fluid injection, and mechanical interaction between fractures. In Chapter 3, the model simulates a wing crack propagation driven by fluid injection and investigates the effect of wing cracks on the reservoir permeability enhancement. The model is utilized to analyze the laboratory scale fracture network creation in Chapters 4 and 5. In Chapter 6, detailed numerical investigation on mechanical interaction between newly formed and preexisting fractures is performed by the numerical model. In Chapter 7, instead of using complementarity formulation, flow equation and DDM formulations are coupled by following McClure (2012) without complementarity formulation so that the reservoir scale simulation becomes computationally reasonable while computing shear sliding under compression and curved fracture propagation and deformation at reasonable accuracy. The model used in Chapter 7 is described in Section 7.2.

Chapter 3

3 Investigating the Effect of Wing Cracks on EGS Reservoir Permeability Enhancement

3.1 Introduction

During hydraulic stimulation treatment, injected fluid flows into preexisting fractures and makes them slip in shear. This shear stimulation occurred at almost all EGS projects based on the microseismicity observations. Shear stimulation is the stimulation mechanism that occurs first because fractures can slip in shear with the fluid pressure lower than the least principal stress. In mixed mechanism stimulation, it is suggested that new fractures are initiated from sheared preexisting natural fractures and propagate in a reservoir. This phenomenon has been observed in laboratory scale experiments (Erdogan & Sih, 1963 and Zoback, 2007) and field scale observations (Joussineau et al., 2007; Mutlu and Pollard, 2008; Andrew et al., 1993). A fracture initiated from a sheared preexisting natural fracture is called a wing crack or a splay fracture. Wing cracks found in rock are tensile fractures but they are different from hydraulic fractures which propagate from an injection well because: 1) wing cracks are initiated from the tension field induced by shear slip of a preexisting natural fracture while hydraulic fractures are initiated from an injection well by fluid pressure; 2) wing cracks are curved cracks while hydraulic fractures tend to propagate straight and perpendicularly to the local least principal stress; 3) tension forces to open wing cracks are supported both by fluid

pressure and shear slip of a preexisting natural fracture while tension forces to open hydraulic fractures are supported only by fluid pressure.

The magnitude of necessary fluid pressure to initiate a wing crack within a well-oriented natural fracture could be less than the fluid pressure to create new hydraulic fractures (Mutlu & Pollard, 2008; Kamali & Ghassemi, 2016, 2018; Zoback & Lund Snee, 2018). Therefore, propagation of wing cracks and shear stimulation of natural fractures need to be considered when we model realistic fracture networks to characterize an enhanced geothermal reservoir. In this study, we modeled the wing crack propagation driven by fluid injection in a setting of hydraulic stimulation by injecting water into a preexisting natural fracture at varied fracture angles and injection pressure in order to investigate the effect of wing cracks on the reservoir permeability enhancement during hydraulic stimulation treatment in an EGS reservoir.

Field observation shows that multiple wing cracks can propagate from a single natural fracture because there are notches, partial cementing, deviations from pure plane, multiple slip events in stages, or sudden change of friction coefficient that make stress concentration at multiple points along a slipping fracture (Cooke, 1997). Also, it is observed that wing cracks propagate from just behind the main natural fracture tip (Joussineau et al., 2007; Martel, 1997) because the maximum circumferential tension occurs just behind the sliding fracture tip (Cooke, 1997). Barenblatt's theory of so-called equilibrium cracks suggested the finite normal stress applied ahead of the fracture tip and the surfaces of the fracture close smoothly (Barenblatt, 1962). With this assumption, the stress intensity factor needs to be zero for a fracture criterion, and the cohesive forces act near the fracture tip to reduce the stress concentration along the near-tip region. Cooke (1997) and Mutlu and Pollard (2008) applied this theory to model the propagation of multiple wing cracks behind the fracture tip. Their numerical results with the linear cohesive end zone showed that the maximum tangential tension appeared just behind the fracture tip.

Although the Barenblatt's equilibrium cracks is more realistic to model fracture propagation from a fracture with Mode II deformation, we assumed uniform cohesion and the coefficient of friction and a single fracture propagation from the tip to simplify

the problem. This assumption may underestimate the effect of wing cracks on the reservoir permeability enhancement because it is more likely that multiple wing cracks propagate from one preexisting natural fracture. This can be considered in future study.

3.2 Wing crack propagation driven by fluid injection

3.2.1 Wing crack propagation from varied fracture angles

In this numerical experiment, wing crack propagation due to shear stimulation to a single preexisting natural fracture was modeled. Water is injected into a preexisting natural fracture at a pressure lower than the least principal stress. The angles of the main preexisting natural fracture are 45, 60, and 75 degrees as they are well oriented to the principal stresses and slide at a lower pressure than the least principal stress. The injection was done at constant injection/production rate with initial reservoir fluid pressure at 18 MPa, the maximum bottomhole pressure (BHP) 23 MPa, and the minimum BHP 18 MPa. Those numbers are taken from the in-situ stress state at around 2 km depth at EE-3 well Fenton geothermal well (Barton et al., 1988) and the initial fluid pressure is hydrostatic.

In this numerical experiment, hydraulic stimulation was performed on a vertical preexisting natural fracture intersecting a well at its center. Water is injected from the well until the wing crack propagation stopped. Then the fluid was produced from the well until the fluid pressure over the entire fracture reached the initial pressure. Then we compared the fracture deformation and the transmissivities at the end of injection and after the fluid pressure was reduced. The parameters used in the simulation are listed in Table 3.1.

The results of the wing crack length are summarized in Table 3.2. Wing cracks observed in the field are driven by the tension field induced by the slip of the main preexisting fracture. On the other hand, the wing cracks driven by the fluid injection propagate due to the effect of both the tension field induced by the slip of the main fracture and the fluid pressure that applies the pressure to open the wing cracks. Even

though the injected fluid pressure is lower than the magnitude of the least principal stress, the slip of the main fracture induces tension near the fracture tips that could initiate wing cracks.

Table 3.1: Parameters used in the numerical simulation

Main fracture grid half length	1.0e-2	m
Main fracture length	2.0	m
Wing crack grid half length	6.25e-4	m
Initial Time Step	1.0e-4	s
Injection/Production Rate	1.0e-8	m ³ /s
Maximum bottomhole pressure	23	MPa
Maximum bottomhole pressure	18	MPa
Maximum horizontal stress	40	MPa
Minimum horizontal stress	24	MPa
Initial fluid pressure	18	MPa
Critical stress intensity factor of granite	1.5	MPa
Shear modulus	15	GPa
Poisson's ratio	0.25	-
Fracture height	1	m
Water density	920	kg/m ³
Water viscosity	1.0e-9	MPa.s
Reference hydraulic aperture	1.0e-4	m
Reference effective normal stress	25	MPa
Dilation angle	2	degree

Fracture static frictional coefficient	0.6	-
Fracture dynamic frictional coefficient	0.4	-
Frictional strength	0.5	MPa

Table 3.2: Wing crack length after injection. θ is the angle of the main preexisting fracture toward the least principal stress, w is wing crack length, f is the main preexisting fracture half length.

θ	45	60	75
$\frac{w}{f}$	1.13	0.61	0.12

The main preexisting fracture has the maximum driving shear stress and shear displacement at 60 degrees, however, the preexisting fracture with 45 degrees has the longest wing crack. The direction of the induced tension field and the direction of the least principal stress align closely when a main fracture orientation is 45 degrees toward the least principal stress. This is one of the reasons the wing crack propagation is enhanced.

The wing crack trajectories are shown in Figure 3.1 to Figure 3.3. The wing cracks curved toward the direction perpendicular to the least principal stress. This is because of the maximum circumferential stress theory by Erdogan and Sih, (1963) that a propagating fracture chooses the path that is perpendicular to the maximum tension. This has also been observed by laboratory experiments (Erdogan & Sih, 1963) and field observations (Joussineau et al. 2007; Mutlu and Pollard 2008; Thomas and Pollard 1993). The entire wing crack opens during the injection because a wing crack is a pure Mode I fracture when it propagates, therefore the transmissivity of a wing crack could be higher than the main preexisting fracture. The transmissivity is still high after the fluid pressure decreases to the initial pressure. Most of the wing crack segments remain open even after the fluid pressure inside decreases. The main reason for this is that the shear displacement of the main fracture remains after the fluid pressure decreases,

therefore the tension field induced by the fracture tips still remains and keeps the wing cracks open at a certain length with lowered fluid pressure.

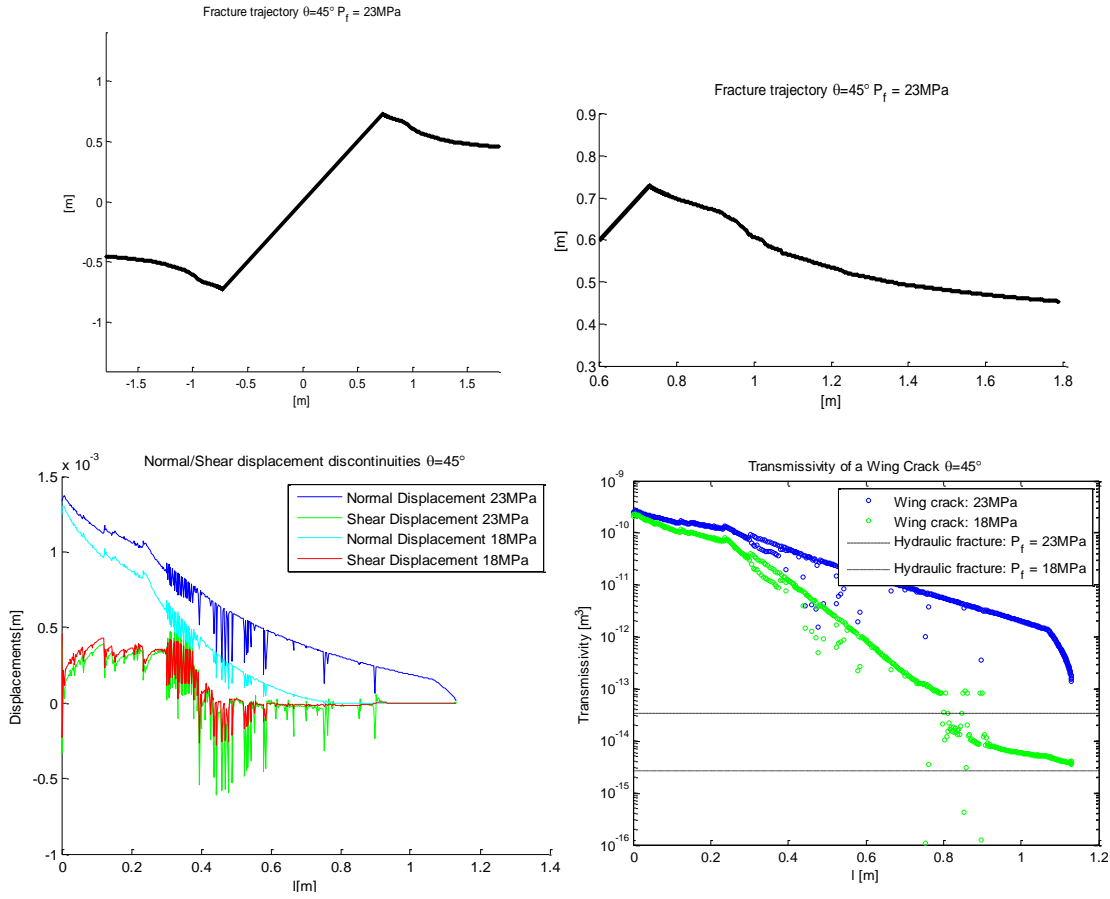


Figure 3.1: The stimulation result for the wing crack for a fracture $\theta=45$. Top: Fracture trajectory, Left bottom: Normal and shear displacements at the end of stimulation when $P_f=23$ MPa and after the stimulation when $P_f=18$ MPa, Right bottom: Fracture transmissivity

As Figure 3.1 to Figure 3.3 show, the transmissivity of the wing crack is much higher than that of the preexisting natural fracture during injection. Shear stimulation enhances the transmissivity of the preexisting natural fracture but the effect of opening displacement along the wing crack has large impact on the transmissivity enhancement.

After fluid pressure is reduced, the closed section of the wing crack has higher transmissivity than that of a hydraulic fracture at the same fluid pressure. A hydraulic fracture here is considered as a planar crack that is perpendicular to the least principal stress. This is because the shear displacement of the main fracture remains after

depressurized, therefore, the compressive normal stress acting on the closed section is smaller than the least principal stress because of the tension field induced by the shear displacement of the main preexisting fracture. The laboratory measurements by Barton et al., (1985) and the numerical results by Co et al. (2017) show that the permeability of close fracture increases as the compressive stress applied decreases. Also the closed section of the wing cracks keep small amount of shear displacements that would have a shear stimulation effects.

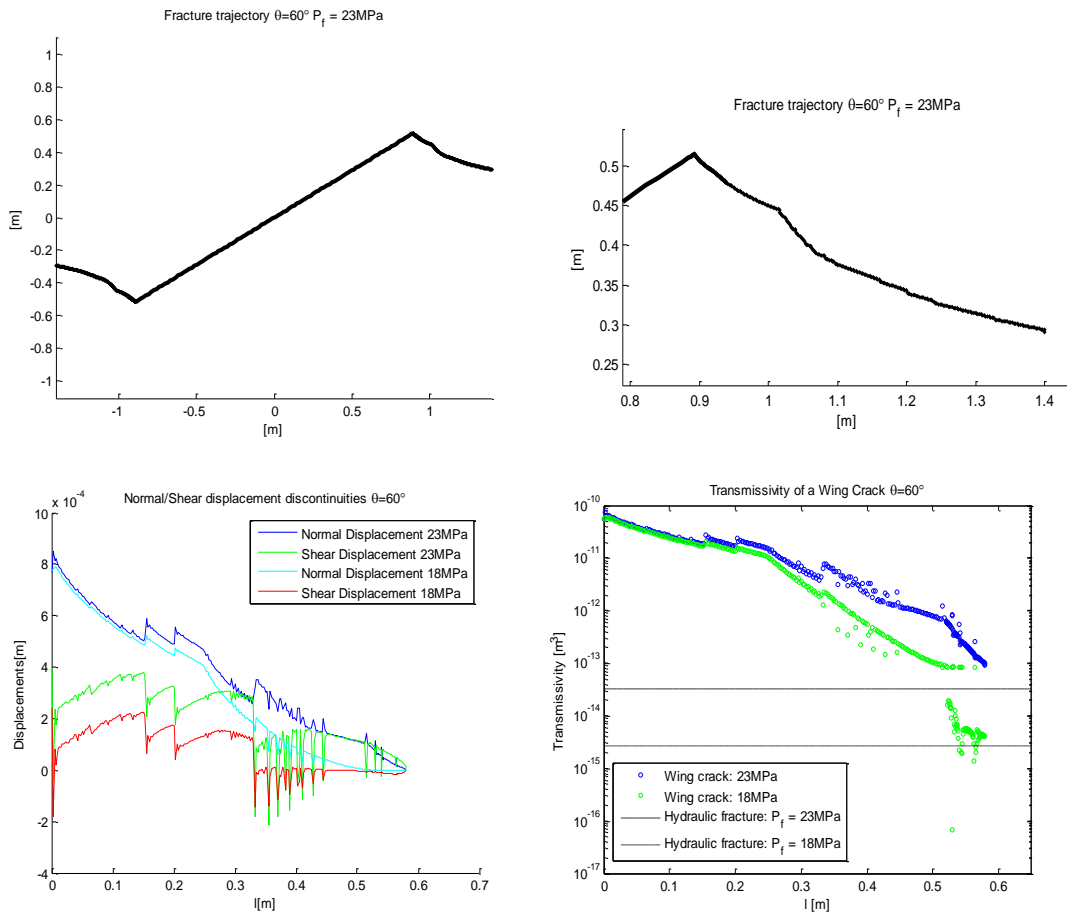


Figure 3.2: The stimulation result for the wing crack for a fracture $\theta=60$. Top: Fracture trajectory, Left bottom: Normal and shear displacements at the end of stimulation when $P_f=23$ MPa and after the stimulation when $P_f=18$ MPa, Right bottom: Fracture transmissivity

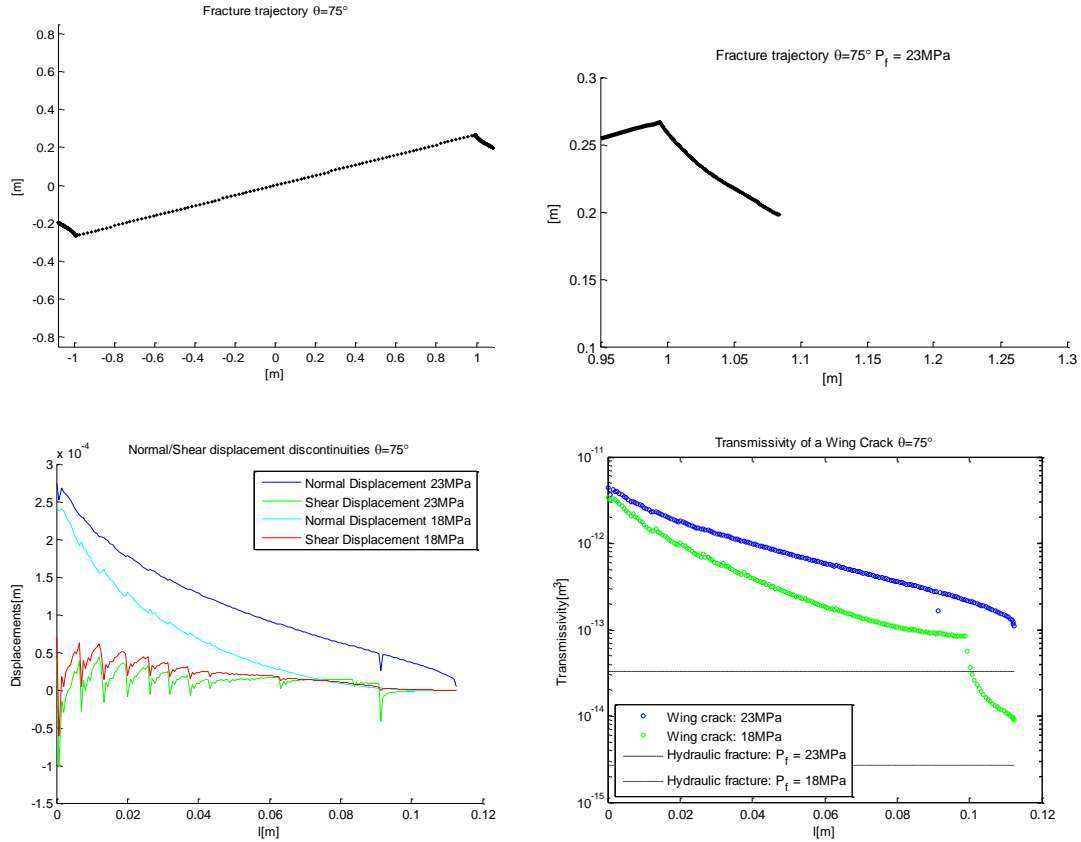


Figure 3.3: The stimulation result for the wing crack for a fracture $\theta=60$. Top: Fracture trajectory, Left bottom: Normal and shear displacements at the end of stimulation when $P_f=23\text{MPa}$ and after the stimulation when $P_f=18\text{MPa}$, Right bottom: Fracture transmissivity

3.2.2 Wing crack propagation from varied injection pressure

To investigate the effect of injection fluid pressure to the wing crack propagation and transmissivity, we simulated the wing crack propagation and fracture deformation with three different injection pressures: 1) 1 MPa below the least principal stress, 2) the same pressure as the least principal stress, and 3) 1 MPa above the least principal stress. The simulation was run until the wing crack propagation stopped. However, the simulation was stopped when the fracture length reached 60 cm with $P_f = 25 \text{ MPa}$ as this fluid pressure could drive the fracture propagation infinitely (Zoback, 2007). After the injection was stopped, the fluid was produced from the well and the fluid pressure was reduced to the initial fluid pressure which was 18 MPa. The material properties and simulation parameters are listed in Table 3.1.

The fracture deformation and its propagation were simulated during the injection and the production phases. The transmissivity of the wing crack at the end of injection and after depressurization were compared. Table 3.3 shows the wing crack length and its angle at each injection pressure. Figure 3.4 shows the wing crack trajectory and its transmissivity at the end of injection and after the fluid pressure was reduced.

The closed section indicated in Figure 3.4 has zero normal displacement $D_n = 0$, and the open section has opening normal displacement $D_n < 0$. The transmissivity of the hydraulic fracture refers to the transmissivity of a single crack that is perpendicular to the least principle stress.

Table 3.3. Wing crack length and its average angles for a preexisting fracture with $\theta = 75$ degrees.

Max BHP	Driving stress	Wing crack length
23 MPa	3.17 MPa	0.120
24 MPa	3.57 MPa	0.223
25 MPa	3.97 MPa	-

When the injection pressure was 23 MPa, which was 1 MPa lower than the least principal stress, the wing crack length was 12% of the half length of the main natural fracture. After fluid pressure was reduced, most of the wing crack stayed open. The closed section near the fracture tip still has higher transmissivity than a hydraulic fracture because the closed section is under less compressive stress than that of the hydraulic fracture due to the induced tension field by the main preexisting natural fracture. Therefore, the transmissivity of the wing crack is higher than the main natural fracture and a hydraulic fracture.

When the injection pressure was at 24 MPa, which is the same magnitude as the least principal stress, the wing crack length was 22% of the half length of the main natural fracture. The wing cracks are not perpendicular to the least principal stress, therefore the normal stress acting on the wing crack is higher than the least principal

stress. The closed section near the fracture tip has the transmissivity which is close to that of the main preexisting natural fracture.

The wing crack kept propagating with the injection pressure of 25 MPa, which is 1MPa higher than the least principal stress. As the wing crack tip is further from the main natural fracture, the effect of the induced tension field becomes weak. So the closed section of the wing crack has higher compressive normal stress as it is closer to the crack tip. The transmissivity of the tip of the wing crack converges to that of a hydraulic fracture. This is because the crack orientation is close to that of a hydraulic fracture, and the effect of induced tension field by the main natural fracture slip. As the total wing crack length increases, the open section also becomes longer even after the injection.

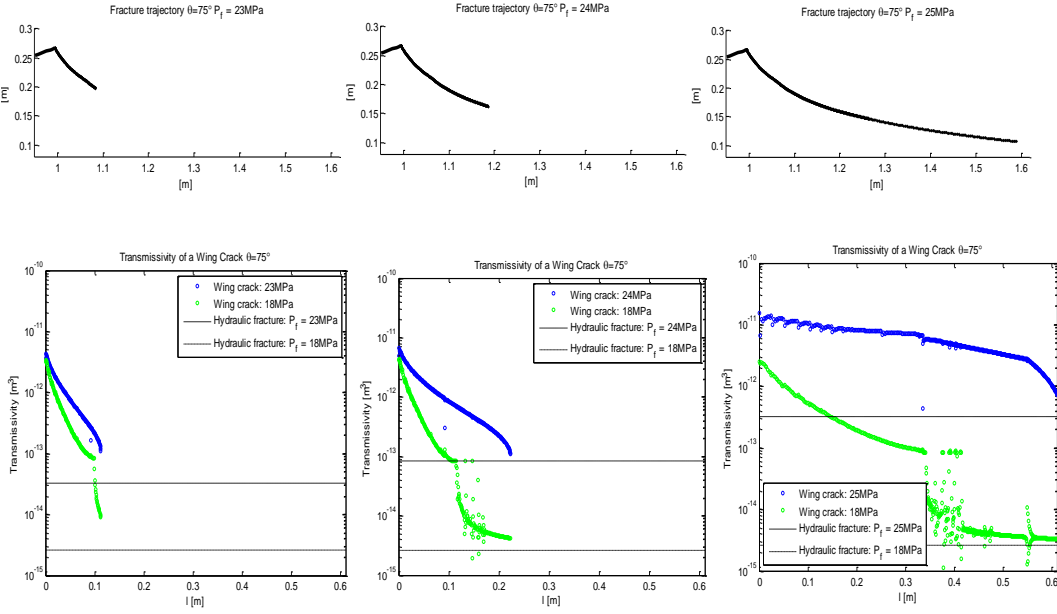


Figure 3.4: Top: Wing crack trajectory, Bottom: Wing crack transmissivity, Left: The maximum BHP 23 MPa, Middle: The maximum BHP 24 MPa, Right: The maximum BHP 25 MPa

3.3 Discussion and Conclusion

In this study, we investigated the impact of wing cracks on the reservoir permeability enhancement. When the injection pressure is below the least principal stress, the wing crack propagation would be contained in a region near the fracture tip where the induced

tension field dominates. However, the results showed that a well-oriented fracture would initiate wing cracks that are longer than their half-length. In a naturally fractured reservoir, it is highly possible that a propagating wing crack intersects another preexisting natural fracture before it stops propagating, which enhances the fracture connectivity in the reservoir. The wing crack length is also related to the magnitude of least principal stress (Horii & Nemat-Nasser, 1986; Mutlu & Pollard, 2008). The length of wing cracks can be longer than the main fracture when the fracture orientation and stress drop are optimal (Cruikshank & Aydin, 1995). Therefore if the dominant preexisting fracture orientation and the least principal stress are suitable to have reasonably long wing cracks in the reservoir, the propagation of wing cracks would not be negligible even though the injection pressure is below the least principal stress. Also wing cracks keep opening displacement after hydraulic stimulation when the fluid pressure is reduced because the shear displacement of the main preexisting natural fracture remains, so this would keep the transmissivity of the created fracture network and increase the fluid storage volume of the reservoir after stimulation. This result will be extended to model a reservoir scale hydraulic stimulation modeling to investigate the actual field observation in the past EGS projects.

Chapter 4

4 3D-Printed Core Hydraulic Stimulation Experiments

4.1 Introduction

In a mixed-mechanism stimulation, newly created fractures intersect with preexisting natural fractures, which creates various patterns of connections. In addition to this, McClure and Horne (2014) suggested that hydraulic fractures may splay out from a natural fracture. Injection pressures in most of the past EGS hydraulic stimulation were usually higher than the least principal stress, meaning that the pressure is high enough to initiate new hydraulic fractures. It is difficult to initiate new fractures as granite has high tensile strength, but preexisting natural fractures slide and dilate at lower pressure than required for initiation of a new fracture. Therefore it is highly probable that new fractures are created from the tips of stimulated preexisting natural fractures as stress concentrates at the crack tips (McClure, 2014).

Although these mixed-mechanism fracture propagation patterns have been suggested based on field observation, how fractures actually propagate and create a fracture network is less clear and still being actively investigated. Thus far, analytical and experimental research that discusses fracture intersection criteria that focus on fracture propagation in Mode I and the mix of Mode I and Mode II has been mainly done in oil and gas settings. For example, Olson (2008) showed a complex fracture network model including the hydraulic fracture with the effect of stress shadow and natural fractures in unconventional oil and gas settings. Physics-based approaches including fluid flow and geomechanics that can simulate fracture propagation and

stimulation in field scale will give insight into many outstanding questions about fracture network creation. How hydraulic fractures intersect with preexisting natural fractures has been studied analytically, numerically, and experimentally especially in unconventional oil and gas settings. In these kinds of reservoirs, hydraulic fractures dominate the fracture network, and thus microseismic events occur and a cloud expands along the direction perpendicular to the least principle stress. In an EGS reservoir, in contrast, the microseismic cloud expands broadly, indicating that natural fracture orientations and distribution are also key factors that affect hydraulic fracture treatment design (Norbeck, 2016). Indeed, unlike in unconventional oil and gas reservoirs, in EGS reservoirs, larger natural fractures dominate the fracture networks because the matrix rock is stiffer and natural fractures are larger compared to those in unconventional oil and gas reservoirs.

In this chapter, as an approach to model hydraulic stimulation in an EGS reservoir, how fractures propagate and intersect with each other was investigated both numerically and experimentally. A numerical method to determine whether a propagating Mode I fracture crosses or follows a preexisting natural fracture with an arbitrary intersection angle is suggested based on the propagation criterion for an orthogonal intersection developed by Renshaw and Pollard (1995), and the results are compared to lab experimental results from the literature.

4.2 Analytical model

Analytical models for the propagation criterion were developed by Renshaw and Pollard (1995) for an orthogonal intersection and later extended for a nonorthogonal intersection (Gu & Weng, 2010; Gu et al., 2011). Renshaw and Pollard (1995) conducted theoretical and experimental work to analyze the mechanism of younger fractures propagating across older fractures oriented perpendicular to the approaching fracture. They stated the criterion as: “compressional crossing will occur if the magnitude of the compression acting perpendicular to the frictional interface is sufficient to prevent slip along the interface at the moment when the stress ahead of the fracture tip is sufficient to initiate a fracture on the opposite side of the interface”. The stress field induced by the fracture

tip was calculated and the condition where the slip along the frictional interface would not occur based on the Mohr–Coulomb failure criterion was derived. Their model is based on the linear elastic fracture mechanics solution for the stresses near a fracture tip and calculates the stresses needed to cause slip on the preexisting interface. Gu and Weng (2010) applied the criterion for a fracture approaching a frictional interface at a nonorthogonal angle. The authors later verified their model with laboratory tests (Gu et al., 2011).

The singular stress field ahead of a crack tip under Mode I loading in an isotropic linear elastic material under the plane-strain condition are expressed in closed form (Anderson, 2005):

$$\sigma_{xx}^{(I)} = \frac{K_I}{\sqrt{2\pi r}} \cos \frac{\theta}{2} \left(1 - \sin \frac{\theta}{2} \sin \frac{3\theta}{2}\right), \quad (4.1)$$

$$\sigma_{yy}^{(I)} = \frac{K_I}{\sqrt{2\pi r}} \cos \frac{\theta}{2} \left(1 + \sin \frac{\theta}{2} \sin \frac{3\theta}{2}\right), \quad (4.2)$$

$$\sigma_{xy}^{(I)} = \frac{K_I}{\sqrt{2\pi r}} \cos \frac{\theta}{2} \sin \frac{\theta}{2} \cos \frac{3\theta}{2}, \quad (4.3)$$

where K_I is the Mode I stress intensity factor, r and θ are the polar coordinate with the origin at the fracture tip. Based on the principle of superposition, the total stress field caused by the remote stresses and the singular stress field are:

$$\sigma_{ij}^{(total)} = \sigma_{ij}^{(remote)} + \sigma_{ij}^{(I)}. \quad (4.4)$$

Maximum magnitude of the stress components is found at the critical radius $r = r_c$ where the least principal stress is the same as the tensile strength. The area within $r = r_c$ is referred to as the *fracture process zone* where the inelastic deformation exists. Then the normal stress and the shear stress along the frictional interface were calculated and plugged in to the Mohr–Coulomb failure criterion:

$$|\sigma_s| < \mu\sigma_n + S_0. \quad (4.5)$$

Then they derived the crossing/terminating threshold for the fracture intersecting the fracture with $\theta = \frac{\pi}{2}$ as:

$$\frac{-\sigma_{xx}^r}{T_0 - \sigma_{yy}^r} > \frac{0.35 + \frac{0.35}{\mu}}{1.06}, \quad (4.6)$$

where σ_{xx}^r and σ_{yy}^r are remote stresses, and μ is the frictional coefficient of the fracture.

In the fracture crossing criterion by Gu and Weng (2010), a hydraulic fracture crosses a preexisting interface when shear stress acting on the preexisting fracture at the point where $\sigma_{yy} = T_0$ with $\geq \frac{\pi}{2}$ is smaller than the Mohr–Coulomb failure criterion as:

$$\sigma_s = K \sin \frac{\theta}{2} \sin \frac{3\theta}{2} \sin 2\theta + K \sin \frac{\theta}{2} \cos \frac{3\theta}{2} \cos 2\theta - \frac{S_{Hmax} - S_{hmin}}{2} \sin 2\theta, \quad (4.7)$$

$$\sigma_n = K + K \sin \frac{\theta}{2} \sin \frac{3\theta}{2} \cos 2\theta - K \sin \frac{\theta}{2} \cos \frac{3\theta}{2} \sin 2\theta + \frac{S_{Hmax} + S_{hmin}}{2} - \frac{S_{Hmax} - S_{hmin}}{2} \cos 2\theta, \quad (4.8)$$

where σ_n and σ_s are the normal and shear stresses acting on the preexisting natural fracture near the crack tip respectively, μ is the frictional coefficient, S_0 is the cohesion of the interface, K represents the stress level required to reinitiate a fracture on the other side of the interface, θ is the angle between the propagating fracture and preexisting fracture, S_{Hmax} is the maximum principal stress, and S_{hmin} is the minimum principal stress. When the interface slips, the propagating fracture cannot initiate fracturing on the other side of the interface surface, and the propagation stops.

4.3 Methodology

Numerical work to investigate whether a propagating fracture crosses another fracture with an arbitrary angle was done by applying the criterion for fracture crossing stated by Renshaw and Pollard (1995) that crossing will happen if the slip along the frictional interface would not occur. When the stress caused by a propagating fracture tip is sufficient to initiate a fracture on the interface, a part of the interface needs to be inside the fracture process zone, which follows the assumption of Wu and Pollard (1992) that the stress concentrating flaw such as an asperity or a notch along a fracture surface reinitiates a fracture. The segment along the interface within the fracture process zone

where there is a possibility to initiate a fracture will be termed a “*fracture-chance segment*” (Figure 4.1).

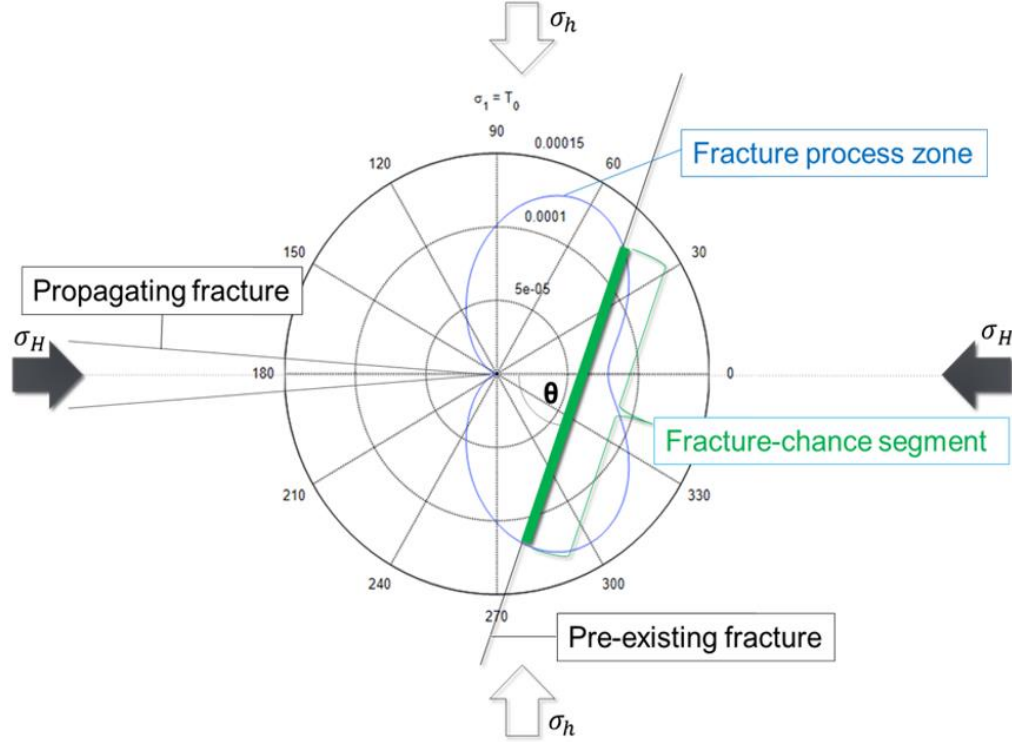


Figure 4.1: An example of a fracture process zone and fracture-chance segment ($\sigma_{xx} = 70$ MPa, $\sigma_{yy} = 35$ MPa, $\sigma_{xy} = 0$ MPa, and $T_0 = -10$ MPa). Fracture-chance segment is shown in green line, fracture process zone is the area surrounded by the blue line. A mode I fracture is located at $x < 0$ and $y = 0$.

The fracture process zone is determined as the area inside the line of $\sigma_1 = -T_0$ (Figure 4.1). The stresses inside the fracture process zone are assumed to be equal to or less than the yield stress (Segall, 2010). In this work, the stress inside the fracture process zone is assumed to be equal to the tensile strength. Therefore the linear elastic fracture mechanics is applied inside the fracture process zone. A Mode I fracture tip induces the tension field expressed in Equations 4.1, 4.2, 4.3, and 4.4. Then the principal stresses are expressed by the following:

$$\sigma_1 = \frac{\sigma_{xx} + \sigma_{yy}}{2} + \sqrt{\left(\frac{\sigma_{xx} - \sigma_{yy}}{2}\right)^2 + \sigma_{xy}^2}, \quad (4.9)$$

$$\sigma_2 = \frac{\sigma_{xx} + \sigma_{yy}}{2} - \sqrt{\left(\frac{\sigma_{xx} - \sigma_{yy}}{2}\right)^2 + \sigma_{xy}^2}, \quad (4.10)$$

$$\theta_p = \frac{1}{2} \tan^{-1} \frac{2\sigma_{xy}}{\sigma_{yy} - \sigma_{xx}}, \quad (4.11)$$

where σ_1 and σ_2 are the maximum and least principal stresses respectively, σ_{ij} is the total stresses, and θ_p is the direction of the maximum principal stress (Pollard & Fletcher, 2005).

In this numerical work, the fracture-chance segment was divided into a sufficient number of small segments. To check if $|\sigma_s| < \mu\sigma_n + S_0$ and $\sigma_n > 0$ are satisfied at all the segments along the fracture-chance segment, the normal stress and shear stress acting on each segment are calculated by:

$$\sigma_n = \sigma_{xx} \sin^2 \theta - 2\sigma_{xy} \sin \theta \cos \theta + \sigma_{yy} \cos^2 \theta, \quad (4.12)$$

$$\sigma_s = -(\sigma_{xx} - \sigma_{yy}) \sin \theta \cos \theta + \sigma_{xy}(\cos^2 \theta - \sin^2 \theta), \quad (4.13)$$

where σ_{ij} are the total stresses and θ is the fracture angle to σ_H . There are three patterns that would occur when a hydraulic fracture approaches a preexisting fracture:

Pattern 1) $|\sigma_s| < \mu\sigma_n + S_0$ and $\sigma_n > 0$ are satisfied along the entire fracture-chance segment. This means that the induced stress field ahead of a crack tip causes neither slip nor opening along a preexisting fracture. Consequently, the propagating hydraulic fracture is expected to cross the preexisting fracture,

Pattern 2) $|\sigma_s| < \mu\sigma_n + S_0$ and $\sigma_n > 0$ are not satisfied along the entire fracture-chance segment. This means that the induced stress field occurring ahead of a crack tip causes slip or opening along the preexisting fracture inside the fracture process zone. The propagating hydraulic fracture is hence expected to follow the preexisting fracture.

Pattern 3) $|\sigma_s| < \mu\sigma_n + S_0$ and $\sigma_n > 0$ are not satisfied on a part of the fracture-chance segment. This means that the induced stress field ahead of a crack tip partially causes slip or opening along the preexisting fracture inside the fracture process zone.

4.3.1 Methodology Comparison with Lab Experiment Data

To verify this numerical method, data from laboratory experiments in previous studies were compared. Those lab experiments showed whether a propagating Mode I fracture, either initiated by hydraulic fracturing or a point force, crossed or terminated at a frictional interface with varied intersection angles and stress state. The numerical results were compared to the lab experiment results of Blanton (1982), Warpinski and Teufel, (1987), Zhou et al., (2008) and Gu and Weng (2010).

As Table 4.1 shows, with the pattern 1 where any region of the fracture-chance segment neither opens nor slides, a propagating fracture crosses a frictional interface in all the cases in the lab experiment results. Moreover, with the Pattern 2 where any region of the fracture-chance segment opens or slides, a propagating fracture follows a frictional interface in all cases. On the other hand, when the results from the numerical method show that the induced stress field partially causes slip or opening along the fracture-chance segment, then in roughly half of the cases, a propagating fracture crosses the frictional interface.

Table 4.1: Comparison with Lab Experiment Results

Numerical Results	Lab Experiment Results	
	crosses	follows
1) Entire fracture-chance segment does not open nor slide $ \sigma_s < \mu\sigma_n + S_0$ and $\sigma_n > 0$	11	0
2) Entire fracture-chance segment opens or slides $ \sigma_s > \mu\sigma_n + S_0$ or $\sigma_n < 0$	0	20
3) A part of the fracture-chance segment opens or slides Partially $ \sigma_s > \mu\sigma_n + S_0$ or $\sigma_n < 0$	3	5

4.3.2 The Offset of Discontinuous Crossing

Helgeson and Aydin, (1991) reported a field observation of joint propagation in layered sedimentary rocks that shows offset at a discontinuous crossing of fractures. This is not an uncommon observation in the field. Such observations support the concept of reinitiation with spatial offsets between fracture segments on either side of the interface, occurring when a fracture crosses a frictional interface (Renshaw & Pollard, 1995). Following the assumption by Renshaw and Pollard (1995) that discontinuous crossing requires less compression than continuous crossing, and reinitiation occurs at an asperity or a notch on the surface of a frictional interface where the maximum principal stress is equal to the tensile strength, the offset of a discontinuous crossing can be calculated analytically.

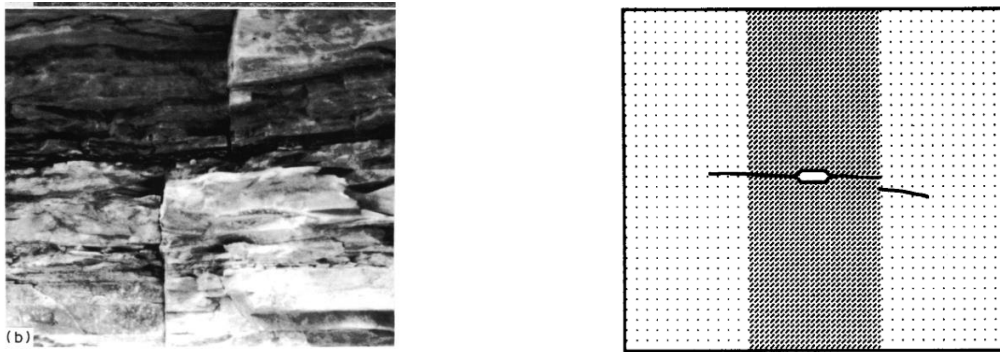


Figure 4.2: (Left) An example of discontinuous crossing observed in the field, (Right) A sketch of a sample showing both continuous and discontinuous crossing (Renshaw & Pollard ,1995)

The singular stress field ahead of a crack tip under Mode I loading in an isotropic linear elastic material under the plane-strain condition can be expressed in the closed form (Anderson, 2005):

$$\sigma_{yy}^{(I)} = \frac{K_I}{\sqrt{2\pi r}} \cos \frac{\theta}{2} \left(1 + \sin \frac{\theta}{2} \sin \frac{3\theta}{2} \right). \quad (4.14)$$

At $r = r_c$, the stress acting parallel to the fracture surface is equal to T_0 , and then, assuming $\theta = \frac{\pi}{2}$ and $K_I = K_{Ic}$ as a hydraulic fracture is propagating, the offset r_c is expressed as:

$$\sigma_{yy}^c = T_0 - \sigma_{yy}^r = \frac{K_{Ic}}{\sqrt{2\pi r_c}} \cos \frac{\pi}{4} \left(1 + \sin \frac{\pi}{4} \sin \frac{3\pi}{4} \right), \quad (4.15)$$

$$r_c = \frac{9}{16\pi} \frac{K_{Ic}}{T_0 - \sigma_{yy}^r}, \quad (4.16)$$

where σ_{yy}^r is the least principal stress. Figure 4.3 shows that the distance of the offset assuming that the preexisting fracture surface at 90 degrees. In a high compressive stress state such that $T_0 - \sigma_{yy}^r$ is larger than 40 MPa, the offset would be less than 0.1mm, which is almost not visible. It would be possible to estimate the magnitude of remote stress σ_h from the offset length when the offset is visible.

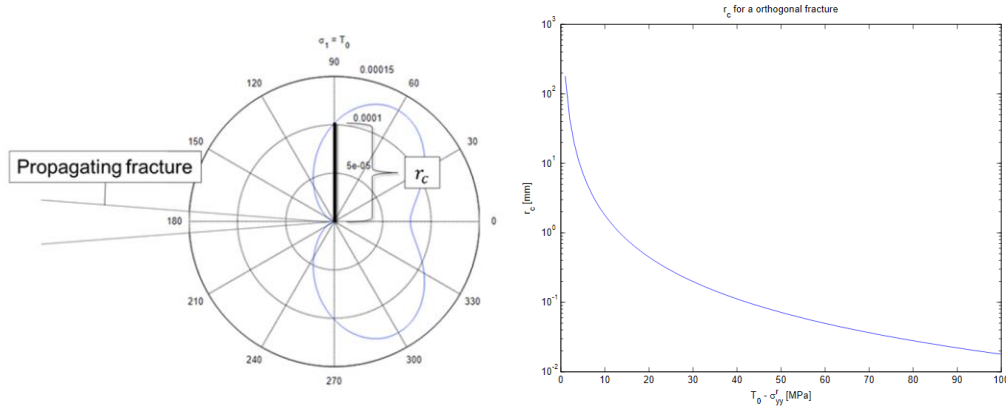


Figure 4.3: (Left) Discontinuous offset length r_c , (Right) The relationship between discontinuous offset length and $T_0 - \sigma_{yy}^r$ ($K_{Ic} = 1 \text{ MPa} \cdot \sqrt{\text{m}}$).

4.3.3 Discussion

The results of this comparison indicate that the numerical method shows a significantly good agreement with the experimental results in past work, especially when the numerical result shows that the entire fracture-chance segment satisfies $|\sigma_s| < \mu\sigma_n + S_0$ and $\sigma_n > 0$ and when the entire fracture-chance segment does not satisfy these criteria. When a part of the fracture-chance segment does not satisfy $|\sigma_s| < \mu\sigma_n + S_0$ or $\sigma_n > 0$, then it could be said that in half of the cases a propagating fracture would cross the frictional interface.

In the experimental results in past work, rocks that typically have homogeneous isotropic properties such as sandstone, cement, and hydrostone were used, and the

preexisting frictional interfaces were ground smooth. In actual field conditions, local heterogeneity, such as the tensile strength varying at a small scale, grain size distribution, or the stress concentrating flaws such as an asperity or a notch along a fracture would affect the result. Chen et al. (2018) investigated a hydraulic fracture propagation intersecting a cemented preexisting natural fracture by DEM. They suggested that the material properties of the cement and matrix rock affect whether a hydraulic fracture keeps a straight trajectory or branches into the cemented natural fracture. These effects by cemented natural fractures should be considered when modeling fracture network creation.

4.3.4 Laboratory Scale Experiments Using 3D Printed Core Samples

The purpose of these experiments was to verify the method to determine how a propagating fracture intersects a preexisting fracture at varied angles. Another purpose was to explore the possibility of using a 3D-printed core sample for hydraulic fracturing experiments. The advantages of using a 3D-printed core sample are: 1) the semitransparent material enables monitoring of fracture propagation and intersection; 2) using the 3D printer makes it easy to design a core sample with well-controlled fracture geometry; and 3) the material is homogeneous and impermeable.

The experimental design is explained in the following sections in detail. Briefly, in these experiments, a hydraulic fracture was initiated by injecting water and the initiated hydraulic fracture intersected a preexisting cut inside the 3D-printed core sample. Fracture intersection angle was 90 degrees. The confining pressure was kept constant and the axial stress was changed to observe the relationship between the stress state and the fracture cross/follow condition. Water pressure was applied until a hydraulic fracture was initiated and the pressure was reduced immediately after the fracture was initiated.

4.4 Sample Materials

The samples used in this study were made using a 3D printer, KEYENCE Agilista-3100. The sample size is 50.0 mm diameter by 50.0 mm height made of transparent plastic

AR-M2. Mechanical properties of the material are listed in Table 4.2. The matrix is impermeable and totally homogeneous.

A cut was printed at the height of 40.0 mm from the bottom. This cut acts as a preexisting natural fracture that is crossed by a propagating hydraulic fracture. The surfaces of the cut were ground for 2 minutes on an Ibaraki granite block. Naniwa Abrasive Coarse Grain GC #30 was used. An initial crack was printed on the bottom. The geometry of the initial crack is a half ellipsoid whose principal semiaxes are 20.0 mm, 30.0 mm, and 0.5 mm.

Table 4.2: Sample material properties

Property	Value	Unit
Tensile strength	40-55	MPa
Compressive strength	70-80	MPa
Bending strength	60-80	MPa
Young's modulus	1.8-2.1	GPa
Flexural modulus	1.9-2.4	GPa

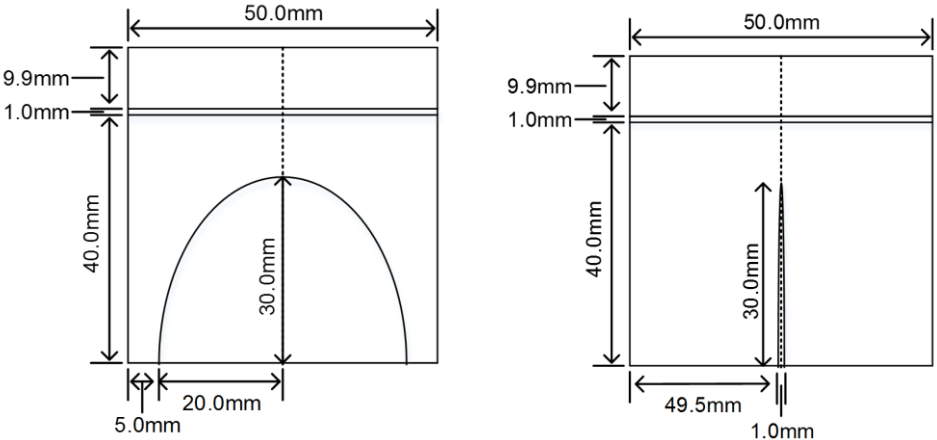


Figure 4.4: Sketches of the sample



Figure 4.5: (Left) Ground surfaces of the cut, (Center and right) Initial crack

4.5 Experiment Preparation

4.5.1 Determination of the Frictional Coefficient

The frictional coefficient of the material after grinding was determined by placing two blocks ground in the same way together and then tilting them until the top block slides. The geometry of the samples are 70.0 mm, 14.0 mm, 20.0 mm and 120.0 mm, 200.0 mm, 5.0 mm. The angle when the upper sample slips is θ , then the frictional coefficient f is $f = \tan\theta$. Based on the measurement data, the average angle θ is 30.15 degrees, the frictional coefficient was therefore determined as $\tan(30.15) = 0.58$.



Figure 4.6: Samples used to measure the frictional coefficient

4.5.2 Determination of the Stress Intensity Factor of the Initial Crack

The first experiment was done to find the parameters to make an initial fracture propagate by water pressure. In this experiment, sample size and initial crack size were different from later experiments. The sample size is 50.0 mm diameter by 100.0 mm height as shown in

Figure 4.7. An initial crack is printed on the bottom. The geometry of the initial crack is a half ellipsoid whose principal semiaxes are 20.0 mm, 20.0 mm, and 0.5 mm.

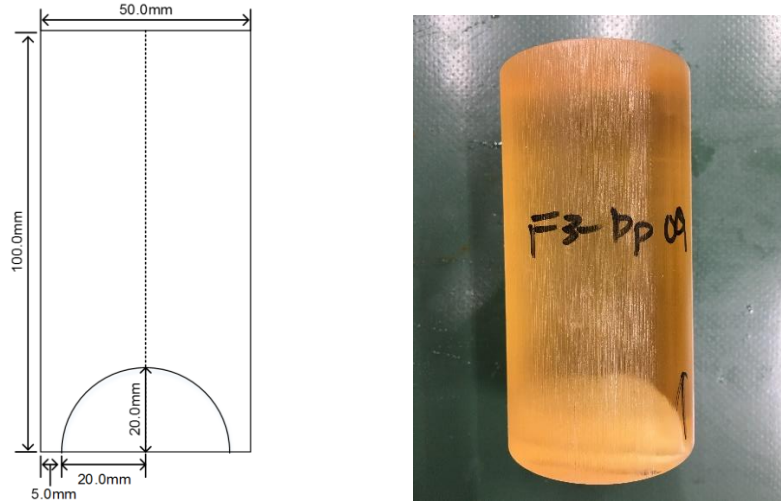


Figure 4.7: (Left) A sketch of the sample, (Right) The sample used in this experiment

The stress intensity factor of this ellipsoid was estimated. Murakami and Nemat-Nasser (1983) suggested that the critical stress intensity factor for a two-dimensional crack is proportional to the biquadratic root of its area. The equation derived empirically by them is:

$$K_{I \max} = 0.629 \sigma'_n \sqrt{\pi \sqrt{\text{area}}}, \quad (4.17)$$

where σ'_n is the effective normal stress and area is the area of the crack. The stress intensity factor of semielliptical cracks can be calculated (Anderson, 2005):

$$K_{I \max} = \lambda_s \sigma'_n \sqrt{\frac{\pi a}{Q}} f(\phi), \quad (4.18)$$

$$Q = 1 + 1.464 \left(\frac{a}{c}\right)^{1.65}, \quad (4.19)$$

$$\lambda_s = (1.13 - 0.09 \frac{a}{c})(1 + 0.1(1 - \sin \phi)^2), \quad (4.20)$$

where a is the principal semiaxis perpendicular to the straight line of the semiellipse, c is the principal semiaxis parallel to the straight line of the semiellipse, and ϕ is the angle from the center point. However, these equations are only valid for a semiellipse where $a \leq c$.

Water was injected into the initial crack and the pressure was increased until it reached 25 MPa. When the effective normal stress σ'_n was 22 MPa, acoustic emission was detected and water injection was stopped immediately. A hydraulic fracture propagated a distance of 50 – 66 mm at this water pressure as shown in Figure 4.8.

When $a = c = 20.0$ [mm] and $\sigma'_n = 22$ [MPa], $K_I = 3.88$ [$MPa\sqrt{m}$] based on Murakami and Nemat-Nasser (1983), or $K_I = 3.28$ [$MPa\sqrt{m}$] based on Anderson (2005). Based on these results, the critical stress intensity factor of the material is estimated to be around $3.3 - 3.9$ $MPa\sqrt{m}$. The critical stress intensity factors of polymers generally range from $0.3 - 4.0$ $MPa\sqrt{m}$. The estimated value is within this general range.

Table 4.3: Stress property during the experiment

Property	Value	Unit
Axial Stress	30	MPa
Confining Stress	3	MPa
Fluid Pressure	3-25	MPa

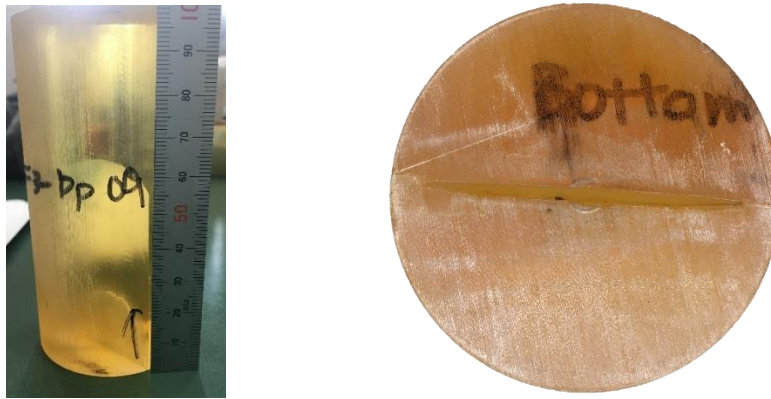


Figure 4.8: The sample after hydraulic fracturing

4.6 Numerical Results

The same parameters for this laboratory experiment were used in the numerical model described in the previous section. For a precut intersecting orthogonally to a hydraulic

fracture, a hydraulic fracture is expected to terminate at $\sigma_H = 20MPa$ and it is expected to cross at $\sigma_H = 60MPa$. When $\sigma_H = 40MPa$, the condition is categorized as pattern 3, which means half of the time, a hydraulic fracture crosses the precut.

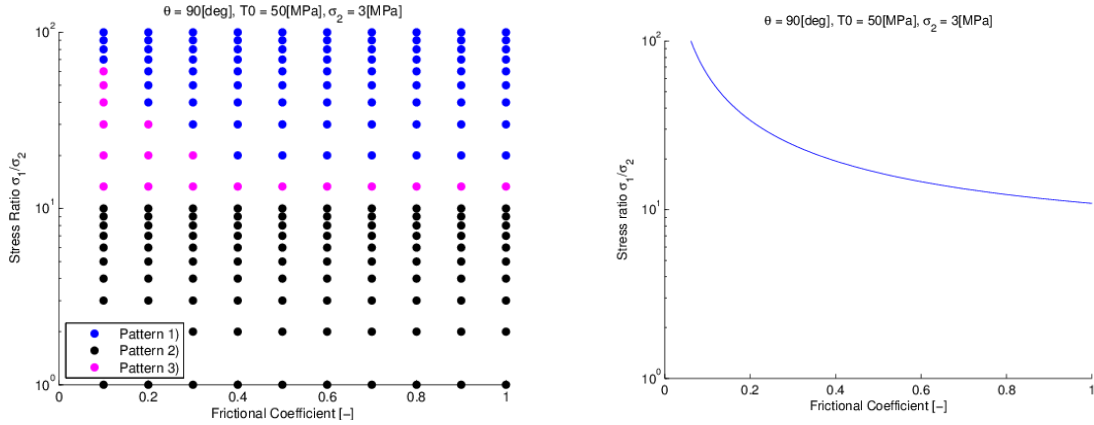


Figure 4.9: (Left) Numerical results with parameters in Table 4.4 and the varied stress ratio and the fracture angle. A hydraulic fracture is expected to cross in the area with blue dots, it is expected to terminate in the area with black dots, and pink dots show the area categorized in pattern3, where a propagating fracture is expected to cross half of the cases. (Right) Analytical results of Renshaw and Pollard (1995) with parameters in Table 4.4. A propagating fracture is expected to cross in the area above the line.

Table 4.4: Parameters used in the numerical experiment

Parameters		Value	Unit
Maximum Horizontal Stress	σ_H	3 - 60	MPa
Least Horizontal Stress	σ_h	3	MPa
Fracture Intersecting Angle	θ	15 - 90	degrees
Mode-I Critical Stress Intensity Factor	K_I	3.5	$\text{MPa} \cdot \sqrt{m}$
Frictional Coefficient	f	0.58	-
Cohesion	S_0	0	MPa
Tensile Strength	T_0	50	MPa

4.7 Experimental Results

During the experiments, we applied the axial stress and the confining pressure simultaneously until they reached the set values, then pure water was injected into the initial hydraulic fracture printed at the bottom of the sample. The water pressure was increased from 0 MPa to 25 MPa, and water injection was stopped immediately after we observed acoustic emission exceeding a certain threshold of amplitude where we assumed hydraulic fracturing occurred. In this work, we fixed the confining pressure, the frictional coefficient of the preexisting fracture, and the geometry of the initial hydraulic fracture. We changed axial stress in each experiment and observed whether a propagating fracture crosses or stops at the preexisting fracture. The results are discussed in the following sections in detail. The summary of the results is shown in Table 4.5.

Table 4.5: The summary of the experiment results

Test Case	σ_H [MPa]	σ_h [MPa]	Result	Numerical result
1	20	3	Stops	Pattern 2 (Stops)
2	40	3	Crosses	Pattern 3 (Sometimes crosses)
3	40	3	Stops	Pattern 3 (Sometimes crosses)

4.7.1 Test Case 1

The result of the cross/follow determination method shown in this chapter for this test case suggests that a hydraulic fracture would follow a preexisting cut. In addition, the analytical criterion derived by Renshaw and Pollard (1995) shows the crossing/terminating threshold for the fracture intersecting the fracture with $\theta = \frac{\pi}{2}$ is:

$$\frac{-\sigma_{xx}^r}{T_0 - \sigma_{yy}^r} > \frac{0.35 + \frac{0.35}{\mu}}{1.06}. \quad (4.21)$$

Here, σ_{xx}^r corresponds to the axial stress and σ_{yy}^r corresponds to the confining pressure in this setting. The frictional coefficient μ is 0.58 and tensile strength is 40-55

MPa. The right hand side of the equation is $0.8995 \approx 0.9$. The left hand side of the equation is:

$$\frac{-\sigma_{xx}^r}{T_0 - \sigma_{yy}^r} = \frac{20}{(40 \text{ to } 55) + 3} = 0.345 \text{ to } 0.465. \quad (4.22)$$

The propagating fracture is therefore expected to stop at a preexisting fracture under these stress conditions, both by the analytical and numerical prediction. The measurement data during the test are shown in Figure 4.10. The axial stress and the confining pressure were applied simultaneously until they reached the set values. Then water was injected at a constant rate of 5 ml/min until we observed acoustic emission exceeding a certain threshold of amplitude where we assumed hydraulic fracturing occurred. The acoustic emission was detected at 654.32 second, when the axial stress was 20.07 MPa, the confining pressure was 3.00 MPa, and the water pressure was 18.42 MPa. After hydraulic fracturing occurred, the water pressure and the confining pressure became close in value, which means that the water and the oil used to apply the confining pressure were connected mechanically inside the triaxial machine.

Figure 4.11 shows the sample after the experiment. A hydraulic fracture propagated to the preexisting fracture, however, it stopped propagating at the interface and did not cross. This result is consistent with the analytical and numerical predictions.

Table 4.6: Stress properties during the experiment

Property	Value	Unit
Axial Stress	20	MPa
Confining Pressure	3	MPa
Fluid Pressure	3-25	MPa
Fracture Intersecting Angle	90	degrees

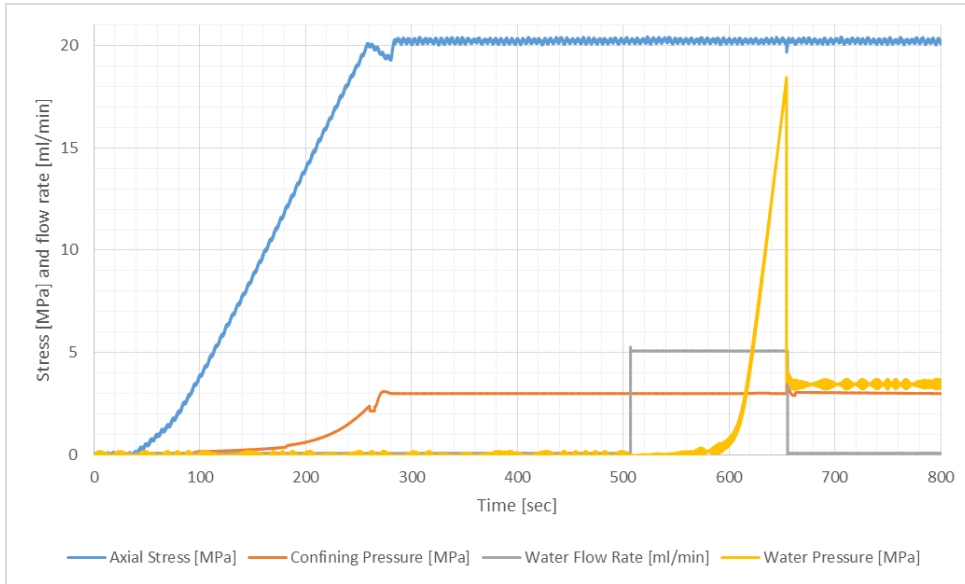


Figure 4.10: Pressure profiles and water flow rate during the experiment

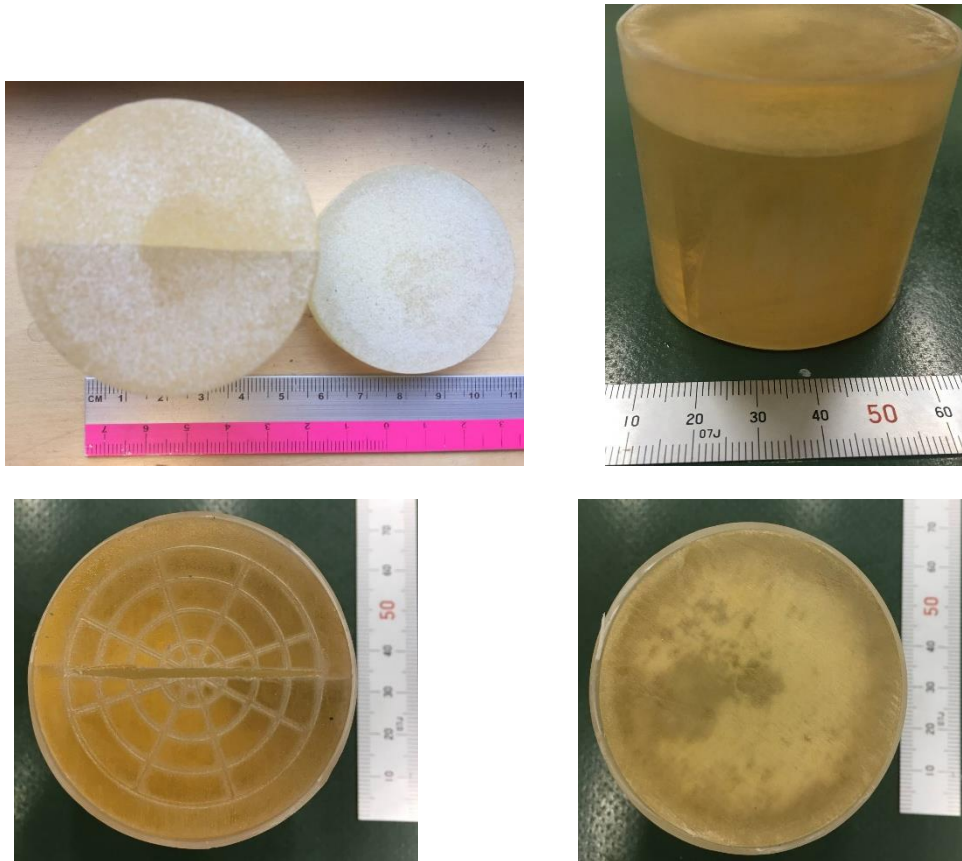


Figure 4.11: The sample after experiment

4.7.2 Test Case 2

The result of the cross/follow determination method shown here for this test case suggests that a hydraulic fracture would cross a preexisting cut when $T_0 = 55$ MPa. Using the analytical criterion derived by Renshaw and Pollard (1995), the crossing criterion is:

$$\frac{-\sigma_{xx}^r}{T_0 - \sigma_{yy}^r} > \frac{0.35 + \frac{0.35}{\mu}}{1.06}. \quad (4.23)$$

The right hand side of the equation is 0.90. The left hand side of the equation is:

$$\frac{-\sigma_{xx}^r}{T_0 - \sigma_{yy}^r} = \frac{40}{(40 \text{ to } 55) + 3} = 0.690 \text{ to } 0.930. \quad (4.24)$$

Consequently, the propagating fracture is expected to cross a preexisting fracture when $T_0 > 43$ MPa and it is expected to follow in the case when $T_0 < 43$ MPa under these stress properties. The numerical result shows that this condition is categorized as pattern 3, which means half of the time, a hydraulic fracture would cross the precut.

The measurement data obtained during the test are shown in Figure 4.13. The axial stress and the confining pressure were applied simultaneously until they reached the set values. Then water was injected at a constant rate of 5 ml/min until we detected acoustic emission exceeding a certain threshold of amplitude where we assumed hydraulic fracturing occurred. The acoustic emission was observed at 1334.7 second, when the axial stress was 40.08 MPa, the confining pressure was 3.00 MPa, and the water pressure was 25.07 MPa. Figure 4.12 shows the sample after the experiment. A hydraulic fracture propagated to the preexisting fracture, and it crossed the interface and continued propagating.

Our original plan was to increase the axial stress to 60 MPa, where a propagating fracture is expected to cross based on numerical and analytical solutions. However, when we increased the axial stress near to 60 MPa around 400 to 600 seconds (Figure 4.13), we observed that the vertical deformation increased significantly. We decreased the axial stress down to 30 MPa then increased it and kept at 40 MPa, where the vertical deformation was within a reasonable amount.

Table 4.7: Stress property during the experiment

Property	Value	Unit
Axial Stress	40	MPa
Confining Stress	3	MPa
Fluid Pressure	3-25	MPa
Fracture Intersecting Angle	90	degrees

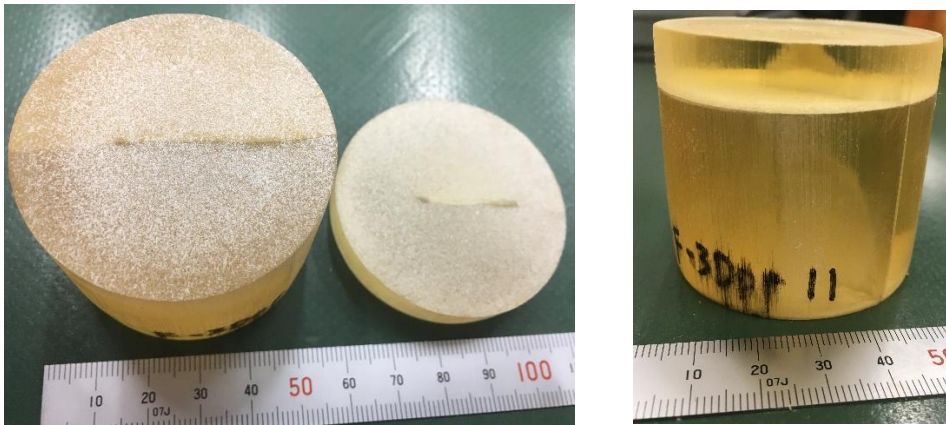


Figure 4.12: The sample after the experiment

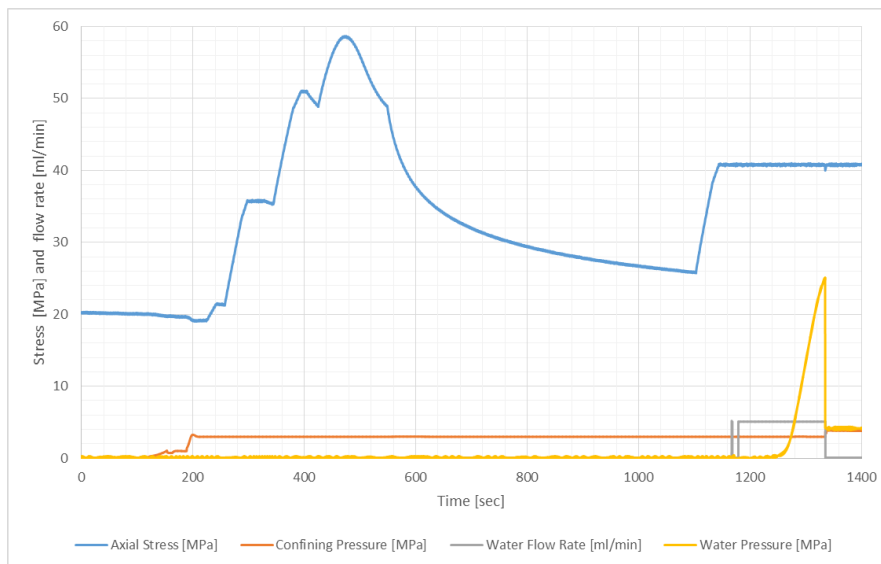


Figure 4.13: Pressure profiles and water flow rate during the experiment

4.7.3 Test Case 3

During Test Case 2, we observed that the sample started yielding when axial stress was around 55 MPa. To avoid plastic strain, we increased the axial stress from 0 MPa to 40 MPa directly this time and tested it with the same settings again.

Table 4.8: Stress property during the experiment

Property	Value	Unit
Axial Stress	40	MPa
Confining Stress	3	MPa
Fluid Pressure	3 - 25	MPa
Fracture Intersecting Angle	90	degrees



Figure 4.14: The sample after experiment

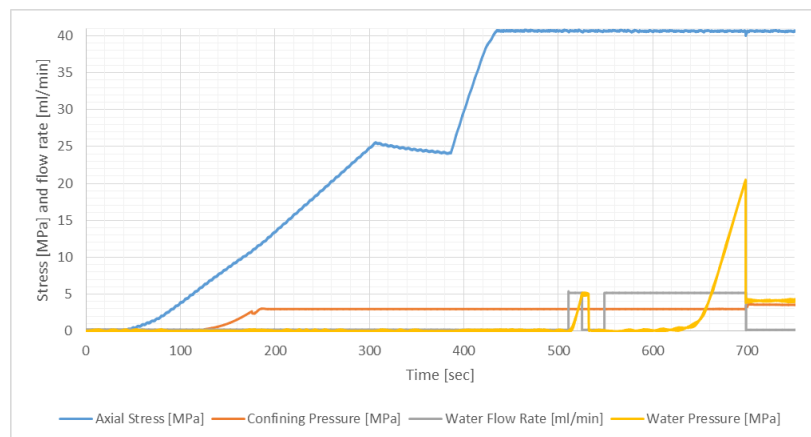


Figure 4.15: Pressure profiles and water flow rate during the experiment

The measurement data during the test are shown in Figure 4.15. The acoustic emission was observed at 698.32 seconds, when the axial stress was 40.62 MPa, the confining pressure was 3.00 MPa, and water pressure was 20.5 MPa. Figure 4.14 shows the sample after the experiment. A hydraulic fracture propagated to the preexisting fracture, and it did not cross the interface and stopped propagating. This result is consistent with the analytical and numerical results, assuming that the tensile strength was larger than 43 MPa.

4.8 Discussion and Summary

The results of the hydraulic fracturing experiment using 3D-printed samples show good agreement with the numerical results and the analytical criterion of Renshaw and Pollard (1995). The reason why the results of the Test Case 2 and 3 were different could be because the sample in Test Case 2 was applied a higher axial stress. The sample expanded horizontally and contracted vertically after the experiment. We suppose that the sample started yielding when the axial stress was near to 60 MPa and it led to this remaining plastic deformation. The remaining deformation would cause residual stress in the sample, which could affect the result.

Our results also demonstrate the possibilities of using 3D-printed core samples for fracturing experiments. There are several specific advantages of using 3D-printed samples. The transparent material enables us to observe how a fracture spreads in the core without breaking it open to see. The highly homogeneous material without any flaws is ideal for a fracturing experiment. The geometries of the initial crack and the precut can be designed precisely, making it potentially useful for more complex fracturing experiments. However, the low compressive strength and the yield strength limited the axial stress that could be applied to the sample, which made it difficult to create the conditions where a propagating fracture would cross a precut. It is useful to extend this experiment using cement which has much higher compressive strength and yield strength and lower tensile strength. Higher compressive strength would enable the application of higher axial stress, and a wider range of stress state could then be applied to a sample. This enables test of precuts with arbitrary angles. Lower tensile strength

enables a sample to be hydraulically fractured with lower fluid pressure, which gives room to apply higher confining pressure. As described in Chapter 5 our next step was to continue the experiment with cement to investigate a propagating fracture intersecting another fracture at arbitrary angle.

In this study, as an approach to model hydraulic stimulation in an EGS reservoir, a numerical model to determine whether a propagating fracture crosses or follows a preexisting natural fracture was developed and verified by comparing to experimental data in previous studies. In addition, laboratory scale experiments were conducted to verify the numerical model and also explore the possibility of using 3D-printed core samples for hydraulic fracturing experiments.

To investigate fracture network creation, physics-based approaches including fluid flow and geomechanics that can simulate fracture propagation and stimulation at a field scale will be necessary. The numerical model introduced in this study will be the first step toward understanding a fracture network creation and will be combined in future work with other geomechanical models to tackle this problem.

Chapter 5

5 Cement Core Hydraulic Stimulation

Experiments

5.1 Introduction

Understanding how a fracture network is created by hydraulic stimulation treatment is necessary for characterizing a reservoir permeability enhancement in an EGS. EGS reservoirs usually consist of granite, which has high tensile strength, where large preexisting natural fractures may dominate. Hydraulic stimulation treatment enhances fracture permeability and connectivity by injecting high pressure fluid into the reservoir. Therefore, preexisting natural fractures play an important role in fracture network creation. In mixed mechanism stimulation, it has been suggested that newly created fractures intersect preexisting natural fractures, and then a newly formed fracture propagates from the preexisting fracture. The effect of natural fractures on propagation of a hydraulic fracture has been observed since the mineback experiment by Warpinski & Teufel (1987) where the authors observed propagating hydraulic fractures often followed preexisting joints and branched into several paths. The fracture initiated from a sheared preexisting natural fracture was investigated in Chapter 3.

Laboratory scale experiments to understand the fracture propagation and resulting fracture geometry in a naturally fractured reservoir have been done as we discussed in Chapter 4 and 5. The main interest in these studies was how a hydraulic fracture propagating from the wellbore intersects preexisting natural fractures in the reservoir. However, in the mixed mechanism stimulation, the behavior of a stimulated natural fracture initiating newly formed fractures (wing cracks) also plays a key role

because the preexisting natural fractures can slide in shear and initiate new fractures from their tips, both of which are important factors of the reservoir stimulation mechanism. Especially in most of the past EGS projects, natural fractures are large and reservoir rocks are harder than those in unconventional oil and gas reservoir (McClure & Horne, 2014), therefore, it is important to have a better understanding of how natural fractures contribute to the creation of a network of fractures. Outcrop observations show that a slipping fracture loaded in compression accumulates local tensile stress concentrations near the fracture tips, and then initiates secondary opening fractures which are called wing cracks or splay fractures (Cooke et al., 2000; Cruikshank & Aydin, 1994; Segall & Pollard, 1983). The mechanism of the creation of a newly formed fracture initiated from a preexisting fracture has been studied based on field observation and analytical, numerical, and experimental works (Erdogan & Sih, 1963; Thomas & Pollard, 1993; Joussineau et al., 2007; Mutlu & Pollard, 2008). As reported by Mutlu and Pollard, (2008), laboratory experiments on wing crack propagation from a single flaw under compression have been carried out in glass or plastic (Brace & Bombolakis, 1963; Hoek & Bieniawski, 1965; Horii & Nemat-Nasser, 1986) as well as in rocks (Bobet & Einstein, 1998; Li et al., 2005; Petit & Barquins, 1988; Sahouryeh et al., 2002). The observations of these laboratory experiments are similar to those observed in outcrops where wing cracks propagate from the tips of the slipping fracture toward the direction perpendicular to the least principal stress. However, only a few research has been done to investigate how those newly formed and preexisting fractures mechanically and hydraulically interact each other to create flow paths and a fracture network.

As noted, the mixed mechanism fracture network creation pattern has been suggested and widely accepted in the geothermal and the unconventional oil and gas industries. The mechanism of a propagating hydraulic fracture intersecting a preexisting fracture, and wing crack initiation and propagation has been well studied experimentally, numerically, and analytically. However, those phenomena are not independent processes but they interact with one another in complex ways. The fluid pressure distribution and the deformations of the upstream fracture affect those of the

downstream fracture, which then affect fractures further downstream. Therefore, how newly formed fractures and preexisting fractures interact with each other and create a fracture network is less clear and is still being investigated actively. This interaction was the focus of the investigation reported here, using both laboratory and numerical studies. To better understand the process of creating a fracture network by hydraulic stimulation in an EGS reservoir, we conducted laboratory-scale hydraulic stimulation experiments using cement samples including an embedded fracture inside. We hydrofractured the sample to make a propagating hydraulic fracture intersect the embedded crack to better understand the fracture network creation including a hydraulic fracture and a preexisting fracture. The results were then compared to a physics-based numerical model including fluid flow and geomechanics that can simulate fracture propagation and stimulation presented earlier by Abe and Horne, (2019, 2020).

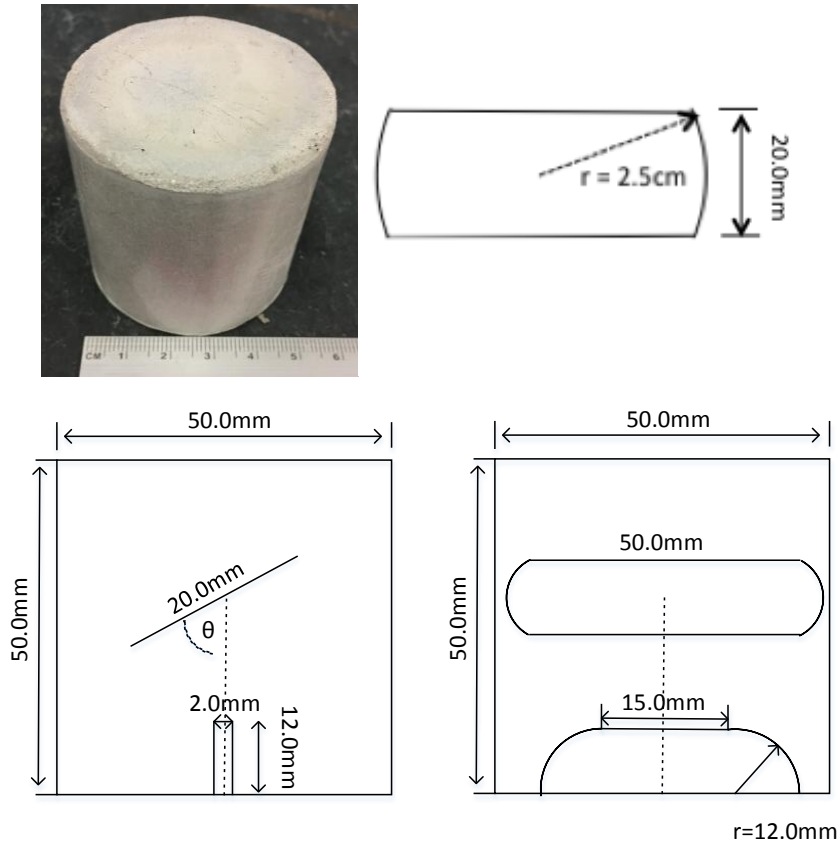


Figure 5.1: Left: A photo of the sample before the experiment, Middle: Shape of the waxed paper embedded in the sample, Right: Sketches of the cross section of the sample, both are side views with 90 degrees difference.

5.2 Laboratory scale hydraulic fracturing experiment

In this study, a hydraulic fracture intersected an embedded fracture inside the cement core sample as the representation of a preexisting natural fracture. The fracture intersection angle ranged from 45 degrees, to 60 degrees, and to 90 degrees. The confining pressure was atmospheric pressure and uniaxial stress was applied in varying magnitude. Deionized water was injected at a constant flow rate until a hydraulic fracture was initiated.

5.2.1 Sample Preparation

Anchor cement (Sakrete® Bolt & Rail Anchor Cement manufactured by Sakrete, Charlotte, NC, U.S.) was used to make the samples. The cement powder was mixed with water at the volumetric ratio of 27:8 of the cement powder to water. Then the mixture was poured into plastic molds. The plastic mold is a cylindrical shape with a height 5 cm and a diameter 5 cm. The samples were left to set for 48 hours at room temperature before being removed from the mold and were tested immediately. In our experiments, a piece of waxed paper (Reynolds KITCHENS® Parchment Paper with SmartGrid® manufactured by Reynolds Kitchens, Auckland, New Zealand) was embedded inside the cement samples to simulate a preexisting natural fracture. The thickness of the paper is 0.1 mm, which is sufficiently thin so that the paper does not disturb the experiment results (Gu et al., 2011; Zhou et al., 2008). A piece of paper was used previously by Zhou et al. (2008) to simulate a preexisting natural fracture in their experiment to investigate the hydraulic fracture propagation behavior. In their study, three different kinds of paper acted as a frictional interface totally embedded in the rock sample without intersecting the boundary of the sample. Their results showed that an embedded paper played the role of a preexisting fracture well if the thickness of the paper is sufficiently thin. Also, the results of their interaction types (cross or follow) were consistent with the analytical criteria and numerical results (Renshaw & Pollard, 1995; Gu et al., 2011; Abe et al., 2019). Therefore, in our experiments, the embedded waxed paper simulates a preexisting natural fracture in the reservoir. An initial slot was

cast at the bottom of the sample to initiate a hydraulic fracture when water was injected. The size and shape of the paper embedded is shown in Figure 5.1.

5.2.2 Determination of Material Properties

The mechanical properties of the sample are summarized in Figure 5.1. The tensile strength, the compressive strength, and the critical stress intensity factor were measured through laboratory measurements.

Table 5.1: Sample material properties

Property	Value	Unit
Tensile strength	3.4	MPa
Compressive strength	19.8	MPa
Critical Stress Intensity Factor	0.39	$MPa\sqrt{m}$.
Frictional Coefficient of the sample with the waxed paper	0.68	-

5.2.2.1 Determination of the Tensile Strength

The tensile strength was determined in Brazilian tests. Following Paterson and Wong (2005), the size of the sample is set to be $\Phi = 2H$ (diameter = 2×(height)) to minimize the shape effect such that the free surface boundaries would affect the measurement results. The sample size used for the Brazilian test was determined to be: $H = 19.0$ [mm], $\Phi = 38.0$ [mm]. The average tensile strength for the six samples 48 hours after being made was 3.4 MPa. The variation was around 20% but when two outliers are removed, the variation is 9%, which is a reasonable value.

5.2.2.2 Determination of the Compressive Strength

The unconfined compressive strength was determined in uniaxial compression tests. Following Paterson and Wong (2005), the size of the sample is set to be $L = 2\Phi$ (height = 2×(diameter)) to minimize the shape effect. The sample size used for the uniaxial compression test was determined as: $L = 50.8$ [mm], $\Phi = 25.4$ [mm]. The average

unconfined compressive strength for the six samples 48 hours after being made was 19.8 MPa.

5.2.2.3 Determination of the Frictional Coefficient

To understand the frictional behavior of the embedded fracture, the frictional coefficient of the waxed paper on the cement was measured. The samples were made such that the waxed paper was embedded inside the cement block then the block was cut to reveal the fracture surfaces to measure the frictional coefficient of the waxed paper on the cement. The geometry of the samples used are length = 70.0 mm, width = 120.0 mm, height = 20.0 mm and length = 120.0 mm, width = 200.0 mm, height = 20.0 mm. Based on the measurement data, the average angle θ is 34.5 degrees, therefore the frictional coefficient is $\tan(34.5) = 0.68$.

5.2.2.4 Determination of the Critical Stress Intensity Factors

This experiment was done to find the parameters to make an initial fracture propagate by water pressure. In this experiment, sample size and initial crack size were different from Figure 5.1. The stresses applied are shown in Table 5.2. The sample is cylindrical in shape with 50.0 mm diameter by 50.0 mm height. An initial crack initiation slot is located at the bottom. The geometry of the slot is a semicircle whose diameter is 25.0 mm. Deionized water was injected into the slot and its pressure was increased up to 2.9 MPa until the water pressure suddenly decreased due to the cracking of the sample. Water injection was stopped immediately after fracturing. The hydraulic fracture propagated to the top boundary of the samples.

The critical stress intensity factor calculated based on the results was $K_I = 0.405[MPa\sqrt{m}]$ when $a = c = 12.5$ [mm] and $\sigma'_n = 2.9$ [MPa], based on the empirical equation $K_{I\ max} = 0.629\sigma'_n\sqrt{\pi\sqrt{area}}$ derived by Murakami and Nemat-Nasser (1983), or $K_I = 0.381 [MPa\sqrt{m}]$ based on $K_{I\ max} = \lambda_s\sigma'_n\sqrt{\frac{\pi a}{Q}}f(\phi)$, where $Q = 1 + 1.464(\frac{a}{c})^{1.65}$, $\lambda_s = (1.13 - 0.09\frac{a}{c})(1 + 0.1(1 - \sin\phi)^2)$, $f(\phi) = \left[\sin^2(\phi) +$

$\left(\frac{a}{c}\right)^2 \cos^2(\phi)\right]^{\frac{1}{4}}$, and $\phi = 90^\circ$ by Anderson (2005). By averaging the results from both equations, the critical stress intensity factor of the material was estimated to be around $0.39 \text{ MPa}\sqrt{\text{m}}$. The critical stress intensity factors of cement generally range from $0.3 - 4.0 \text{ MPa}\sqrt{\text{m}}$. The estimated value is within this general range.

Table 5.2: Stress properties during the experiment to determine the critical stress intensity factor

Property	Value	Unit
Axial Stress	2.75	MPa
Confining Stress	0.1 (Atmospheric)	MPa
Fluid Pressure at breakdown	2.9	MPa

5.2.3 Experiment Apparatus

The experiment apparatus consists of a hydraulic shop press, a custom sample holder, and two syringe pumps (500D, Teledyne ISCO) (Figure 5.2). The hydraulic shop press (20 ton Pneumatic Shop Press with Gauge manufactured by Stark Tools UAS, Inc., California, USA) has a maximum axial load of 20 tons. One syringe pump is filled with hydraulic oil and connected to the hydraulic shop press to control the uniaxial load to the samples. The other syringe pump is filled with deionized water and connected to a sample's initial crack slot to control the injection fluid pressure. The syringe pumps monitor and record the fluid pressure, flow rate, and injected volume. In all the test cases, we injected water until the monitored water pressure stabilized at 0.06 MPa then injected water at a constant flow rate of 5.0 ml/min. As shown in Figure 5.2, the sample is held by the sample holder which is connected to the syringe pump. The water is injected from the bottom of the sample where the initial crack slot is located to create hydraulic fracture propagation. Water injection was stopped immediately once a fracture propagated into the sample. The experiments were conducted at room temperature around 25 °C.

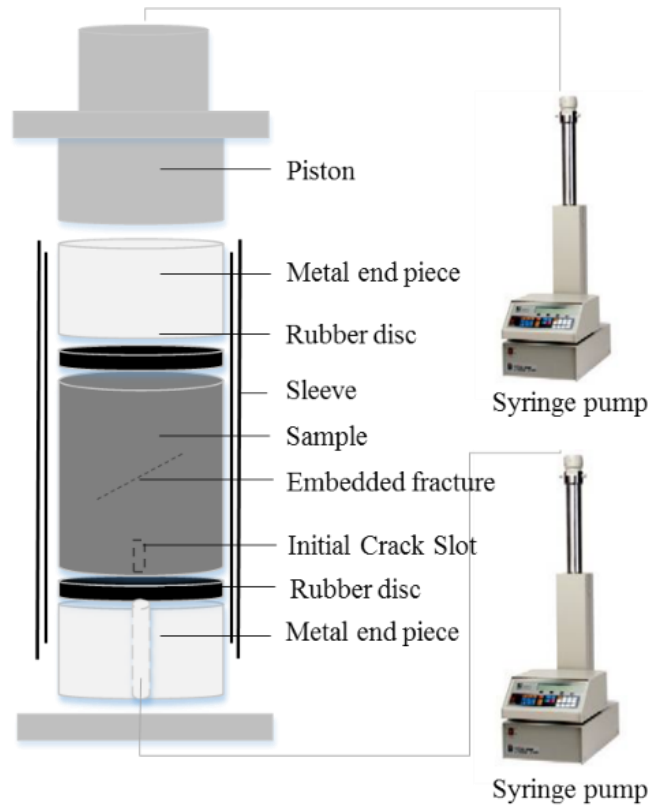


Figure 5.2: Experiment apparatus and sample assembly

5.2.4 Results

Experiments were conducted under uniaxial stress. The axial stress was applied by the uniaxial apparatus and the confining stress was atmospheric pressure. Deionized water was injected by the syringe pump into the initial crack slot at the bottom of the sample. The initial crack slot, as shown in Figure 5.1, was cast into the cement sample during its molding. A hydraulic fracture initiated from the initial crack slot when the injected water pressure reached around 1 MPa. In the six test cases, the break down pressures were between 0.7 MPa and 1.1 MPa. A hydraulic fracture propagated in the direction of the axial stress and intersected the preexisting fracture created by the embedded paper. The magnitude of the applied uniaxial stress was chosen based on Abe et al., (2019) so that we would be able to observe both of the cases where the propagating hydraulic fracture follows or crosses the embedded fracture. The results of their interaction types (cross or follow) were consistent with the analytical criteria and

numerical results by Renshaw & Pollard (1995) and Gu et al. (2011). The results are summarized in Table 5.3.

Table 5.3: The results of the experiments

Test Case #	Angle [degree]	Uniaxial Stress [MPa]	Intersection	Wing crack
1	90	1.75	Stop	No
2	90	7.0	Cross	No
3	60	5.25	Stop	Yes
4	60	7.0	Cross	No
5	45	5.25	Stop	Yes
6	45	3.0	Stop	Yes

The samples were cut in half after the experiments to examine the fractures that had been created during the experiment. The key observation here is that when a hydraulic fracture terminated at a nonorthogonal preexisting fracture, a wing crack was initiated and propagated in the sample. As shown in Table 5.4, in all the test cases only one side of the preexisting fracture tip initiated a wing crack and the other side did not. The side that initiated a wing crack has an angle larger than 90 degrees to the hydraulic fracture. The numerical investigation of this phenomenon is discussed in detail in the next section. When a hydraulic fracture crossed the preexisting fracture, the hydraulic fracture kept propagating until it reached the top boundary of the sample. In this case, no wing crack was initiated from the preexisting fracture.

The wing crack initiated from the tip of the preexisting fracture and propagated in the maximum principal stress direction. Figure 5.3 also shows a part of the hydraulic fracture bypassing the preexisting fracture. A bypassing hydraulic fracture was discussed by Fu et al. (2015) and Fu, et al. (2016) numerically and experimentally. Bypassing a fracture occurs when the height of a propagating fracture is larger than the

preexisting fracture. If the preexisting fracture is larger than the propagating fracture, the propagating fracture in three-dimensional space would stop at the preexisting fracture and branch into the wing crack from the preexisting fracture tip.

Table 5.4: Photos of the fracture pattern created during the experiment. HF shows a hydraulic fracture, NF shows a preexisting natural fracture, and WC shows a wing crack.

Test Case#	Photo of the sample	Test Case#	Photo of the sample
1		2	
3		4	
5		6	



Figure 5.3: Photo of a wing crack surface (Test case #6)

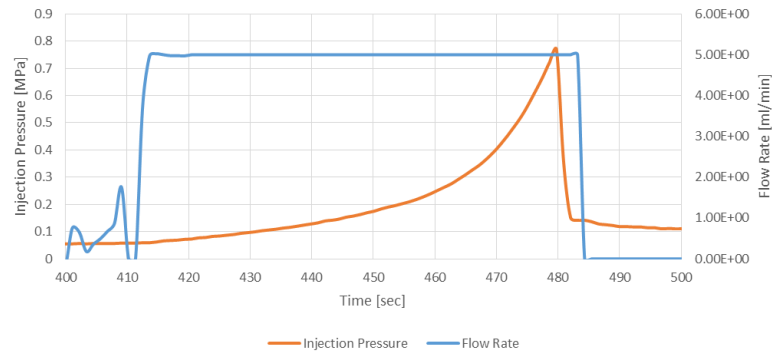


Figure 5.4: Injection pressure and flow rate profiles during the test case with preexisting fracture orienting at 45 degrees and uniaxial stress 5.25MPa (Test case #5).

5.3 Numerical Analysis

To analyze the result of the experiments described in the previous section, we modeled a propagating hydraulic fracture intersecting a preexisting fracture with our numerical model coupling fluid flow and fracture deformation. The simulated space of the numerical model is a full space, isotropic, and homogeneous two-dimensional domain assuming the plane strain condition.

In this study, we used a physics-based numerical model that combines fluid flow between fracture surfaces, fracture deformation, and fracture propagation driven by fluid injection which is described in Abe and Horne (2019, 2020) in detail. We modeled hydraulic fracture propagation, shear stimulation of a preexisting fracture, and wing crack propagation driven by fluid injection. To model fracture deformation, we used Ritz et al.'s (2015) two-dimensional displacement discontinuity boundary element method (DDM) with integrated complementarity. DDM is a powerful method that is useful to compute the stress shadow effect, which is the stress field induced by the deformation of other nearby fractures in a computationally effective way because only the fractures are discretized. Fluid flow in a fracture is assumed to be a single-phase flow described by the unsteady-state fluid mass conservation equation.

In this study, we used our numerical model to analyze the results of the laboratory experiments. We then investigated the stress concentrations at the embedded fracture tips, fracture deformation, and displacement fields with the numerical model.

5.3.1 Numerical Experiment Setup

Parameters used in this numerical experiment are listed in Table 5.5 and the model setup is shown in Figure 5.5. The parameters and the model setup used in the numerical experiment follow the measured parameters during the laboratory experiments described in the previous section. The model assumes a reservoir in a full space, horizontal, isotropic, and homogeneous two-dimensional domain with vertical fractures, assuming the plane strain condition.

In this numerical experiment, water is injected to the initial crack and initiates a hydraulic fracture. The model assumes a symmetric setting so that it can model the bottom boundary conditions of the experiment samples which are $u_y(y = 0) = 0$ and $\frac{\partial}{\partial y}(y = 0) = 0$, where $u_y(y = 0)$ is the displacement in y direction along $y = 0$. In the simulation setup, the injector is located at the center of the initial crack. The hydraulic fracture propagates to both direction and intersects a preexisting fracture at each side.

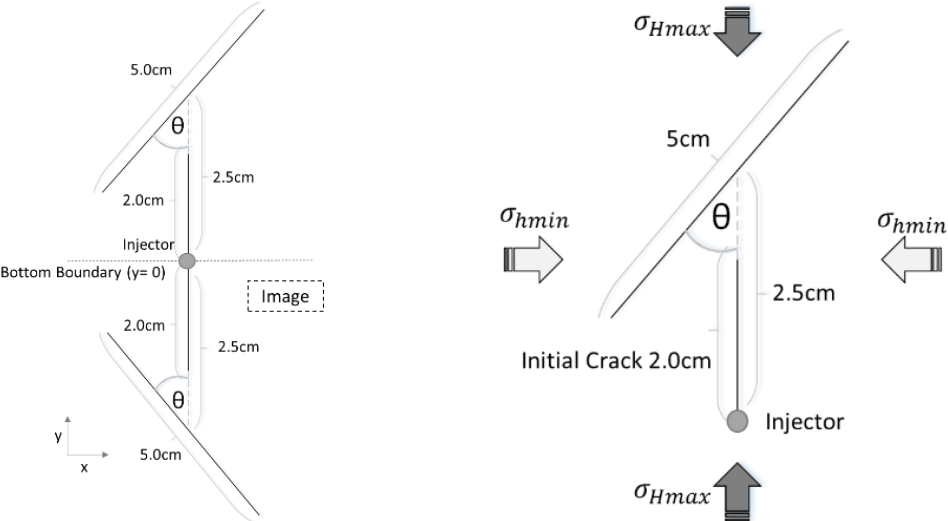


Figure 5.5: Numerical experiment setup. Left: The symmetry setting with image displacements across $y = 0$ to render the bottom boundary condition with the full-space solution, Right: the main simulation domain.

The frictional coefficient calculated from the Mohr-Coulomb failure criterion and the fracture cross or follow conditions by Renshaw and Pollard (1995) and Gu et al., (2011) based on the lab tests results is $f \approx 1.0$. Therefore, in this numerical experiment, we used the static frictional coefficient $f = 1.0$ and the dynamic frictional coefficient $f = 0.7$. When the critical stress intensity factor was set to be the same as the measured value, the breakdown pressure in the numerical setting was 1.7 MPa, which is much higher than the break down pressure during the cement sample experiments which was between 0.7 MPa and 1.1 MPa. This is because the stress intensity factor at the propagating fracture tips is calculated as that of an edge crack in a semiinfinite body because we assume that the domain is in plane strain condition in full space in this numerical model. The stress intensity factor at a tip of an edge crack in a semiinfinite body is smaller than that of a semicircle in a semiinfinite body with the same effective normal stress. The fluid pressure inside the fractures is an important parameter to model and analyze the experiment results, therefore, to adjust the breakdown pressure and the fluid pressure inside fractures, the critical stress intensity factor for the numerical model was set to be $0.15 [MPa\sqrt{m}]$. Fluid properties are assumed to be those of saturated water at 150 °C at 4.8 bars.

Table 5.5: Parameters used in the numerical simulation

Initial Time Step	1.0e-3	s
Injection Rate	8.3e-8	m ³ /s
Maximum horizontal stress	5.25 or 7.0	MPa
Minimum horizontal stress	0.1	MPa
Initial fluid pressure	0.0	MPa
Young's modulus	12	GPa
Poisson's ratio	0.21	-
Fracture height	0.05	m
Water density	920	kg/m ³

Water viscosity	1.0e-9	MPa.s
Reference hydraulic aperture	2.0e-5	m
Reference effective normal stress	25	MPa
Dilation angle	2	degree
Critical Stress Intensity Factor	0.15	$MPa\sqrt{m}$
Fracture static frictional coefficient	1.0	-
Fracture dynamic frictional coefficient	0.7	-
Fracture cohesion	0.0	MPa

5.3.2 Comparison between Laboratory and Numerical Experiments

We compared the numerical results from our model to the laboratory experiment results shown in the previous section to assess its accuracy before going into detailed analyses. In this paper, the newly developed numerical model results are compared to the laboratory test results, and the model then used to infer the sample, fracture deformations, and stress fields.

Table 5.6: The results of the numerical experiments

Test Case #	Angle [degree]	Uniaxial Stress [MPa]	Intersection	Wing crack
1	90	1.75	Stop	No
2	90	7	Cross	No
3	60	5.25	Stop	Yes
4	60	7	Cross	No
5	45	5.25	Stop	Yes

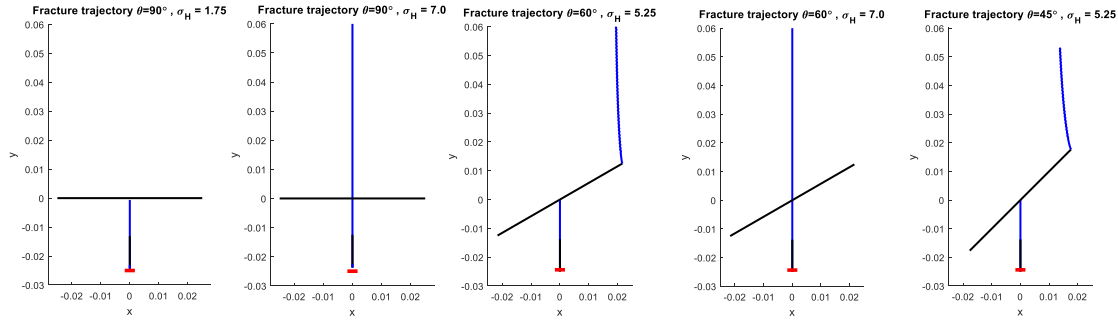


Figure 5.6: Summary of the results: The red line shows the location of the injection well; the black lines are the preexisting fractures, while the blue lines show the newly formed fractures, including a hydraulic fracture initiated from the injection well and wing cracks.

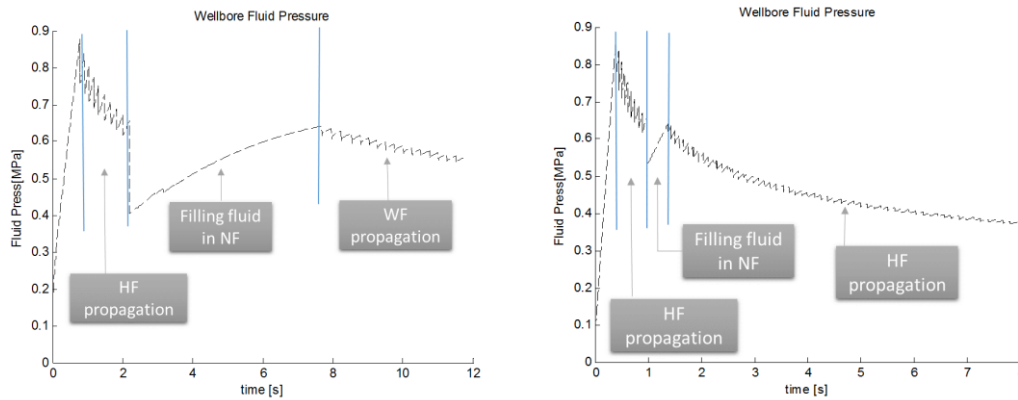


Figure 5.7: The wellbore fluid pressure observed during numerical simulation. Left: The case with preexisting fracture orientation of 45 degrees and the uniaxial stress 5.25 MPa (Test case #5), Right: The case with preexisting fracture orientation of 60 degrees and the uniaxial stress 7.0 MPa (Test case #4).

The fracture propagation patterns show a perfect match between the laboratory tests and numerical simulation (Figure 5.6). When a propagating hydraulic fracture crosses the preexisting fracture, the preexisting fracture does not initiate new fractures. On the other hand, when a propagating hydraulic fracture follows the preexisting fracture, it initiates one wing crack as observed during the laboratory experiments. Figure 5.7 shows the breakdown pressure and the wellbore fluid pressure of the numerical experiments. The breakdown pressures are close to that of lab tests. However, the wellbore fluid pressure change shows different trends. The wellbore fluid pressure drops to a value close to atmospheric pressure within 3 seconds during the laboratory

tests (Figure 5.4), however, the pressure during numerical simulation drops slower than that. This is because the injected fluid leaked off to outside the sample soon after the hydraulic fracture initiated during the lab tests, while the injected fluid is fully contained between fractures in the numerical model. From these results, the numerical model and parameters used were deemed reasonable to analyze the lab test results.

5.3.3 Analysis of Deformation and Stress Concentrations

The numerical results also show that a wing crack is initiated from the preexisting fracture tip at the side with the angle larger than 90 degrees, while the side with the angle smaller than 90 degrees does not initiate a wing crack as shown in Table 5.4. We analyzed the displacements and the stresses acting along the preexisting fracture. The hydraulic fracture induces compressive stress along the preexisting fracture as the opening displacement pushes the matrix rock in the direction perpendicular to the hydraulic fracture. The displacement also induces the tension field around the fracture tip. This induced tension field near the hydraulic fracture tip and the compressive stress field around the hydraulic fracture body induce the asymmetric shear displacement distribution along the preexisting fracture as shown in Figure 5.8. On the other hand, when a propagating hydraulic fracture crosses the preexisting fracture, no deformation occurs despite the asymmetric shear stress distribution (Figure 5.9).

A wing crack is initiated and propagates when the equation below is satisfied at a fracture tip.

$$K = \cos \frac{\theta_0}{2} \left[K_I \cos^2 \frac{\theta_0}{2} + \frac{3}{2} K_{II} \sin \theta_0 \right] \geq K_{IC}, \quad (5.1)$$

where θ_0 is the fracture propagating direction, K_{IC} is the critical stress intensity factor (Ingraffea, 1987, Thomas and Pollard, 1993). K_I and K_{II} are the stress intensity factors for Mode I and Mode II respectively given by:

$$K_I = 0.798 \frac{D_n E \sqrt{\pi}}{4(1-\nu^2)\sqrt{P}}, \quad (5.2)$$

$$K_{II} = 0.798 \frac{D_s E \sqrt{\pi}}{4(1-\nu^2)\sqrt{P}}, \quad (5.3)$$

where D_n and D_s are the normal and the shear displacements for a fracture tip element, E is the Young's modulus, ν is the Poisson's ratio, and P is the length of the fracture tip element (Olson, 1991).

The side with the angle larger than 90 degrees deforms in shear in larger amount than the other side because of the stress shadowing effects induced by the hydraulic fracture propagating from the injector (Abe & Horne, 2019, 2020). The stress changes and deformations of the matrix rock show the effects of stress shadowing (Figure 5.8). Therefore, the stress intensity factor at the tip of the larger angle side reaches at the critical stress intensity factor first, then it initiates a wing crack from its tip. After a wing crack starts propagating, the fluid pressures inside the fractures start decreasing because the fluid flow into the propagating fracture that has large volume to store fluid. With the experiment setup, the preexisting fracture does not have normal displacements. Therefore, the amount of shear displacement around the fracture tips affects whether the fracture tip initiates a wing crack or not. Stress fields induced by the propagating hydraulic fracture cause smaller normal stress along the side with the angle larger than 90 degrees. Therefore, the amount of shear displacement is larger as the Mode II driving stress $|\sigma_s^f| - (-f\sigma'_n + S_f)$ is larger along this side as described by the Coulomb criterion (Jaeger et al., 2007). Therefore, the stress intensity factor at the side with the angle larger than 90 degrees is larger than that of the side with the angle smaller than 90 degrees. This leads to the result that only one side of the preexisting fracture initiates a wing crack. With this laboratory experiment setup, the pattern where two wing cracks are initiated from the preexisting fracture was not seen, because the length of the hydraulic fracture was not sufficiently long that the effective normal stress along the hydraulic fracture was large enough to induce strong stress shadowing effect around the fracture tip. The preexisting fracture size is so small that both sides of the preexisting fracture are inside the strong influence of the induced stress field by the hydraulic fracture.

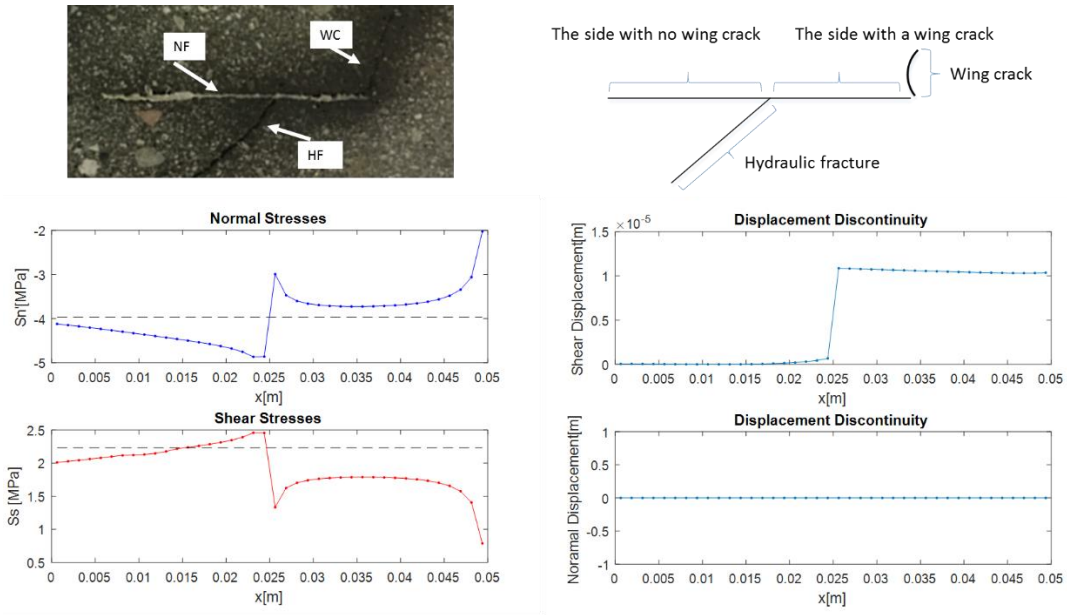


Figure 5.8: The shear displacement and the normal and shear stresses along the preexisting fracture orienting at 45 degrees with uniaxial stress 5.25 MPa (Test case #5). HF indicates a hydraulic fracture, NF indicates a preexisting natural fracture, and WC indicates a wing crack.

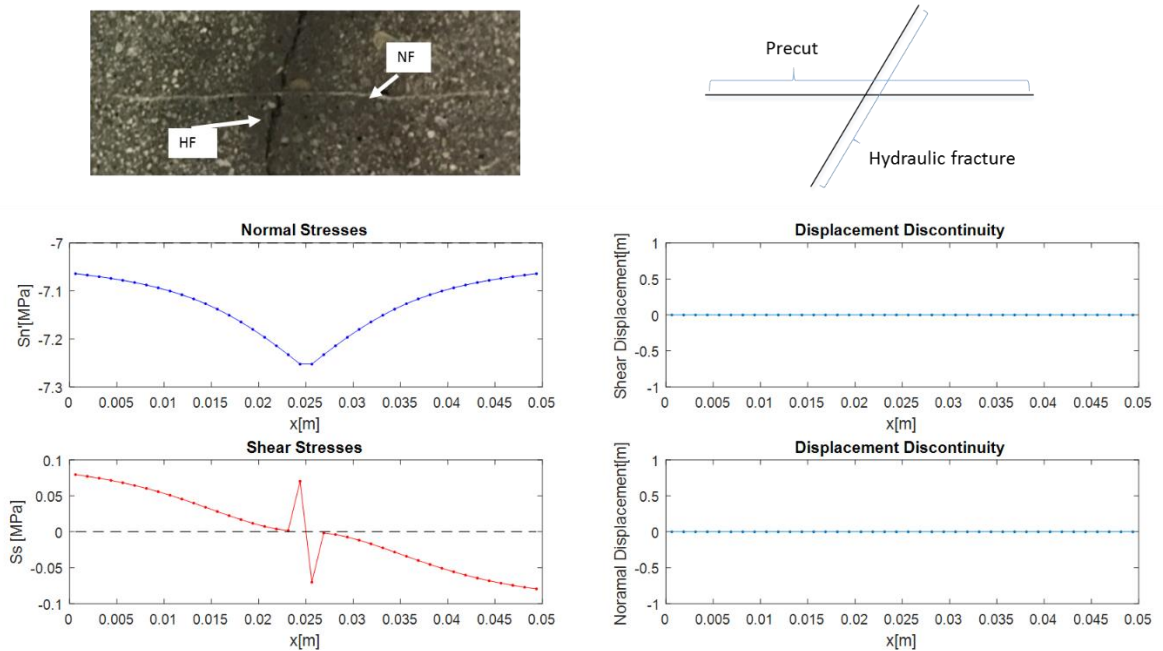


Figure 5.9: The normal and shear displacements and the normal and shear stresses along the preexisting fracture orienting at 60 degrees with uniaxial stress 5.25 MPa (Test case #3). HF indicates a hydraulic fracture, NF indicates a preexisting natural fracture, and WC indicates a wing crack.

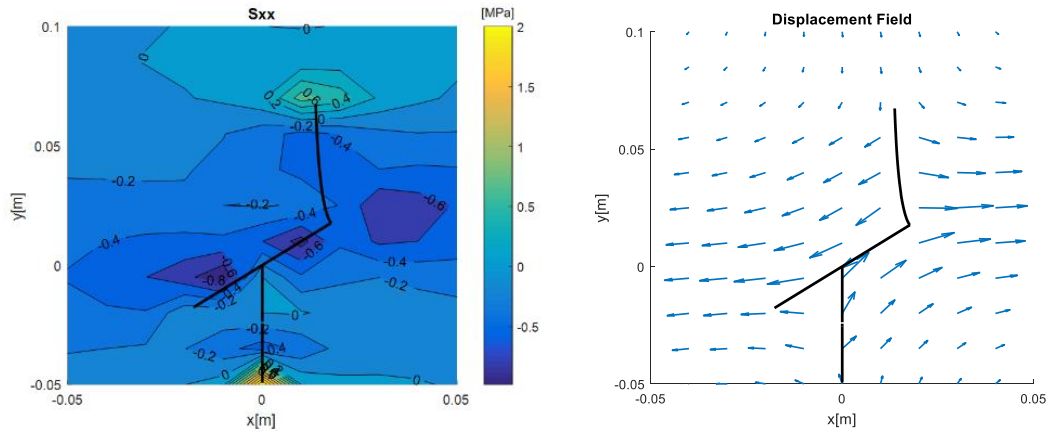


Figure 5.10: Left: The contour of the magnitude of σ_{xx} , Right: The displacement field. Both show the domain when the length of the wing crack is 5 cm with a preexisting fracture orienting at 45 degrees and uniaxial stress 5.25 MPa.

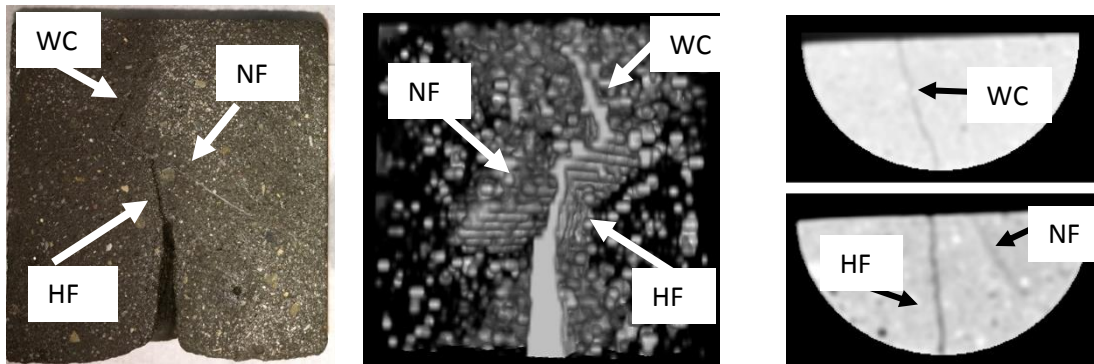


Figure 5.11: Left: The photo of the sample cut in half after experiment (Test case #3), Center: CT data 3D visualization. White area expresses low density region, Right: CT data two-dimensional visualization showing the wing crack (above) and the hydraulic fracture (below). White area expresses high density region. HF indicates a hydraulic fracture, NF indicates a preexisting natural fracture, and WC indicates a wing crack.

5.1 Analysis of Aperture along newly formed fractures

The sample with a preexisting fracture oriented at 60 degrees and uniaxial stress 5.25 MPa (Test case #3) was CT scanned after the hydraulic fracturing experiments in a GE HiSpeed CT fifth generation instrument with four detectors 140 kV voltage and 120 mA tube current with a slice interval of 0.625 mm, one exposure time per slice. The voxel size is $195 \times 195 \times 625 \mu\text{m}^3$ and each two-dimensional slice has $195 \mu\text{m}/\text{pixel}$

resolution. The raw CT data was processed by Fiji ImageJ version 1.52p (64-bit) on Java 1.8.0_172 to build two-dimensional and three-dimensional visualization of the sample. CT images from scans made perpendicular to the core axis.

The CT image successfully captured the newly formed fractures as well as the embedded preexisting fracture (Figure 5.11). The three-dimensional visual shows that the hydraulic fracture propagating from the injection point terminated at the preexisting fracture, and that the edge of preexisting fracture initiated a wing crack. Although this type of lower resolution medical CT scanner is known to be limiting in the study of fracture aperture and roughness (Crandall et al., 2017; Kling et al., 2016), we estimated the aperture of the hydraulic fracture and the wing crack and then compared to the simulated apertures.

It is known that the size of the low density region in the CT image is much larger than the actual fracture aperture when the aperture is close to or smaller than the scanner resolution. A fracture with small aperture does not show the CT data reducing all the way to the CT number of the air. To estimate the width of the aperture from CT data, Johns et al. (1993) suggested the relationship between the apparent fracture aperture in the CT image and the true fracture aperture by using the linear relationship between the integrated missing mass at the gap calculated from the CT response and the actual sample gap size with the least squares linear fit as:

$$m_g = 2607.8a_g - 75.015, \quad (5.4)$$

where m_g is the integrated missing mass at the gap in mm g/L and a_g is the gap size in mm.

By following Johns et al. (1993), we took six points from each fracture and calculated the integrated missing mass at the gap, and then estimated the size of the apertures. In this study, the CT number of cement and air are 1750 and -1000, respectively, while Johns et al., (1993) used granodiorite samples with a system with CT number of granodiorite and air were 2700 and 0, respectively. Therefore, the integrated missing mass at the gap is adjusted by multiplying 2700/2750 so that it has the same scale with that of Johns et al. (1993).

Table 5.7: The average aperture and its standard deviations of six points from the hydraulic fracture and the wing crack in test case #3.

	Aperture [mm]	Standard Deviation
Hydraulic Fracture	0.167	0.023
Wing Crack	0.235	0.041

Table 5.7 shows the results. The difference of aperture size between the hydraulic fracture and the wing crack is about 0.07 mm. Five out of six points from the wing crack aperture exceeded those of the hydraulic fracture. The aperture of a wing crack is likely to be larger than that of a hydraulic fracture because the opening displacements are held both by the fluid pressure inside and the shear displacements of the main slipping fracture, and the shear displacements of the main fracture is held after stimulation (Abe & Horne, 2019). Our numerical results reproducing the same conditions with this sample with a preexisting fracture orienting at 60 degrees and uniaxial stress 5.25 MPa shows that the wing crack has 0.04 mm remaining opening displacement after the sample dries. Aside from opening displacements, mechanical apertures of a fracture are created by roughness of fracture surfaces which is typically of the order of 0.1 – 1.0 mm when the normal stress is zero or compressive (Bandis et al., 1983; Barton et al., 1985). In this experiment, the sample was CT scanned after the experiments at room temperature with no stresses applied. Therefore, the measured aperture of the hydraulic fracture is considered to be the mechanical aperture created by the roughness of the fracture surfaces, and the difference of apertures between the wing crack and the hydraulic fracture is likely to be the opening displacement held by the shear slip of the preexisting fracture.

5.2 Discussion

Experimental, numerical, analytical, and field study to understand reservoir stimulation has been conducted from many different aspects such as the works focusing on fracture

propagation (e.g. Geertsma & de Klerk, 1969; Nordgren, 1972; Perkins & Kern, 1961), fracture intersection (e.g. Gu & Weng, 2010; Gu et al., 2011; Renshaw & Pollard, 1995, Warpinski & Teufel, 1987), shear stimulation (e.g. Bandis et al., 1983; Barton et al., 1985; Willis-Richards et al., 1996)), and wing cracks (e.g. Erdogan & Sih, 1963; Horii & Nemat-Nasser, 1986; Mutlu & Pollard, 2008). Based on those previous studies, our experimental and numerical results show that a certain fracture network pattern is created when newly formed fracture and a preexisting fracture intersect by interacting mechanically and hydraulically.

We confirmed that the cracks we observed during the hydraulic fracturing experiments are newly formed fractures during the experiments, not preexisting defects nor cracks induced by cutting the samples, for the following reasons; the cracks were observed in all samples with the same patterns, the wing cracks are where we expected, and they match the numerical model results. If they were preexisting defects, the cracks would exist randomly. We also cut the cement samples before the hydraulic fracturing experiments, and we observed they are intact samples. During the experiments, we observed a crack propagated to the outer wall of the samples in real-time which were consistent with the cracks we observed inside the samples. Finally, we had imaged the fractures with the CT scanner before cutting the samples. Therefore, we determined that the newly formed fractures were induced by fluid injection during the experiments.

This section of the study focused on the laboratory scale experiment, however, to better understand the fracture network creation, further study needs to be done to the pattern of a fracture network at a reservoir scale. In this study, the preexisting fracture length was not very long so that almost entire preexisting fracture was under the influence of induced stress field by a propagating fracture tip. The effect of induced stress field around a propagating fracture tip decreases with distance. Therefore, if the size of the preexisting fracture is much longer than the radius of the induced stress field, the fracture surface near the intersection is under the asymmetric normal and shear stress distribution while the fracture surface far from the intersection is only under the influence of the remote stresses. The effect of fracture size should be further investigated in future studies.

We analyzed the results of the laboratory experiments using our numerical model which is a full space, isotropic, and homogeneous two-dimensional domain assuming the plane strain condition. The fracture propagation is assumed to be quasistatic crack propagation while dynamic crack propagation including kinetic energy occurs during the laboratory experiments.

In this study, we assumed that newly formed fractures are all Mode I fractures and did not consider Mode II and Mode III propagation because in general, the Mode I critical stress intensity factor of rocks is $\sim 1/10$ smaller than the Mode II and the Mode III critical stress intensity factors under compressive stress field (e.g. Mutlu & Pollard, 2008; Zang & Stephansson, 2010). Also, pure Mode II and Mode III propagations are rarely observed in the field nor in experiments with brittle materials (Petit & Barquins, 1988). With these assumptions, the numerical results agreed with the laboratory experiment results. Therefore, the newly formed fractures during the laboratory experiments were supposed to propagate perpendicular to the local least principal stress with pure Mode I.

The frictional coefficient and the Mode I critical stress intensity factor were modified for the numerical experiment to better match the laboratory experiment results. The frictional coefficient was calculated from the Mohr-Coulomb failure criterion and the fracture cross or follow conditions by Renshaw and Pollard (1995) and Gu et al. (2011) based on the lab tests results, which is $f \approx 1.0$. This is much higher than the measured value with two cement blocks which was $f \approx 0.7$. A possible reason for this is that the fracture surfaces are not completely smooth and there are asperities that prevent sliding in the cement samples.

We observed that injected fluid leaked off to the matrix rock (cement) during the hydraulic fracturing experiments. Our numerical model does not assume fluid leak-off to the surrounding matrix rock. However, fracturing occurred instantaneously around a minute after the start of the injection. Moreover, the fracture patterns agree with numerical model which does not include fluid leak-off. From this point, we infer that fluid leak off does not have significant impacts on fracture propagation patterns in this case. The numerical model has infinite domain while the actual laboratory

experiments have a finite sample size. Therefore, the injected fluid leaked off to outside the sample soon after the hydraulic fracture initiated during the laboratory tests, while the injected fluid is fully contained between fractures in the numerical model. This difference made a different pattern of the injection fluid pressure after a hydraulic fracture initiated from the initial crack slot.

In this study, our two-dimensional numerical model properly reproduced the hydraulic fracturing experiments which occurred in three-dimensional space. The cement samples were designed to show close behavior to that in the plane strain condition at the center of the sample. Our purpose in the study is to better understand the fracture network creation by hydraulic stimulation in an EGS reservoir. We are interested in a fracture network creation in a reservoir scale problem with multiple fractures. For our purpose, the two-dimensional model with the boundary element method is suitable because modeling fracture deformation, propagation, and interaction is computationally expensive process especially in three dimensions, which makes it more difficult to model a reservoir with multiple fractures.

However, a physic-based three-dimensional numerical model is useful when solving some three-dimensional specific problems such as a bypassing hydraulic fracture (Fu et al., 2015; Fu, et al., 2016) which occurs on the intersection of two fractures with sufficiently different in height or on the intersection with partially cemented fracture. A three-dimensional model is also useful when considering vertical fracture propagation into layers with vertical stress variations (Singh et al., 2020). There are some three-dimensional reservoir models with a discrete fracture network not considering fracture deformation and propagation.

As this study shows, when a propagating hydraulic fracture crosses the preexisting fracture, the fluid flows more to the hydraulic fracture than the intersecting preexisting fracture because of the higher transmissivity of the hydraulic fracture. The same phenomenon is expected to occur when a propagating wing crack crosses an intersecting preexisting fracture. In this case, preexisting fractures connected to the wells may not contribute to the flow network and may not supply heat to the fluid. Additionally, a wing crack is likely to have wide aperture which improves reservoir

permeability. On the other hand, wing cracks may supply lower heat exchange area to a unit volume of fluid. A better EGS reservoir should have a complex fracture network consisting of both preexisting fractures and newly formed fractures with multiple flow paths between injectors and producers for a sustainable heat extraction and permeability.

5.3 Summary

In this study, we conducted a laboratory scale hydraulic fracturing experiment to investigate how a fracture network is created when a propagating hydraulic fracture and a preexisting fracture intersect each other. The results of the experiment show that when a hydraulic fracture follows a nonorthogonal preexisting fracture, a wing crack is initiated from only one side of the preexisting fracture tip. The side that initiated a wing crack has an angle larger than 90 degrees to the hydraulic fracture. When a hydraulic fracture crossed the preexisting fracture, the hydraulic fracture propagated until it reached the sample boundary and no wing cracks were initiated. The numerical results are consistent with the laboratory test results. Based on the numerical analyses, the tension fields near the hydraulic fracture tip and the compressive stress field around the hydraulic fracture body cause an asymmetric shear displacement distribution along the preexisting fracture that results in initiation of a wing crack from only one side of the preexisting fracture. If the sample size is sufficiently large to contain a preexisting fracture whose tips are far from the strong effect of stress shadowing by an upstream fracture, it is possible that wing cracks propagate from both tips of the preexisting fracture, however, the condition to make the propagation pattern was limited with the experiment setup used in this study. These results imply that the pattern of a fracture network growth is likely to be affected by stress states, preexisting fracture orientations, and whether a propagating fracture crosses or terminates at the preexisting fracture. According to Renshaw and Pollard (1995), the fracture cross or terminate condition is related to the stress state, the frictional coefficient of fracture, and the preexisting natural fracture orientation. Therefore, a fracture network pattern may be affected by those reservoir conditions.

The wing cracks observed in the experiments are an important factor in improving the permeability in an EGS reservoir. It has been observed at the field scale that secondary fractures that form as a result of fault slip can link originally discontinuous faults and enhance hydraulic conductivity underground (Bürgmann & Pollard, 1994; Martel & Boger, 1998; National Academy of Sciences, 1996). Similar reservoir permeability enhancement will occur by hydraulic stimulation because slipping preexisting fractures are better connected to one another by forming wing cracks. This study focused on the laboratory scale experiment, however, to better understand the fracture network creation, further study needs to be done to the pattern of a fracture network at a reservoir scale.

Chapter 6

6 Investigating Stress Shadowing Effects and Fracture Propagation Patterns

6.1 Introduction

The mixed-mechanism process is now accepted as a way to model hydraulic stimulation in geothermal reservoirs (Kamali & Ghassemi, 2016, 2018; Norbeck et al., 2018; Norbeck & Shelly, 2018). In Chapter 5, we observed that mixed-mechanism stimulation occurred in a laboratory scale hydraulic fracturing experiment and analyzed the stress distribution along fracture by our numerical model. In Chapter 3 and 5, wing crack propagation and shear stimulation were modeled, and the displacements and propagation patterns were analyzed. Based on those analyses on top of the past research, wing cracks found in rock are tensile fractures but they are different from a hydraulic fracture propagating from a wellbore because: 1) wing cracks initiate from the tension field induced by shear slip of a preexisting natural fracture while hydraulic fractures are initiated by fluid pressure; 2) wing cracks are usually curved while hydraulic fractures propagate mostly straight and perpendicularly to the least principal stress; and 3) tension forces to open wing cracks are supported both by fluid pressure inside and shear slip of a preexisting natural fracture while tension forces to open hydraulic fractures are supported only by fluid pressure.

The magnitude of fluid pressure necessary to initiate a wing crack within a well-oriented natural fracture can be less than the fluid pressure to create new hydraulic

fractures (Abe & Horne, 2019; Kamali & Ghassemi, 2016, 2018; Mutlu & Pollard, 2008; Zoback & Lund Snee, 2018). Also, it is suggested that wing cracks play an important role in the mixed-mechanism stimulation because they improve the fracture connectivity and supply much larger storativity and transmissivity than those of preexisting fractures in a reservoir (Abe & Horne, 2019). Therefore, propagation of wing cracks and shear stimulation of natural fractures need to be considered when modeling a realistic fracture network to characterize an enhanced geothermal reservoir.

It has been long observed in field tests that a hydraulic fracture induces local stress changes, which affect the trajectories and breakdown pressure of other hydraulic fractures (e.g. Warpinski et al., 1989). These mechanical interactions between fractures influencing fracture growth has been shown in many outcrops as well (e.g. Pollard & Aydin, 1988). These induced stress fields are referred to as stress shadow. In recent years, stress shadowing has been studied experimentally and numerically in the context of multiple hydraulic fracture stimulation in unconventional oil and gas settings because stress shadowing is key to designing an optimal stimulation of this type to achieve successful production (Wu & Olson, 2016). Stress shadowing induced by fracture shear displacements has also been studied in the context of natural earthquakes, such as Harris (1998), Martel et al. (1988), and Harris and Simpson (1992).

During hydraulic stimulation in an EGS reservoir, natural fractures stimulated in shear and newly formed fractures interact mechanically with one another. A natural fracture stimulated in shear can initiate a wing crack, whose propagation is affected strongly by stress shadowing induced by the stimulated natural fracture. A newly formed fracture, such as a hydraulic fracture propagating from an injection well or a wing crack, perturbs the local stress fields, which can affect deformations of a natural fracture. Deformed natural fractures due to stress shadowing are often observed in hydraulic fracturing treatments in unconventional oil and gas reservoirs, as seen in microseismicity (Kettlety et al., 2020; Kettlety et al., 2019; Nagel & Sanchez-Nagel, 2011). To better understand fracture network creation in an EGS reservoir where natural fractures dominate, it is important to understand these stress shadowing effects on fracture propagation patterns.

As discussed so far, fracture propagation from a natural fracture and the interaction between newly formed fractures and preexisting fractures play an important role in modeling the creation of a complex fracture network. Especially in an EGS reservoir, preexisting fractures are expected to be large and dominant in a reservoir, while planar hydraulic fractures extending from an injection well dominate in an unconventional reservoir. Hydraulic stimulation is performed in a less permeable geothermal reservoir, which may mean that the preexisting fractures are poorly connected. To better understand how fractures interact mechanically, how newly formed fractures propagate in a reservoir, and how fluid flows in a fracture network, it is essential to develop a numerical model based on fracture mechanics and fluid mechanics.

In this study, we developed a physics-based numerical model that combines fluid flow between fracture surfaces, fracture deformation, and fracture propagation driven by fluid injection. We modeled hydraulic fracture propagation, shear stimulation of a preexisting fracture, and wing crack propagation driven by fluid injection, to investigate the effects on fracture network creation of the mechanical interaction between newly formed fractures and preexisting fractures. With this model, we firstly analyzed how stress shadowing affects the creation of a fracture network pattern with varied stress states and fracture orientations. In these numerical experiments, we modeled a propagating hydraulic fracture intersecting two natural fractures in an EGS reservoir. Next, we investigated the effects of injection rate, fluid pressure distributions, and length ratios on a fracture network pattern. Finally, we considered the results and implications for reservoir scale hydraulic stimulation.

6.2 Investigating the effect of fracture orientation and stress state

In this study, we modeled wing crack propagation from a stimulated preexisting fracture and hydraulic fracture propagation from a wellbore driven by fluid injection. We compared fracture propagation patterns when a propagating hydraulic fracture crosses

a preexisting fracture and when a propagating hydraulic fracture stops at a preexisting fracture, in order to analyze the effects of stress state and mechanical interaction between fractures on the creation of the fracture network.

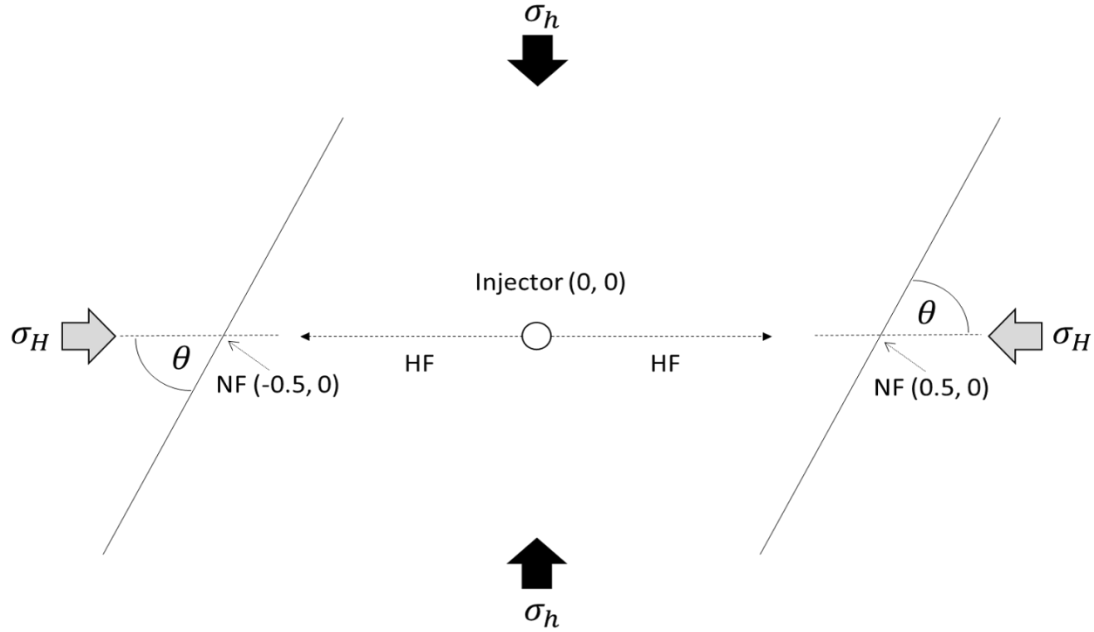


Figure 6.1: Model configuration: An injection well located at the center of the domain initiates a hydraulic fracture (HF). The propagating hydraulic fracture intersects a preexisting natural fracture (NF) at each side.

6.2.1 Parameters

The reservoir we modeled is a full-space, horizontal, isotropic, and homogeneous two-dimensional domain with a vertical fracture assuming the plane-strain condition. An injection well located at the center of the domain initiates a hydraulic fracture, then the propagating hydraulic fracture hits two preexisting natural fractures at both of its sides (Figure 6.1). Those two preexisting natural fractures are located so that the fracture network will be symmetric.

In this study, we investigated the effects of stress states and fracture orientations on the creation of a fracture network pattern. The stress ratios used in the experiments were 1.1, 1.5, 2.0 and 3.0 with the fixed value of least principal stress $\sigma_h = 10\text{MPa}$. The fracture orientations were 45 and 60 degrees to the maximum horizontal stress

orientation. We investigated all combinations of the stress ratios and the fracture orientations in this study.

6.2.2 Propagating fracture cross or follow decision

Fracture cross/follow conditions are determined based on the method described in Section 2.7. The fracture cross/follow conditions depend on the stress state, the frictional coefficient of the fracture, and the tensile strength of the rock. With the parameters used in this study, a propagating hydraulic fracture terminates at a preexisting fracture oriented at 45 degrees under any stress states from 1.1 to 3.0. The stress states that induce slip without fluid injection are not included in this experiment.

Values of stress ratio over 2.0 make the propagating fracture cross the preexisting fracture oriented at 60 degrees. The propagating fracture may either cross or follow the preexisting fracture with stress ratios below 2.0 (Abe et al., 2019). In this experiment, we made the propagating fracture follow the preexisting fracture orienting at 60 degrees with the stress ratio 1.1 and 1.5, and made the propagating fracture cross with the stress ratio 2.0 or greater in this condition.

6.2.3 Results on varied orientations and stress states

The results of the experiments show that the fracture propagation patterns depend on the orientations of the intersecting preexisting fracture and the stress ratios. The model results show three fracture network patterns; 1) a hydraulic fracture crosses the preexisting fracture, and continues propagating; 2) a hydraulic fracture follows the preexisting fracture, and the preexisting fracture initiates only one wing crack; and 3) a hydraulic fracture follows the preexisting fracture, and the preexisting fracture initiates two wing cracks. With a stress ratio lower than 2.0, a preexisting fracture with orientations of both 45 and 60 degrees initiates only one wing crack. With a stress ratio 2.0 or larger, the patterns differ depending on the preexisting fracture orientations.

When there is a preexisting fracture with a 60-degree orientation, a propagating fracture follows when the stress ratio is low, and crosses when the stress ratio is high. We modeled fracture propagation with varied stress ratios to compare the results for

both scenarios: when a propagating fracture follows and when it crosses the preexisting fracture. When a propagating fracture crosses the preexisting natural fracture, the propagating fracture continues to propagate while the natural fracture remains without deforming (Figure 6.2 e and g). The fluid pressures inside the fractures are almost uniform and close to the magnitude of the least horizontal stress (Figure 6.3). On the other hand, when a propagating fracture follows the preexisting fracture with a 60-degree orientation, the side with the larger angle to the hydraulic fracture slips, while the other side does not (Figure 6.2 a and c). As a result, a wing crack initiates and propagates from the slipping side of the preexisting fracture. In both cases, the fluid flow path mainly remains as one pathway, creating a less complex fracture network.

Figure 6.4 compares the normal and shear stresses acting along the preexisting fractures. The side that initiates a wing crack ($x = 0.5$ m to 1.0 m) is under larger shear stresses and smaller normal stresses compared to the other side ($x = 0.0$ m to 0.5 m). This asymmetric stress distribution makes one side slip earlier than the other side despite the fluid pressure distribution being almost symmetric. A wing crack propagates at a lower fluid pressure than that needed to make the other side of the preexisting fracture slip, with the result that only one wing crack propagates from each preexisting fracture (Figure 6.5). When a propagating fracture crosses the preexisting fracture, the fluid pressure necessary to drive the hydraulic fracture propagation is lower than that needed to induce slip along the preexisting fracture. Therefore, the hydraulic fracture keeps propagating without branching into the preexisting fractures (Figure 6.2 e and g).

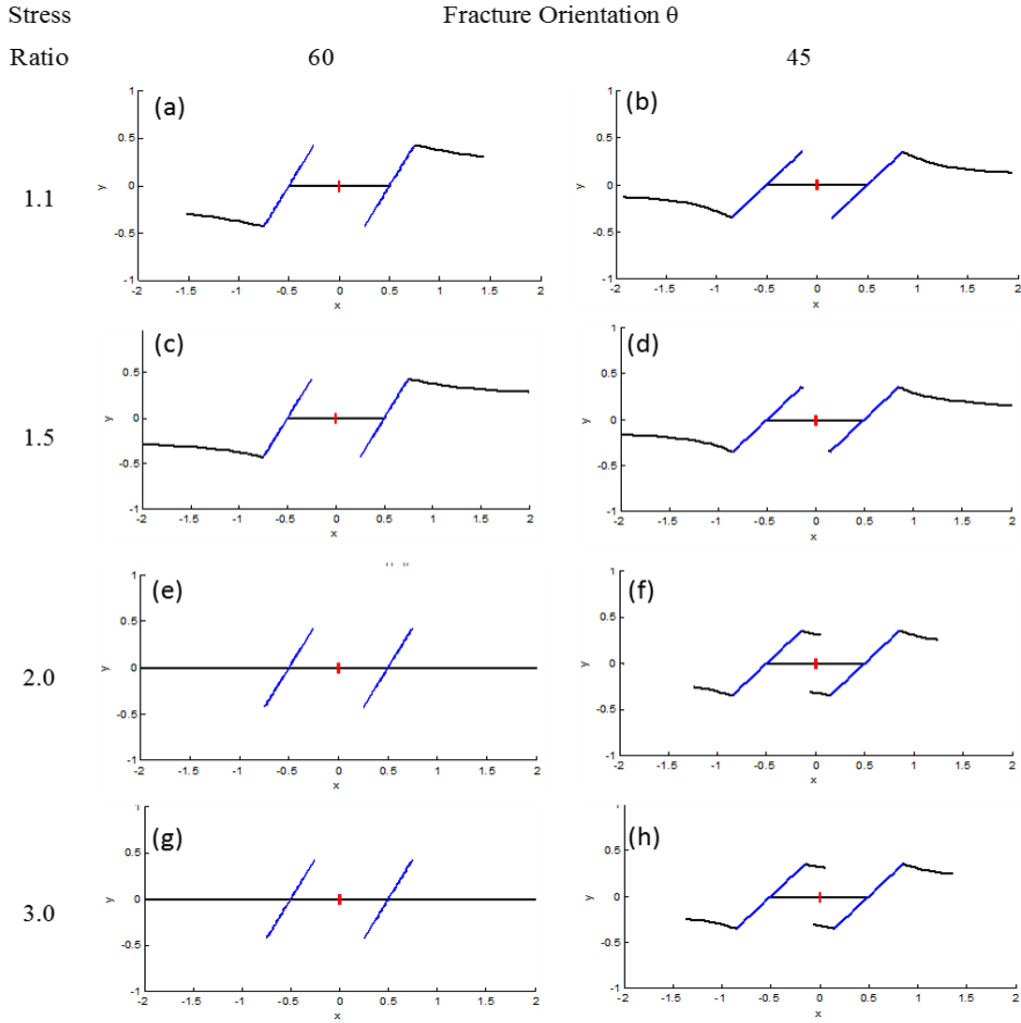


Figure 6.2: Summary of the results: Each plot shows the fracture pattern at the end of simulation of 100 sec. The red dot shows the location of the injection well; the blue lines are the preexisting fractures, while the black lines show the newly formed fractures, including a hydraulic fracture initiated from the injection well and wing cracks.

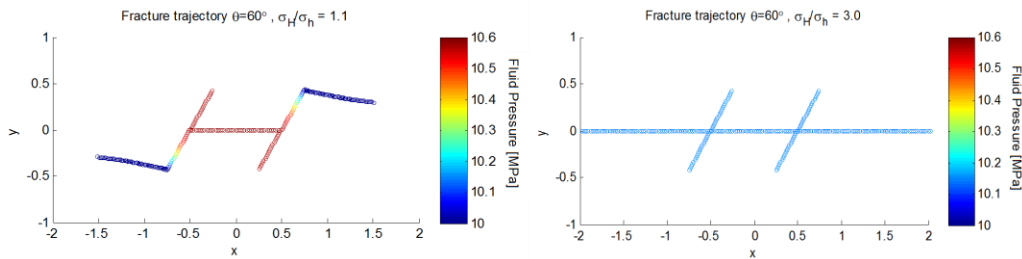


Figure 6.3: The fracture trajectories and fluid pressures when the preexisting fractures are oriented at 60 degrees to the maximum horizontal stress at the end of simulation.

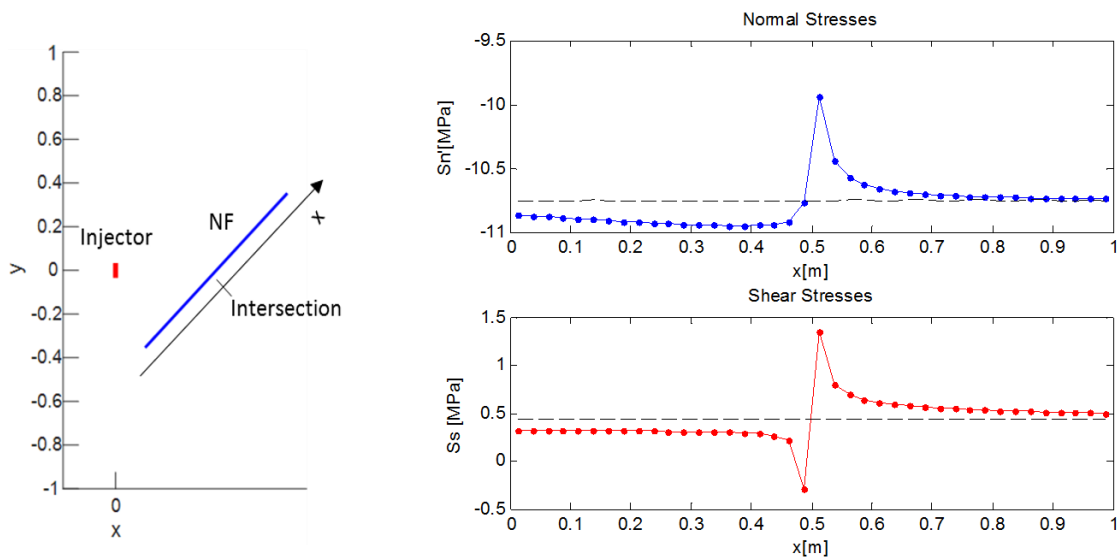


Figure 6.4: The normal stress and shear stress distribution along a preexisting fracture with the stress ratio 1.1 when a propagating fracture hits the preexisting fracture. The dotted lines show the normal and shear stress by the remote stresses. The plot shows that the side that initiates a wing crack ($x = 0.5$ m to 1.0 m) is under larger shear stresses and smaller normal stresses compared to the other side ($x = 0.0$ m to 0.5 m).

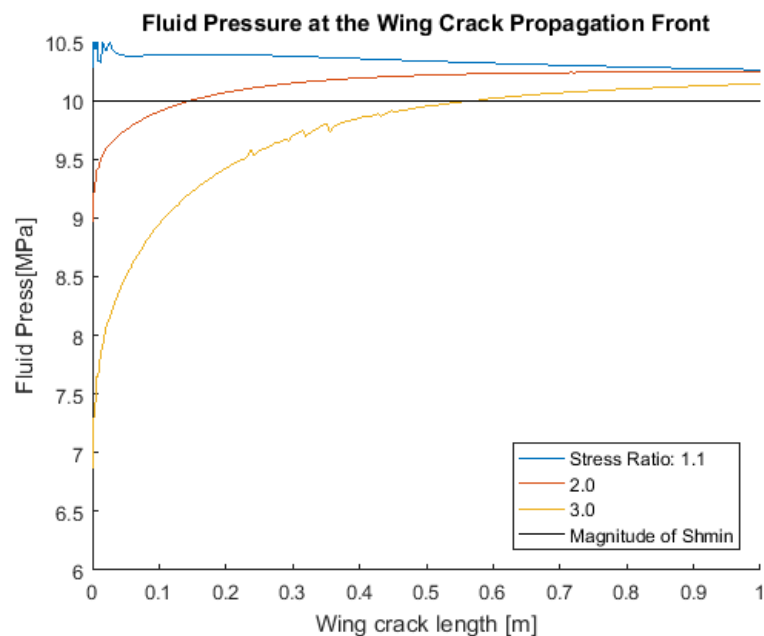


Figure 6.5: The fluid pressure at the propagation front of a wing crack fracture vs wing crack length

We compared the fracture propagation patterns with different stress states for the fractures orienting at 45 degrees. For all the test cases, the propagating fracture cross/follow condition was “follow.” When the stress ratio is close to 1, a wing crack initiates from only one side of the preexisting fracture (Figure 6.2 b and d), with the same pattern as that we observed with a preexisting fracture oriented at 60 degrees. However, when the stress ratio is 2.0 or greater, both sides of the preexisting fracture orienting at 45 degrees initiate wing cracks (Figure 6.2 f and h).

When the propagating hydraulic fracture intersects the preexisting fractures, the fluid pressure inside is almost the same as the minimum horizontal stress (Geertsma & de Klerk, 1969; Perkins & Kern, 1961; Zoback, 2007). With a large stress ratio, the slip induced by the injected fluid then becomes sufficiently high to initiate wing cracks on both sides (Figure 6.6). With a small stress ratio, the magnitude of the local stress field induced by the propagating fracture tip is large relative to the stresses acting along the preexisting fracture. Therefore, the amount of shear slip is insufficient on the side that does not initiate a wing crack (Figure 6.6). Once the preexisting fracture slips and initiates a wing crack, the wing crack propagation is driven by the shear slip at a certain length; later, the propagation is driven by the fluid pressure inside the wing crack (Figure 6.5) (Abe & Horne, 2019; Kamali & Ghassemi, 2018). The fluid pressure to drive wing crack propagation is below or almost the same as the minimum horizontal stress because the fluid pressure necessary to propagate a Mode I crack decreases as the crack lengthens (Anderson, 2005; Zoback, 2007).

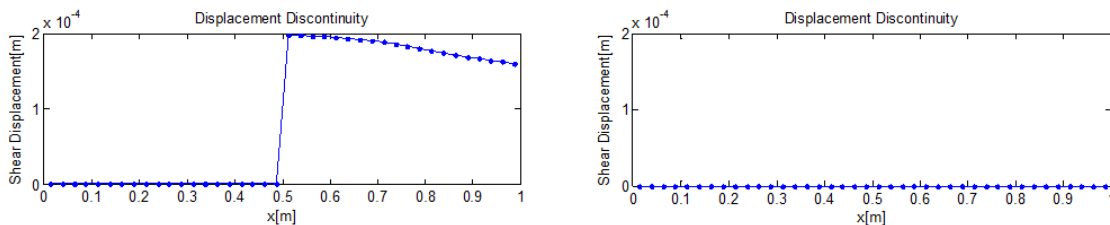


Figure 6.6: The shear displacements of a preexisting fracture orienting at 60 degrees. Left: when the stress ratio is 1.1, Right: when the stress ratio is 3.0. The left plot shows that the side that initiates a wing crack ($x = 0.5$ m to 1.0 m) has larger shear displacement while the other side has no shear displacement ($x = 0.0$ m to 0.5 m).

6.2.4 Analysis of stresses along natural fracture

The numerical experiment results show that a flow path remains as a single pathway when the stress ratio is below 2.0, while a flow path branches into two when the stress ratio is 2.0 or greater for the fractures oriented at 45 degrees. Having multiple flow paths is preferable in EGS because it increases the heat exchange areas and reservoir permeability. We analyzed the local stress field induced by the propagating fracture tip to investigate fracture propagation pattern differences. These induced local stress fields from other fractures are referred to as stress shadowing effects, which is the mechanical interaction among nearby fractures.

The hydraulic fracture propagating from the injector has opening displacements, which perturb the local stress field affecting the deformation of the preexisting natural fractures. Figure 6.8 shows the normal and shear stresses acting along the natural fractures orienting at 15 to 75 degrees when they intersect with a hydraulic fracture. These plots show the stresses induced by a Mode I fracture with an effective normal stress of 1 MPa and a crack length of 1 m. As shown in the plots, the stress shadow effect decreases with distance. The effect is negligible at 3 m from the intersection because the induced stresses are only approximately 3% compared to the peak value.

Normal stress components σ_n take tension as positive, while the positive components of σ_s take the right-lateral direction, the same sign as the shear stress induced by the remote stresses. Overall, the stress shadow effect from a propagating fracture induces larger shear stresses and smaller normal stresses on the side with a larger angle ($x > 0$ in Figure 6.7). The perturbation of normal stresses is larger with a smaller natural fracture orientation, while the perturbation of shear stresses is larger with a larger natural fracture orientation.

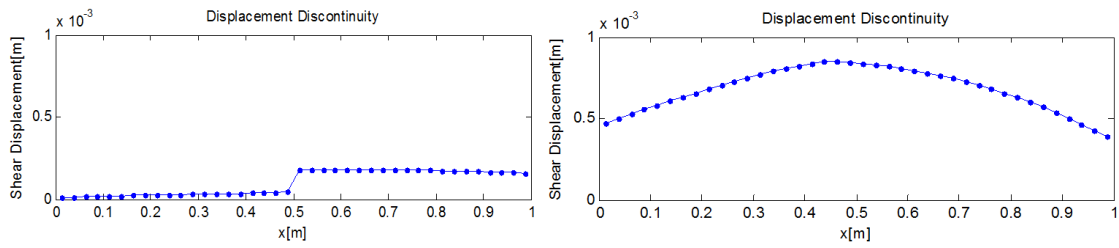


Figure 6.7: The shear displacements of a preexisting fracture orienting at 45 degrees. Left: when the stress ratio is 1.1, Right: when the stress ratio is 3.0. The left plot shows that the side that initiates a wing crack ($x = 0.5 \text{ m}$ to 1.0 m) has larger shear displacement compared to the other side ($x = 0.0 \text{ m}$ to 0.5 m).

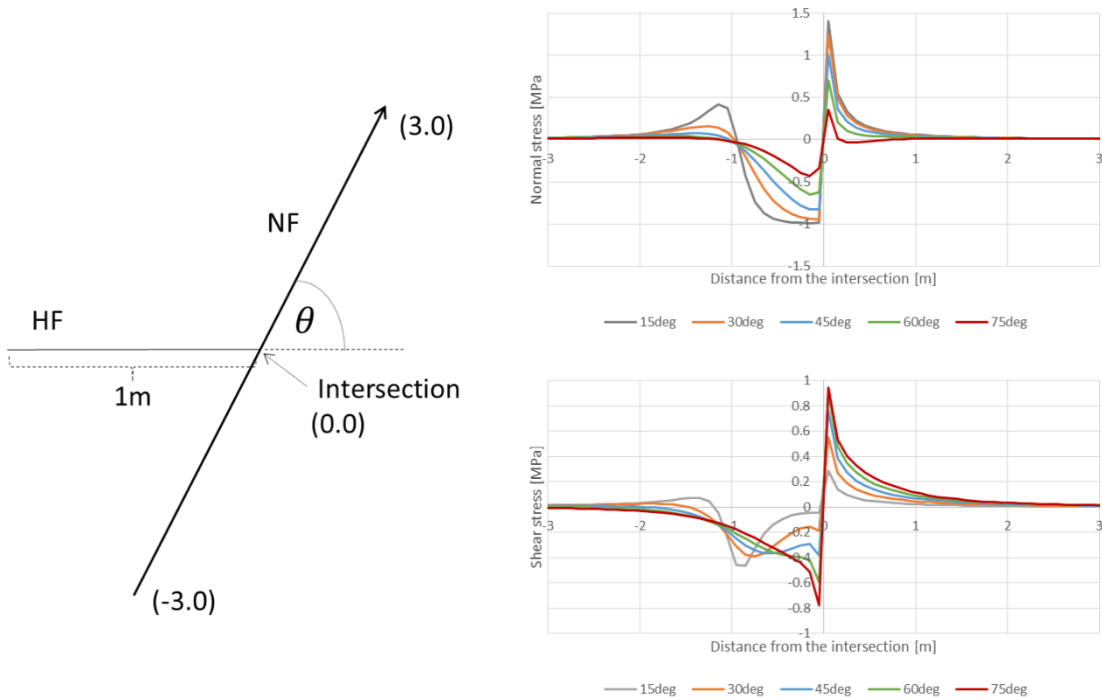


Figure 6.8: The normal and shear stresses acting on a natural fracture orienting at 15, 30, 45, 60, and 75 degrees, respectively with net pressure of 1MPa, and fracture length of 6m.

The magnitude of stress shadowing increases linearly with the fluid pressure and the crack length. Pollard and Segall (1987) described relative displacements across a fracture as:

$$\begin{array}{l}
\text{Mode I} \\
\text{Mode II} \\
\text{Mode III}
\end{array}
\begin{array}{l}
\left\{ \Delta u_I \right\} \\
\left\{ \Delta u_{II} \right\} \\
\left\{ \Delta u_{III} \right\}
\end{array}
= \begin{array}{l}
\left\{ \Delta \sigma_I \right\} \\
\left\{ \Delta \sigma_{II} \right\} \\
\left\{ \Delta \sigma_{III} \right\}
\end{array}
\frac{2(1-\nu)}{\mu} (a^2 - x^2)^{\frac{1}{2}}, \quad (6.1)$$

where Δu_m and $\Delta \sigma_m$ are displacement components and driving stresses in Mode m , respectively, and a is a fracture half length. The stresses at an arbitrary point due to opening displacements u_I is proportional to u_I assuming linear elasticity. Therefore, the magnitudes of displacements along a fracture are proportional to the driving stresses and fracture half length, while the induced stresses around the fracture are proportional to the fracture displacements.

Stress shadowing causes asymmetrical distributions of the fluid pressures which are needed to make a fracture element slip. We calculated the necessary fluid pressures to initiate a wing crack from each side of the natural fracture. We numerically calculated the stress state acting along a natural fracture orienting at 15° , 30° , 45° , 60° , and 75° intersecting with a hydraulic fracture. Based on Equation 6.1 assuming that $K_I = 0$ and $K_{II} = \Delta \tau \sqrt{\pi a}$ (Anderson, 2005), the necessary shear stress drop to initiate a wing crack is:

$$\Delta \tau^w = K_{IC} \left[\frac{3}{2} \sin \theta_0 \cos \frac{\theta_0}{2} \sqrt{\pi a} \right]^{-1}, \quad (6.2)$$

where θ_0 is the fracture propagating direction which is 70.5° for pure Mode II based on the maximum circumferential stress theory (Erdogan & Sih, 1963), a is the fracture half length, and K_{IC} is the Mode I critical stress intensity factor (Ingraffea, 1987). The fluid pressure needed to initiate a wing crack is calculated as:

$$p_f^w = -\frac{1}{f} |\Delta \tau^r + \Delta \tau^s - \Delta \tau^w| - \Delta \sigma^r - \Delta \sigma^s, \quad (6.3)$$

where $\Delta \tau^r$ and $\Delta \tau^s$ are shear stresses induced by remote stresses and stress shadowing, respectively, while $\Delta \sigma^r$ and $\Delta \sigma^s$ are normal stresses induced by remote stresses and stress shadowing, respectively.

We calculated the fluid pressure needed to initiate a wing crack on each side of a natural fracture by assuming a uniform fluid pressure. The needed fluid pressure to initiate a wing crack was calculated including the effect of the stress state and the

induced stress field by a propagating hydraulic fracture. The induced stress field ahead of a crack tip under Mode I loading in an isotropic linear elastic material under the plane-strain condition can be expressed in closed form (Anderson, 2005):

$$\sigma_{xx}^{(I)} = \frac{K_I}{\sqrt{2\pi r}} \cos \frac{\theta}{2} \left(1 - \sin \frac{\theta}{2} \sin \frac{3\theta}{2}\right), \quad (6.4)$$

$$\sigma_{yy}^{(I)} = \frac{K_I}{\sqrt{2\pi r}} \cos \frac{\theta}{2} \left(1 + \sin \frac{\theta}{2} \sin \frac{3\theta}{2}\right), \quad (6.5)$$

$$\sigma_{xy}^{(I)} = \frac{K_I}{\sqrt{2\pi r}} \cos \frac{\theta}{2} \sin \frac{\theta}{2} \cos \frac{3\theta}{2}, \quad (6.6)$$

where K_I is the Mode I stress intensity factor, r and θ are the polar coordinate with the origin at the fracture tip. Based on the principle of superposition, the total stress field caused by the remote stresses and the singular stress field are:

$$\sigma_{ij}^{(total)} = \sigma_{ij}^{(remote)} + \sigma_{ij}^{(I)}. \quad (6.7)$$

In this analysis, we assume that the fluid pressure flowing into the natural fracture was uniformly 0.3 MPa above the minimum horizontal stress, which is 10.3 MPa. The plots in Figure 6.9 show the fluid pressure needed to make a necessary shear displacement to initiate a wing crack. The points below the fluid pressure 10.3 MPa mean that a wing crack initiates from the side of a fracture. The fluid pressure exceeds the necessary pressure only on the larger angle side of a natural fracture in the test cases with a stress ratio below 2.0 (shown in the blue box in Figure 6.9). The case with the stress ratio 1.1 and fracture orientation 60 degrees, the necessary pressure on both sides are initially higher than the fluid pressure. The fluid pressure then increases when there is no propagating fracture in the fracture network, so the fluid pressure increases until a wing crack starts propagating from the larger angle side of a natural fracture. In the test cases with a natural fracture orientation of 45 degrees and a stress ratio of 2.0, the fluid pressure exceeds the necessary pressure to initiate a wing crack on both sides (shown in the yellow box in Figure 6.9). When an orienting fracture is at 60 degrees, the fluid pressure is insufficient to initiate a wing crack, but sufficient to propagate a hydraulic fracture (shown in the green box in Figure 6.9). This implies that we can estimate the fracture propagation patterns with simple approximation.

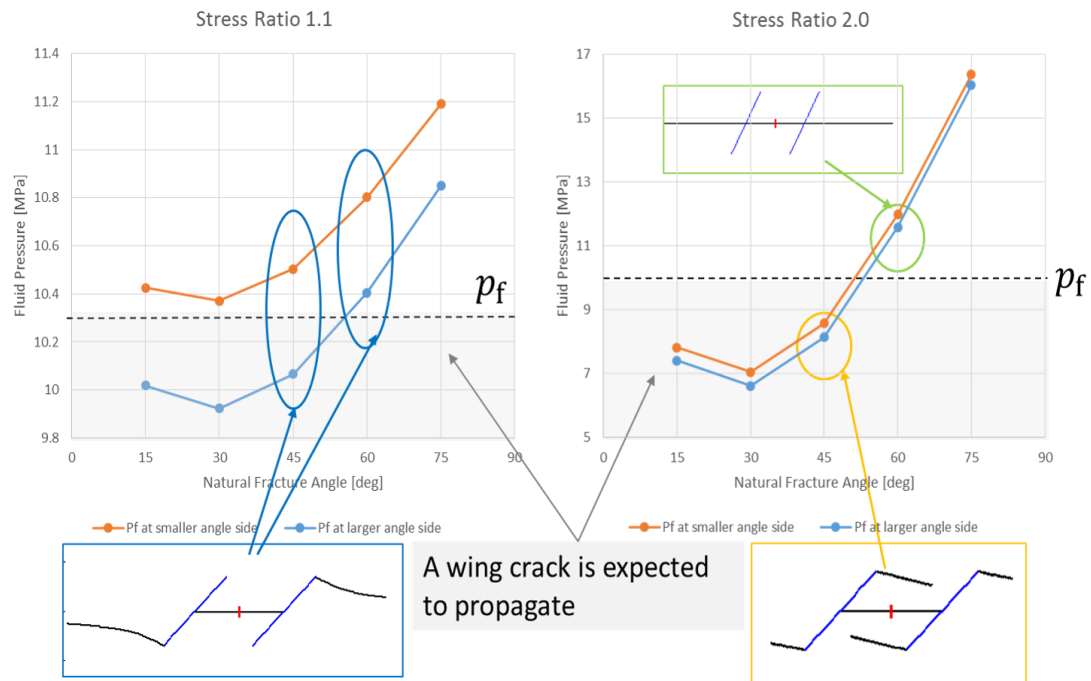


Figure 6.9: The fluid pressure needed to initiate a wing crack on each side of a natural fracture. The results of the experiments are shown in blue, yellow, and green boxes.

6.3 Investigating the effect of fracture size

The analysis in Section 6.2.4 shows that the further away preexisting natural fracture tips are from a hydraulic fracture, the smaller the magnitude of the stress shadowing effect. We also investigated the effects of natural fracture sizes compared to that of a hydraulic fracture. The simulation setup and parameters used are the same as the numerical experiments in Section Investigating the effect of fracture orientation and stress state (Figure 6.1). The simulations were done until the propagated fracture length exceeds 50% of the natural fracture length. The stress ratios were varied either 1.1 or 3.0 with the fixed value of least principal stress $\sigma_h = 10\text{MPa}$. The fracture orientations used in this study are 45 and 60 degrees to the maximum horizontal stress orientation. The length of the natural fractures are 2 m and 5 m.

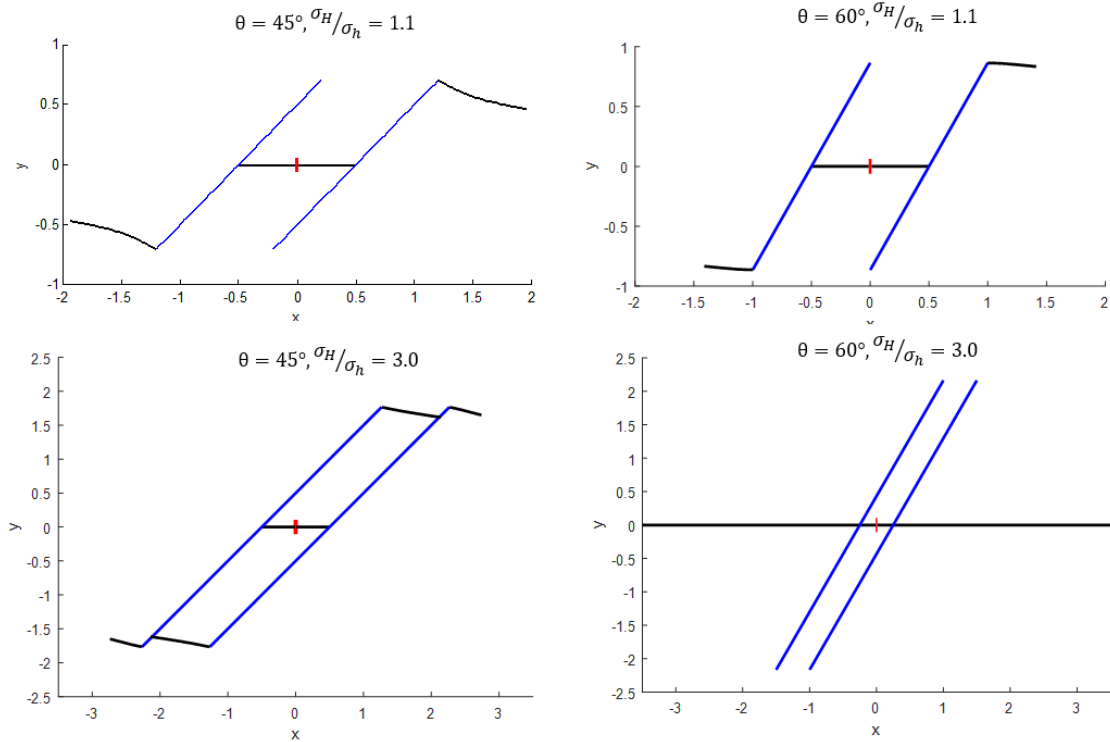


Figure 6.10: Summary of the results: Each plot shows the fracture pattern at the end of simulation of 100 sec. The red dot shows the location of the injection well; the blue lines are the preexisting fractures, while the black lines show the newly formed fractures, including a hydraulic fracture initiated from the injection well and wing cracks. The upper plots show the cases with a natural fracture with a length of 2 m, the lower plots show the cases with a natural fracture with a length of 5 m.

6.3.1 Results

The propagation patterns are consistent with the base cases in which the length of a natural fracture is 1 m. With preexisting natural fractures with a length of 2 m, the stress shadowing from the hydraulic fracture makes a condition where the side initiating a wing crack is under larger shear stresses and smaller normal stresses compared to the other side, although the magnitude of the stress shadow effect is smaller near the fracture tips than that of a natural fracture with a length of 1 m (Figure 6.10). These asymmetric stress distributions make the propagation patterns with a natural fracture with a length of 2 m the same as those with a natural fracture with a length of 1m.

With natural fractures with a length of 5 m, the stress shadowing effects around the fracture tips are negligible because the stress perturbation by a hydraulic fracture decreases with distance. However, once one side of a fracture starts sliding, shear stimulation improves the fracture transmissibility, enhancing fluid flow to the sliding side.

6.4 Comparison of Injection Rate

A common practice in hydraulic fracturing at unconventional oil and gas reservoirs is to inject highly viscous crosslinked-gel to generate wider fracture width and to increase the effective reservoir conductivity and continuity with the wellbore (Chen et al., 2020; Palisch et al., 2010). Warpinski et al. (2005) showed microseismic traces of two hydraulic stimulation performed at a Barnett shale unconventional reservoir where the first treatment was performed with crosslinked gel which had a high viscosity, while the following treatment was done with slickwater which had a low viscosity. They observed that the complexity of the resulting fracture geometry was higher when slickwater was used. Their results suggested that the viscosity of fluid may affect the complexity of a fracture network (Palisch et al., 2010). Beugelsdijk et al. (2000) showed that increasing a flow rate or fluid viscosity results in smaller near-wellbore hydraulic fracture tortuosity by laboratory scale experiments. Injecting fluids with varied viscosity is uncommon in hydraulic stimulation in EGS where water is usually used as an injection fluid. However, the fluid pressure distribution when injecting at a higher rate is equivalent to that when injecting more viscous fluid based on Darcy's law although the time scale is different.

In this experiment, we simulated a reservoir with multiple preexisting natural fractures to investigate if changing injection rates affects fracture network patterns. The initial reservoir condition is shown in Figure 6.10. The injection well is located at the center of the domain, and natural fractures orienting at 45 degrees are located so that they intersect to propagating wing cracks. The stress ratios used were 1.1, 1.5, and 3.0 with the fixed value of least principal stress $\sigma_h = 10\text{MPa}$. For the low injection rate cases, the injection rates were $4.0 \times 10^{-6} \text{ [m}^3/\text{s]}$ and simulation time was 250 seconds,

while for the high injection rate cases, the injection rates were 1.0×10^{-3} [m³/s] and simulation time was 3 seconds.

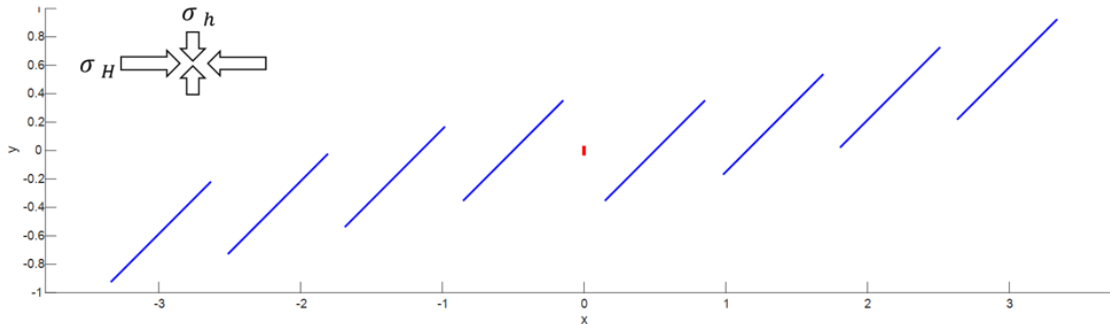


Figure 6.11: Simulation setup. An injection well located at the center of the domain initiates a hydraulic fracture (red dot). Propagating hydraulic fracture and wing cracks intersect to preexisting natural fractures (blue lines).

6.4.1 Results

With an anisotropic stress state condition in the case of the stress ratios 1.5 and 3.0, the injection at a low flow rate made more complex fracture networks than those by injecting at a high flow rate. By injecting slowly, preexisting natural fractures initiate wing cracks from both tips, which resulted in flow path branching. On the other hand, by injecting at a high rate, the flow path remains as a single pathway from the injector. With a stress state close to isotropic (a stress ratio 1.1), changing injection rate did not have a significant effect on changing the fracture propagation pattern. With a stress ratio 1.1, the stress shadowing effect of upstream fractures made the larger angle sides of natural fractures open. This leads to a larger transmissivity to one side, which makes the one-path the preferred flow pathway in both low and high injection rate cases. The stimulation front went further with lower stress ratio because the lower maximum principal stress led to the higher transmissivity of natural fractures.

The flow behavior when injecting at a higher rate is equivalent to that when injecting viscous fluid based on Darcy's law. Figure 6.13 shows the transmissivity of each element. When a flow path remains as one pathway, the difference of transmissivity between each side of a natural fracture is large. On the other hand, when

a flow path branches after intersecting a natural fracture, both sides of a natural fracture are stimulated equally, which makes the natural fracture initiate two new wing cracks.

These transmissivity differences are induced by stress shadowing by an upstream fracture which deforms earlier than the downstream fracture. The magnitude of an induced local stress field along an intersecting natural fracture is proportional to the effective normal stress inside an intersecting upstream fracture based on the linear elasticity. With a high injection rate, the fluid pressure inside an upstream fracture can be much higher than that in a low injection rate case. Therefore, the balance between stress shadowing by the upstream fracture and the effect of fluid pressures determines the deformation of the downstream natural fracture. This can be better understood by the change in Coulomb stress by stress shadowing. The Coulomb stress is expressed as:

$$\Delta\sigma_c = |\sigma_s| + f\sigma_n. \quad (6.8)$$

When $\Delta\sigma_c$ is positive, the fracture interval is likely to fail in shear. Figure 6.14 shows the Coulomb stress along the first natural fracture of the case of the stress ratio 1.5. The fluid pressures inside intersecting fractures are assumed to be the same as the wellbore fluid pressure, which are 12.0 MPa with the high injection rate case and 10.5 MPa with the low injection rate case. As Figure 6.14 shows, the entire natural fracture is subject to shear failure with the low injection rate case, while the larger angle side is subject to slip but the smaller angle side does not slip with the high injection rate case. This explains why the entire natural fracture is stimulated in the low injection rate case while only the larger side of the natural fracture is stimulated in the high injection rate case. Therefore, the flow behaviors of different injection rates in combination with the effects of stress shadowing made the fracture propagation pattern different in these experiments. On the other hand, with a stress state close to isotropic, even though we injected fluid at a low rate, the effect of stress shadowing by an upstream fracture was large enough to induce sufficient transmissivity differences between the larger angle side and the smaller angle side because fluid pressure at the propagation front is close to the least principal stress, which is already high enough to prevent the smaller angle side from slipping.

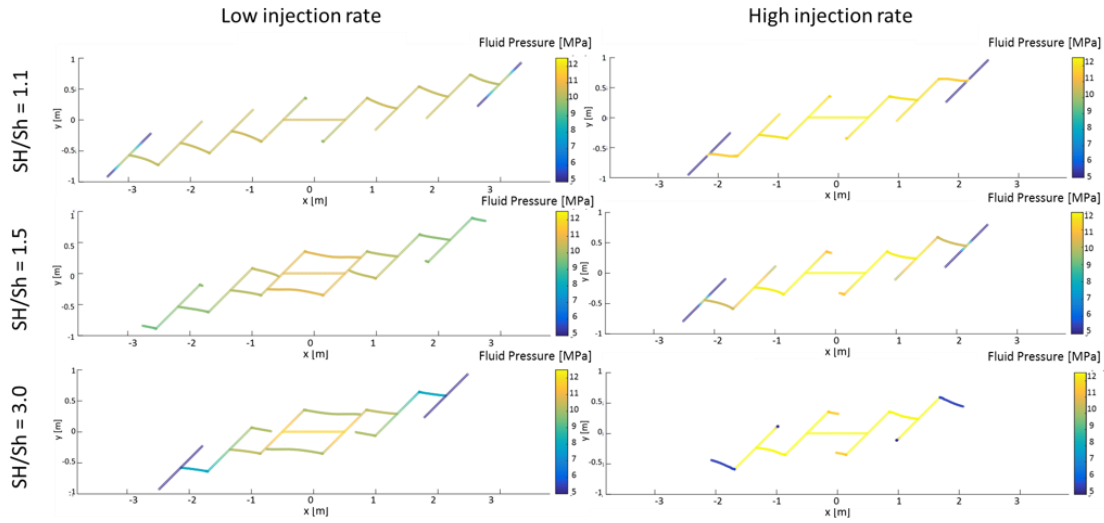


Figure 6.12: Fracture trajectories and fluid pressures in each stress ratio and injection rate at the end of simulation time.

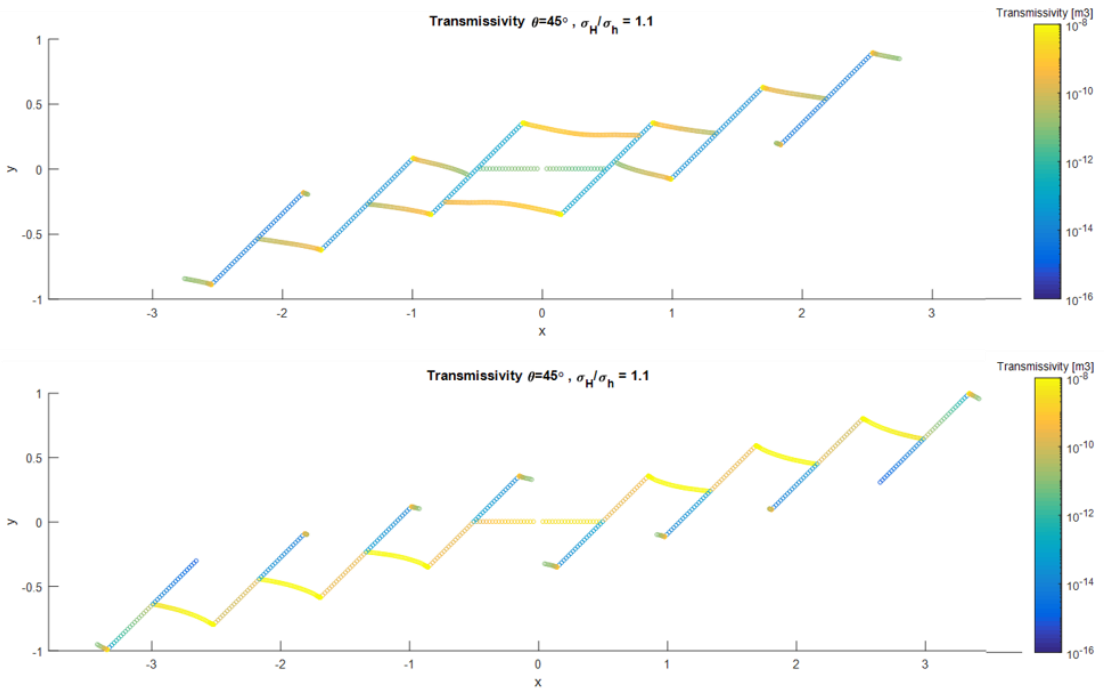


Figure 6.13: Transmissivity of fractures with the stress ratio 1.5 cases (low injection rate: above, high injection rate: below)

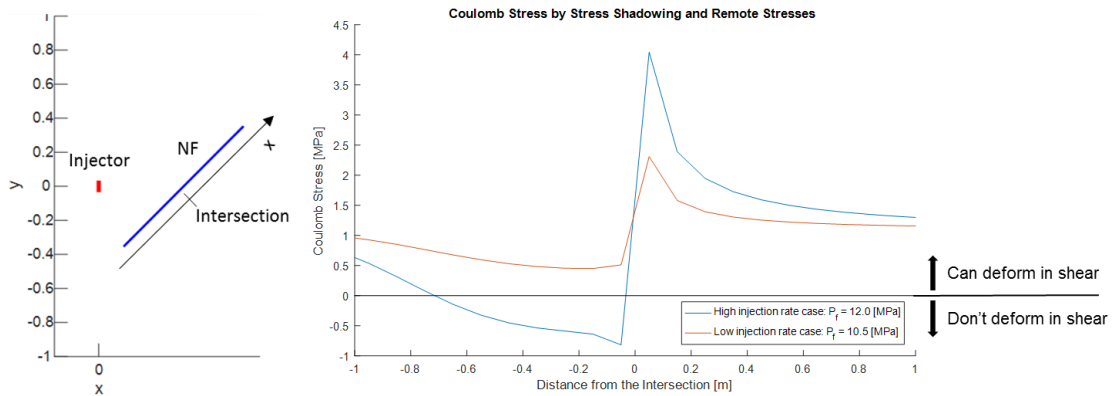


Figure 6.14: Left: The location of the natural fracture and x axis, Right: The Coulomb stress along the natural fracture with high injection and low injection rate cases. The fluid pressures inside intersecting fractures are assumed to be the same as the wellbore fluid pressure, which are 12.0 MPa with the high injection rate case and 10.5MPa with the low injection rate case.

6.5 Discussion and Summary

In this study, we modeled hydraulic stimulation in an EGS reservoir with preexisting natural fractures. The model results show three fracture network patterns; 1) a hydraulic fracture crosses the preexisting fracture, and continues propagating, 2) a hydraulic fracture follows the preexisting fracture, and the preexisting fracture initiates only one new wing crack, and 3) a hydraulic fracture follows the preexisting fracture, and the preexisting fracture initiates two new wing cracks. Furthermore, by injecting fluid at a low injection rate, the created fracture network is likely to be more complex than that created by a high injection rate. When a preexisting fracture slips, shear dilation and a wing crack propagation increase the volume to store fluid in the reservoir. This volume change causes a decrease of the fluid pressure inside the preexisting fracture. Hence, the injected fluid flows into the slipping fracture, creating a preferred flow path. Once the preexisting fracture slips and initiates a wing crack, the wing crack propagation is driven by the shear slip until it extends to a certain length; the propagation is then driven by the fluid pressure inside the wing crack (Abe & Horne, 2019; Kamali & Ghassemi, 2018). The length of a wing crack can be as long as the main preexisting fracture when it is well-oriented. Most of the past EGS projects did not observe a propagating planar fracture perpendicular to the least principal stress unlike in an unconventional oil and

gas reservoir. Therefore, when a bottomhole pressure exceeds the least principal stress, it is highly likely that new fractures initiate from a preexisting fracture and propagate in a reservoir with the existence of well-oriented fractures.

These results also indicate that the poorly-oriented fractures, which a propagating newly formed fracture can cross, likely have a smaller contribution to the fracture network creation and reservoir permeability enhancement. The fractures that are not critically stressed are often partially or entirely cemented because they were created a long time ago in most cases. On the other hand, well-oriented fractures with sufficient stress drop when stimulated have shear displacements that lead to shear dilation and eventually wing crack initiations from the edges. Those fractures likely dominate a fracture network and contribute to reservoir permeability enhancement. The stress state and fracture cross/follow condition also play a critical role in the fracture network complexity. Additionally, low injection rates may stimulate more preexisting natural fracture area and lead to the creation of more flow paths. The numerical model does not consider fluid leak-off to the formation; therefore, the fluid pressure inside fractures may be overestimated by neglecting leak-off, which enhances fracture propagation length and shear sliding (Fu et al., 2020; Norbeck et al., 2016). However, the assumption is reasonable to model fracture propagation patterns in an EGS reservoir because the permeability of the formation is usually low and the effect of leak-off is limited. The effect of leak-off could be considered in future research.

As Figure 6.5 shows, the fluid pressures inside a propagating wing crack are slightly above or below the least principal stress because wing crack propagation is driven by both fluid pressure inside and stress shadowing of slipping main natural fracture (Abe & Horne, 2019). When the stimulation front is along a natural fracture, the pressure at the front is close to the fluid pressure that induces slip. Therefore, the fluid pressure at the propagation front is almost constant. As Figure 6.13 shows, the transmissivity of the flow path between the wellbore and the propagation front is high because natural fractures deform in shear or open when the fluid pressure exceeds the normal stress and improve their transmissivity. Therefore, the increase of wellbore pressure is limited at a certain value. In these experiments, we observed pressure

limiting behavior. Pressure limiting is the behavior where the bottomhole pressure stabilizes at a certain value even after the injection rate increased. The stabilized wellbore pressure differs by the injection rate and stress state. The pressure limiting has been observed in most of the past EGS projects (McClure & Horne, 2014).

Having flow path complexity is advantageous in EGS because it increases the heat exchange areas, the fracture surface to rock volume ratio, and the general reservoir permeability. Therefore, the implication from the results of this study to make a better EGS reservoir would be to simulate an EGS reservoir with 1) well-oriented fractures, 2) a high stress ratio, and 3) a low injection rate. These reservoir conditions and stimulation design will likely make more flow paths and create a more complex fracture network.

In almost all EGS projects, fluid was injected into a preexisting fracture intersecting the injection well, with the result that the injection pressure exceeded the least principal stress (McClure & Horne, 2014). This observation and the results of this study support the mixed-mechanism stimulation and the possibility of new fractures being formed from preexisting fractures. In the Fenton Hill EGS project, it was observed that Massive Hydraulic Fracture (MHF) treatment formed a broad microseismic cloud roughly 200 m wide, 1000 m long, and 1000 m high. The estimated dominant preexisting fracture orientation toward the least principal stress was 53 degrees. The MHF treatment was performed at extremely high net-pressures of over 70 MPa, for 60 hours for most of the treatment. The fluid injection pressure exceeding 70 MPa was sufficient to open the preexisting fractures (Brown et al., 2012; Norbeck et al., 2018). This implies that a complex fracture network was created by the mixed-mechanism stimulation because the stress drop induced maximum shear displacement resulting in the entire fracture slipping at the fluid pressure opening preexisting fractures (Norbeck et al., 2018). It is likely that a flow path from the injection well branched as it intersected natural fractures, which resulted in forming a broad microseismic cloud.

In this study, we modeled the initiation of a hydraulic fracture from an injection well. However, because fluid injection from a wellbore flows through a preexisting fracture in most of the EGS projects (McClure & Horne, 2014), future work could

investigate scenarios in which the fluid is injected into a preexisting fracture causing wing cracks to propagate and intersect with other preexisting fractures in reservoir scale. In an actual EGS reservoir, the stress state is rather uncertain and preexisting fractures are expected to be distributed in a complex pattern with varied orientations, size distributions, and fracture connectivity; however, the simple reservoir setting in this study is reasonable to help us understand how preexisting fractures and newly formed fractures interact with each other to create a fracture network. This is because this numerical model handles fluid flow between fracture surfaces, shear dilation of a preexisting fracture, fracture propagation, and mechanical interactions between fractures. In future work, we will model a realistic reservoir containing a number of fractures with reasonable variation, to confirm the implications of this study and better understand fracture network creation at a reservoir scale.

Chapter 7

7 Fracture Network Creation and Stimulation Mechanism of Basel-1 and Fenton Hill Phase-2 EGS Reservoirs

7.1 Introduction

In the previous chapters, we investigated how a preexisting fracture and a newly formed fracture interact with each other and create a fracture network. To better understand the hydraulic stimulation mechanisms in an actual EGS reservoir, we chose two past EGS projects to investigate how a fracture network is created by the mixed-mechanism stimulation in this study.

For the mixed-mechanism stimulation to occur, injection pressure needs to exceed the pressure that induces sufficient shear slip on preexisting fractures, and the initial connectivity of permeable preexisting fractures is poor. We reviewed past EGS projects and chose Fenton Hill Phase-2 reservoir and Basel EGS site because the injection pressure exceeded the minimum horizontal stress during the stimulation, the reservoirs did not utilize a known fault system, and there are sufficient datasets in the literature for both cases. During the hydraulic stimulation treatment at the Fenton Hill Phase-2 reservoir, the observed microseismic cloud formed a broad shape while the microseismic cloud formed a thin lens shape at the Basel EGS site. We reviewed those two projects and summarize in the following sections.

7.1.1 Fenton Hill Phase-2 EGS Project

The Hot Dry Rock Project by the Los Alamos National Laboratory included 23 years of field scale experiments that attempted to extract thermal energy from deep hot jointed basement rock at Fenton Hill site in New Mexico, the United States. The project covered from formation evaluation, successful hydraulic stimulation, long-term flow testing, to electricity generation (Brown et al., 2012). Two separate reservoirs were successfully stimulated ranging from a minifrac test to a massive hydraulic fracture and achieved flow connection between two wells. The summary of the project is described in Brown et al. (2012) and Norbeck et al. (2018). In this section, we introduce the information we used for our study as extracted from literature.

Stress State and its Orientation:

The orientation of the minimum horizontal stress of N119°E was estimated from borehole breakouts visualized in borehole televiewer images (Barton et al., 1988). The magnitude of the minimum principal stress varied from 14.5 MPa/km to 19 MPa/km. Barton et al. (1988) calculated the fracture gradient based on the relationship between the coefficient of friction and the ratio of maximum to minimum effective principal stress assuming normal faulting or strike/slip regime. They suggested that the state of stress at the Well EE-3 as $S_v = S_H = 26.5$ MPa/km, $S_h = 14.5$ MPa/km, and $P_p = 9.9$ MPa/km. The high profile of fracture gradient of 19.0 MPa/km was suggested by Kelkar et al. (1986) based on several minifrac tests. However, as Norbeck et al. (2018) mentioned, Brown (1989) analyzed the injection test data and microseismicity, and stated that the minimum horizontal stress above 3 km, which showed low profile, reflected the gradient more accurately because the minimum principal stress estimated below 3 km did not reflect the effect of opening natural fractures. Norbeck et al. (2018) used the stress state assuming the low stress profile by Barton et al. (1988) in their study. The authors interpreted that the natural fractures intersecting the injection well opened when the injectivity significantly increased at the BHP of 74 MPa. The stress state used in their study was $S_H = 90$ MPa, $S_h = 46$ MPa, $P_0 = 31$ MPa, and the orientation of S_h of N30 °E at the depth of 3.6 km.

Fracture Orientation

The analysis of the focal planes of the seismicity observed during the massive hydraulic fracturing treatment at Fenton Hill Phase-2 reservoir suggested that the predominant preexisting fractures were striking NNW and almost vertical (Brown, 1989; Fehler et al., 1987; House et al., 1985). The analysis of Fehler et al. (1987) showed that there were five fracture planes determined by microearthquake observation and that the most dominant orientation determined was N31°W and dip 74°E. Norbeck et al. (2018) interpreted that the dominant natural fracture orientation was N23°W based on the fracture opening pressure of 74 MPa and the state of stress at the reservoir. They showed that a stochastic fracture realization with the dominant orientation of N23°W showed good agreement with the observed microseismicity cloud assuming mixed-mechanism stimulation.

Stimulation Mechanisms and the resulting stimulated region

The original concept of Hot Dry Rock (HDR) in the 1970s was to utilize a single vertical penny-shaped fracture in a flawless homogeneous reservoir as a conduit (Gringarten et al., 1975). The hydraulic stimulation performed at the Phase-1 reservoir aimed to create those vertical penny-shaped fracture that connected two deviated wells. However, the treatment did not create a penny-shaped fracture normal to the least principal stress, but rather opened the sealed preexisting fractures (Brown et al., 2012). This was because the breakdown pressure to open partially sealed preexisting joints was much lower than that required to create a newly formed hydraulic fracture. The hydraulic stimulations both at Fenton Hill Phase-1 and Phase-2 reservoirs were done through preexisting fractures intersecting the injector as shown in the temperature survey in well EE-2 that a couple of joints were flowing in the upper part of the openhole interval (Brown et al., 2012). The crystalline basement which is typically a good candidate for an EGS reservoir is highly fractured and fractures located deeper are resealed by minerals dissolved in heated geothermal fluid. The major finding from the Phase-1 hydraulic stimulation was that preexisting fractures controlled the reservoir permeability and stimulation region growth. It was also possible that newly formed fractures propagated

in the reservoir because the injection pressure exceeded the least principal stress and pressure limiting behavior observed (McClure & Horne, 2014).

Norbeck et al. (2018) suggested that mixed-mechanism stimulation was the stimulation mechanism at the Fenton Hill Phase-2 reservoir. The authors argued that the growth of the microseismicity was in a direction that was inconsistent with the orientation of the maximum principal stress and with the dominant preexisting fractures. They then assumed the mixed-mechanism stimulation in their model and showed a good agreement with the observed injectivity enhancement and its reversible behavior, and the direction of the microseismicity migration.

7.1.2 Basel EGS Project

The Deep Heat Mining (DHM) Project was a project conducted to create an enhanced geothermal system at a depth around 5 km in granitic basement in Basel, Switzerland (Häring et al., 2008). Hydraulic stimulation was performed for 6 days, however, the injection was stopped after a M_L 2.6 seismic event occurred and the well was shut-in and bled-off. After the well was shut-in, the largest seismic event M_L 3.4 occurred and three aftershocks larger than M_L 3.0 occurred in total (Häring et al., 2008). The project was terminated due to the concerns of induced seismicity.

Stress State and its Orientation:

The orientation of the principal stresses was estimated by borehole breakouts as the maximum horizontal stress in the basement granite was $N144\pm 14^\circ E$ (Häring et al., 2008; Valley & Evans, 2009). The orientations were consistent with the large-scale pattern of stress in Europe, which appeared to be dominated by NW-oriented compression and the estimated value at a nearby well (Häring et al., 2008). The stress regime at the Basel 1 well is a mix of normal and strike-slip (Valley & Evans, 2019). The magnitude of the minimum horizontal stress was estimated based on the observation that no pressure limiting behavior nor hydraulic fracturing was observed at the wellbore. Therefore, the least principal stress was estimated to be value larger than the maximum injection pressure during the stimulation (Häring et al., 2008; Valley & Evans, 2019). The vertical stress was calculated based on the density log acquired in the sedimentary

section of a nearby well and the density log from the crystalline basement of Basel 1. The maximum horizontal stress was firstly estimated based on the differential strain-curve analysis, the stress state diagram, and the focal mechanism solutions (Håring et al., 2008). Valley and Evans (2019) later derived the magnitude of the maximum horizontal stress by analyzing wellbore breakout data from a UBI log run in the granitic basement section of the Basel 1 borehole. Their analysis proposed much smaller gradient of the maximum horizontal stress profile than those previously suggested; however, given the fact that their result showed reasonable consistency with the focal mechanism of the observed microseismicity and the constraints by a Mohr-Coulomb/Rankine failure criterion, their maximum horizontal stress profile is likely to be more reasonable.

In this study, we used the magnitudes of minimum and maximum horizontal stresses in the depth interval between 2500 m to 5000 m proposed by Valley and Evans (2019) as:

$$S_{hmin} = 7z + 42, \quad (7.1)$$

$$S_{Hmax} = 5z + 90, \quad (7.2)$$

where S_{hmin} is the minimum horizontal stress in MPa, S_{Hmax} is the maximum horizontal stress in MPa, and z is the depth from the surface in km.

Properties of the reservoir rock

The rock properties were determined as 39 GPa for the Young's modulus and 0.22 for the Poisson's ratio by a single multistage confined compression test that was performed on a core sample of the Basel monzogranite core taken from the wellbore. The initial Young's modulus calculated from the test was much lower than the value acquired from sonic and density logs which was 80 GPa. Valley and Evans (2019) corrected the initial value for the Young's modulus to 65 GPa because they assumed that possible core damage might have caused this low value for the Young's modulus.

Fracture Orientation

To determine the dominant fracture orientations in the reservoir, UBI log analysis, microseismicity waveform analysis, and failure criterion analysis have been done. Häring et al. (2008) analyzed the UBI log to identify the frequency and orientation of the preexisting fractures intersecting the Basel 1 borehole from 2557 m to 5000 m depth. They determined that the dominant natural fracture set strikes NW-SE to NNW-SSE, with steep dips exceeding 60° with fracture density of 0.2–0.3 per meter in the lower part of the well that includes the open hole section. The authors also analyzed the nodal planes and the shear failure criteria, and calculated the optimal fracture orientation should be from 22° to 30° to the orientation of the maximum horizontal stress. The UBI log was also analyzed by Ziegler et al. (2015). They corrected the stick-slip motion of the UBI sonde to get more reliable dip angles for the natural fractures. They found that the fracture sets with different orientations dominated in specific wellbore intervals. However, one fracture set striking about NNW-SSE existed along the entire imaged borehole especially below 4 km.

Another approach to determine the fracture orientation was done by analyzing the waveforms of the seismic events observed during the hydraulic stimulation. Deichmann et al. (2014) analyzed the waveforms of the seismic events with magnitude $0.7 \leq M_L \leq 3.4$ recorded during the hydraulic stimulation to define the structures of the fractures that were stimulated during the hydraulic stimulation by conducting cluster analysis of the locations and focal mechanism solutions. The authors suggested that the N–S striking fault-plane suggested by Häring et al. (2008) was more of the activation of the E–W striking fault-plane. The authors stated that the strike and dip of the identified fractures deviated from the NNW-SSW orientation of the overall microseismic cloud.

The studies conducted to investigate the stimulation mechanism at Basel 1 EGS reservoir support that the stimulation was mainly through a fracture set with one dominant orientation. For example, Jung (2013) suggested that the stimulation mechanism at the EGS project in Basel occurred with the mixed-mechanism stimulation. The author assumed the wing crack model in which the parallel preexisting fractures were connected by wing cracks. The model fit best when the dominant

preexisting fracture orientation was 10° to the maximum principal stress. Serbeto and Meier (2021) suggested that the fracture network created by the hydraulic stimulation was in the form of en-echelon network by comparing the focal mechanism catalog and the fracture orientations observed by UBI. The authors examined the orientations of the clustered seismicity catalogue to best fit the whole microseismic cloud geometry and showed good agreement between the Riedel shear structures and the nodal plane clusters. Also, Ziegler and Evans (2020) analyzed the microseismic clusters by Monte-Carlo and principal component analyses. Their analysis suggested that the large, stimulated fracture zones in the deep crystalline rock mass below Basel consisted mainly of subparallel or ‘anastomosing’ fractures

Stimulation Mechanisms and the resulting stimulated region

The observed microseismicity cloud indicated the volume of the reservoir that was stimulated by injection. Häring et al. (2008) reported that the microseismicity cloud observed was a steeply dipping lens-shaped structure trending $N155\pm 5^\circ E$. The stimulated reservoir size was about 1 km to the dominant horizontal axis and 1 km to the vertical direction and the estimated stimulated volume was 35 million m^3 . The direction that the microseismicity cloud migrated was slightly deviated from the dominant fracture orientation of $N166\pm 14^\circ E$. The stimulated region grew in a direction slightly deviating from the dominant preexisting fracture orientation.

Häring et al. (2008) reported that they observed the improvement of injectivity above 8 MPa and with higher flow rates. Pressure limiting behavior was not observed during the stimulation. These observations support that fluid flowed into preexisting natural fractures intersecting the injection well and no hydraulic fractures propagated from the injection well. Figure 7.1 shows that preexisting natural fractures with the dominant orientation start sliding in shear at the bottomhole pressure around 63.5 MPa assuming the coefficient of friction to be 0.6. Above this bottomhole pressure, shear stimulation was supposed to occur and contribute to the reservoir permeability enhancement. At the last step of stimulation before the M_L 2.6 induced earthquake occurred, the well head pressure reached around 29.6 MPa, which was close to the magnitude of the least principal stress at downhole. The magnitude of fluid pressure

needed for a wing crack to propagate from a well-oriented natural fracture can be less than the least principal stress (Abe & Horne, 2019, 2021; Kamali & Ghassemi, 2018; Kamali et al., 2019; Mutlu & Pollard, 2008; Zoback & Lund Snee, 2018). Also, it is suggested that wing cracks play an important role in the mixed-mechanism stimulation because they improve the fracture connectivity and supply much larger storativity and transmissivity than those of preexisting fractures in a reservoir (Abe & Horne, 2019). Therefore, there is a possibility that newly formed wing cracks propagated in the reservoir during the stimulation.

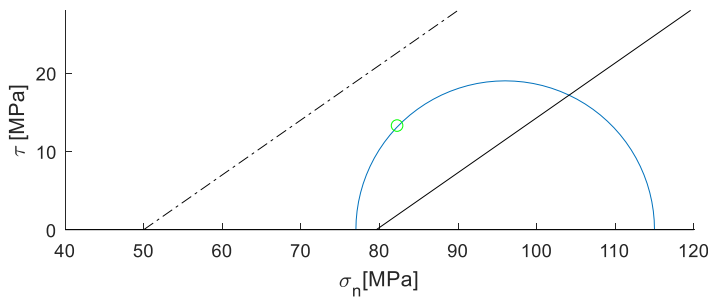


Figure 7.1: Mohr diagram showing the the coefficient of friction 0.6. 1) hydrostatic condition, 2) 79.6MPa, maximum BHP during stimulation

7.2 Simulator Overview

To create a reservoir model, a fracture set was generated from defined distributions of length and orientation. With the mixed-mechanism stimulation assumption, preexisting fractures are from a set generated from one dominant fracture orientation. Preexisting fractures are initially not connected to each other. When a propagating wing crack reaches to a certain defined length, a preexisting fracture is drawn from the fracture set and placed in front of the propagating fracture. The propagating wing crack then crosses or follows the preexisting fracture depending on the result of fracture cross/follow criteria. The fractures are placed not to overlap each other. The detailed procedure for generating discrete fracture network is described in Section 7.3.2.

In Chapter 2, we described how we computed the fracture deformation by complementarity formulation. Complementarity formulation has a huge advantage in

computing more accurate displacements of nonplanar fractures. One drawback of using complementarity formulation is its high computational cost. Because an iterative method is used to solve the complementarity formulation, the overall computational cost becomes high as the number of boundary elements increases which makes the formulation less suitable for a reservoir scale simulation.

In this study, the flow equations and DDM are solved by fully implicit sequential strategy (Kim et al. 2011; McClure 2012; Norbeck 2016). Flow equation and DDM formulations are coupled by following McClure (2012) without complementarity formulation so that the reservoir scale simulation becomes computationally reasonable while computing shear sliding under compression and curved fracture propagation and deformation at reasonable accuracy. The model verification is described in Section 2.9.4.

Inside an iteration within a time step, the flow equation and DDM for normal displacements are solved first, the DDM for shear displacements are then solved considering the Coulomb criterion. The flow equation for p_f and the DDM for D_n with D_s at the previous iteration are solved by the residual equations as:

$$R_{p_f} = \nabla \cdot (q_{flux}) + s_a - \frac{\partial(\rho E)}{\partial t}, \quad (7.3)$$

$$R_{D_n} = \sigma_n^r + P_f + A_{nn}' D_n + A_{ns} D_s^{v-1}, \quad (7.4)$$

where R_{p_f} is the residual equation for fluid pressure, R_{D_n} is the residual equation for normal displacement, ρ is the fluid density, t is time, q_{flux} is the mass flow rate per cross sectional area of flow, E is the aperture, and s_a is a source term (mass per time) such as well injection or production (Aziz & Settari, 1979), σ_n^r is the normal component of remote stress, P_f is the fluid pressure between fracture surfaces, A_{nn}' and A_{ns} are the coefficient of influence from the DDM formulation, D_s^{v-1} is the value calculated at the previous iteration (Crouch & Starfield, 1983). The DDM allows two fracture surfaces overlapping each other with compressive normal stress, which is not physically appropriate (Crouch & Starfield, 1983). To correct the overlapping elements, A_{nn}' is modified from A_{nn} not to incorporate the stresses induced by an overlapping

element. If the k-th element has overlapping $D_n^k < 0$ as a result of DDM solution, the coefficient of influence A_{nn} is modified as:

$$A_{nn}^{ij'} = A_{nn}^{ij} \quad (i \neq k \text{ and } j \neq k), \quad (7.5)$$

$$A_{nn}^{ij'} = 0 \quad (i = k \text{ or } j = k). \quad (7.6)$$

After solving for fluid pressure and normal displacements, the simulator solves the DDM for D_s with the fixed fluid pressure p_f^v and the normal displacement D_n^v at the current iteration considering the Coulomb criterion. If the k-th element has overlapping $D_n^k < 0$ as a result of DDM solution, the coefficient of influence A_{sn} is modified as:

$$A_{sn}^{ij'} = A_{sn}^{ij} \quad (i \neq k \text{ and } j \neq k), \quad (7.7)$$

$$A_{sn}^{ij'} = 0 \quad (i = k \text{ or } j = k). \quad (7.8)$$

If the k-th element has opening displacement $D_n^k > 0$, the residual vector for shear displacement is:

$$R_{D_s} = \sigma_s^r + A'_{sn} + A_{ss}D_s = 0. \quad (7.9)$$

If the k-th element is closed $D_n^k = 0$ or overlapping $D_n^k < 0$, D_n^k is corrected as $D_n^k = 0$. When the shear stress acting on the element is larger than the frictional strength $|\sigma_s^f| \geq -f\sigma'_n + S_f$, the element slides. The residual vector for shear displacement of a sliding element is:

$$R_{D_s} = \sigma_s^r + A'_{sn} + A_{ss}D_s - \left| -f\sigma'_n + S_f \right|. \quad (7.10)$$

When the shear stress acting on the element is larger than the frictional strength $|\sigma_s^f| \leq -f\sigma'_n + S_f$, the element is in the stick condition. In this case, shear displacement will not change in the current iteration, therefore, the equations for sticking elements are not included in the residual vector and the Jacobian matrix. Finally, the computation proceeds to the next time step after the convergence of p_f , D_n , and D_s .

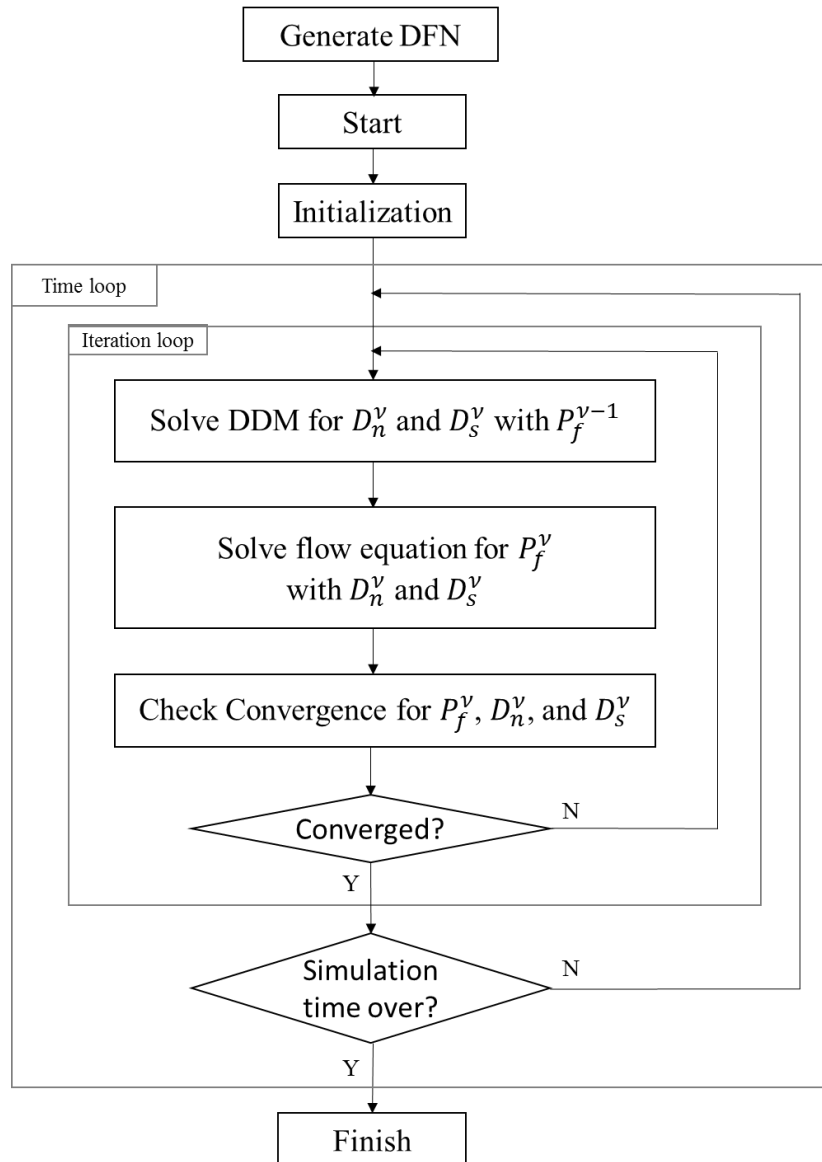


Figure 7.2: Flow chart for this numerical simulation. Superscript v is the number of iterations in the current time step. The variable with superscript v means the value is the one calculated from the current iteration. The variable with superscript $v-1$ means the value is the one calculated from the previous iteration.

7.3 Investigation on Fracture Network Creation and Stimulation Mechanism of Basel-1 and Fenton Hill Phase-2 EGS Reservoirs

The objective of this study was to investigate the mixed-mechanism stimulation with the injection rate, stress state, fracture orientation, and other field scale data from the actual EGS projects. To better understand the stimulation region growth in the past EGS projects, we modeled the reservoir and hydraulic stimulation treatment by using the data sets extracted from literature and compared the numerical results with the observed BHP and microseismic cloud in the actual EGS projects.

7.3.1 Initial conditions, boundary conditions, and assumptions

The reservoir we modeled is a full-space, horizontal, isotropic, and homogeneous two-dimensional domain with vertical fractures assuming the plane-strain condition. Initially, the preexisting natural fractures do not have deformations. Natural fractures created by a tension field a long time ago often do not have either normal or shear displacements based on the field observation. Matrix rock permeability is negligible. The orientation of remote stresses is uniform. The boundary condition of the injection well is specified as a constant-rate mass flow rate. In this study, we did not consider heat transfer and thermoelasticity. These assumptions are sufficient because the dominant fracture orientations is almost vertical (Deichmann et al. 2014; Brown, 1989), and the reservoir is located in the granitic basement in both EGS sites (Håring et al., 2008). In the model, matrix rock permeability is negligible and no leak-off from fractures occurs because observed reservoir rock permeability was very low and the flow regime indicates that the fluid flow was dominated by a few fractures (Håring et al., 2008; Brown et al., 2012). Preexisting natural fractures in the modeled reservoir consist of one dominant orientation.

7.3.2 Discrete Fracture Network (DFN) Stochastic Generation

Discrete Fracture Network (DFN) stochastic generation is widely used to model a fracture network in a reservoir. The fracture properties such as fracture size, orientation, location, density, transmissibility, aperture, etc., are generated uniformly or stochastically to represent the realistic geometry of fractures and the reservoir

properties. (e.g. Finnila et al., 2019; Xing et al., 2021). Having a DFN as realistic as possible is necessary to acquire realistic modeling results for fluid flow, heat extraction, and microseismicity. The fracture models and used statistics are defined by the observations of the area of interest. Subsurface measurements such as the state of stress, injectivity, observation of microseismicity, wellbore imaging logs, and core samples are used to estimate fracture properties. Outcrop fracture information is also used to characterize fracture network geometry in a reservoir. The advantages of utilizing outcrop observations are that the fractures and their network are characterized in two dimension, and the information of fracture size, aperture, connectivity, and density are acquired, which are hard to understand from wellbore one-dimensional datasets or indirect subsurface observations (e.g. Bruna et al. 2019; National Research Council 1996; Pollard & Aydin 1988; Wu & Pollard 2002).

Fracture size distributions are known to follow a certain distribution (Aydin & Zhong, 2018). The power-law distribution is widely observed in outcrop data collection on granitic rocks such as the observation by Segall and Pollard (1983) from granitic rocks of the central Sierra Nevada Mountains, California. Also Barton and Larsen (1985) observed log-normal distribution of fracture lengths from the three pavements of tuffaceous volcanic ash of Yucca Mountain, Nevada. The development of fracture size distributions was well studied by laboratory experiments by Wu and Pollard (1992). The authors investigated the effect of uniaxial strain cycling on the development of a fracture set on PMMA sheets covered with a thin brittle coating. They showed that as the number of strain cycles increased from early stage, through intermediate stage, and to advanced stage, the fracture length distribution changes from power-law, through log-normal, and then to normal distribution. The stage of strain cycles is known as the saturation stage that represents the maturity of the fracture set.

7.3.2.1 DFN in Fenton Hill Phase-2 Reservoir

In this study, we generated a DFN based on the estimation of dominant fracture orientation by Norbeck et al. (2018). The authors estimated the dominant fracture orientation of natural fractures as N23°W based on the fracture opening pressure and the state of stress in the reservoir. The natural fractures were estimated to be near vertical

(Barton et al., 1988; Brown, 1989). The domain is two-dimensional perpendicular to the gravity assuming plane strain condition. The distribution of fracture sizes, orientations, and spacing are not known in the field. The length distribution of the fracture set at Fenton Hill Phase-2 reservoir was generated with a power-law distribution because we assumed that the reservoir was not mature as the initial permeability and the fracture density of the reservoir were low. The form of the length distribution here was $Y = X^{0.55}$ with the minimum length of 20 m and the maximum length of 200 m. Fracture orientation distribution followed the normal distributions.

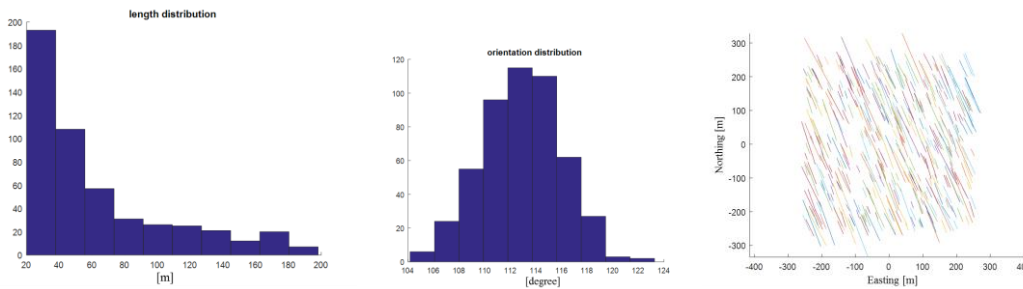


Figure.7.3: Left: Fracture length distribution, Center: Fracture orientation distribution, Right: An illustration of a realization of initial natural fracture geometry used in the simulation.

7.3.2.2 DFN in Basel EGS Reservoir

We generated a DFN based on the estimation of dominant fracture orientation of N166°E. Although Deichmann et al. (2014) suggested that the fracture orientations identified from the seismic events were rather E-W striking fractures, we employed the observation that the dominant fracture orientation was striking N166±14°E with steep dips exceeding 60° as observed with UBI log calculated by assuming a reasonable frictional coefficient (Häring et al., 2008; Ziegler et al., 2015). It may be too simplified to assume the single dominant fracture orientation as it was also suggested that there were clusters of fractures with varied orientations that deviated from the overall microseismic cloud orientation of NNW–SSE (Deichmann et al., 2014). However, we assumed that the preexisting fractures in the reservoir were from one fracture set with a single dominant orientation. It is highly likely that the aperture and the transmissibility of this fracture set is larger than the other sets of fractures. The orientation of this

fracture set was under the normal stress close to the least principal stress. Fluid flows preferably to the higher permeable paths, therefore, the fluid was likely to flow into this fracture set. Also, Ziegler and Evans (2020) analyzed the microseismic clusters by Monte-Carlo and principal component analyses. Their analysis suggested that the large, stimulated fracture zones in the deep crystalline rock mass below Basel consisted mainly of subparallel or anastomosing fractures.

We generated the fracture set stochastically because the distribution of fracture sizes, orientations, and spacing are not known in the field. The length distribution of the fracture set at Basel reservoir was generated with a power-law distribution because we assumed that the reservoir was not mature as the initial permeability and the fracture density of the reservoir were low. The form of the length distribution here is $Y = X^{0.55}$ with the minimum length of 50 m and the maximum length of 500 m. Fracture orientation followed the normal distribution.

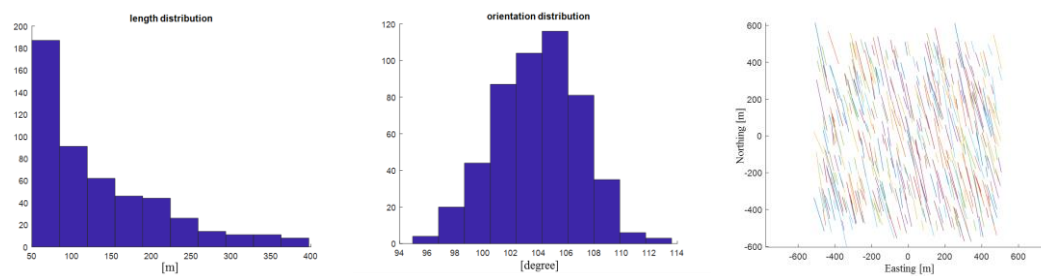


Figure 7.4: Left: Fracture length distribution, Center: Fracture orientation distribution, Right: An illustration of a realization of initial natural fracture geometry used in the simulation.

7.3.3 Choosing an Aperture Model

Choosing right parameters for an aperture model to accurately analyze the fracture transmissivity and injectivity transition is necessary to model shear stimulation in an actual EGS reservoir. In this study, we used the empirical model that describes the apertures as a function of effective normal stress and shear displacements by Willis-Richards et al. (1996) and used the parameters that best fit the observed injectivity transition.

7.3.3.1 Fenton Hill EGS Phase-2 Reservoir

To decide an aperture model for this study, by following Brown et al. (2012), 5.37kg/s was injected to a single fracture with stress state and fracture orientation that are following Table 7.1 to decide the fracture aperture model. With an aperture model with shear stimulation (dilation angle 2 degrees), the fracture transmissibility started improving with shear displacements which occurred around 45 MPa, which is much lower than the observed wellbore fluid pressure. With an aperture model without shear dilation, the fracture transmissibility improves around 70 MPa, which is the pressure necessary to open the fracture. This is close to the observed wellbore fluid pressure.

Norbeck et al. (2018) did an analysis to investigate the stimulation mechanism at the Fenton Hill Phase-2 reservoir. The authors reproduced the reversible behavior of injectivity observed during each hydraulic stimulation at the injection well (Brown, 1989) by setting the shear dilation angle 0 degrees. We reconfirmed that the shear stimulation was not one of the permeability enhancement mechanisms in Fenton Hill EGS Phase-2 reservoir case as Norbeck et al. (2018) suggested and used the shear dilation angle 0 degrees.

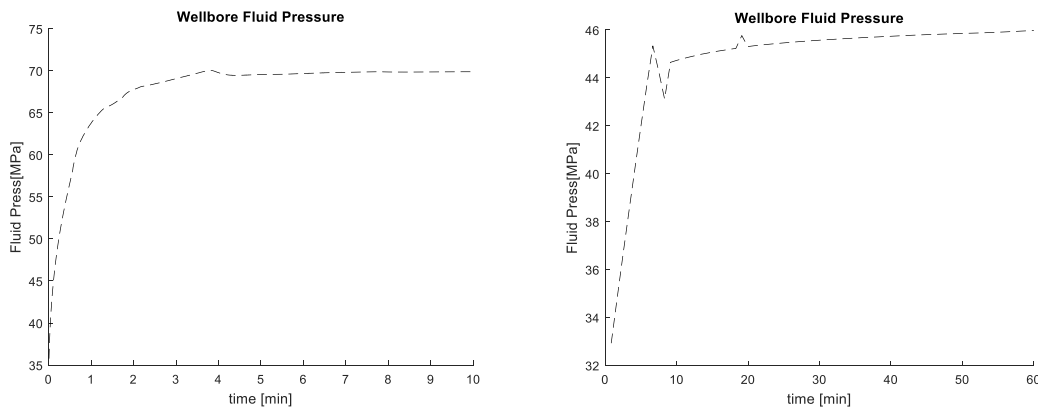


Figure 7.5: Wellbore fluid pressure. Left: with shear dilation angle of 0 degree, Right: with shear dilation angle of 2 degrees.

7.3.3.2 Basel EGS Reservoir

The aperture model used to model Basel reservoir was decided based on the observation of Häring et al. (2008). The fact that they observed improvement of injectivity above 80 bar with higher flow rates, the irregular wellhead pressure curve, and no pressure-limiting behavior, indicates that the near wellbore fracture transmissivity enhancement occurred mainly by shear stimulation. Figure 7.1 shows that fractures with the dominant orientation can start sliding when the WHP exceeds around 10MPa. By following Häring et al. (2008), 100 l/min was injected to a single fracture with stress state and fracture orientation following Table 7.2 to decide the fracture aperture model for this study.

With an aperture model with no shear stimulation (dilation angle 0), the wellbore pressure increased up to the magnitude of the minimum horizontal stress. The fracture then opened as the effective normal stress became tension, then the fracture transmissibility improved and the wellbore fluid pressure stabilized at the fracture opening pressure. On the other hand, with an aperture model with shear dilation (dilation angle 2), the wellbore pressure increased to the magnitude that made the fracture slip, the fracture transmissibility then improved and the wellbore fluid pressure stabilized. Therefore, in the Basel EGS case, shear stimulation is one of the near-wellbore permeability enhancement mechanisms.

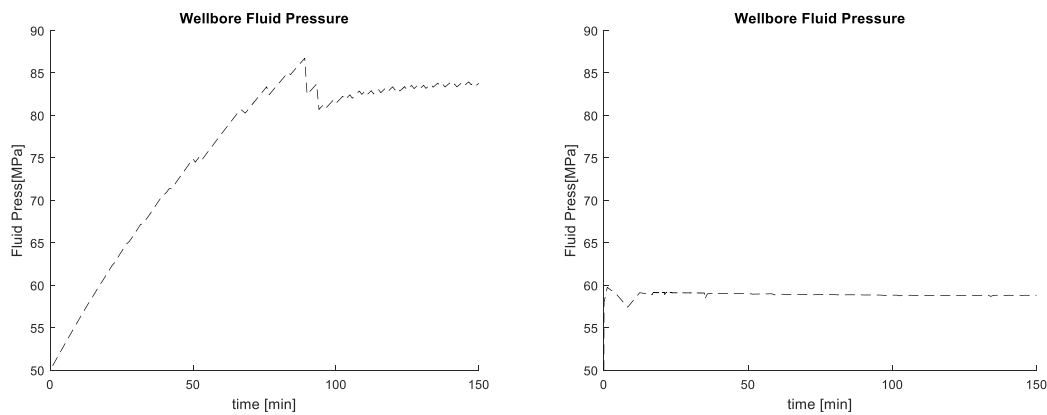


Figure 7.6: Wellbore fluid pressure. Left: with shear dilation angle of 0 degree, Right: with shear dilation angle of 2 degrees.

7.3.4 Analysis of the Fracture Cross/Follow Criteria in Fenton Hill Phase-2 Reservoir

We analyzed if a newly formed fracture propagating in the reservoir crosses or follows an intersecting preexisting natural fracture in Fenton Hill Phase-2 reservoir. We used the interpretation of the fracture orientation and the stress state that the dominant natural fracture orientation was N23°W (Norbeck et al., 2018) and the orientation of the maximum horizontal stress was N30°E (Barton, et al., 1988). We assumed that wing cracks, which propagated during the stimulation, propagated perpendicular to the least horizontal stress. Based on those assumptions, the intersection angles between a propagating wing crack and a preexisting natural fracture are 53° and 233° counterclockwise from the propagating direction. The combination of K_I and K_{II} satisfies the propagation criteria with $K_{IC} = 1.5MPa\sqrt{m}$ and $T_0 = 10.0MPa$. Only left-lateral shear displacement was considered because wing cracks have only left-lateral shear component in this setting.

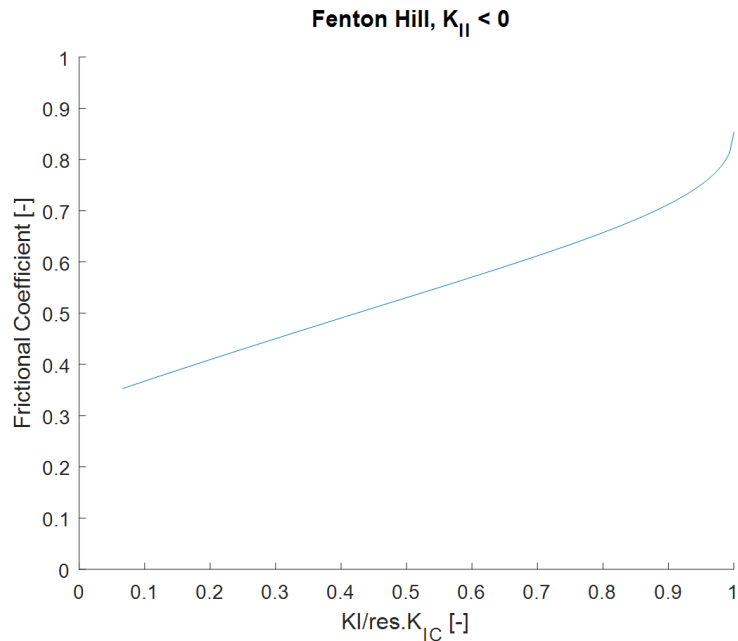


Figure 7.7: The propagating fracture cross/follow criteria with left-lateral shear displacement ($K_{II} < 0$). The area above the blue line shows the condition where a propagating fracture crosses a preexisting natural fracture intersecting with 53 degrees.

Figure 7.7 shows the propagating fracture cross/follow criteria with varied combinations of K_I and K_{II} . Following Renshaw and Pollard (1995), a propagating wing crack crosses the intersecting preexisting natural fracture when the natural fracture does not open or slide due to the induced stress field by the propagating wing crack. Assuming the friction coefficient of 0.6 to 0.7, the propagating wing crack may cross the preexisting fracture if the wing crack has reasonable magnitude of shear displacements in the left-lateral direction. With a propagating wing crack with the right-lateral shear displacements, the induced stress field makes the preexisting fracture open or slide, therefore, it is unlikely that the propagating wing crack crosses the intersecting preexisting fracture.

7.3.5 Analysis of the Fracture Cross/Follow Criteria in Basel EGS Reservoir

We analyzed if a newly formed fracture propagating in the reservoir crosses or follows the preexisting natural fractures in the Basel EGS reservoir. Based on the interpretations of the dominant fracture orientation, the intersection angles between a propagating wing crack and a preexisting natural fracture are 22° and 202° counterclockwise from the propagating direction. The combination of K_I and K_{II} satisfies the propagation criteria with $K_{IC} = 1.5MPa\sqrt{m}$ and $T_0 = 10.0MPa$. Only right-lateral shear displacement is considered because wing cracks have only right-lateral shear component in this setting.

Figure 7.8 shows the propagating fracture cross/follow criteria with varied combinations of K_I and K_{II} . With strong shear displacements and friction coefficient, crossing may occur, but by assuming $f = 0.6 - 0.7$, no crossing occurs.

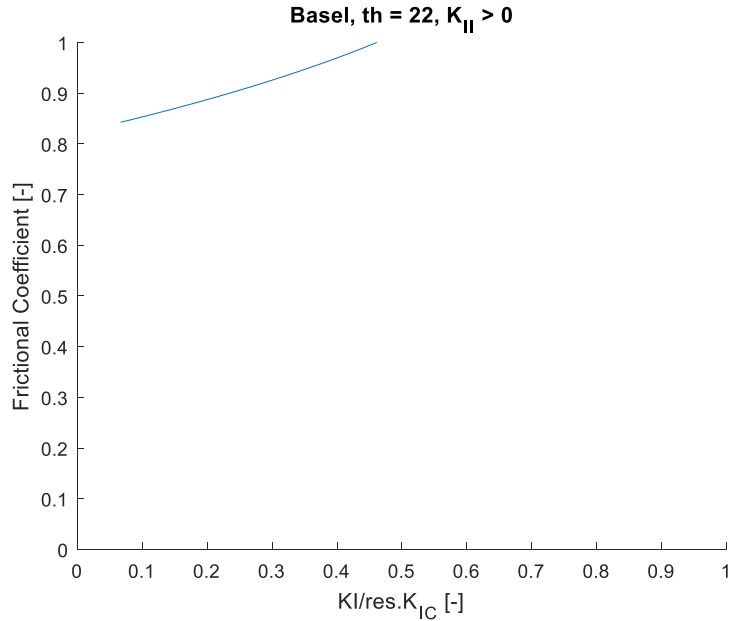


Figure 7.8: The propagating fracture cross/follow criteria with right-lateral shear displacement ($K_{II} > 0$). The area above the blue line shows the condition where a propagating fracture crosses a preexisting natural fracture intersecting with 22° .

7.3.6 Model parameters

Elastic properties of the matrix rock for both Fenton Hill and Basel EGS reservoir models are based on an interpretation of the measurement data performed on a core sample of the Basel monzogranite core taken from the wellbore (Valley and Evans, 2019) because there were no measurements done for the rock properties at Fenton Hill. The fractures have a constant friction coefficient of $f = 0.6$. Fracture mesh size, matrix rock properties, and fluid properties are common for both Fenton Hill and Basel reservoir models (Table 7.3).

For the Fenton Hill EGS reservoir model, we used the interpretation of fracture orientation and state of stress by Norbeck et al., (2018) (Table 7.1). The magnitude of the maximum and the minimum horizontal stresses at the depth of 3.6 km where hydraulic stimulation was performed are 90 MPa and 46 MPa respectively. The initial reservoir fluid pressure was 36 MPa.

Table 7.1: Parameters used for Fenton Hill setting

Parameter	Value	Unit
Dominant preexisting fracture orientation	N23°W	-
Maximum horizontal stress	90	MPa
Maximum horizontal stress orientation	N30°E	-
Minimum horizontal stress	46	MPa
Fracture height	200	m
Reference hydraulic aperture	1.0e-4	m
Reference effective normal stress	25	MPa
Dilation angle	0	degree
Initial fluid pressure	36	MPa

For the Basel EGS reservoir model, we used the interpretation of fracture orientation by Häring et al. (2008) and Ziegler et al. (2015), stress orientations by Häring et al. (2008) and Valley and Evans (2009), and state of stress by Valley and Evans, (2019) (Table 7.2). The magnitude of the maximum and the minimum horizontal stresses at the depth of 5.0 km where hydraulic stimulation was performed were 115 MPa and 77 MPa respectively. The initial reservoir fluid pressure was 50 MPa.

Table 7.2: Parameters used for Basel setting

Parameter	Value	Unit
Dominant preexisting fracture orientation	N166°E	-
Maximum horizontal stress	115	MPa
Maximum horizontal stress orientation	N144°E	-

Minimum horizontal stress	77	MPa
Minimum horizontal stress orientation	N54°E	-
Fracture height	200	m
Reference hydraulic aperture	1.0e-4	m
Reference effective normal stress	25	MPa
Dilation angle	2	degree
Initial fluid pressure	50	MPa

Table 7.3: Parameters used in the numerical simulation for both Fenton Hill and Basel settings

Parameters	Value	Unit
Main fracture grid length	1.0	m
Wing crack grid length	1.22e-2	m
Young's modulus	65	GPa
Poisson's ratio	0.22	-
Critical stress intensity factor	0.39	MPa \sqrt{m}
Water density	920	kg/m ³
Water viscosity	1.0e-3	Pa.s
Fracture static frictional coefficient	0.6	-
Fracture dynamic frictional coefficient	0.6	-
Frictional strength	0.0	MPa

The boundary condition at the injection well was specified as a constant mass flow rate. The injection rates were extracted from Brown et al. (2012) for Fenton Hill Phase-2 EGS reservoir case and for Basel EGS reservoir case from Häring et al. (2008).

The injection schedules were modified from the actual schedule because of the limitations of our numerical model. Our model does not consider matrix rock permeability and the number of fractures is limited. Therefore, the stimulated volume may be overestimated by the same injected fluid. We used the same injection rate steps but the injection time was reduced to $\frac{1}{4}$ to avoid the overestimated stimulated volume.

7.4 Results

We assumed the mixed-mechanism stimulation for both Fenton Hill Phase-2 reservoir and Basel EGS reservoir in this experiment. With this assumption, the preexisting natural fractures in the reservoir were initially not connected to each other and keep a fracture spacing each other. The preexisting natural fractures were generated from one dominant orientation by following the method described in Section 7.3.2. Our model did not consider fluid leak-off to the matrix rock and the number of fractures included was limited. The fluid storage volume in the model was much smaller than the actual reservoir, therefore, we modified the injection schedule so that the resulting stimulation region was close to the actual size.

7.4.1 Fenton Hill Phase-2 EGS reservoir

For our study, we modeled Experiment 2018 which was the initial testing at well EE-2 for the Phase-2 reservoir. The injection was done for 9.5 hours and no shut-in was done due to the failure of the frac string. The temperature log following the experiment showed that there were three feed zones in the openhole section (Brown et al., 2012).

During the experiment, significant injectivity improvement was observed when the bottomhole pressure exceeded 77 MPa (Figure 7.9). The observed microseismicity cloud extended to the overall N-S direction. The size of the cloud was roughly 400 m to the N-S, 200 m to the E-W directions, and 300 m to the vertical direction (Fig. 6-8 in Brown et al., 2012).

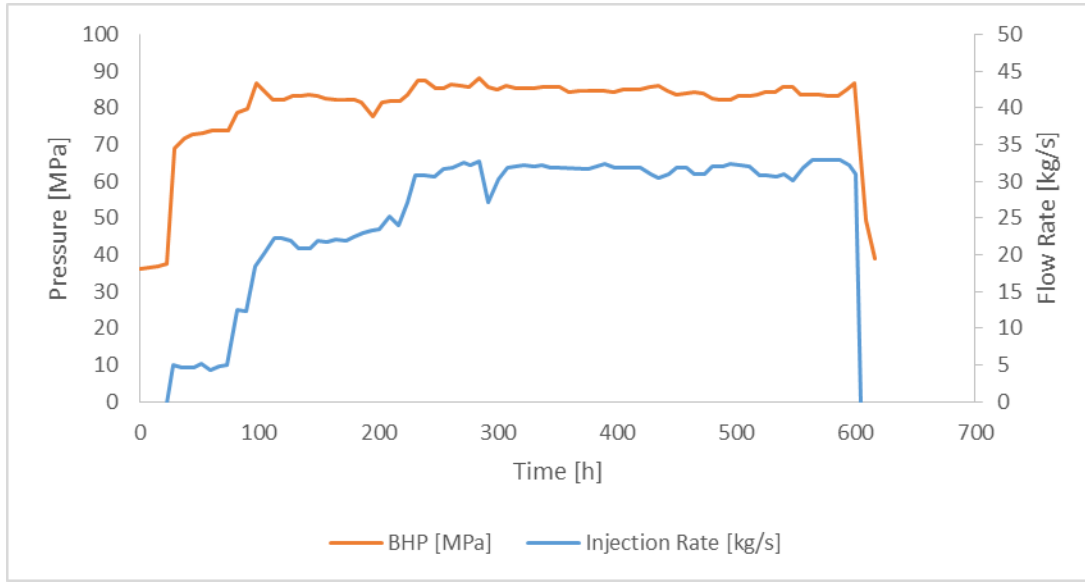


Figure 7.9: Bottomhole pressure at 3.6km depth and injection rate during the Expt. 2018 at well EE-2 (extracted from Fig. 6-5 in Brown et al., 2012)

Figure 7.10 shows the resulting fracture network created by the hydraulic stimulation in this numerical experiment. The overall growth dimension was in the N-S direction, which shows good agreement to the actual observation. Preexisting fractures oriented in the NNW direction while the wing cracks propagated in the NE direction which was perpendicular to the least principal stress. However, the fracture network consists of preexisting fractures and newly propagated wing cracks. Therefore, the stimulation region migrated to the NS direction.

Figure 7.11 shows the fluid pressure in the fracture network. The fluid pressure at the stimulation region front was around the minimum horizontal stress (46 MPa) where wing cracks propagated. The flow paths from the injection well to the stimulation region front had numerous branches. The wellbore pressure showed pressure limiting behavior because: 1) the fluid pressure at the front was constrained by the magnitude of the minimum horizontal stress, and 2) the injectivity and the fracture transmissibility significantly increased when the fluid pressure exceeds the normal stress acting to the natural fracture (Figure 7.12).

Figure 7.12 shows the bottomhole pressure and the injection schedule used in the experiment. The bottomhole pressures modeled show good agreement with the observed pressure. The injectivity improvement was reproduced well by this model. The wellhead pressure showed fluctuation in the actual measurement because friction reducer was injected during the injection. The fluctuation shown in Figure 7.12 was caused by the increase of fluid storage volume when a wing crack propagated and new natural fracture was connected to the fracture network.

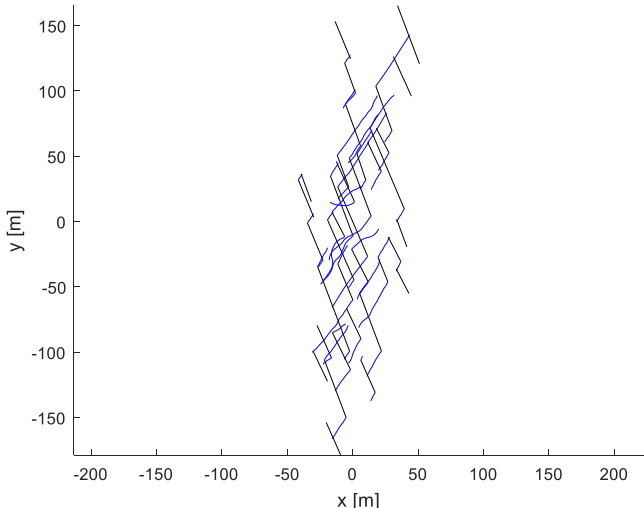


Figure.7.10: Fracture network created during the numerical experiment. The black lines are preexisting fractures and the blue lines are newly formed wing cracks.

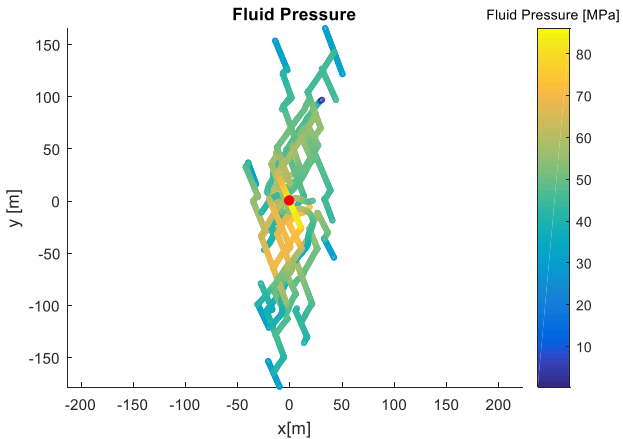


Figure 7.11: Fluid pressure distribution after injection.

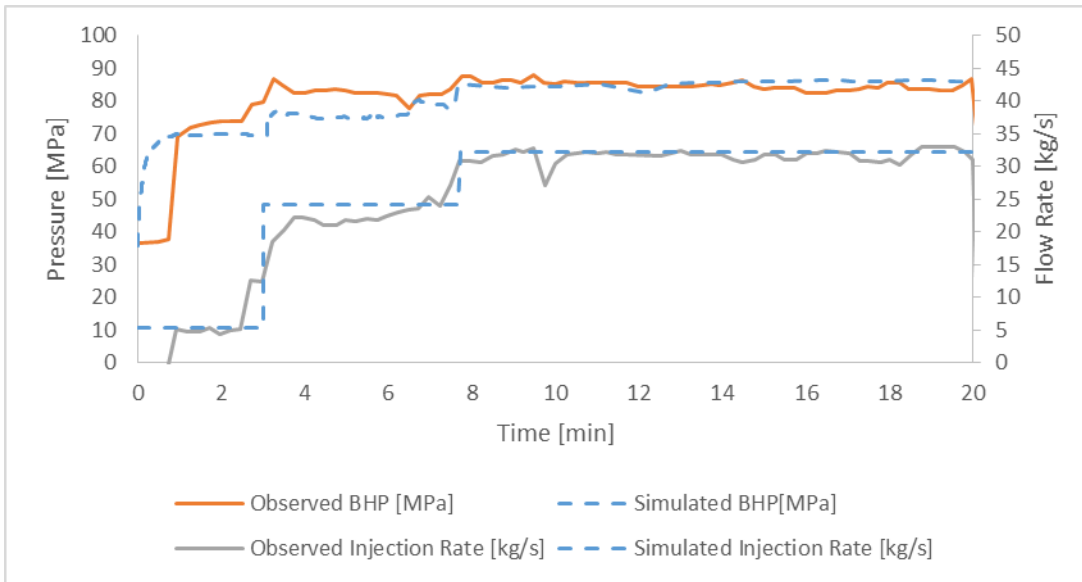


Figure 7.12: Observed and simulated bottomhole pressures and observed and input injection rates.

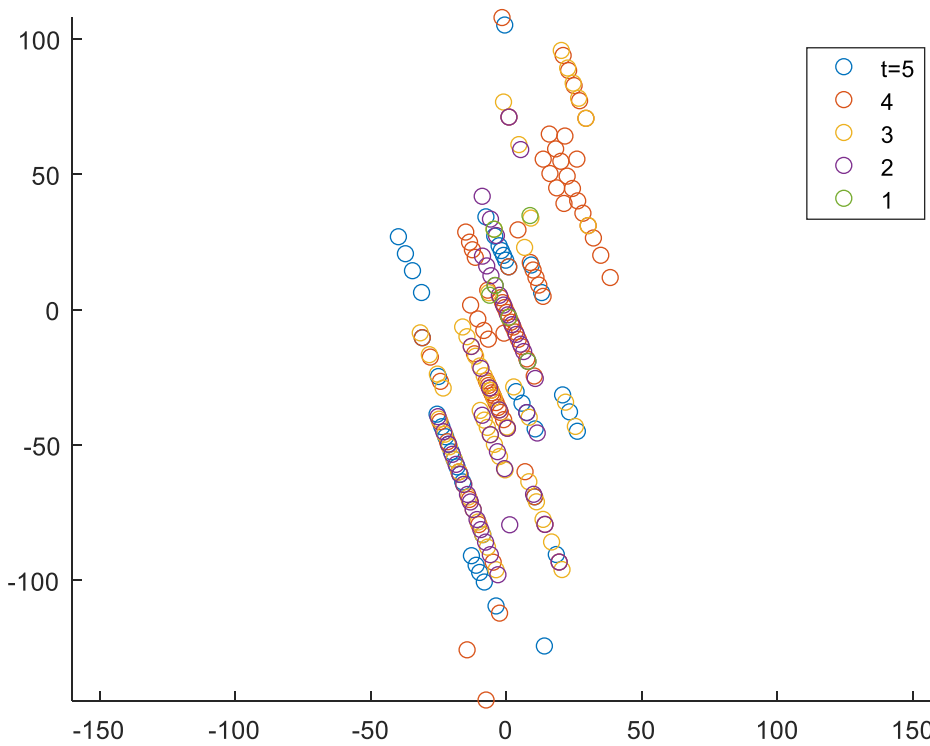


Figure 7.13: Distribution of the microseismicity.

7.4.2 Basel EGS reservoir

The injection was done for 6 days and shut-in and bleed-off followed after injection during the hydraulic stimulation experiment at the Basel EGS site (Figure 7.14). The observed microseismicity cloud formed a thin lens shape extending to the overall NW direction. The size of the cloud was roughly 1000 m to the NW and 1000 m to the depth (Häring et al., 2008).

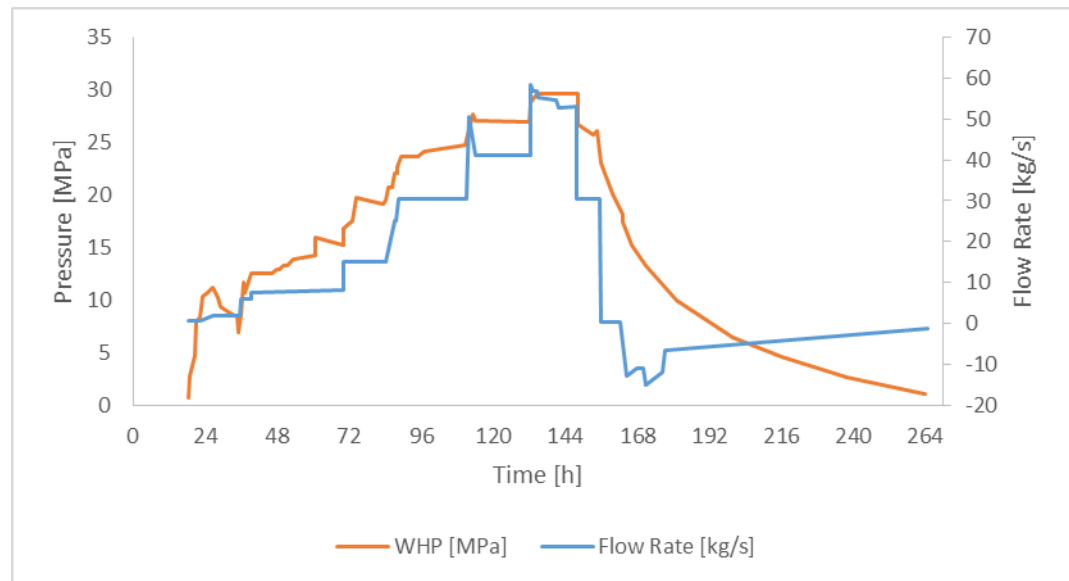


Figure 7.14: Wellhead pressure and injection rate (Häring et al., 2008).

Figure 7.15 shows the resulting fracture network created by the hydraulic stimulation in this numerical experiment. The overall growth dimension was in the NW direction, which shows good agreement to the actual observation. Preexisting fractures oriented at N166°E direction while the wing cracks propagated at N144°E direction which was perpendicular to the minimum horizontal stress. The fracture network consisted of preexisting fractures and newly propagated wing cracks, therefore, the stimulation region migrated to the direction between the dominant preexisting fracture orientation and the wing crack propagation direction.

The pressure gradient inside the fracture network was small (Figure 7.16). This is because the transmissibility of the preexisting fractures was relatively high and

preexisting fractures showed shear stimulation behavior (discussed in Section 7.3.3.2). Additionally, wing cracks had high transmissibility due to their opening displacements (Abe & Horne, 2019). The pressure limiting behavior around 74 MPa reflects the magnitude of the fluid pressure necessary for a wing crack to propagate (Figure 7.17). The wellbore pressure increased up to the pressure necessary to propagate wing cracks at the stimulation region front, then the pressure stabilized due to the increase of the fluid storage volume.

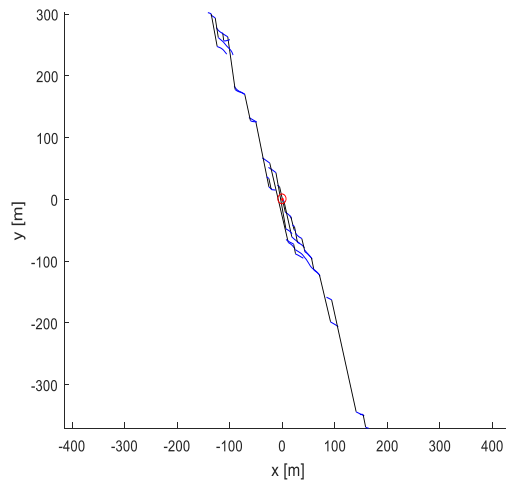


Figure 7.15: Fracture network created during the numerical experiment. The black lines are preexisting fractures and the blue lines are newly formed wing cracks. Red circle shows the injection well location.

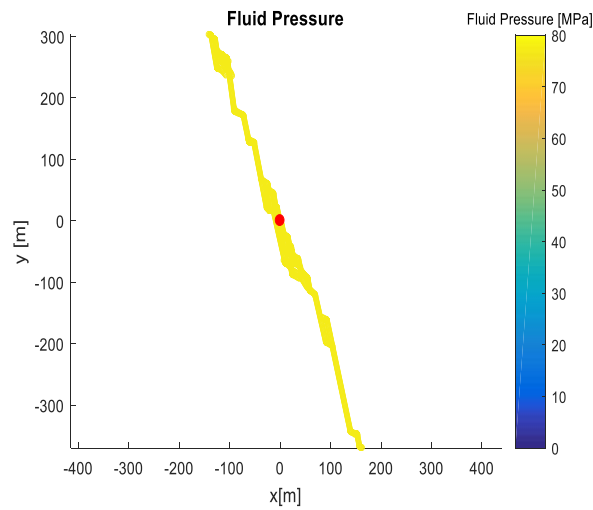


Figure 7.16: Fluid pressure distribution after injection. The red dot shows the injection well location.

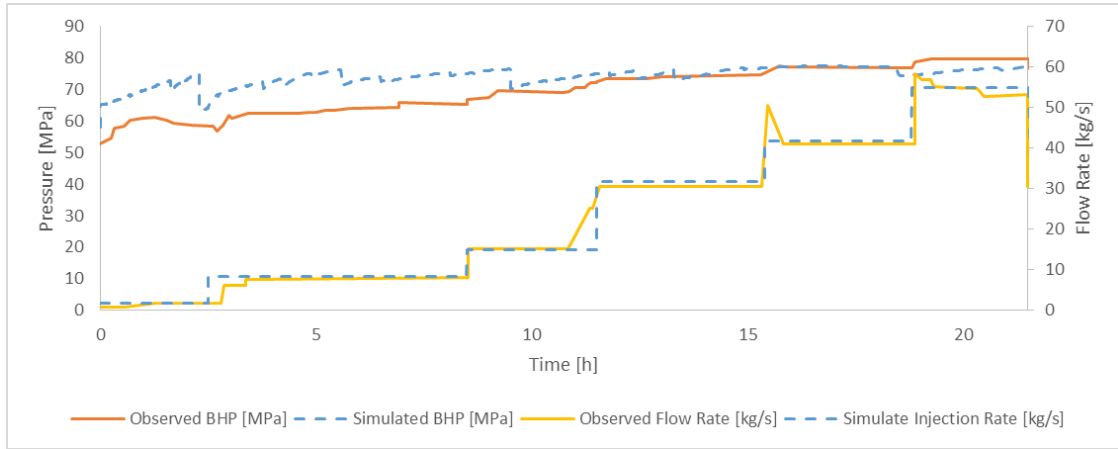


Figure 7.17: The observed and simulated BHP and flow rate. The bottomhole pressure was calculated by adding the hydrostatic pressure at 5km depth and the effect of wellbore friction. The bottomhole pressure was calculated from the wellhead pressure profile including the effect of friction. The effect of pressure loss due to the friction was less than 0.3 MPa.

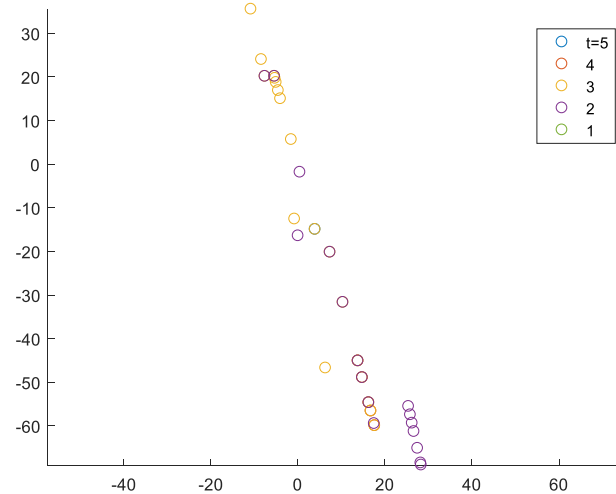


Figure 7.18: Distribution of the microseismicity on the top view.

Although the created fracture network had good match with the dimension of the observed microseismicity cloud, the bottomhole pressure showed higher values and pressure limiting behavior that was not observed during the field experiments. The mixed-mechanism stimulation may not be the main stimulation mechanism that occurred at the early stage at the Basel EGS site. However, this study shows that mixed-

mechanism stimulation could occur when the bottomhole pressure exceeded around 74 MPa, which happened when the injection rate exceeded 1900 l/min during the latter half of the stimulation.

7.4.3 Comparison between Fenton Hill and Basel cases

The created fracture networks in the Fenton Hill Phase-2 reservoir and the Basel EGS site settings showed different features. The network created in the Fenton Hill setting showed a broad shape with more flow paths branching while the network created in the Basel setting showed a narrow shape with rather straight flow paths. The possible causes of these differences are: 1) if a propagating wing crack crosses or follows the intersecting preexisting fracture, 2) the magnitude of the stress state, and 3) the stress shadowing effect.

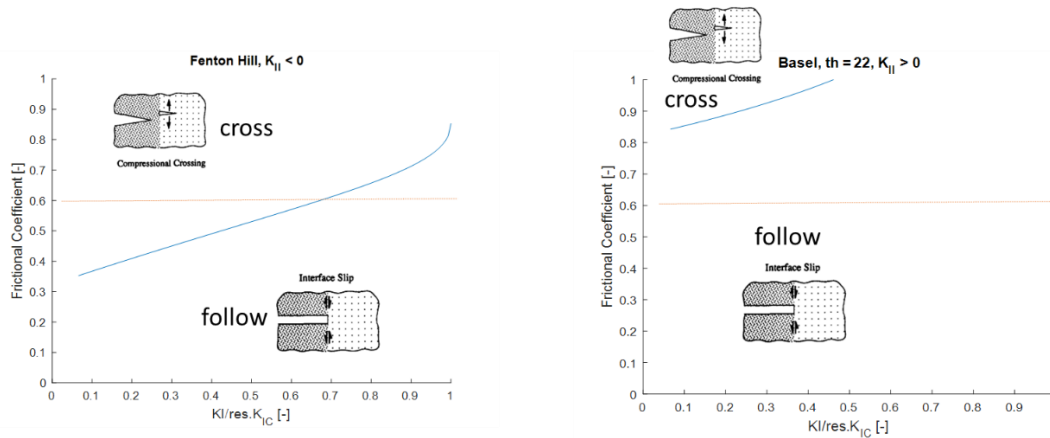


Figure 7.19: Plots showing the criteria of fracture cross/follow in Fenton Hill and Basel settings. The orange line shows the friction coefficient 0.6 used in this study.

The state of stress and the angle between the orientations of the dominant preexisting fracture and the minimum horizontal stress affect if a propagating wing crack crosses or follows the intersecting preexisting fracture (Abe et al., 2019; Gu & Weng, 2010; Gu et al., 2011; Renshaw & Pollard, 1995; Wu & Olson, 2014b). As discussed in Section 2.7, a propagating wing crack may cross the intersecting fracture when the shear component of the propagating fracture tip is sufficiently large in the

Fenton Hill setting. However in the Basel setting, a propagating wing crack may not cross the intersecting fracture in any cases (Figure 7.19). With wing cracks crossing preexisting fractures, the fracture network migrates in the direction of both dominant orientation of preexisting fractures and the maximum horizontal stress, while with wing cracks following preexisting fractures, the migration in the maximum horizontal stress orientation was limited.

In the Fenton Hill setting, wing cracks propagated with the fluid pressure around 46 MPa, which was the magnitude of the minimum horizontal stress. Preexisting fractures showed significant injectivity increase over 75 MPa, which was the fluid pressure necessary to open the preexisting fractures (Brown et al., 2012). Therefore, larger amount of fluid flowed into wing cracks at a fracture intersection because the transmissibility of a wing crack was greater than that of a preexisting fracture at the same fluid pressure. On the other hand, in the Basel setting, wing cracks propagated with the fluid pressure around 77 MPa, and preexisting fracture showed injectivity increase over 65 MPa (Häring et al., 2008). Therefore, larger amount of fluid flowed into preexisting fractures than into wing cracks.

At a fracture intersection, the upstream fracture induces a stress field by its deformation, which affects the transmissibility of each flow path at the intersection (Abe & Horne, 2021; Abe et al., 2021). The transmissibility of a flow path that has larger angle toward the upstream path is higher than that with a smaller angle. In the Basel setting, the angle between a wing crack and a preexisting fracture is around 22 degrees, which is sufficiently small to create a transmissibility difference on each branch. In the Fenton Hill setting, the angle between a wing crack and a preexisting fracture is around 58 degrees, which does not make a significant transmissibility difference on each branch at the intersection.

7.5 Discussion and Summary

This study was done to investigate the possibility of the mixed-mechanism stimulation for past large scale hydraulic stimulation in example EGS reservoirs. The results of this

study suggest that the dimension, migrating orientation, and complexity of a fracture network are controlled by the state of stress, dominant orientation of preexisting fractures and their initial connectivity, and injection rates. The observed stimulation behavior near wellbore such as the reversibility of injectivity and the pressure at which the injectivity increases, needs to be considered to better match the wellbore pressure response in respect to the injection rate.

A Fenton Hill type of reservoir may be good for EGS because the resulting fracture network is likely to have more flow paths branching and longer flow paths, which is able to extract heat effectively from the reservoir. The hypothesis of Fenton Hill's mixed mechanism stimulation and wing crack propagations are promising because the simulated stimulated region growth and bottomhole pressure response show good agreement with the observed microseismicity cloud migration and the measured wellhead pressure. Observed pressure limiting behavior can be explained by the volume increase within the reservoir. Brown et al., (2012) reported that the fluid recovery during venting after each hydraulic stimulation was less than 50% while the fluid recovery during the circulation tests was nearly 90% (Rinaldi & Rutqvist, 2019). The matrix permeability was almost negligible and the reservoir permeability showed reversible behavior because the surfaces of the preexisting fractures were smooth and did not show the shear stimulation behavior, which means that the increase of the storage volume between closed preexisting fractures should be negligible. The preexisting fractures open near the wellbore because the bottomhole pressure exceeded the normal stress acting on the preexisting fractures. Also wing crack propagation supplies volume to store fluid within the reservoir because wing cracks provide high permeability and large volume to store fluid in the reservoir even after the stimulation (Abe & Horne, 2019).

The simulated fracture network created in the Basel EGS site setting formed a straight, less flow path branching as shown in Figure 7.15. The dimension and the migrating directions of the simulated stimulated volume was close to the observed microseismic cloud. However, the simulated bottomhole pressure showed pressure limiting behavior while the actual project did not observe such behavior. The last step of the injection was done at the pressure close to the least principal stress, therefore it is

possible that the mixed-mechanism stimulation occurred at the last stage of the stimulation. One of the possible reasons why the mixed-mechanism stimulation assumption did not reproduce the pressure response in respect to the injection rates was that the connectivity of the preexisting fractures in the actual reservoir could be relatively high and fractures showed strong shear stimulation behavior.

The bottomhole pressure increase was limited at the first stage of injection, meaning the transmissibility of the fractures near the wellbore was relatively high. As injection rate increased at later stages, the bottomhole pressure started to rise close to the magnitude of the least principal stress. Mukuhira et al., (2017) analyzed the fluid pressure that induced shear sliding of preexisting fractures in the reservoir. Their analysis suggests that the pressure gradient between the wellbore and the stimulation front was around 20 MPa. The numerical model used in this study did not reproduce the pressure gradient well. Therefore, the stimulation mechanism at the Basel EGS site was not conclusive, however it is highly possible that the mixed-mechanism stimulation occurred at the later stages of the hydraulic stimulation treatment.

One of the implications of this study is that stimulating a reservoir with poorly oriented preexisting fractures may make a complex and broad shaped fracture network because: 1) the orientation between preexisting fractures and wing cracks is optimal, 2) there is higher chance that a propagating fracture crosses an intersecting preexisting fracture, 3) bottomhole pressure is likely to be higher than the least principal stress. Stimulating a poorly oriented fracture may cost more and injecting fluid at a higher pressure is known to be a risk for injection-induced earthquakes. However, bottomhole pressure exceeded the least principal stress in most of the past EGS projects (McClure, 2014), and injecting at lower pressure than the least principal stress does not guarantee to prevent felt injection-induced earthquakes. Mitigating the risk of injection-induced earthquakes while achieving better reservoir stimulation will remain a key research question for EGS.

Chapter 8

8 Conclusion

8.1 Summary

In this thesis, we described our approach including laboratory experiments and numerical simulations to better understand fracture network creation in a low permeability reservoir, especially in an EGS reservoir where large preexisting fractures dominate. The physics-based numerical model developed in this work is described in Chapter 2. The numerical model was used to investigate fracture network creation in a small scale area including small number of fractures to a reservoir scale with tens of fractures. The numerical simulator can model fracture network creation by incorporating mechanical interaction between fractures and how the deformation of upstream fracture affects the fluid flow and the deformation of downstream fracture. Laboratory experiments showed how preexisting fractures and newly formed fractures interact with each other by performing hydraulic fracturing to a cement sample and a 3D printed material.

In Chapter 3, we investigated how a wing crack contributes to reservoir permeability enhancement and the increase of reservoir storativity by modeling a single preexisting fracture initiating wing cracks from its tips. The results indicate that a wing crack keeps its opening displacement even after the fluid pressure decreases after the hydraulic stimulation treatment concludes. Therefore, wing cracks enhance permeability and storativity after stimulation treatment. Chapters 4 and 5 describe laboratory hydraulic fracturing experiments that were performed with cement core samples and 3D printed core samples. The results were compared with numerical results for fracture propagation patterns. In Chapter 4, we reviewed past laboratory experiments

of propagating fracture crossed or followed preexisting fracture and compared our fracture cross/follow criteria. We also explored the possibility of using 3D printer for investigating geomechanical problems such as hydraulic fracturing. In Chapter 5, cement core samples including an embedded preexisting fracture were fractured by water injection. We cut the samples and observed the fracture network patterns including a hydraulic fracture that propagated from the injection point, the embedded preexisting fracture, and a wing crack that had propagated from the tip of the preexisting fracture. We reproduced the same pattern with the numerical model and analyzed the anisotropic stress distribution along the preexisting fracture. The result showed that the stress shadowing effect from the upstream fracture affects the deformation pattern of the intersecting downstream fracture, which affects the overall network pattern because fluid flows into the more preferable path that has higher permeability.

In Chapter 6, detailed numerical investigation on mechanical interaction between newly formed and preexisting fractures was described. The numerical experiments investigated the effect of fracture orientations, stress state, and injection rates on the overall fracture network. The implication from the results of this study to make a better EGS reservoir would be to stimulate an EGS reservoir with: 1) well-oriented fractures, 2) a high stress ratio, and 3) a low injection rate. These reservoir conditions and stimulation design will likely make more flow paths and create a more beneficially complex fracture network. In Chapter 7, we investigated the stimulation mechanisms at the Fenton Hill Phase-2 reservoir and the Basel EGS project with our numerical model. The results showed that a Fenton Hill type reservoir made a more complex fracture network with broad shape while a Basel type reservoir made more of a straight fracture network. Throughout these studies, we investigated the stimulation mechanisms in an EGS reservoir with numerical and laboratory experimental approach and applied the understanding to analyze field scale experiments. Our research still has remaining unanswered research questions. We will explain those possible future research topics in the following section.

8.2 Recommendations for Future Work

In our work, we focused on numerical simulation to understand mechanical interaction between fractures to better understand fracture network creation by hydraulic stimulation. There are unanswered research questions that could extend the presented research in the future.

To understand fracture network creation in the mixed-mechanism stimulation, whether a propagating fracture crosses or follows another fracture plays an important role. We applied the fracture cross/follow criteria for a wing crack, which has both Mode I and II displacements, and analyzed the conditions in which a propagating wing crack crosses/follows a preexisting fracture. The limitations of these analyses are that the domain is two-dimensional with fractures of the same height, and preexisting fractures are assumed to be not cemented. In our study, we observed that a part of the propagating hydraulic fracture bypassed an intersecting preexisting fracture. A bypassing hydraulic fracture was investigated by Fu et al. (2015) numerically, and a hydraulic fracture crossing a partially cemented fracture by Fu et al. (2016) experimentally. Bypassing a fracture occurs when the height of a propagating fracture is larger than the preexisting fracture. A propagating fracture can cross another fracture when they are cemented and the properties of the cement and the matrix rock satisfy certain criteria. The model could be extended in three dimensions or include different type of materials in a domain with other numerical methods such as FEM or DEM.

We simplified the fracture sliding by assuming that the friction coefficient was constant (in Chapter 3, we used different constant values for static and dynamic friction coefficients). This made the fracture slip aseismic. To better analyze the microseismicity or injection-induced earthquake, the friction coefficients need to be considered to be able to model seismicity such as rate-and-state friction. Considering more accurate seismicity will enable analysis of the stimulation region growth with observed microseismicity and larger injection-induced earthquakes. Heat transfer and leak-off to the matrix rock can be included to better understand the stimulation mechanism. Thermal contraction, leak-off, and pore pressure increase in the rock around fractures affect fracture transmissibility and wellbore pressure response. The main approach of

this work was numerical modeling. Results from numerical modeling can be interpreted effectively by comparing the observable data from actual fields or experiments. Therefore extending the current research to be able to model observable data such as tracer tests, thermal breakthrough, and wellbore pressure transients, will be good future research topics.

In this research, we investigated Stimulation mechanism by using core-scale laboratory experiments and numerical experiments, then compared the numerical results with two past EGS projects. There are some other ongoing EGS research projects such as EGS Collab project, Utah FORGE in the US, Äspö Hard Rock Laboratory Experiment in Sweden, and Bedretto Underground Laboratory for Geoenergies in Switzerland. Utilizing the data sets and observations from those EGS experiment projects would improve the model to give a deeper insight of the stimulation mechanisms at those sites.

9 Bibliography

- Abe, A., & Horne, R. N. (2019). Investigating the Effect of Wing Cracks on the EGS Reservoir Permeability Enhancement by Hydraulic Stimulation. *American Rock Mechanics Association*.
- Abe, A., & Horne, R. N. (2021). Investigating Mechanical Interactions between Fractures and Fracture Propagation Patterns in an EGS Reservoir. *International Journal of Rock Mechanics and Mining Sciences*, 1–13.
- Abe, A., Ishibashi, T., Asanuma, H., & Horne, R. N. (2019). Numerical Modeling and Laboratory Experiments on a Propagating Hydraulic Fracture Intersecting with a Preexisting Fracture. In *PROCEEDINGS, 43rd Workshop on Geothermal Reservoir Engineering Stanford University* (pp. 1–15). Stanford, California.
- Abe, A., Kim, T. W., & Horne, R. N. (2021). Laboratory hydraulic stimulation experiments to investigate the interaction between newly formed and preexisting fractures. *International Journal of Rock Mechanics and Mining Sciences*, 141(May), 104665.
<https://doi.org/10.1016/j.ijrmms.2021.104665>
- Amann, F., Gischig, V., Evans, K., Doetsch, J., Jalali, R., Valley, B., ... Giardini, D. (2018). The seismo-hydromechanical behavior during deep geothermal reservoir stimulations: Open questions tackled in a decameter-scale in situ stimulation experiment. *Solid Earth*.
<https://doi.org/10.5194/se-9-115-2018>
- Anderson, T. L. (2005). *Fracture Mechanics – Fundamentals and Applications* (Third edit). Boca Raton: CRC Press. [https://doi.org/https://doi.org/10.1201/9781420058215](https://doi.org/10.1201/9781420058215)
- Aydin, A., & Zhong, J. (2018). Rock Fracture Knowledgebase.
<https://doi.org/10.7910/DVN/BKJYNI>
- Aziz, K., & Settari, A. (1979). *Petroleum reservoir simulation*. Applied Science Publishers. Retrieved from <http://www.springer.com/la/book/9780853347873>
- Bandis, S. C., Lumsden, A. C., & Barton, N. R. (1983). Fundamentals of rock joint deformation. *International Journal of Rock Mechanics and Mining Sciences And*, 20(6), 249–268. [https://doi.org/10.1016/0148-9062\(83\)90595-8](https://doi.org/10.1016/0148-9062(83)90595-8)

- Bandis, S., Lumsden, A. C., & Barton, N. R. (1981). Experimental studies of scale effects on the shear behaviour of rock joints. *International Journal of Rock Mechanics and Mining Sciences & Geomechanics Abstracts*, 18(1), 1–21. [https://doi.org/10.1016/0148-9062\(81\)90262-X](https://doi.org/10.1016/0148-9062(81)90262-X)
- Barenblatt, G. I. (1962). The Mathematical Theory of Equilibrium Cracks in Brittle Fracture. *Advances in Applied Mechanics*, 7(C), 55–129. [https://doi.org/10.1016/S0065-2156\(08\)70121-2](https://doi.org/10.1016/S0065-2156(08)70121-2)
- Barton, C. A., Zoback, M. D., & Burns, K. L. (1988). In-Situ Stress Orientation and Magnitude at the Fenton Geothermal Site, New Mexico, Determined From Wekkbore Breakouts. *Geophysical Research Letters*, 15(5), 467–470.
- Barton, C. C. ., & Larsen, E. (1985). Fractal geometry of two-dimensional fracture networks at Yucca Mountain, southwestern Nevada. In *Fundamentals of rock joints: International Symposium on Fundamentals of Rock Joints* (p. Pp.77-84). Bjorkliden, Lapland, Sweden.
- Barton, N., Bandis, S., & Bakhtar, K. (1985). Strength, deformation and conductivity coupling of rock joints. *International Journal of Rock Mechanics and Mining Sciences And*, 22(3), 121–140. [https://doi.org/10.1016/0148-9062\(85\)93227-9](https://doi.org/10.1016/0148-9062(85)93227-9)
- Beugelsdijk, L. J. L., De Pater, C. J., & Sato, K. (2000). Experimental hydraulic fracture propagation in a multi-fractured medium. *Proceedings of the SPE Asia Pacific Conference on Integrated Modelling for Asset Management*, 177–184. <https://doi.org/10.2523/59419-ms>
- Blanton, T. L. (1982). An Experimental Study of Interaction Between Hydraulically Induced and Pre-Existing Fractures. *Society of Petroleum Engineers*. <https://doi.org/10.2118/10847-MS>
- Bobet, A., & Einstein, H. H. (1998). Fracture coalescence in rock-type materials under uniaxial and biaxial compression. *International Journal of Rock Mechanics and Mining Sciences*, 35(7), 863–888. [https://doi.org/10.1016/S0148-9062\(98\)00005-9](https://doi.org/10.1016/S0148-9062(98)00005-9)
- Boese, C., Renner, J., and Dresen, G., & Team, the S. (2020). The STIMTEC experiment at the Reiche Zeche ULab. In *EGU General Assembly 2020*. Online. <https://doi.org/https://doi.org/10.5194/egusphere-egu2020-14117>
- Boese, C., Kwiatek, G., Dresen, G., Renner, J., & Fischer, T. (2021). Characterising induced

acoustic emission activity observed during a mine-scale hydraulic-fracturing experiment in anisotropic crystalline rock.

- Brace, W. F., & Bombolakis, E. G. (1963). A note on brittle crack growth in compression. *Journal of Geophysical Research*, 68(12), 3709–3713. <https://doi.org/10.1029/jz068i012p03709>
- Brown, D. W. (1989). The potential for large errors in the inferred minimum earth stress when using incomplete hydraulic fracturing results. *International Journal of Rock Mechanics and Mining Sciences And*, 26(6), 573–577. [https://doi.org/10.1016/0148-9062\(89\)91437-X](https://doi.org/10.1016/0148-9062(89)91437-X)
- Brown, Donald W., Duchane, D. V., Heiken, G., & Hriscu, V. T. (2012). *Mining earth's heat: Hot dry rock geothermal energy. Mining the Earth's Heat: Hot Dry Rock Geothermal Energy*. Berlin, Heidelberg: Springer-Verlag Berlin Heidelberg. <https://doi.org/10.1007/978-3-540-68910-2>
- Bruna, P.-O., Straubhaar, J., Prabhakaran, R., Bertotti, G., Bisdom, K., Mariethoz, G., & Meda, M. (2019). A new methodology to train fracture network simulation using multiple-point statistics. *Solid Earth*, 10(2), 537–559. <https://doi.org/10.5194/se-10-537-2019>
- Bürgmann, R., & Pollard, D. D. (1994). Strain accommodation about strike-slip fault discontinuities in granitic rock under brittle-to-ductile conditions. *Journal of Structural Geology*, 16(12), 1655–1674. [https://doi.org/10.1016/0191-8141\(94\)90133-3](https://doi.org/10.1016/0191-8141(94)90133-3)
- Chen, Z., Elsworth, D., & Wang, M. (2020). Does Low-Viscosity Fracturing Fluid Always Create Complex Fractures? *Journal of Geophysical Research: Solid Earth*, 125(9), 1–15. <https://doi.org/10.1029/2020JB020332>
- Chen, Z., Yang, Z., & Wang, M. (2018). Hydro-mechanical coupled mechanisms of hydraulic fracture propagation in rocks with cemented natural fractures. *Journal of Petroleum Science and Engineering*, 163(January), 421–434. <https://doi.org/10.1016/j.petrol.2017.12.092>
- Co, C. K. D., Pollard, D. D., & Horne, R. N. (2017). Towards a Better Understanding of the Impact of Fracture Roughness on Permeability-Stress Relationships using First Principles. *PROCEEDINGS Geothermal Reservoir Engineering*.

- Cooke, M. L., Mollema, P. N., Pollard, D. D., & Aydin, A. (2000). Interlayer slip and joint localization in the East Kaibab Monocline, Utah: Field evidence and results from numerical modelling. *Geological Society Special Publication*, 169, 23–49.
<https://doi.org/10.1144/GSL.SP.2000.169.01.03>
- Cooke, Michele L. (1997). *Fracture localization along faults with spatially varying friction*. *JOURNAL OF GEOPHYSICAL RESEARCH* (Vol. 102).
<https://doi.org/10.1029/97JB01829>
- Crandall, D., Moore, J., Gill, M., & Stadelman, M. (2017). CT scanning and flow measurements of shale fractures after multiple shearing events. *International Journal of Rock Mechanics and Mining Sciences*, 100(November), 177–187.
<https://doi.org/10.1016/j.ijrmms.2017.10.016>
- Crouch, S. L., & Starfield, A. M. (1983). *Boundary element methods in solid mechanics : with applications in rock mechanics and geological engineering*. London ; Allen & Unwin.
- Cruikshank, K. M., & Aydin, A. (1994). Role of fracture localization in arch formation, Arches National Park, Utah. *Geological Society of America Bulletin*, 106(7), 879–891.
[https://doi.org/10.1130/0016-7606\(1994\)106<0879:ROFLIA>2.3.CO;2](https://doi.org/10.1130/0016-7606(1994)106<0879:ROFLIA>2.3.CO;2)
- Cruikshank, K. M., & Aydin, A. (1995). Unweaving the joints in Entrada Sandstone, Arches National Park, Utah, U.S.A. *Journal of Structural Geology*, 17(3), 409–421.
[https://doi.org/10.1016/0191-8141\(94\)00061-4](https://doi.org/10.1016/0191-8141(94)00061-4)
- Deichmann, N., Kraft, T., & Evans, K. F. (2014). Identification of faults activated during the stimulation of the Basel geothermal project from cluster analysis and focal mechanisms of the larger magnitude events. *Geothermics*, 52, 84–97.
<https://doi.org/10.1016/j.geothermics.2014.04.001>
- Dirkse, S. P., & Ferris, M. C. (1993). The Path Solver: A Non-Monotone Stabilization Scheme for Mixed Complementarity Problems. *Optimization Methods and Software*, 5(2), 123–156.
- Dresen, Georg; Renner, Joerg; Bohnhoff, Marco; Konietzki, Heinz; Kwiatek, Grzegorz; Plenkers, Katrin; Klee, Gerd; Backers, T. (2019). STIMTEC – a mine-back experiment in the Reiche Zeche underground laboratory. *Geophysical Research Abstracts*, 21, 1.
- Dutler, N., Valley, B., Gischig, V., Jalali, M., Brixel, B., Krietsch, H., ... Amann, F. (2020).

- Hydromechanical insight of fracture opening and closure during in-situ hydraulic fracturing in crystalline rock. *International Journal of Rock Mechanics and Mining Sciences*, 135(September). <https://doi.org/10.1016/j.ijrmms.2020.104450>
- Dutler, N., Valley, B., Gischig, V., Villiger, L., Krietsch, H., Doetsch, J., ... Amann, F. (2019). Hydraulic fracture propagation in a heterogeneous stress field in a crystalline rock mass. *Solid Earth*, 10(6), 1877–1904. <https://doi.org/10.5194/se-10-1877-2019>
- Erdogan, F., & Sih, G. C. (1963). On the Crack Extension in Plates Under Plane Loading and Transverse Shear. *Journal of Basic Engineering*, 85(4), 519–525. <https://doi.org/10.1115/1.3656897>
- Erdogan, Fazil. (1967). Crack Propagation Theories. *Natinal Aeronautics and Space Administration*
- Fehler, M., House, L., & Kaieda, H. (1987). Determining planes along which earthquakes occur: Method and application to earthquakes accompanying hydraulic fracturing. *Journal of Geophysical Research*, 92(B9), 9407. <https://doi.org/10.1029/jb092ib09p09407>
- Ferris, M. C., & Munson, T. S. (1999). Interfaces to PATH 3.0: Design, Implementation and Usage. *Computational Optimization and Applications*, 12(1/3), 207–227. <https://doi.org/10.1023/A:1008636318275>
- Ferris, M. C., & Munson, T. S. (2000). Complementarity Problems in GAMS and the PATH Solver. *Journal of Economic Dynamics and Control*, 24(2), 165–188. [https://doi.org/https://doi.org/10.1016/S0165-1889\(98\)00092-X](https://doi.org/https://doi.org/10.1016/S0165-1889(98)00092-X)
- Finnila, A., Forbes, B., & Podgorney, R. (2019). Building and Utilizing a Discrete Fracture Network Model of the FORGE Utah Site. *Proceedings of the 44th Workshop on Geothermal Reservoir Engineering Stanford University, Stanford, California, February 11-13, 2019*, 1–12.
- Fu, P., Cruz, L., Moos, D., Settgest, R. R., & Ryerson, F. J. (2015). Numerical Investigation of a Hydraulic Fracture Bypassing a Natural Fracture in 3D. In *American Rock Mechanics Association*.
- Fu, Pengcheng, Wu, H., Ju, X., & Morris, J. (2020). Analyzing Fracture Flow Channel Area in EGS Collab Experiment 1 Testbed. In *PROCEEDINGS, 45th Workshop on Geothermal*

Reservoir Engineering.

- Fu, W., Ames, B. C., Bungler, A. P., & Savitski, A. A. (2016). Impact of Partially Cemented and Non-persistent Natural Fractures on Hydraulic Fracture Propagation. *Rock Mechanics and Rock Engineering*, 49, 4519–4526. <https://doi.org/10.1007/s00603-016-1103-0>
- Geertsma, J., & de Klerk, F. (1969). A Rapid Method of Predicting Width and Extent of Hydraulically Induced Fractures. *Journal of Petroleum Technology*, 1571–1581.
- Gidley, J. L., Holditch, S. A., Nierode, D. E., & Veatch Jr, R. W. (1989). *Recent advances in hydraulic fracturing*. (S. of P. E. (U.S.), Ed.). Henry L. Doherty Memorial Fund of AIME, Society of Petroleum Engineers.
- Gischig, V. S., Giardini, D., Amann, F., Hertrich, M., Krietsch, H., Loew, S., ... Valley, B. (2020). Hydraulic stimulation and fluid circulation experiments in underground laboratories: Stepping up the scale towards engineered geothermal systems. *Geomechanics for Energy and the Environment*, 24, 100175. <https://doi.org/10.1016/j.gete.2019.100175>
- Gringarten, A. C., Witherspoon, P. A., & Ohnishi, Y. (1975). Theory of heat extraction from fractured hot dry rock. *Journal of Geophysical Research*, 80(8), 1120–1124. <https://doi.org/10.1029/JB080i008p01120>
- Gu, H., & Weng, X. (2010). Criterion for Fractures Crossing Frictional Interfaces at Non-orthogonal Angles. *American Rock Mechanics Association* .
- Gu, H., Weng, X., Lund, J., Mack, M., Ganguly, U., & Suarez-Rivera, R. (2011). Hydraulic Fracture Crossing Natural Fracture at Non-orthogonal Angles, A Criterion, Its Validation and Applications. *Society of Petroleum Engineers*. <https://doi.org/10.2118/139984-PA>
- Haiqing Wu, & Pollard, D. D. (1992). Propagation of a set of opening-mode fractures in layered brittle materials under uniaxial strain cycling. *Journal of Geophysical Research*, 97(B3), 3381–3396. <https://doi.org/10.1029/91jb02857>
- Häring, M. O., Schanz, U., Ladner, F., & Dyer, B. C. (2008). Characterisation of the Basel 1 enhanced geothermal system. *Geothermics*, 37, 469–495. <https://doi.org/10.1016/j.geothermics.2008.06.002>
- Harris, R. A. (1998). Introduction to Special Section: Stress Triggers, Stress Shadows, and

- Implications for Seismic Hazard. *Journal of Geophysical Research: Solid Earth*, 103(B10), 24347–24358. <https://doi.org/10.1029/98jb01576>
- Helgeson, D. E., & Aydin, A. (1991). Characteristics of joint propagation across layer interfaces in sedimentary rocks. *Journal of Structural Geology*, 13(8), 897–911.
- Hoek, E., & Bieniawski, Z. T. (1965). Brittle fracture propagation in rock under compression. *International Journal of Fracture Mechanics*, 1(3), 137–155. <https://doi.org/10.1007/BF00186851>
- Hoek, E., & Martin, C. D. (2014). Fracture initiation and propagation in intact rock: A review. *Journal of Rock Mechanics and Geotechnical Engineering*, 6, 287–300. <https://doi.org/10.1016/j.jrmge.2014.06.001>
- Horii, H., & Nemat-Nasser, S. (1986). Brittle Failure in Compression: Splitting, Faulting and Brittle-Ductile Transition. *Philosophical Transactions of the Royal Society A: Mathematical, Physical and Engineering Sciences*, 319(1549), 337–374. <https://doi.org/10.1098/rsta.1986.0101>
- House, L., Keppeler, H., & Kaieda, H. (1985). Seismic Studies of a Massive Hydraulic Fracturing Experiment. In *Geothermal Resources Council* (Vol. August 26-). Kailua-Kona, Hawaii, United States.
- Ingraffea, A. R. (1987). 3. Theory of Crack Initiation and Propagation in Rock. In B. K. Atkinson (Ed.), *Fracture Mechanics of Rock* (pp. 71–110). Academic Press.
- Irwin, G. R. (1957). Analysis of Stresses and Strains Near the End of a Crack Traversing a Plate.
- Jaeger, J. C. (John C., Cook, N. G. W., & Zimmerman, R. W. (2007). *Fundamentals of rock mechanics*. Blackwell Pub.
- Johns, R. A., Steude, J. S., Castanier, L. M., & Roberts, P. V. (1993). Nondestructive measurements of fracture aperture in crystalline rock cores using X ray computed tomography. *Journal of Geophysical Research*, 98(B2), 1889–1900. <https://doi.org/10.1029/92JB02298>
- Joussineau, G. de, Mutlu, O., Aydin, A., & Pollard, D. D. (2007a). Characterization of strike-slip fault-splay relationships in sandstone. *Journal of Structural Geology*, 29(11), 1831–1842. <https://doi.org/10.1016/j.jsg.2007.08.006>

- Joussineau, G. de, Mutlu, O., Aydin, A., & Pollard, D. D. (2007b). Characterization of strike-slip fault-splay relationships in sandstone. *Journal of Structural Geology*, 29(11), 1831–1842. <https://doi.org/10.1016/j.jsg.2007.08.006>
- Jung, R. (2013). EGS — Goodbye or Back to the Future. In *Effective and Sustainable Hydraulic Fracturing* (pp. 95–121). <https://doi.org/10.5772/56458>
- Kamali, A., & Ghassemi, A. (2016). Analysis of Natural Fracture Shear Slip and Propagation in Response to Injection. *PROCEEDINGS Geothermal Reservoir Engineering Stanford University*.
- Kamali, A., & Ghassemi, A. (2018). Analysis of injection-induced shear slip and fracture propagation in geothermal reservoir stimulation. *Geothermics*, 76, 93–105. <https://doi.org/10.1016/j.geothermics.2018.07.002>
- Kamali, A., Ghassemi, A., McLennan, J., & Moore, J. (2019). Analysis of FORGE DFIT Considering Hydraulic and Natural Fracture Interactions. In *PROCEEDINGS, 44th Workshop on Geothermal Reservoir Engineering*.
- Karimi-Fard, M., Durlofsky, L. J., & Aziz, K. (2004). An Efficient Discrete-Fracture Model Applicable for General-Purpose Reservoir Simulators. *SPE Journal*.
- Kelkar, S., Murphy, H., & Dash, Z. (1986). Earth Stress Measurements in Deep Granitic Rock. In *The 27th U.S. Symposium on Rock Mechanics (USRMS)* (p. June). Tuscaloosa, Alabama.
- Kettlety, T., Verdon, J. P., Werner, M. J., & Kendall, J. M. (2020). Stress Transfer From Opening Hydraulic Fractures Controls the Distribution of Induced Seismicity. *Journal of Geophysical Research: Solid Earth*, 125(1). <https://doi.org/10.1029/2019JB018794>
- Kettlety, Tom, Verdon, J. P., Werner, M. J., Kendall, J. M., & Budge, J. (2019). Investigating the role of elastostatic stress transfer during hydraulic fracturing-induced fault activation. *Geophysical Journal International*, 217(2), 1200–1216. <https://doi.org/10.1093/gji/ggz080>
- Kim, J., Tchelepi, H. A., & Juanes, R. (2011). Stability, accuracy, and efficiency of sequential methods for coupled flow and geomechanics. *SPE Journal*, 16(2), 249–262. <https://doi.org/10.2118/119084-PA>
- Kling, T., Huo, D., Schwarz, J.-O., Enzmann, F., Benson, S., & Blum, P. (2016). Simulating

- stress-dependent fluid flow in a fractured core sample using real-time X-ray CT data. <https://doi.org/10.5194/se-2016-41>
- Kneafsey, T. J., Blankenship, D., Knox, H. A., Johnson, T. C., Ajo-Franklin, J. B., Schwering, P. C., ... Collab, E. (2019). EGS Collab Project: Status and Progress. In *PROCEEDINGS, 44th Workshop on Geothermal Reservoir Engineering*. Stanford, California.
- Lehner, F., & Kachanov, M. (1996). On modelling of “winged” cracks forming under compression. *International Journal of Fracture*, 77(4), 69–75. <https://doi.org/10.1007/BF00036257>
- Li, Y. P., Chen, L. Z., & Wang, Y. H. (2005). Experimental research on pre-cracked marble under compression. *International Journal of Solids and Structures*, 42(9–10), 2505–2516. <https://doi.org/10.1016/j.ijsolstr.2004.09.033>
- López-Comino, J. A., Cesca, S., Heimann, S., Grigoli, F., Milkereit, C., Dahm, T., & Zang, A. (2017). Characterization of Hydraulic Fractures Growth During the Äspö Hard Rock Laboratory Experiment (Sweden). *Rock Mechanics and Rock Engineering*, 50(11), 2985–3001. <https://doi.org/10.1007/s00603-017-1285-0>
- Martel, S. J. (1997). Effects of cohesive zones on small faults and implications for secondary fracturing and fault trace geometry. *Journal of Structural Geology*, 19(6), 835–847. [https://doi.org/10.1016/S0191-8141\(97\)00002-3](https://doi.org/10.1016/S0191-8141(97)00002-3)
- Martel, S. J., & Boger, W. A. (1998). Geometry and mechanics of secondary fracturing around small three-dimensional faults in granitic rock. *Journal of Geophysical Research: Solid Earth*, 103(9), 21299–21314. <https://doi.org/10.1029/98jb01393>
- Martel, S. J., Pollard, D. D., & Segall, P. (1988). Development of simple strike-slip fault zones, Mount Abbot quadrangle, Sierra Nevada, California. *Geological Society of America Bulletin*, 100, 1451–1465.
- Maxwell, S. C., Weng, X., Kresse, O., & Rutledge, J. (2013). Modeling Microseismic Hydraulic Fracture Deformation. In *SPE Annual Technical Conference*.
- McClure, M. W. (2014). Stimulation Mechanism and the Direction of Propagation of Microseismicity. *PROCEEDINGS, Thirty-Ninth Workshop on Geothermal Reservoir Engineering Stanford University*.

- McClure, M. W. (2012). *Modeling and Characterization of Hydraulic Stimulation and Induced Seismicity in Geothermal and Shale Gas Reservoirs*. Stanford University.
- McClure, M. W. (2014). The Relationship between Stimulation Mechanism and Sweet Spot Identification*. <https://doi.org/10.1029/95JB00862>
- McClure, M. W., & Horne, R. N. (2014). An investigation of stimulation mechanisms in Enhanced Geothermal Systems. *International Journal of Rock Mechanics and Mining Sciences*, 72, 242–260. <https://doi.org/10.1016/j.ijrmms.2014.07.011>
- Mériaux, C., & Lister, J. R. (2002). Calculation of dike trajectories from volcanic centers. *Journal of Geophysical Research: Solid Earth*, 107(B4), ETG 10-1-ETG 10-10. <https://doi.org/10.1029/2001JB000436>
- Moore, J., McLennan, J., Pankow, K., Simmons, S., Podgorney, R., Wannamaker, P., ... Xing, P. (2020). The Utah Frontier Observatory for Research in Geothermal Energy (FORGE): A Laboratory for Characterizing, Creating and Sustaining Enhanced Geothermal Systems. In *PROCEEDINGS*.
- Mukuhira, Y., Dinske, C., Asanuma, H., Ito, T., & Häring, M. O. (2017). Pore pressure behavior at the shut-in phase and causality of large induced seismicity at Basel, Switzerland. *Journal of Geophysical Research: Solid Earth*, 122(1), 411–435. <https://doi.org/10.1002/2016JB013338>
- Murakami, Y., & Nemat-Nasser, S. (1983). Growth and stability of interacting surface flaws of arbitrary shape. *Engineering Fracture Mechanics*, 17(3), 193–210. [https://doi.org/10.1016/0013-7944\(83\)90027-9](https://doi.org/10.1016/0013-7944(83)90027-9)
- Mutlu, O., & Pollard, D. D. (2008). On the patterns of wing cracks along an outcrop scale flaw: A numerical modeling approach using complementarity. *Journal of Geophysical Research: Solid Earth*, 113(6), 1–20. <https://doi.org/10.1029/2007JB005284>
- Nagel, N. B., & Sanchez-Nagel, M. (2011). Stress Shadowing and Microseismic Events: A Numerical Evaluation. *SPE*.
- National Academy of Sciences. (1996). *Rock Fractures and Fluid Flow: Contemporary Understanding and Applications*. Rock Fractures and Fluid Flow. NATIONAL ACADEMY PRESS Washington, D.C. <https://doi.org/10.17226/2309>
- National Research Council. (1996). *Rock Fractures and Fluid Flow: Contemporary*

- Understanding and Applications. Rock Fractures and Fluid Flow*. Washington, DC: The National Academies Press. <https://doi.org/10.17226/2309>
- Neuzil, C. E., & Tracy, J. V. (1981). Flow Through Fractures. *WATER RESOURCES RESEARCH*, 17(1), 191–199.
- Niemz, P., Cesca, S., Heimann, S., Grigoli, F., Von Specht, S., Hammer, C., ... Dahm, T. (2020). Full-waveform-based characterization of acoustic emission activity in a mine-scale experiment: A comparison of conventional and advanced hydraulic fracturing schemes. *Geophysical Journal International*, 222(1), 189–206. <https://doi.org/10.1093/gji/ggaa127>
- Norbeck, J. H. (2016). Hydromechanical and frictional faulting behavior of fluidinjectioninduced earthquake. *Stanford PhD Dissertation*.
- Norbeck, J. H., McClure, M. W., & Horne, R. N. (2018). Field observations at the Fenton Hill enhanced geothermal system test site support mixed-mechanism stimulation. *Geothermics*, 74(February), 135–149. <https://doi.org/10.1016/j.geothermics.2018.03.003>
- Norbeck, J. H., McClure, M. W., Lo, J. W., & Horne, R. N. (2016). An embedded fracture modeling framework for simulation of hydraulic fracturing and shear stimulation. *Comput Geosci*, 20, 1–18. <https://doi.org/10.1007/s10596-015-9543-2>
- Norbeck, J. H., & Shelly, D. R. (2018). Exploring the Role of Mixed-Mechanism Fracturing and Fluid-Faulting Interactions During the 2014 Long Valley Caldera, California, Earthquake Swarm. In *PROCEEDINGS Geothermal Reservoir Engineering Stanford University*.
- Nordgren, R. P. (1972). Propagation of a Vertical Hydraulic Fracture. *Society of Petroleum Engineering*, 3009.
- Olson, J. E. (1991). *Fracture mechanics analysis of joints and veins*. Stanford University.
- Olson, J. E. (2008). Multi-fracture propagation modeling: Applications to hydraulic fracturing in shales and tight gas sands. *The 42nd US Rock Mechanics Symposium*.
- Palisch, T. T., Vincent, M. C., & Handren, P. J. (2010). Slickwater Fracturing: Food for Thought. *SPE Production & Operations*, 327.
- Paterson, M. S., & Wong, T. (2005). *Experimental rock deformation--the brittle field*. Springer.

- Perkins, T. K., & Kern, L. R. (1961). Widths of Hydraulic Fractures. *Journal of Petroleum Technology*, 13(09), 937–949. <https://doi.org/10.2118/89-PA>
- Petit, J., & Barquins, M. (1988). Can natural faults propagate under mode II conditions? *Tectonics*, 7(6), 1243–1256.
- Pollard, D. D., & Aydin, A. (1988). Progress in understanding jointing over the past century. *Geological Society of America Bulletin*, 100, 1181–1204.
- Pollard, D. D., & Fletcher, R. C. (2005). *Fundamentals of structural geology*. Cambridge University Press.
- Pollard, D. D., & Segall, P. (1987). 8. Theoretical Displacements and Stresses Near Fractures in Rock: with Applications to Faults, Joints, Veins, Dikes, and Solution Surfaces. In B. K. Atkinson (Ed.), *Fracture Mechanics of Rock* (pp. 277–313). Academic Press Inc. (London) Ltd.
- Renshaw, C. E., & Pollard, D. D. (1995). An Experimentally Verified Criterion for Propagation Across Unbounded Frictional Interfaces in Brittle, Linear Elastic Materials. *J. Rock Mech. Min. Sci. & Geomech. Abstr.*, 32(3), 237–249.
- Rinaldi, A. P., & Rutqvist, J. (2019). Joint opening or hydroshearing? Analyzing a fracture zone stimulation at Fenton Hill. *Geothermics*, 77, 83–98. <https://doi.org/10.1016/j.geothermics.2018.08.006>
- Ritz, E., Mutlu, O., & Pollard, D. D. (2012). Integrating complementarity into the 2D displacement discontinuity boundary element method to model faults and fractures with frictional contact properties. *Computers & Geosciences*, 45, 304–312. <https://doi.org/10.1016/J.CAGEO.2011.11.017>
- Ritz, E., Pollard, D. D., & Ferris, M. (2015). The influence of fault geometry on small strike-slip fault mechanics. *Journal of Structural Geology*, 73, 49–63. <https://doi.org/10.1016/j.jsg.2014.12.007>
- Ruth A. Harris & Robert W. Simpson. (1992). Changes in static stress on southern California faults after the 1992 Landers earthquake . *NATURE*, 360(19). Retrieved from <https://www.nature.com/articles/360251a0.pdf>
- Sahouryeh, E., Dyskin, A. V., & Germanovich, L. N. (2002). Crack growth under biaxial compression. *Engineering Fracture Mechanics*, 69(18), 2187–2198.

[https://doi.org/10.1016/S0013-7944\(02\)00015-2](https://doi.org/10.1016/S0013-7944(02)00015-2)

Schoenball, M., Ajo-Franklin, J. B., Blankenship, D., Chai, C., Chakravarty, A., Dobson, P., ... Wood, T. (2020). Creation of a Mixed-Mode Fracture Network at Mesoscale Through Hydraulic Fracturing and Shear Stimulation. *Journal of Geophysical Research: Solid Earth*, 125(12), 1–21. <https://doi.org/10.1029/2020jb019807>

Segall, P. (2010). *Earthquake and volcano deformation*. Princeton University Press.

Segall, P., & Pollard, D. D. (1983). Joint formation in granitic rock of the Sierra Nevada. *Geological Society of America Bulletin*, 94, 563–575.

Shakas, A., Maurer, H., Giertzuch, P. L., Hertrich, M., Giardini, D., Serbeto, F., & Meier, P. (2020). Permeability Enhancement From a Hydraulic Stimulation Imaged With Ground Penetrating Radar. *Geophysical Research Letters*, 47(17), 1–10. <https://doi.org/10.1029/2020GL088783>

Singh, A., Zoback, M., & McClure, M. (2020). Optimization of multi-stage hydraulic fracturing in unconventional reservoirs in the context of stress variations with depth. *Proceedings - SPE Annual Technical Conference and Exhibition, 2020-October(2019)*. <https://doi.org/10.2118/201739-ms>

Thomas, A. L., & Pollard, D. D. (1993). The geometry of echelon fractures in rock: implications from laboratory and numerical experiments. *Journal of Structural Geology*, 15(3–5), 323–334. [https://doi.org/10.1016/0191-8141\(93\)90129-X](https://doi.org/10.1016/0191-8141(93)90129-X)

Valley, B., & Evans, K. F. (2009). Stress orientation to 5 km depth in the basement below Basel (Switzerland) from borehole failure analysis. *Swiss Journal of Geosciences*, 102(3), 467–480. <https://doi.org/10.1007/s00015-009-1335-z>

Valley, B., & Evans, K. F. (2019). Stress magnitudes in the Basel enhanced geothermal system. *International Journal of Rock Mechanics and Mining Sciences*, 118(April), 1–20. <https://doi.org/10.1016/j.ijrmms.2019.03.008>

Warpinski, N. R., & Branagan, P. T. (1989). Altered-Stress Fracturing. *Journal of Petroleum Technology*, 41(9). <https://doi.org/10.2118/17533-PA>

Warpinski, N. R., Kramm, R. C., Heinze, J. R., & Waltman, C. K. (2005). Comparison of single- and dual-array microseismic mapping techniques in the barnett shale. In *Proceedings - SPE Annual Technical Conference and Exhibition* (pp. 913–922).

- Warpinski, N. R., & Teufel, L. W. (1987). Influence of Geologic Discontinuities on Hydraulic Fracture Propagation. *Journal of Petroleum Technology*, 39(02), 209–220.
<https://doi.org/10.2118/13224-pa>
- Weng, X. (2015). Modeling of complex hydraulic fractures in naturally fractured formation. *Journal of Unconventional Oil and Gas Resources*, 9, 114–135.
<https://doi.org/10.1016/j.juogr.2014.07.001>
- Weng, X., Kresse, O., Cohen, C., Wu, R., & Gu, H. (2011). Modeling of Hydraulic-Fracture-Network Propagation in a Naturally Fractured Formation. *SPE Production & Operations*, 26(4), 368–380.
- Willis-Richards, J., Watanabe, K., & Takahashi, H. (1996). Progress toward a stochastic rock mechanic model of engineered geothermal systems. *Journal of Geophysical Research*, 101(88), 17, 481–17, 496.
- Wu, H., & Pollard, D. D. (2002). Imaging 3-D Fracture Networks Around Boreholes. *The American Association of Petroleum Geologists Bulletin*, 86(4), 593–604.
- Wu, K., & Olson, J. E. (2014a). Mechanics analysis of interaction between hydraulic and natural fractures in shale reservoirs. *Society of Petroleum Engineers - SPE/AAPG/SEG Unconventional Resources Technology Conference*. <https://doi.org/10.15530/urtec-2014-1922946>
- Wu, K., & Olson, J. E. (2014b). Mechanics Analysis of Interaction Between Hydraulic and Natural Fractures in Shale Reservoirs. *Proceedings of the 2nd Unconventional Resources Technology Conference*, (January). <https://doi.org/10.15530/urtec-2014-1922946>
- Wu, K., & Olson, J. E. (2016). Mechanisms of Simultaneous Hydraulic-Fracture Propagation From Multiple Perforation Clusters in Horizontal Wells. *SPE Journal*.
<https://doi.org/10.2118/178925-PA>
- Xing, P., Damjanac, B., Radakovic-guzina, Z., Finnilla, A., Podgorney, R., & Moore, J. (2021). Numerical Simulation of Injection Tests at Utah FORGE Site. In *46th Workshop on Geothermal Reservoir Engineering* (pp. 1–14). Stanford, California.
- Zang, A., & Stephansson, O. (2010). Stress field of the earth's crust. *Stress Field of the Earth's Crust*, 1–322. <https://doi.org/10.1007/978-1-4020-8444-7>
- Zang, A., Stephansson, O., Stenberg, L., Plenkers, K., Specht, S., Milkereit, C., ... Weber, M.

- (2017). Hydraulic fracture monitoring in hard rock at 410 m depth with an advanced fluid-injection protocol and extensive sensor array. *Geophysical Journal International*, 208(2), 790–813. <https://doi.org/10.1093/gji/ggw430>
- Zhou, J., Chen, M., Jin, Y., & Zhang, G.-Q. (2008). Analysis of fracture propagation behavior and fracture geometry using a tri-axial fracturing system in naturally fractured reservoirs. *International Journal of Rock Mechanics & Mining Sciences*, 45, 1143–1152. <https://doi.org/10.1016/j.ijrmms.2008.01.001>
- Ziegler, M., & Evans, K. F. (2020). Comparative study of Basel EGS reservoir faults inferred from analysis of microseismic cluster datasets with fracture zones obtained from well log analysis. *Journal of Structural Geology*, 130(June 2019), 103923. <https://doi.org/10.1016/j.jsg.2019.103923>
- Ziegler, M., Valley, B., & Evans, K. F. (2015). Characterisation of Natural Fractures and Fracture Zones of the Basel EGS Reservoir Inferred from Geophysical Logging of the Basel-1 Well. *Proceedings World Geothermal Congress 2015*, (April), 19–25. Retrieved from <https://pangea.stanford.edu/ERE/db/WGC/papers/WGC/2015/31003.pdf>
- Zimmerman, R. W., & Bodvarsson, G. S. (1996). Hydraulic conductivity of rock fractures. *Transport in Porous Media*, 23(1), 1–30. <https://doi.org/10.1007/BF00145263>
- Zoback, M. D. (2007). *Reservoir geomechanics*. Cambridge University Press.
- Zoback, M. D., & Lund Snee, J.-E. (2018). Predicted and observed shear on preexisting faults during hydraulic fracture stimulation, 3588–3592. <https://doi.org/10.1190/segam2018-2991018.1>